# Features of Vector Boson Dark Matter and Discovery Potential

Basabendu Barman

*A thesis*
*submitted for the degree of*

**Doctor of Philosophy**

Supervisor

**Dr. Subhaditya Bhattacharya**


Department of Physics
Indian Institute of Technology Guwahati
Guwahati - 781039, Assam, India

# Features of Vector Boson Dark Matter and Discovery Potential

*A thesis submitted by*

Basabendu Barman

to

Indian Institute of Technology Guwahati
in partial fulfillment of the requirements
for the award of the degree of
Doctor of Philosophy in Physics

Supervisor

**Dr. Subhaditya Bhattacharya**


Department of Physics
Indian Institute of Technology Guwahati
Guwahati - 781039, Assam, India

"We shall not cease from exploration
And the end of all our exploring
Will be to arrive where we started
And know the place for the first time."

**-T. S. Eliot, Four Quartets**

# *Declaration*

**Basabendu Barman**
Roll No. 156121033
Department of Physics
IIT Guwahati
Guwahati, India

---

I hereby declare that works presented in the thesis entitled "**Features of Vector Boson Dark Matter and Discovery Potential**" has been carried out by me under the supervision of Dr. Subhaditya Bhattacharya at the Department of Physics, Indian Institute of Technology Guwahati, India. The thesis has not been submitted anywhere else for any degree. Works presented in the thesis are all my own unless referenced to the contrary in the thesis.

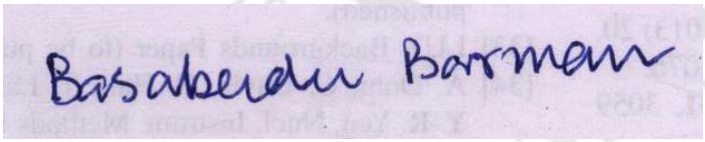

Basabendu Barman

Date 9/11/20

# *Certificate*

**Dr. Subhaditya Bhattacharya**
Associate Professor
Department of Physics
Indian Institute of Technology Guwahati
Guwahati, India
email:subhab@iitg.ac.in

---

It is certified that the work contained in the thesis entitled "**Features of Vector Boson Dark Matter and Discovery Potential**" by Mr. Basabendu Barman (Roll No - 156121033), a Ph.D. student in the Department of Physics, Indian Institute of Technology Guwahati is carried out under my supervision and has not been submitted elsewhere for the award of any other degree.

Dr. Subhaditya Bhattacharya

Date : 9/11/2020

# *Acknowledgements*

First and foremost, I would like to express my deepest gratitude towards my supervisor Dr. Subhaditya Bhattacharya for all the guidance, stimulation and support he has given to me during my PhD. Most importantly, he gave me every freedom to span my research interest, explore challenging things and work as an individual with new collaborations. I have learned a great deal from him not just about how to be a good researcher or an eloquent speaker, but also to be patient, honest and diligent. It was indeed a great learning experience for me altogether.

I am grateful to my doctoral committee members Dr. Arunansu Sil, Dr. Debasish Borah and Dr. Budhaditya Hazra for their insightful comments and suggestions whenever needed. I must acknowledge Hemanta Da and Basab Da for their cooperation with computational issues. I would also like to thank all the members of the HEP journal club for providing a platform to keep myself updated with new trends in high energy physics. Keep brainstorming fellas! Cheers!

I thank all my collaborators and co-authors: Dr. Debasish Borah, Dr. Tapobroto Bhanja, Dr. Joydeep Chakrabortty, Dr. Debottam Das, Prof. Bohdan Grzadkowski, Dr. Debaprasad Maity, Dr. Soumitra Nandi, Dr. Narendra Sahu, Dr. Mohammedreza Zakeri, Saurabh Kadam, Lopamudra Mukherjee and Avik Paul. It was because of them that I got the opportunity to work on various problems and in the process acquired a great extent of knowledge and experience. I am especially thankful to friends cum collaborators Amit Dutta Banik, Purusottam Ghosh, Abhijit Kumar Saha and Rishav Roshan for having exciting academic discussions (that includes where to find good restaurants in the city). I extend my gratitude to Dr. Anirban Biswas, Dr. Ashmita Das, Dr. Biswajit Karmakar and Dr. Manoj Kumar Mandal with whom I had many fascinating discussions. I am also grateful to Dr. Joydeep Chakrabortty and IIT Kanpur for their hospitality and partial support during my visits.

The list of acknowledgement would be incomplete without mentioning three of my seniors: Dr. Sunando Kumar Patra, Dr. Subhadeep Mondal and Dr. Rasidul Islam to whom I am indebted. It is for them that now I am 'pretty decent' in handling programming language. Also, a special thanks to Dr. Flip Tanedo for sharing his notes with me during very early stage of my PhD. I thank all my friends and colleagues, particularly Krishnanjan, Srimoy, Sreemanti, Sneha, Ramiz, Kallol, Asish, Sourav, Dibyendu, Rajesh with whom I exchanged many valuable thoughts on physics and non-physics topics. I am thankful to everyone who have been a part of this journey.

Since this thesis is being completed amidst a global pandemic, hence I must acknowledge every individual who is fighting COVID-19. Together we will come through this.

Last, but not the least, I would like to convey a very special thanks to my parents for their unconditional love as well as their invaluable support and understanding throughout my academic career.

# Acronyms

| | | |
|---|---|---|
| SM | : | Standard Model |
| EW | : | Electroweak |
| EWSB | : | Electroweak Symmetry Breaking |
| SSB | : | Spontaneous Symmetry Breaking |
| VEV | : | Vacuum Expectation Value |
| BSM | : | Beyond Standard Model |
| DM | : | Dark Matter |
| CDM | : | Cold Dark Matter |
| VDM | : | Vector Dark Matter |
| VBDM | : | Vector Boson Dark Matter |
| WIMP | : | Weakly Interacting Massive Particles |
| FIMP | : | Feebly Interacting Massive Particles |
| SIMP | : | Strongly Interacting Massive Particles |
| LHC | : | Large Hadron Collider |
| BR | : | Branching Ratio |
| BP | : | Benchmark Points |
| H.c. | : | Hermitian Conjugate |
| NP | : | New Physics |
| MeV | : | Mega electron Volt |
| GeV | : | Giga electron Volt |
| TeV | : | Tera electron Volt |
| BEQ | : | Boltzmann Equation |
| EFT | : | Effective Field Theory |
| DOF | : | degrees of freedom |

# Abstract

The discovery of the 'Higgs' boson, the last missing piece of the Standard Model (SM) of particle physics, at the Large Hadron Collider (LHC) in 2012 validates SM as the fundamental governing theory of strong, weak and electromagnetic interactions. SM is remarkably successful and has withstood over two decades of precision tests. It does, however, leave several questions unanswered, motivating the search for new physics (NP) beyond the SM. One of them being a particle description of non-luminous and non-baryonic form of matter, popularly known as dark matter (DM), well established via several astrophysical observations to constitute almost 26% energy budget of the universe. These observations suggest that DM is electromagnetically neutral and stable at the scale of universe's life time; although we do not have any idea about the intrinsic properties *e.g.,* its spin (whether it is a spin-0, spin-1 or spin-1/2 particle) or the nature of its interaction with the visible sector. The focal theme of the thesis is to analyze the possibilities of a vector boson (spin-1) particle to be a potential DM candidate, its production via (i) thermal freeze-out and (ii) non thermal freeze-in to achieve correct relic density and its detection possibilities in direct and collider searches. Existence of non-zero but tiny neutrino mass is also a known feature that can not be explained within the SM paradigm. Seesaw mechanisms of different types thus have been ideated, and we aspire to address both DM and neutrino mass generation in the same model framework and highlight the connection wherever possible. Apart from Ultra Violet (UV) complete models, effective theory (EFT) approach to address vector boson DM has also been studied here. The thesis contains four main chapters of original work. The first work (Chapter. 3) elaborates upon a non-abelian ($SU(2)$) vector boson DM which can couple to SM quarks (along with exotic ones), and have interesting phenomenology at direct search and at the Large Hadron Collider (LHC). Unification of gauge couplings at high energy provide important constraints to the available parameter space. In the second work (Chapter. 4), a different realization of non-abelian vector DM is considered that can give rise to a multipartite DM scenario enabling DM-DM interactions to play a part. Freeze-in realization of vector boson DM is discussed in Chapter. 5 where the DM-SM interaction becomes feeble and provides distinguishable phenomenological consequences. In this context, we derive a generic prescription of DM freeze-in from late decays of particle(s) frozen out of equilibrium. Finally, we focus on a dimension five operator that inherits an abelian vector boson DM and discuss the freeze-in production for large new physics scale in Chapter. 6. Importantly, we show the limitations of the vanilla UV freeze-in when the reheat temperature of the universe becomes comparable to the TeV-scale DM mass. Apart from that, SM along with its limitations are introduced in Chapter. 1. Chapter. 2 provides an in-depth description of DM, neutrino mass and GUT physics. We conclude in Chapter. 7, mentioning future directions to explore.

# List of Publications

1⋆. Non-Abelian Vector Boson Dark Matter, its Unified Route and signatures at the LHC,
**Basabendu Barman**, Subhaditya Bhattacharya, Sunando Kumar Patra (IIT, Guwahati), Joydeep Chakrabortty (IIT, Kanpur),
*e*print: arXiv:1704.04945 (hep-ph),
published in **JCAP12(2017)021**.

2⋆. Multipartite Dark Matter in $SU(2)_N$ extension of Standard Model and signatures at the LHC,
**Basabendu Barman**, Subhaditya Bhattacharya (IIT, Guwahati), Mohammadreza Zakeri (Institute of Theoretical Physics, Chinese Academy of Sciences),
*e*print: arXiv:1806.01129 (hep-ph),
published in **JCAP09(2018)023**.

3. Correlating the anomalous results in $b \to s$ decays with inert Higgs doublet dark matter and muon $g-2$,
**Basabendu Barman**, Debasish Borah, Lopamudra Mukherjee, Soumitra Nandi (IIT, Guwahati),
*e*print: arXiv:1808.06639 (hep-ph),
published in **Phys. Rev. D 100, 115010** .

4. Fermion Dark Matter with Scalar Triplet at Direct and Collider Searches,
**Basabendu Barman**, Subhaditya Bhattacharya, Purusottam Ghosh (IIT, Guwahati), Saurabh Kadam (IISER, Pune), Narendra Sahu (IIT, Hyderabad),
*e*print: arXiv:1902.01217 (hep-ph),
published in **Phys. Rev. D 100, 015027**.

5⋆. Non-Abelian Vector Boson as FIMP Dark Matter,
**Basabendu Barman**, Subhaditya Bhattacharya (IIT, Guwahati), Mohammadreza Zakeri (Institute of Theoretical Physics, Chinese Academy of Sciences),
*e*print: arXiv:1905.07236 (hep-ph),
published in **JCAP02(2020)029**.

6. Flavoured gauge extension of singlet-doublet fermionic dark matter: neutrino mass, high scale validity and collider signatures,
**Basabendu Barman**, Debasish Borah, Purusottam Ghosh (IIT, Guwahati), Abhijit Kumar Saha (Theoretical Physics Division, Physical Research Laboratory),
*e*print: arXiv:1907.10071 (hep-ph),
published in **JHEP10(2019)275**.

7. A Minimal Model of Torsion Mediated Dark Matter,
**Basabendu Barman**, Tapobroto Bhanja (IIT, Guwahati), Debottam Das (Institute of Physics, Bhubaneswar), Debaprasad Maity (IIT, Guwahati),
*e*print: arXiv:1912.09249 (hep-ph),
published in **Phys.Rev.D 101 (2020) 7, 075017**.

8. Singlet-Doublet Fermionic Dark Matter and Gravitational Wave in Two Higgs Doublet Extension of the Standard Model,
**Basabendu Barman** (IIT, Guwahati), Amit Dutta Banik (Key Laboratory of Quark and Lepton Physics (MoE) and Institute of Particle Physics, Central China Normal University), Avik Paul (Astroparticle Physics and Cosmology Division, Saha Institute of Nuclear Physics),
*e*print: arXiv:1912.12899 (hep-ph),
published in **Phys.Rev.D 101 (2020) 5, 055028.**.

9. Effective Theory of Freeze-in Dark Matter,
**Basabendu Barman**, Debasish Borah, Rishav Roshan (IIT, Guwahati),
*e*print: arXiv:2007.08768 (hep-ph),
accepted for publication in JCAP.

10⋆. Feebly coupled vector boson dark matter in effective theory,
**Basabendu Barman**, Subhaditya Bhattacharya (IIT, Guwahati), Bohdan Grzadkowski (Faculty of Physics, University of Warsaw)
*e*print: arXiv:2009.07438 (hep-ph),
submitted to JHEP.

---

Note: ⋆ marked publications are included in the thesis.

# Contents

Chapter 1

# Introduction

## Contents



## 1.1 The irrefutable Standard Model

At the very outset, we would like to discuss the Standard Model (SM) of particle physics very briefly mentioning its particle content, underlying symmetry principles and some of its pitfalls to pave the way for discussion on physics beyond the Standard Model, the thematic topic of this thesis.

The Standard Model (SM) of particle physics describes the fundamental constituents of the universe and their interaction under three fundamental forces of nature, namely: strong, weak and electromagnetic interaction [1–5]. Quantum field theory is the basic building block of this model where physical particles and their interactions are described by quantum fields. The main ingredient of interactions between all the particles under different forces lies in the concept of gauge theory. The underlying gauge symmetry of SM is $\mathcal{G}_{\rm SM} \equiv SU(3)_C \otimes SU(2)_L \otimes U(1)_Y$, where $SU(3)_C$ describes strong interaction ($'c'$ stands for corresponding colour charge), and $SU(2)_L \otimes U(1)_Y$ embeds weak and electromagnetic interaction. The transformation properties of the fields under the above symmetry are mentioned in Tab. 1.1. Quarks take part in all interactions and therefore transforms under all the gauge groups, while leptons only possess weak and electromagnetic interactions and are singlets under $SU(3)$. Importantly, left and right-chiral components (helicity states in massless limit) of four component Dirac fermion fields ($\psi$) transform differently under $SU(2)_L \otimes U(1)_Y$.

$$\psi_L = \frac{1}{2}\left(1 - \gamma_5\right)\psi \equiv P_L\psi \tag{1.1}$$

$$\psi_R = \frac{1}{2}\left(1 + \gamma_5\right)\psi \equiv P_R\psi. \tag{1.2}$$

In SM, neutrinos are assumed only to be left handed with right chiral components absent to yield a massless state.

| Fields | | | $SU(3)_C \otimes SU(2)_L \otimes U(1)_Y$ |
|---|---|---|---|
| Quarks | LH: $Q_L = \begin{pmatrix} q_L^u \\ q_L^d \end{pmatrix}$ | $\begin{pmatrix} u_L^i \\ d_L^i \end{pmatrix}, \begin{pmatrix} c_L^i \\ s_L^i \end{pmatrix}, \begin{pmatrix} t_L^i \\ b_L^i \end{pmatrix}$ | $(3,\ 2,\ 1/3)$ |
| | RH: $q_R^u$ | $u_R^i,\ c_R^i,\ t_R^i$ | $(3,\ 1,\ 4/3)$ |
| | RH: $q_R^d$ | $d_R^i,\ s_R^i,\ b_R^i$ | $(3,\ 1, -2/3)$ |
| Leptons | LH: $L_L = \begin{pmatrix} \nu_{\ell L} \\ \ell_L \end{pmatrix}$ | $\begin{pmatrix} \nu_{eL} \\ e_L \end{pmatrix}, \begin{pmatrix} \nu_{\mu L} \\ \mu_L \end{pmatrix}, \begin{pmatrix} \nu_{\tau L} \\ \tau_L \end{pmatrix}$ | $(1,\ 2, -1)$ |
| | RH: $\ell_R$ | $e_R,\ \mu_R,\ \tau_R$ | $(1,\ 1,\ -2)$ |
| Gauge bosons | $SU(3)_C$ mediator: | $G_\mu^a$ | $(8,\ 1,\ 0)$ |
| | $SU(2)_L$ mediator: | $W_\mu^{1,2,3}$ | $(1,\ 3,\ 0)$ |
| | $U(1)_Y$ mediator: | $B_\mu$ | $(1,\ 1,\ 0)$ |
| Scalar | Higgs: $H$ | $\begin{pmatrix} \phi^+ \\ \phi_0 \end{pmatrix}$ | $(1,\ 2,\ 1)$ |

**Table 1.1:** Charge assignment of SM fields under the SM gauge group $\mathcal{G}_{\rm SM} \equiv SU(3)_C \otimes SU(2)_L \otimes U(1)_Y$. Electromagnetic charge is obtained by: $Q = I_3 + \frac{Y}{2}$, where $I_3$ is the third component of isospin and $Y$ is the $U(1)_Y$ hypercharge quantum number. Here $i = r, g, b$ and $a = 1, 2, .., 8$ represent colour charges of quarks and gluon respectively.

The left-handed (LH) fermions transform as doublet under the weak isospin symmetry $SU(2)_L$, while the right-handed (RH) ones are singlets under the same gauge group. Corresponding to each gauge group gauge bosons transform under adjoint representation to allow an interaction with the fermionic matter content of the universe and therefore dubbed as the 'force carriers' for that interaction. For example, there are eight gluons corresponding to eight $(3^2-1=8)$ $SU(3)_C$ generators, which mediate strong force. The $SU(2)_L \otimes U(1)_Y$ or the electroweak sector has four gauge bosons, out of which $(W^\pm, Z)$ mediate weak interaction and and photon $(A)$ mediates electromagnetic interaction. The only scalar field in the SM is the Higgs boson, responsible for mass generation has been long-sought-after, which has been discovered in 2012 at the Large Hadron Collider (LHC) and thus completes the picture of the SM. The Higgs is colour singlet but doublet under $SU(2)_L$ and also has non-zero hypercharge. With all the candidates and the symmetry introduced, the SM Lagrangian under the gauge symmetry $SU(3)_c \times SU(2)_L \times U(1)_Y$ can be written as:

$$\mathcal{L}_{\rm SM} \;=\; \mathcal{L}_{\rm Gauge} + \mathcal{L}_{\rm Fermion} + \mathcal{L}_{\rm Yukawa} + \mathcal{L}_{\rm Scalar}. \tag{1.3}$$

The $\mathcal{L}_{\rm Gauge}$ in Eqn.1.3 involving $SU(3)_C$, $SU(2)_L$ and $U(1)_Y$ gauge fields can be written as

$$\mathcal{L}_{\rm Gauge} \;=\; -\frac{1}{4} W^i_{\mu\nu} W^{\mu\nu i} - \frac{1}{4} B_{\mu\nu} B^{\mu\nu} - \frac{1}{4} G^a_{\mu\nu} G^{\mu\nu a}, \tag{1.4}$$

where $(i = 1, 2, 3,\ a = 1, 2, ..8)$

$$
\begin{aligned}
B_{\mu\nu} &= \partial_\mu B_\nu - \partial_\nu B_\mu \\
W^i_{\mu\nu} &= \partial_\mu W^i_\nu - \partial_\nu W^i_\mu + g_2 \epsilon^{ijk} W^j_\mu W^k_\nu \\
G^a_{\mu\nu} &= \partial_\mu G^a_\nu - \partial_\nu G^a_\mu + g_s f^{abc} G^b_\mu G^c_\nu;
\end{aligned}
\tag{1.5}
$$

where $\epsilon^{ijk}$, $f^{abc}$ represent structure constants of $SU(2)$ and $SU(3)$ gauge groups; $g_1$, $g_2$ and $g_s$ represent characteristic coupling constants corresponding to $U(1)_Y$, $SU(2)_L$ and $SU(3)_c$ gauge groups respectively. The kinetic terms for fermions (leptons and quark) are given by

$$
\begin{aligned}
\mathcal{L}_{\text{Fermion}} &= \overline{Q_L}\, i\gamma^\mu \Big(\partial_\mu - i g_s \frac{\lambda^a}{2} G^a_\mu - i g_2 \frac{\sigma^i}{2} W^i_\mu - i g_1 \frac{Y_{Q_L}}{2} B_\mu\Big) Q_L \\
&+ \overline{q^u_R} i\gamma^\mu \Big(\partial_\mu - i g_s \frac{\lambda^a}{2} G^a_\mu - i g_1 \frac{Y_{q^u_R}}{2} B_\mu\Big) q^u_R + \overline{q^d_R}\, i\gamma^\mu \Big(\partial_\mu - i g_s \frac{\lambda^a}{2} G^a_\mu - i g_1 \frac{Y_{q^d_R}}{2} B_\mu\Big) q^d_R \\
&+ \overline{L_L} i\gamma^\mu \Big(\partial_\mu - i g_2 \frac{\sigma^i}{2} W^i_\mu - i g_1 \frac{Y_{L_L}}{2} B_\mu\Big) L_L + \overline{\ell_R} i\gamma^\mu \Big(\partial_\mu - i g_1 \frac{Y_{l_R}}{2} B_\mu\Big) \ell_R,
\end{aligned}
\tag{1.6}
$$

where $Y_{Q_L}$, $Y_{q^u_R}$, $Y_{q^d_R}$, $Y_{L_L}$ and $Y_{\ell_R}$ denote weak hypercharge (generator of $U(1)_Y$) of $Q_L$, $q^u_R$, $q^d_R$, $L_L$ and $\ell_R$ fields respectively, mentioned in Tab. 1.1. The kinetic term contains the interaction pieces with the gauge bosons to respect the gauge symmetry and serves as one of the key features of this construct. Here $\frac{\sigma^i}{2}$ $(i = 1, 2, 3)$ are the generators of $SU(2)_L$ group where $\sigma^a$ are the Pauli spin matrices and $\frac{\lambda^a}{2}$ $(a = 1...8)$ denote Gell-Mann matrices, the generators of the fundamental representation of the $SU(3)$ group. The Lagrangian is written only for one generation for brevity and family index $\alpha = 1, 2, 3$ is suppressed.

The Yukawa Lagrangian in the SM involves the interaction with Higgs boson as,

$$
\mathcal{L}_{\text{Yukawa}} = -\sum_{i,j=1,2,3} \Big( y^{ij}_u \overline{Q_{iL}} \widetilde{H} q^u_{jR} + y^{ij}_d \overline{Q_{iL}} H q^d_{jR} + y^{ij}_\ell \overline{L_{iL}} H \ell_{jR} + \text{H.c} \Big),
\tag{1.7}
$$

where $i, j$ denote three generation of quarks and leptons, resulting $y^{ij}$ a three cross three matrix and $\widetilde{H} = i\sigma^2 H^*$.

Finally, the scalar part of the Lagrangian is given by

$$
\mathcal{L}_{\text{Scalar}} = \left| \Big(\partial_\mu - i\, g_2 \frac{\sigma^a}{2}\, W^a_\mu - i\, g_1 \frac{Y_H}{2}\, B_\mu\Big) H \right|^2 - V(H),
\tag{1.8}
$$

where the scalar potential reads

$$
V(H) = \mu^2 \left(H^\dagger H\right) + \lambda_H \left(H^\dagger H\right)^2.
\tag{1.9}
$$

The SM Higgs doublet, $H$ is defined as a complex $SU(2)_L$ doublet

$$H = \frac{1}{\sqrt{2}} \begin{pmatrix} \phi_1 + i\phi_2 \\ \phi_3 + i\phi_4 \end{pmatrix} \equiv \begin{pmatrix} \phi^+ \\ \phi_0 \end{pmatrix}, \tag{1.10}$$

where $\phi_{1,2,3,4}$ are the four real scalar degrees of freedom. Electromagnetic charge assignments of the fields in the last step arises from $Q = I_3 + \frac{Y_H}{2}$, with $Y_H = 1$ as mentioned in Table 1.1. The fermion and gauge boson masses in the SM are generated through Higgs mechanism via spontaneous symmetry breaking (SSB) [3–5]. This is what we are going to discuss next in order to complete the review on the SM.

### 1.1.1 Spontaneous Symmetry Breaking & The Higgs Mechanism

As mentioned before, in the SM, the scalar potential is constructed by writing all renormalizable Higgs ($H$) self couplings:

$$V(H) = \mu^2 \left(H^\dagger H\right) + \lambda \left(H^\dagger H\right)^2. \tag{1.11}$$

A few comments in order:

- If $\lambda < 0$, then V is unbounded from below and there is no stable vacuum state.
- When $\mu^2 > 0$ and $\lambda > 0$, the potential energy function has a minimum at $|H| \equiv \sqrt{(H^\dagger H)} = 0$ as in the top left plot in Fig. 1.1. In this case the electroweak symmetry is unbroken in the vacuum.
- When $\mu^2 < 0$ and $\lambda > 0$, the potential energy as a function of $|H|$ has a minimum away from zero, as shown in the top right panel in Fig. 1.1. In this case there are degenerate vacua, or minimum energy states. Once we choose one vacuum to expand our theory, the symmetry of the potential is broken, or in other words the gauge symmetry is *spontaneously broken* by the chosen vacuum.

Therefore, with $\mu^2 < 0$ and $\lambda > 0$, the minimum of this potential has a $O(4)$ symmetry and possesses an infinite set of degenerate states dictated by:

$$\left|\langle 0 \left|\phi^0\right| 0\rangle\right| = \sqrt{\frac{-\mu^2}{2\lambda}} \equiv \frac{v}{\sqrt{2}}, \tag{1.12}$$

This is shown in the bottom panel of Fig. 1.1. When one of the directions is chosen among the infinite possibilities, the symmetry is spontaneously broken and the expectation value of this Higgs field for which the potential attains the minimum is called the vacuum expectation value (VEV). A particular choice of vacuum corresponds to the configuration $\langle \phi_{1,2,4} \rangle = 0$ , $\langle \phi_3 \rangle = v$ when the neutral component of the Higgs field acquire a VEV and respects $U(1)_{\rm EM}$ symmetry. Thus, SSB breaks $SU(2)_L \otimes U(1)_Y$ gauge symmetry spontaneously to a remnant electromagnetic symmetry $U(1)_{EM}$ as:

$$SU(2)_L \times U(1)_Y \xrightarrow{\langle H \rangle = v/\sqrt{2}} U(1)_{\rm EM}. \tag{1.13}$$

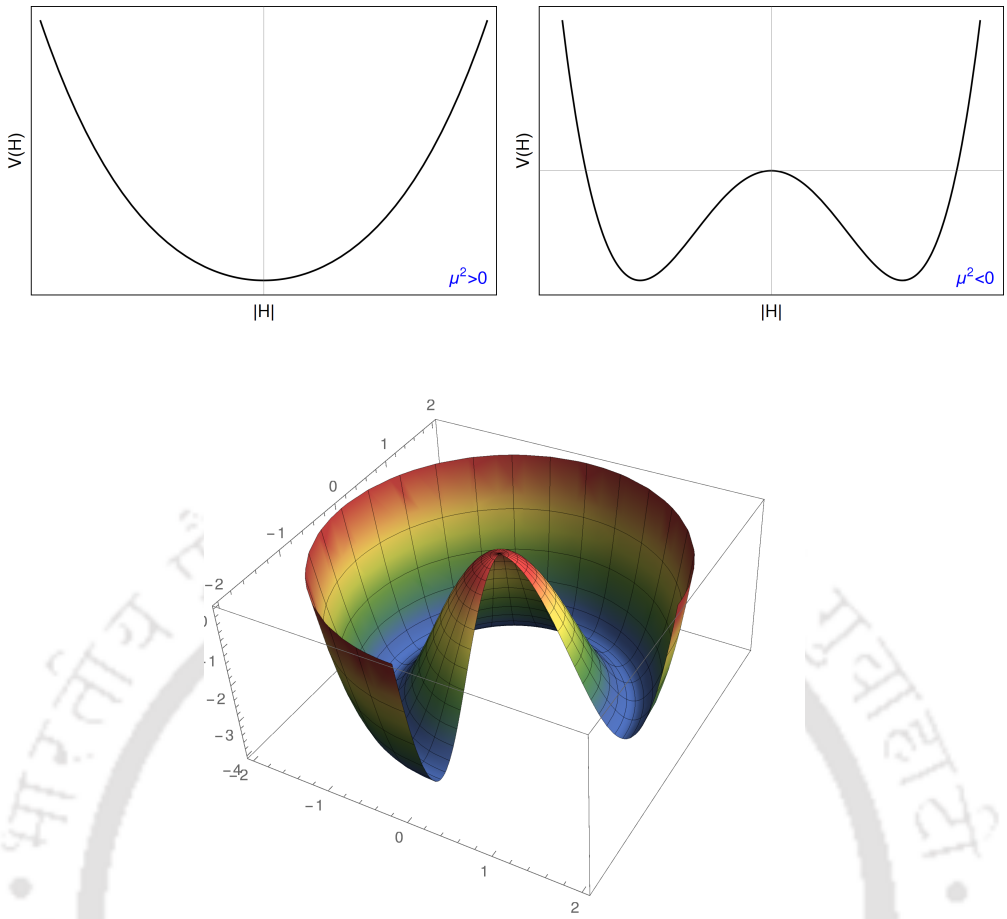


**Figure 1.1:** Top panel: Plots for scalar potential $V(H)$ as in Eq. 1.11 as a function of $|H|$ for $\mu^2 > 0$ (left) and $\mu^2 < 0$ (right). $\lambda \simeq 0.13$ has been used corresponding to measured values of Higgs mass $m_h \simeq 125$ GeV and VEV $v \simeq 246$ GeV. For the case $\mu^2 < 0$, the minimum of the potential is at $|H| = \frac{v}{\sqrt{2}}$. Bottom panel: 3D representation of the mexican hat potential in Eq. (1.11).

The electric charge is then obtained as the the combination of isospin and hypercharge keeps the vacuum intact:

$$Q = I_3 + \frac{Y}{2}. \tag{1.14}$$

This is required to keep photon massless. The Higgs field is expanded around this minima and can be expressed in the unitary gauge as:

$$H = \begin{pmatrix} 0 \\ \frac{h+v}{\sqrt{2}} \end{pmatrix}, \tag{1.15}$$

where $h$ is the CP even physical Higgs boson of mass $\sim 125$ GeV. Out of the four degrees of freedom, three become Nambu Goldstone boson. Following *Goldstone theorem* we can easily determine the number of Goldstone bosons in the theory as follows:

$$\begin{aligned}&\text{No. of unbroken generators before SSB} = (3+1) = 4\\&\text{No. of unbroken generators after SSB} = 1\\&\therefore \text{No. of broken generators} = \text{No. of Goldstone bosons} = (4-1) = 3.\end{aligned} \tag{1.16}$$

Among the four electroweak gauge bosons three become massive by 'eating' the Goldstone modes:

$$m_{W^\pm} = \frac{1}{2}gv, \;\; m_Z = \frac{1}{2}\sqrt{g_1^2+g_2^2}v, \tag{1.17}$$

while the third gauge boson remains massless $m_A = 0$ and can be identified as the photon corresponding to the unbroken $U(1)_{EM}$ symmetry. The above relations can easily be derived from the kinetic term of the Higgs field in Eq. 1.8 using the unitary gauge in vacuum as in Eq. 1.15. Here $v \equiv \sqrt{\frac{-\mu^2}{\lambda}}$ is the VEV of the scalar field, which should be $\sim 246$ GeV to agree with the experimentally measured masses and couplings of the gauge bosons and the Higgs. The physical gauge fields can be obtained by performing the rotation:

$$\begin{pmatrix} Z_\mu \\ A_\mu \end{pmatrix} = \begin{pmatrix} c_w & -s_w \\ s_w & c_w \end{pmatrix} \begin{pmatrix} W_\mu^3 \\ B_\mu \end{pmatrix}, \tag{1.18}$$

where $c_w \equiv \cos\theta_w$ and $s_w \equiv \sin\theta_w$, and the weak mixing/Weinberg angle is given by:

$$\tan\theta_w = \frac{g_1}{g_2}. \tag{1.19}$$

From Eq. 1.17 and Eq. 1.19 it is straightforward to obtain the mass relation:

$$m_W = \rho m_Z \cos\theta_w, \tag{1.20}$$

where the parameter $\rho$ has been introduced. $\rho = 1$ at tree-level but radiative quantum effects give corrections to this relation. The $SU(2)$ gauge structure of the electroweak theory ensures a feature known as *custodial symmetry*. In passing we would like to mention that the colour symmetry remains intact after SSB, and thus the gluons are massless.

Next we turn to the issue of generating masses for the fermions. In the unitary gauge, after SSB, the fermions (leptons and quarks) obtain masses through the Yukawa interactions as

$$-\mathcal{L}^{\text{mass}}_{\text{Yukawa}} = \sum_{i,j=1,2,3} \left( \frac{y_u^{ij} v}{\sqrt{2}} \overline{q_{iL}^u}\, q_{jR}^u + \frac{y_d^{ij} v}{\sqrt{2}} \overline{q_{iL}^d}\; q_{jR}^d + \frac{y_\ell^{ij} v}{\sqrt{2}} \overline{\ell_{iL}}\, \ell_{jR} + H.c \right). \tag{1.21}$$

In a simpler form one can re-cast the fermion Yukawa interaction, together with the fermion masses under unitary gauge as:

$$-\mathcal{L}^{\text{mass}}_{\text{Yukawa}} = \left(1 + \frac{h}{v}\right)\left(m_d \bar{d}d + m_u \bar{u}u + m_e \bar{e}e\right), \tag{1.22}$$

where $m_{ij} = \frac{y_{ij}v}{\sqrt{2}}$. One can note that all Yukawa couplings are fixed in terms of the fermion masses.

After the LHC discovery of the SM like Higgs Boson at the ATLAS and CMS [6, 7], the SM has confirmed itself as the most convincing theory at the electroweak scale. However, experimentally we are not hundred percent sure whether the discovered particle is exactly the SM Higgs as discussed here. Therefore, till we measure all the couplings of the Higgs accurately, we can not vouch that there is nothing else but one scalar doublet as described here.

It is also important to mention here that in our case, new physics beyond the SM that originates from a gauge extension of the SM gauge group, necessarily requires an extended scalar sector. The reason is pretty obvious that the new gauge group should also be broken to remnant electromagnetic symmetry. Thus, the very mass generation mechanism brings non-minimality in the scalar sector for an extended gauge symmetry if we wish to address vector boson dark matter that (mainly) originates from gauge extension of the SM. However, we must ensure that we have one scalar particle that behaves very similar to observed Higgs boson.

## 1.2 Beyond the Standard Model

SM is an extremely successful theory to explain a host of elementary particle interactions. Although SM has been tested to a remarkable precision at electroweak scales, it leaves many questions unanswered. Here we would like to point out some of them relevant for this thesis.

- **The Dark Matter:** The fact that our present universe has a large proportion (about 27%) of its energy density contained in a mysterious, non-luminous and non-baryonic dark matter (DM), we seek a particle explanation of this. However, SM does not offer a potential DM candidate that can account for the observed DM credentials. The thesis aims to discuss possibilities of vector boson to constitute DM.

- **Non-zero neutrino mass:** Existence of non-zero but tiny neutrino mass has been well established via short and long baseline neutrino oscillation experiments, contrary to the assumptions of SM having zero neutrino mass and no right handed neutrinos. It is perhaps one of the most compelling reasons to consider physics beyond the SM and we address it in the thesis.

- **The hierarchy problem:** The gauge hierarchy problem is the observation that the Higgs squared mass parameter can be much larger than the observed masses of the electroweak gauge bosons. In the Standard Model, Higgs boson mass is totally unprotected by any symmetry argument, while fermion masses are protected by chiral symmetry. Higgs mass can be as large as the 'Grand Unified Theory (GUT)' scale ($10^{16}$ GeV) or the 'Planck Scale' ($10^{19}$ GeV) when radiative corrections are included. Its therefore a fine tuning of parameters for

all orders in perturbation theory to obtain Higgs mass at 125 GeV. This is the so called gauge hierarchy problem.

- **Gauge coupling unification:** Grand Unification Theory (GUT) is arguably the complete theory of all fundamental interactions except gravity. GUT has been a long quest for physicists after the unified picture of electromagnetism and then electroweak unification in $SU(2)_L \times U(1)_Y$ gauge group of SM. GUT models are also supported by the fact that the running of the three SM gauge couplings makes them approach each other at some high scale. However, within SM they really never meet! A gauge group extension with suitable fields can do the job as we discuss in the thesis.

- **Higgs vacuum stability:** Given that current measured value of Higgs boson is $m_h = 125.09$ GeV and top quark mass $m_t = 173.1$ GeV [8], the electroweak (EW) vacuum can be unstable, questioning the existence of our universe [9–16]. This suggests that existence of another deeper minimum at high energy scale ($\Lambda_I \sim 10^{9-10}$ GeV) where running of Higgs quartic coupling $\lambda_H$ can turn negative is a finite possibility. To study this effect systematically, one needs to consider the radiatively corrected one loop effective Higgs potential [17, 18]:

$$V_h^{\text{eff}} = \frac{\lambda_H^{\text{eff}}(\mu)}{4} h^4, \tag{1.23}$$

  with $\lambda_H^{\text{eff}} = \lambda_H^{\text{SM,eff}} + \lambda_H^{\text{BSM,eff}}$. Here $\lambda_H^{\text{(B)SM,eff}}$ is the loop correction provided by the (B)SM fields. An extended scalar sector help the SM Higgs vacuum stable upto the Planck scale, which is also a requirement to address vector boson DM as we discus.

On top of these, there is also strong CP problem in the QCD sector, matter-antimatter asymmetry in the universe and many more, none of which can be addressed within the SM indicating inevitable existence of physics beyond the SM. This thesis makes an attempt to address a few of these limitations, like, the existence of DM & its probable nature, explanation of non-zero neutrino mass, and a possibility of gauge coupling unification. In the next chapter we elaborate upon these topics. Before moving on we must mention that the SM does not accommodate gravity, the quantum description of which is long sought after. This thesis does not address this issues.

Chapter 2

# The Trinity: Dark Matter, Neutrino mass, Unification

## Contents



Out of several limitations of the Standard Model (SM), the thesis emphasizes mainly on explaining the Dark Matter (DM), while the existence of tiny neutrino mass and possibility of gauge coupling unification are also addressed in parallel. But since DM is the central theme of this thesis we would like to elaborate upon it in this chapter and summarize neutrino mass generation and gauge coupling unification.

## 2.1 Dark Matter

### 2.1.1 Observational evidences of Dark Matter

The most convincing and direct evidence for dark matter on *galactic scales* comes from the observations of the rotation curves of galaxies. In the early 1930s, J. H. Oort discovered that the motion of stars in the Milky Way required a presence of far more galactic mass than was previously imagined [19]. Later in 1933, a Swiss astronomer named F. Zwicky found similar indications of the missing mass but on a much larger scale. Using the Doppler shift of galaxies in the Coma cluster, Zwicky was able to calculate the velocity dispersion of galaxies in the cluster [20]. Around 1970's, following the discoveries of Oort, Zwicky, and others, V. Rubin and W.Ford performed an extensive study of the rotation curves of 60 isolated galaxies [21]. Abiding Newtonian mechanics, the rotational velocity at a distance $r$ from the centre of a galaxy should obey the relation:

$$v_{\rm rot}\,(r) = \sqrt{\frac{G_N M(r)}{r}}, \tag{2.1}$$

where $G_N$ is universal gravitational constant and $M(r)$ is the total mass contained within the radius $r$. In the absence of any non-luminous mass, $M(r)$ is expected to be approximately constant beyond the optical disk and consequently circular velocities should fall off showing the Keplerian behaviour $\propto \frac{1}{\sqrt{r}}$. Instead, rotation curves are observed to be approximately constant up to very large radii as shown in Fig. 2.1. The result implied $M(r) \propto r$ *i.e.*, an extended halo of non-luminous matter beyond the optical disk.

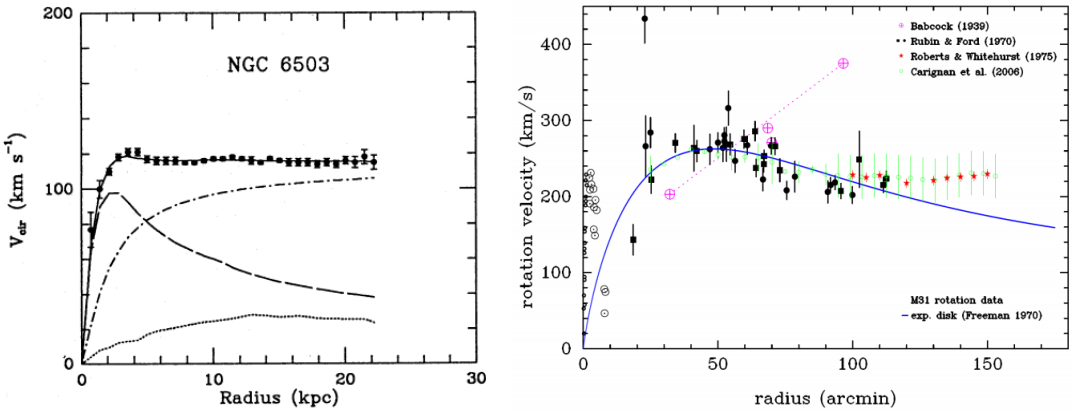


**Figure 2.1:** Left: Rotation curve of the NGC6503 galaxy, showing contributions of the gas (dotted curve), luminous matter (dashed curve) and a DM component (dot-dashed curve) fitting the experimental data. Figure taken from [22]. Right: Rotation curve data for M31. The figure is taken from [19].

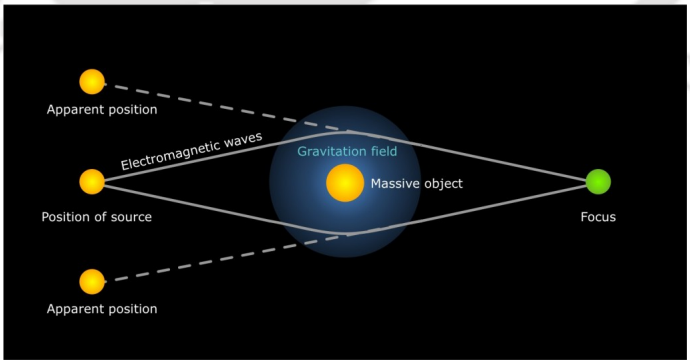


**Figure 2.2:** A schematic diagram of the gravitational lensing effect. The gravity of a foreground object distorts the light coming from a distant object. This image is taken from One-Minute Astronomer.

In the 1970s, gravitational lensing offered a new way to probe the amount and distribution of DM in the universe. This is an impressive way to map the total gravitating mass of a galaxy cluster by exploiting the fact that gravitational fields affect the propagation of light. A schematic diagram of this lensing effect is shown in Fig. 2.2.

In the *strong lensing* regime, where a very dense region is present between a source and an observer, light emitted from the source could follow several geodesics to reach the observer, resulting in multiple images of the same physical source in the field of view. The *weak lensing* regime corresponds to distortions of the apparent shape of luminous objects by the gravitational potential of some massive structure located near to the line of sight, between the source and the observer, resulting in a possible magnification or shear of the source image.

**Figure 2.3:** Image of Bullet cluster seen by NASA's Hubble Space Telescope. The red coloured regions show the distribution of gas, inferred from its X-ray emission. The blue tinted regions show the distribution of gravitating matter, which is reconstructed using weak gravitational lensing. This clearly shows that the total mass of the system is dominated by the non-luminous component [23].

The evidence that serves as the smoking gun signature for the existence of DM comes from the 'Bullet Cluster' (1E0657-558) [23, 24], where gravitational lensing can be used to demonstrate a clear mismatch between the distribution of luminous and gravitating matter as shown in Fig. 2.3. In a collision of galaxy clusters, the hot gas of both systems dissipate energy because of electromagnetic interactions and therefore they are held up at the point of the collision. DM halos pass straight through one another and consequently can be separated from the gas. This expectation indeed agrees with observations. These results also confirmed the collisionlessness of the DM.

On *cosmological scales*, the ubiquitous Cosmic Microwave Background Radiation (CMB) provides the strongest evidence of the existence of DM. The CMB is a radiation emitted at a redshift $z \sim 1100$, right after the photons are decoupled from the thermal bath due to drop in the density of the free electrons after recombination ($z \sim 1300$) resulting to decrease in the interaction rate of the photons with the primordial plasma [25, 26]. The existence of background radiation originating from the propagation of photons in the early Universe (once they decoupled from matter) was predicted by George Gammow and his collaborators in 1948 and inadvertently discovered by Arno Penzias and Robert Wilson in 1965 [27]. Although the temperature fluctuations in the CMB are extraordinarily uniform, after many decades of experimental effort, the CMB is known to be isotropic at the $10^{-5}$ level and to follow with extraordinary precision the spectrum of a black body corresponding to a temperature $T \simeq 2.73$ K. The analysis of CMB anisotropies enables accurate testing of cosmological models and puts stringent constraints on cosmological parameters. Data from Wilkinson Microwave Anisotropy Probe (WMAP) [28] and PLANCK

suggest that the universe consists of: (i) around $5\%$ baryonic matter like baryons, leptons, gas, stars, galaxies etc. ; (ii) around $27\%$ non baryonic matter known as Dark matter and (iii) rest $68\%$ is known as dark energy [28–30] assuming FRW model or Standard Model of cosmology. This spectacular observation can be confirmed independently by comparing the predictions from Big Bang nucleosynthesis (BBN) with the observed abundances of elements. All of these can be summarized in the pie-chart shown in Fig. 2.4. Besides CMB, the other most reliable cosmological measurements are from Sloan Digital Sky Survey (SDSS) [31, 32].

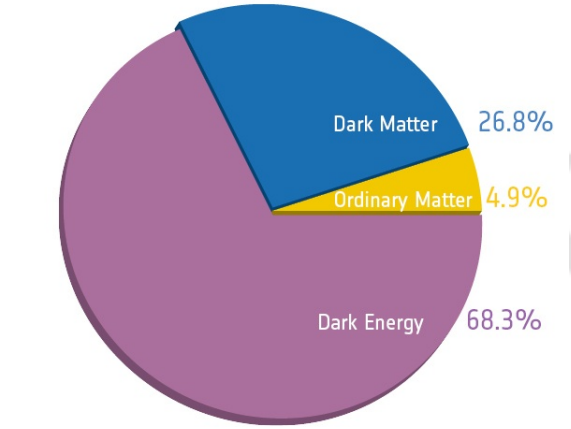


**Figure 2.4:** Approximate energy budget of the universe as predicted by WMAP and PLANCK observation of the CMB spectrum. Image from [33].

Evidence for DM is also inferred from analyzing the large-scale structures in the universe. But as our understanding of formation of large scale structures from primordial density fluctuations is far from satisfactory level, we rely on $N$-body simulations. $N$-body simulations without DM does not form the familiar filament and void structures as observed by SDSS and other surveys within proper timescale. The $N$-body simulations also provide the evidence that not only is DM required in the universe, it must be cold or non-relativistic during the period of structure formation [34, 35].

### 2.1.2 The Dark Matter Zoo

The total matter content of the universe according to recent data: $\Omega_m h^2 \sim 0.31$ [36], while the amount of *luminous* matter, in the form of stars, dust clouds etc, gives a much smaller contribution: $\Omega_{lum} h^2 \sim 0.005$. On the other hand, the amount of baryonic matter: $\Omega_b h^2 \sim 0.04$. Thus we have:

$$\Omega_{lum} < \Omega_b < \Omega_m.$$

The inequalities suggest that DM can be either *baryonic* or *non-baryonic*. The baryonic nature of DM is actually strongly constrained from the big-bang nucleosynthesis (BBN). The abundance of light elements predicted by BBN depends on the baryon density and, in fact, measurements constrain the baryon density to a value

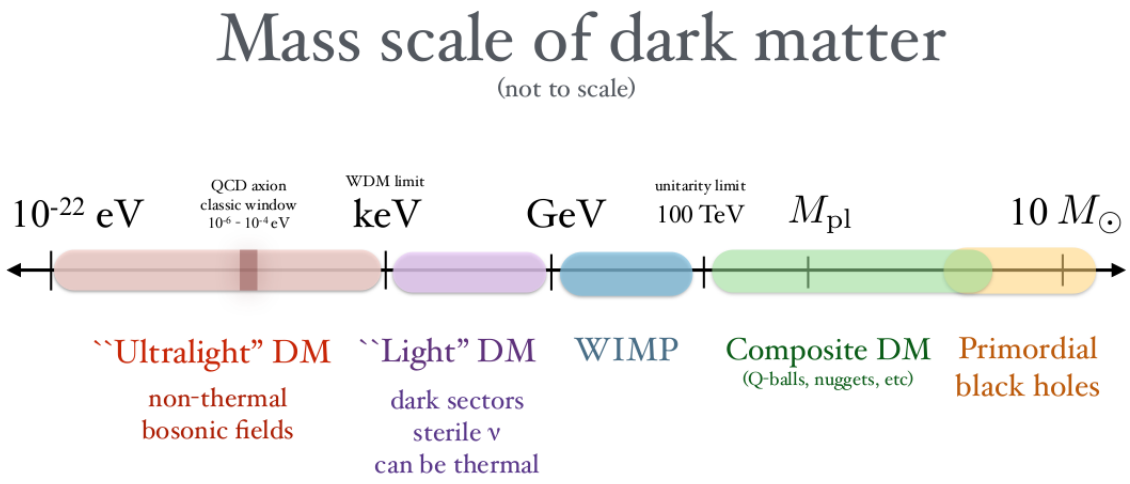


**Figure 2.5:** The mass range (not to the scale) of allowed DM candidates, comprising both particle candidates and primordial black holes. Figure from [37].

around $\Omega_b \sim 0.04$, close to the value derived from CMB. Some part of the baryonic matter density may well contribute to baryonic DM, e.g, MACHOs [1] and they are detectable by gravitational lensing. However, DM composed entirely of MACHOs has been ruled out [38]. On the other hand, there exist a garden variety of non-baryonic DM [39–43]:

- A major classification of non-baryonic dark matter is based on its temperature at the time of galaxy formation. On the basis of this, DM can broadly divided into:
  - **Hot Dark Matter (HDM):** *Relativistic* at the time of galaxy formation. Typically lies $\sim$ eV scale. Light neutrinos are the example of HDM.
  - **Cold Dark Matter (CDM):** Non-relativistic at the time of galaxy formation. The masses lie in the range {MeV-GeV}. Weakly Interacting Massive Particles (WIMP) are the best example of CDM.
  - **Warm Dark Matter (WDM)**: Such DM candidates have properties in between cold and hot regime. Sterile neutrinos and gravitinos are popular WDM candidates. The masses are usually $\sim$ KeV range.

Because of extremely high velocities, HDM wipes out structures on small scale. Hence CDMs are physically viable as they can explain small scale structure formation. A combination of theoretical and cosmological constraints have considered the so-called $\Lambda$CDM (dark energy with cold dark matter) paradigm as an accurate description of our universe. Throughout the thesis, we will consider CDM as our DM candidate.

- Based on production mechanism, DM can be divided into two categories:

[1] MACHOs or Massive Compact Halo Objects include black holes or neutron stars or brown dwarfs.

- **Thermal relics:** Particle DM that were in thermal equilibrium with the primordial plasma in the early universe, *e.g.*, neutrinos, Weakly interacting massive particles (WIMP).
- **Non-thermal relics:** Particle DM that never came into thermal equilibrium in the early universe, and produced by some non-thermal mechanism (for example, decay of a particle in the SM bath), *e.g.*, feebly interacting massive particles (FIMPs), axions, solitons, WIMPZILLAs.

SM neutrinos being massive, electromagnetic charge neutral and weakly interacting are supposed to be excellent DM candidate. But one can easily show that if $m_i$ is the mass of the $i$-th neutrino, their total relic density is predicted to be [41, 44]:

$$\Omega_\nu h^2 \simeq \sum_{i=1}^{3} \frac{m_i}{94 \text{ eV}}.$$

Now, given the present bound on neutrino mass from cosmology [45] we find that $\Omega_\nu h^2 \lesssim 0.001$, which means that neutrinos are simply not abundant enough to be the dominant component of DM. On top of that, neutrinos being relativistic at the time of galaxy formation, erase small-scale fluctuations [46] implying a *top-down* formation of the universe which is essentially against the observational data (which implies a *bottom-up* formation). Hence neutrinos fail to be viable DM candidates. Thus, the Standard Model (SM) does not contain any potential DM candidate. As the detailed nature of DM is not revealed yet, many DM candidates have been proposed so far from the point of view of physics beyond the standard model (BSM). Among those, WIMPs are known to be good candidate for particle DM. Assuming that DM number density depletion occurs to SM via $2-2$ interaction of weak interaction strength, then DM with masses $\sim \mathcal{O}(100)$ GeV can satisfy the desired relic density. This feature called the **WIMP Miracle** [44], has made WIMP models a favorite amongst the theorists. Apart from WIMPs, there are more exotic DM candidates, for example, the lightest Kaluza-Klein mode that emerges from the Universal Extra Dimensions (UED) framework (for a review see [47]), axion-like particle (ALPs) [48], primordial black holes (PBH) [49–52], SuperWIMPs (e.g., gravitino) [53–56] or particles that have super weak interactions are produced non-thermally by the decay of a heavier state etc. The schematic diagram in Fig. 2.5 shows a non-exhaustive representation of possible DM mass range for some of the DM candidates.

## 2.2 WIMP: Thermal freeze-out and detection possibilities

Of all the hypothetical DM candidates, none have been studied in more detail than the weakly interacting massive particles (WIMPs). In this section we would like to elaborate upon the thermal freeze-out of WIMPs and discuss some of its detection prospects in different experiments.

### 2.2.1 Boltzmann Equation (BEQ) for single component WIMP

In thermal freeze-out scenario, DM particle is assumed to be in thermal and chemical equilibrium with the SM bath at early Universe. As the universe expands adiabati-

cally and the temperature drops, at a particular epoch when the interaction rate ($\Gamma$) becomes smaller than the universe expansion rate (Hubble constant $H$): $\Gamma \lesssim H$, the DM particles decouple from the thermal bath. The DM particles then "freeze-out" with their number asymptotically approaching a constant (in co-moving volume), namely their thermal relic density. The DM number density in the present epoch is found by solving the Boltzmann equation [26, 44]. For a single-component WIMP ($X$) having $2 \to 2$ interaction with SM, the Boltzmann Equation (BEQ) governing the number density reads

$$\begin{aligned}\dot{n}_X + 3Hn_X &= -\int \frac{\xi_X d^3p}{(2\pi)^3 2E_p}\frac{\xi_X d^3p'}{(2\pi)^3 2E'_p}\frac{\xi_{SM} d^3q}{(2\pi)^3 2E_q}\frac{\xi_{SM} d^3q'}{(2\pi)^3 2E'_q}(2\pi)^4\,\delta^4(p+p'-q-q')\times \\ &\quad |\mathcal{M}_{XX\to SMSM}|^2\left(f_X f_X - f_{X^{\rm EQ}} f_{X^{\rm EQ}}\right), \end{aligned} \tag{2.2}$$

where $n_X$ denote the number density of WIMP ($X$), $\dot{n}_X$ is the time derivative of the number density, $\mathcal{M}_{i\to f}$ is the amplitude for the process $i \to f$, including the spin average and symmetry factors, $H$ denotes the Hubble parameter and $\xi_X$ indicates the internal degrees of freedom associated to the particular DM species. For example, for a massive vector boson DM, we have $\xi_X = 3$. Phase space density $f_X$ is related to $n_X$ and equilibrium density $f_X^{EQ}$ are related to corresponding $n_X^{EQ}$, as follows:

$$n_X = \int \frac{\xi_X d^3p}{(2\pi)^3 2E} f_X, \quad n_X^{EQ} = \int \frac{\xi_X d^3p}{(2\pi)^3 2E} f_X^{EQ}, \quad f_X^{EQ} = \frac{1}{e^{E/k_B T} - 1}. \tag{2.3}$$

Thermally averaged cross section (see Appendix. A for derivation) $\langle \sigma_{XX\to SMSM}\, v\rangle$ is defined as [44, 57, 58]:

$$\begin{aligned}\langle \sigma_{XX\to SMSM} v\rangle &\equiv \frac{1}{\left(n_X^{EQ^2}\right)}\int \frac{\xi_X d^3p}{(2\pi)^3 2E_p}\frac{\xi_X d^3p'}{(2\pi)^3 2E'_p}\frac{\xi_{SM} d^3q}{(2\pi)^3 2E_q}\frac{\xi_{SM} d^3q'}{(2\pi)^3 2E'_q}\times \\ &\quad (2\pi)^4\,\delta^4(p+p'-q-q')|\mathcal{M}_{XX\to SMSM}|^2 e^{-(E_p+E'_p)/T} \\ &= \int_{s_0}^{\infty} ds\, \frac{\xi_X^2 s\sqrt{s-4m_X^2}\; K_1(\frac{\sqrt{s}}{T})\; (\sigma v)_{XX\to SMSM}}{16T\, m_X^4\, K_2(\frac{m_X}{T})^2}, \end{aligned} \tag{2.4}$$

where $\langle \sigma_{XX\to SMSM} v\rangle$ has been expressed in terms of annihilation cross-section and the kinematic variable $s = (p_X + p_X^{'})^2$. The threshold energy required for the reaction to occur is $s_0 = 4m_X^2$. $K_{1,2}(x)$ are the first and second modified Bessel functions as a function of $x = \frac{m_X}{T}$ with $T$ being the temperature of the thermal bath. BEQ for the single-component case then be simplified as [44]:

$$\dot{n}_X = -3Hn_X - \langle \sigma_{XX\to SM} v\rangle \left(n_X^2 - n_X^{EQ2}\right). \tag{2.5}$$

On the right hand side (RHS) of the above equation, the first term accounts for dilution due to expansion while the second term corresponds to the so called 'collision term' that accounts for the rate of reaction. The equation is often recasted in terms of DM yield $Y$ defined as:

$$Y = \frac{n_X}{s} \tag{2.6}$$

where $n_X$ is the number density (per co-moving volume) of the DM $X$ as defined earlier and $s$ is the entropy density (per co-moving volume) given by [44]

$$s = \frac{2\pi^2}{45} g_{\star s}(T) T^3 \,; \quad g_{\star s}(T) = \sum_k r_k g_k \left(\frac{T_k}{T}\right)^3 \theta(T - m_k). \tag{2.7}$$

Here $k$ runs over all particles, $T_k$ is the temperature of particle $k$, $g_k$ its number of internal degrees of freedom and $r_k = 1\,(7/8)$ when $k$ is a bosons (fermion). It is easy to rewrite the BEQ in terms of $Y$ as a function of $x = \frac{m_X}{T}$

$$\frac{dY}{dx} = -\frac{x\langle\sigma v\rangle s}{H(m)} \left[\langle\sigma_{XX\to SMSM} v\rangle (Y^2 - Y^{EQ^2})\right]. \tag{2.8}$$

In the above,

$$H(m) = 1.66\sqrt{g_{\star\rho}}\frac{m^2}{m_{Pl}};\; g_{\star\rho} = \sum_{i=bosons} g_i \left(\frac{T_i}{T}\right)^4 + \frac{7}{8}\sum_{i=fermions} g_i \left(\frac{T_i}{T}\right)^4, \tag{2.9}$$

and the equilibrium distribution is given by

$$Y^{EQ} = 0.145 \frac{g}{g_{*s}} \left(\frac{m_X}{T}\right)^{\frac{3}{2}} e^{-\frac{m_X}{T}} \tag{2.10}$$

where $g_{\star s}$ is given by Eq. (2.7) and $g$ is the number of internal DOF of the particle concerned. Note again, $m_{Pl} = \frac{1}{\sqrt{8\pi G}} = 2.43 \times 10^{18}$ GeV denotes reduced Plank mass. Finally, one needs to solve Eq. 2.8 for thermal freeze out. As the equation can not be solved analytically, a numerical solution is done assuming $Y(x = 0) = Y^{EQ}$. In Fig. 2.6 we show the freeze-out corresponding to some choices of thermally averaged cross-sections $\langle\sigma.v\rangle = \{10^{-12}, 10^{-11}, 10^{-10}, 10^{-8}\}$GeV$^{-2}$ shown by black, blue, green and red thick lines respectively. As expected, with larger interaction cross-section the freeze-out gets delayed. Black dashed line shows the equilibrium distribution $Y^{EQ}$ for DM mass 100 GeV. The yield in green corresponds to correct relic abundance while the ones above (black and blue) yield over abundance and the one below in red provide under abundance. In the DM model building exercise it is of immense importance to find the parameters that justify correct annihilation cross-section leading to right relic abundance. Although the thermal relic abundance is determined by solving the BEQ *e.g.*, Eq. (2.8) numerically, it is possible to derive an approximate analytical expression for the DM relic density. Defining freeze out to be the time when $n\,\langle\sigma_{\rm ann} v\rangle = H$, we have:

$$n_f \langle\sigma_{\rm ann}.v\rangle \sim \frac{T_f^2}{M_{\rm pl}}, \tag{2.11}$$

where the subscript $f$ denotes quantities at freeze out and $M_{\rm pl}$ is the Planck's mass. The ratio $x_f = \frac{m_X}{T_f}$ has a typical value of $x_f \sim 20$ for freeze-out. The thermal relic abundance is then given by the cosmological density parameter defined by

$$\Omega_X = \frac{m_X\, n_0}{\rho_c} = \frac{m_X\, T_0^3}{\rho_c}\frac{n_f}{T_0^3} \sim \frac{x_f\, T_0^3}{\rho_c\, M_{\rm pl}}\langle\sigma_{ann} v\rangle^{-1}. \tag{2.12}$$

Here $\rho_c$ is the critical density defined as: $\rho_c = \frac{3H_0^2}{8\pi G}$, $H_0$ being the present day value of the Hubble's constant and $G$ is the universal gravitational constant. We see that the thermal relic density depends mainly on the annihilation cross section $\langle\sigma_{\rm ann} v\rangle$ inversely, the kind of behaviour that we see in Fig. 2.6.

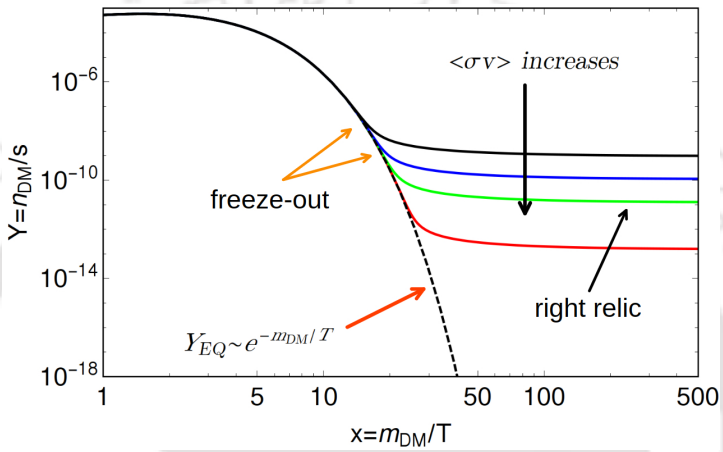


**Figure 2.6:** The figure shows freeze out of WIMP DM in terms of the abundance $Y$ (as mentioned in the text). The dashed black line shows the equilibrium abundance of the thermal relic $Y^{EQ}$. The solid black, blue, green and red coloured lines correspond to different numerical values of annihilation cross-section $\langle\sigma.v\rangle = \{10^{-12}, 10^{-11}, 10^{-10}, 10^{-8}\}$GeV$^{-2}$ respectively, which are in the increasing order from top to bottom. The green coloured curve gives rise to observed DM relic abundance. Here we choose the DM mass to be $m_{\rm DM} = 100$ GeV.

It is often easier to recast Eq. (2.8) in terms of a modified yield $y = \lambda Y$, where $\lambda = (0.264\, m_{Pl}\frac{g_{*s}}{\sqrt{g_*}})$ such that it simplifies to:

$$\frac{dy}{dx} = -\frac{m_X}{x^2}\left[\langle\sigma_{XX\to SMSM} v\rangle(y^2 - y^{EQ^2})\right]. \tag{2.13}$$

We can also approximate $\langle\sigma v\rangle$ with the non-relativistic expansion in powers of $v^2$ (since $v$ is small):

$$\langle\sigma v\rangle = a + bv^2 + \mathcal{O}(v^4), \tag{2.14}$$

where $a$ and $bv^2$ stand for $s$-wave and $p$-wave annihilation respectively. If we consider only $s$-wave contribution in Eq. (2.13) (present which the p-wave is negligible) then the BEQ simply becomes:

$$\frac{dy}{dx} = -\frac{m_X}{x^2}\left[\sigma_0(y^2 - y^{EQ^2})\right]. \tag{2.15}$$

Then following the approximate solution already described, it is possible to show that the relic density (in terms of the reduced Hubble parameter, $h = H_0/100\,\mathrm{kms}^{-1}\,\mathrm{Mpc}^{-1}$) can be obtained from the yield $y$ at a large value of $x$ as:

$$\Omega h^2 = \frac{\rho}{\rho_c} = \frac{m_X s_0 \sqrt{g_*}}{3H_0^2\, m_{pl}^3\, 0.26 g_{*s}} y(x_\infty) \simeq \frac{2.4\times 10^{-10}\mathrm{GeV}^{-2}}{\sigma_0}. \tag{2.16}$$

In the above $x_\infty$ defines large enough $x$ after decoupling and $s_0$ is the present day entropy density. From the last equality in Eq. 2.16, one can see that in order to obtain the observed relic abundance for the DM, the annihilation cross-section required is $\sigma_0 \sim 10^{-9}$ GeV$^{-2}$, which is the typical weak interaction cross-section. This is what has been termed as the 'WIMP miracle' in the end of the last section.

In many models the DM sector consists of more than one particle. If there are two DM particles $X_1$ and $X_2$ with $m_{X_1} < m_{X_2}$ then they can annihilate into a pair of SM particles through the set of processes:

$$X_1\overline{X_1} \to f\overline{f}, \quad X_1\overline{X_2} \to f\overline{f}, \quad X_2\overline{X_2} \to f\overline{f}. \tag{2.17}$$

Assuming two particles are present at the time of decoupling, then all of the processes in Eq. (2.17) contribute to the DM relic and the BEQ can be re-written as [59, 60]

$$\dot{n}_X + 3Hn_X = -\langle\sigma v\rangle_{\text{eff}}\left(n_X^2 - n_X^{2\text{eq}}\right), \tag{2.18}$$

with $n_X = n_{X_1} + n_{X_2}$, $\Delta m = m_{X_2} - m_{X_1}$ and

$$\begin{aligned}\langle\sigma v\rangle_{\text{eff}} = \frac{\xi_1^2}{\xi_{\text{eff}}^2}\langle\sigma v\rangle_{X_1X_1} + \frac{2\xi_1\xi_2}{\xi_{\text{eff}}^2}\langle\sigma v\rangle_{X_1X_2}\left(1+\frac{\Delta m}{m_{X_1}}\right)^{3/2}\exp\left(-x\frac{\Delta m}{m_{X_1}}\right) + \\ \frac{\xi_2^2}{\xi_{\text{eff}}^2}\langle\sigma v\rangle_{X_2X_2}\left(1+\frac{\Delta m}{m_{X_1}}\right)^{3}\exp\left(-2x\frac{\Delta m}{m_{X_1}}\right);\end{aligned} \tag{2.19}$$

where $\xi_{\text{eff}}$ is the *effective* degrees of freedom given by

$$\xi_{\text{eff}} = \xi_1 + \xi_2\left(1+\frac{\Delta m}{m_{X_1}}\right)^{3/2}\exp\left(-x\frac{\Delta m}{m_{X_1}}\right) + \mathcal{O}\left[\Delta m\right]^3. \tag{2.20}$$

Such processes like $X_1\overline{X_2} \to f\overline{f}$, $X_2\overline{X_2} \to f\overline{f}$ are called co-annihilation and serves as a very important feature of multipartite DM sector. We will provide more concrete examples when we discuss our model set up. In order for the co-annihilation partner $X_2$ to have a significant effect on DM relic density, its number density should remain close to the DM number density during freeze-out. Co-annihilation is expected to be important for $m_{X_2} - m_{X_1} \sim T_F$, which is typically the freeze-out temperature. Large mass splitting reduces co annihilation effects significantly due to Boltzmann suppression as seen from Eq. 2.19 and therefore contributions from $X_1\overline{X_2} \to f\overline{f}$ usually dominates over $X_2\overline{X_2} \to f\overline{f}$.

### 2.2.2 WIMP searches: Review & Current Status

The overwhelmingly huge number of evidences of DM (as described in Sec. 2.1.1) and a plethora of well-motivated particle DM candidates (as partially enlisted in Sec. 2.1.2) makes the identification of DM a key challenge. Since WIMPs have a finite weak coupling with the visible sector that gives rise to observed relic abundance, hence they could be detected via following three ways:

- DM scattering off a SM particle via DM+SM $\rightarrow$ DM+SM: Direct Detection.
- Dark Matter annihilation via DM + DM $\rightarrow$ SM + SM: Indirect Detection.
- Dark Matter production via SM + SM $\rightarrow$ DM + SM: Collider Searches.

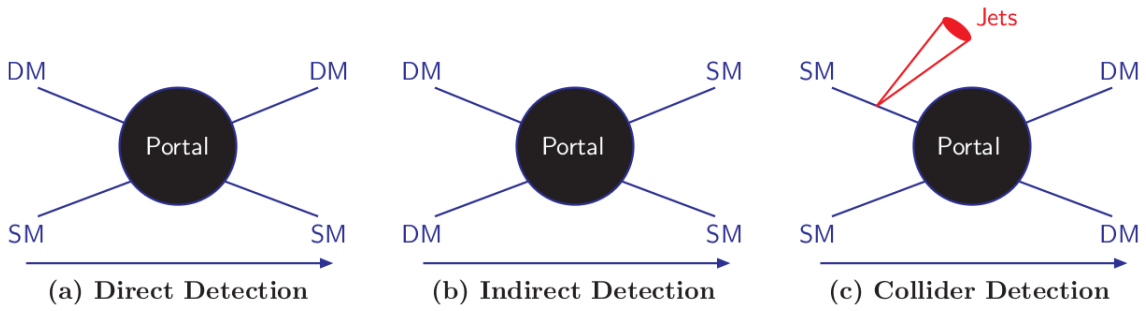


**Figure 2.7:** Illustration of the three main DM detection strategies. This cartoon is taken from [61].

In Fig. 2.7 these methods are summarized, which shows these three search strategies are complementary to each other. In the following sections we would like to elaborate upon DM direct detection and collider searches, while indirect detection, although not addressed in this thesis, shall be discussed briefly.

#### Direct Detection

The principle behind DM direct search is that since we are moving through a WIMP halo, DM can scatter off an earthly detector, deep underground, shielded from noises. The goal of direct detection experiments is therefore to detect and record the rare occasion that particle DM scatters off a target material producing measurable amount of recoil energy. This idea was first suggested by M. Goodman and E. Witten [62]. The relevant physics behind these scattering experiments can be identified if we look more closely into the kinematics of such a scattering process. This is depicted in Fig. 2.8. Total initial energy and momentum, following the momentum labels in Fig. 2.8 can be written as

$$E_i = \frac{\vec{p}^2}{2m_X}, \quad \vec{p} = m_X \vec{v}, \tag{2.21}$$

while the final energy

$$E_f = \frac{(\vec{p}-\vec{q})^2}{2m_X} + \frac{\vec{q}^2}{2m_N}. \tag{2.22}$$

The energy conservation then gives rise to:

$$\frac{|\vec{p}|\,|\vec{q}|\cos\theta}{m_X} = \frac{\vec{q}^2}{2\mu_{XN}}, \tag{2.23}$$

where $\cos\theta = \hat{p}.\hat{q}$ and $\mu_{XN} = \frac{m_X m_N}{m_X+m_N}$ is the DM-nucleus reduced mass. For a WIMP scattering off a typical nucleus (say, Xenon), $\mu_{XN} \simeq 10 - 100$ GeV and $|\vec{q}|_{\text{max}} \simeq 20 - 200$ MeV. Then corresponding maximum recoil energy is given by:

$$E_R^{\text{max}} = \frac{|\vec{q}|^2_{\text{max}}}{2m_N} = \frac{2\mu_{XN}^2 v^2}{m_N} \simeq 20 - 200 \text{ keV}, \tag{2.24}$$

where we have used the typical velocity of DM in the local DM halo: $v \sim 10^{-3}$. For a given recoil energy, the minimum incoming speed for the DM would then be:

$$v_{\text{min}} = \sqrt{m_N E_R / 2\mu_{XN}^2}. \tag{2.25}$$

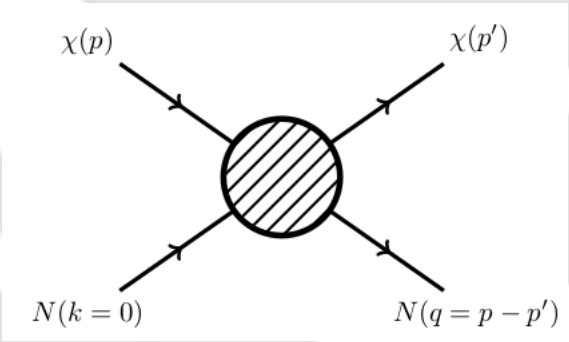


**Figure 2.8:** Scattering of DM candidate $X$ from the local DM halo on a nucleus $N$ which at rest on earth. This diagram is taken from [37].

The key ingredients for the calculation of the signal in direct detection experiments are the density and the velocity distribution of WIMPs in the solar neighbourhood and the WIMP-nucleon scattering cross section. With this information, it is then possible to evaluate the rate of events expected in an experiment (WIMP-nucleon scattering events) per unit time, per unit detector material mass. The differential event rate expressed in terms of number of events per kilogram and per day as:

$$\frac{dR}{dE_R} = N_T n_X \int \frac{d\sigma}{dE_R} v f(\vec{v})\, d^3\vec{v}, \tag{2.26}$$

where $N_T$ is the number of nuclei per unit target mass, $n_X = \rho_X/m_X$ is the DM number density, $f(v)$ is the DM velocity distribution in the lab frame. A simple analytic approximation for the DM velocity distribution is that of a truncated

Maxwellian distribution, since we expect the DM in the solar neighbourhood to be mostly virialized. The differential DM-nucleus scattering cross section $d\sigma/dE_R$ depends on the nature of WIMP-nucleus interaction [37]

$$\frac{d\sigma}{dE_R} = \frac{\sigma_{Xn}}{\mu_{XN}^2}\frac{m_N}{2v^2}F^2(q)\,\Theta\left(v - \sqrt{\frac{m_N E_R}{2\mu_{XN}^2}}\right), \tag{2.27}$$

where the step function enforces the DM velocity to be $v_{\min}$ (as in Eq. 2.25) to produce a recoil of energy $E_R$. Here $F(q)$ is the form factor containing the entire dependence on the momentum transfer $q$ which may be expressed as a simple analytic form known as the Helm form factor [63]

$$F(q) = \frac{3j_1(qr_n)}{qr_n}\exp\left(-q^2s^2/2\right), \tag{2.28}$$

with $r_n \approx 1.14A^{1/3}$ ($A$ is the atomic number of the nucleus) and $s \approx 0.9$ fm. The likelihood of an incident DM with larger velocities eventually becomes exponentially suppressed and it is typically assumed there is essentially no DM above the local escape velocity, which is $v_{\text{esc}} \simeq 550$ km/s.

WIMP scattering of nuclei is discussed in the context of two class of possibilities:

- **Elastic and inelastic scattering:** The elastic scattering of a WIMP of a nucleus in a detector is simply the interaction of the WIMP with a nucleus as a whole, causing it to recoil, as depicted in Fig. 2.8. As we already have discussed, such a scattering event can give rise to a recoil energy $\sim \mathcal{O}$ (keV). In inelastic scattering, on the other hand, all of the energy does not go into the nuclear recoil; rather a nucleus is excited into a higher energy state which decays by photon emission leaving a detectable direct search signal.

- **Spin-independent and spin-dependent scattering:** Typically a scalar or a pure vector WIMP-nucleus interaction gives rise to a spin-independent (SI) direct search cross-section that does not depend on the spin of the target nucleus. In this case the cross-section leads to a coherent enhancement in scattering rates by $A^2$ (as the electrically neutral DM should identically couple to proton and neutron inside the nucleus), where $A$ is the atomic number of the target nucleus. An axial vector interaction between the DM and the nucleus, on the other hand, gives rise to a spin-dependent (SD) direct search cross-section where the cross-section $\sigma_{\text{SD}} \propto \frac{J+1}{J}$, $J$ being the total nuclear spin. The lack of benefit from the coherent enhancement for SD interactions results in most models being more accessible experimentally via their SI interactions than by their SD interactions. Since the WIMPs are non relativistic, the zero-momentum cross section for a WIMP of arbitrary spin and general Lorentz-invariant WIMP-nucleus cross section may be written in terms of a spin-independent (mostly scalar) and a spin-dependent (mostly axial vector) term [65]:

$$\sigma_{Xn} = \frac{4\mu_{XN}^2}{\pi}\Big[Zf_p + (A-Z)f_n\Big]^2 + \frac{32G_F^2\mu_{XN}^2}{\pi}\frac{J+1}{J}\Big(a_p\langle S_p\rangle + a_n\langle S_n\rangle\Big)^2 \tag{2.29}$$

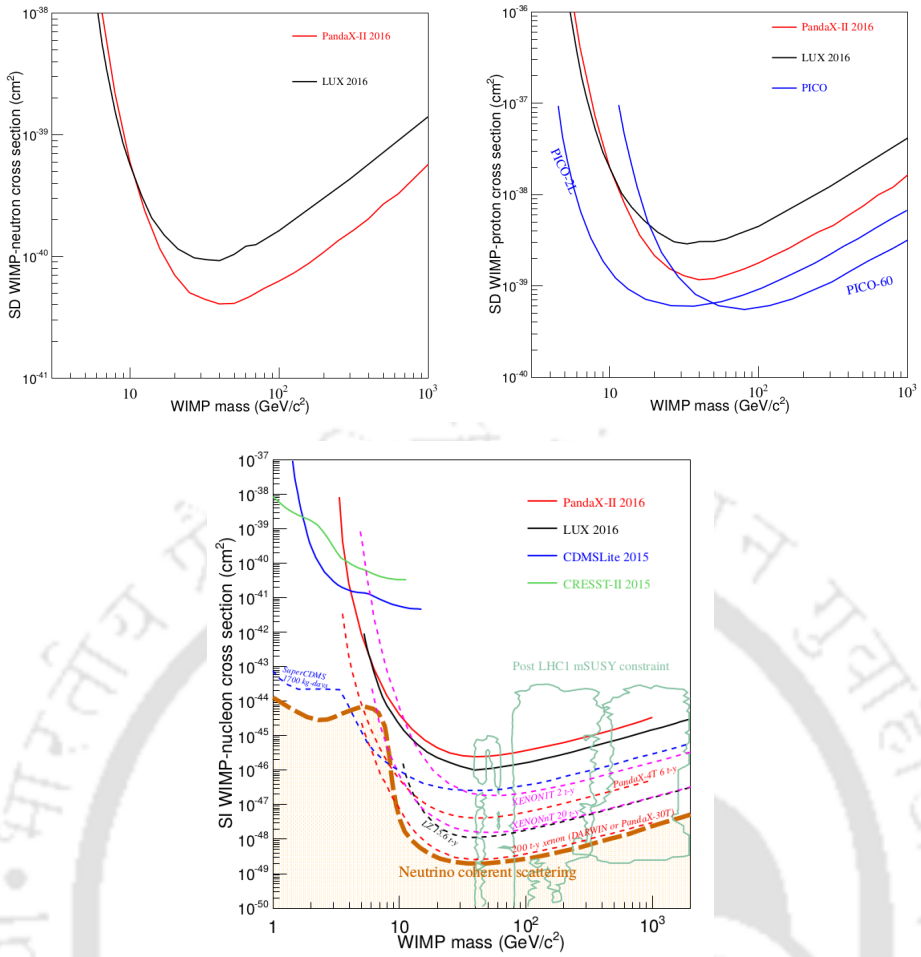


**Figure 2.9:** Top Left: Upper limits on the spin-dependent WIMP-neutron scattering cross-section set by different xenon-based experiments. Top Right: Same but for WIMP-proton scattering. Bottom: The projected sensitivity (dashed curves) on the spin-independent WIMP-nucleon cross-sections of a selected number of upcoming and planned direct detection experiments. The orange thick dashed line shows the background limit from solar, atmospheric and diffuse supernovae neutrinos while the orange shaded region below shows the neutrino floor. Figures taken from [64].

Here $f_p$ and $f_n$ ($a_p$ and $a_n$) are effective SI (SD) couplings of the WIMP to the proton and neutron, respectively. $A, Z$ are the atomic and mass number of the target material; $\langle S_{p,n} \rangle$ is the expectation values of the proton and neutron spins within the nucleus.

At present, there is a tight ongoing race between a few xenon experiments. By combining the 95 live days of data taken in 2013 and another 332 live days of data taken from 2014 to 2016, LUX collaboration [66] has reported a minimum of $10^{-46}$ cm$^2$ upper limit on SI direct search cross-section for a WIMP mass of $50$ GeV/c$^2$. PandaX-II which also utilizes dual-phase xenon detector, has reported a similar limit SI WIMP-nucleon cross-section [67, 68]. XENON1T experiment, the successor of XENON100, a $\sim$ 2000-kg-target-mass dual-phase (liquid-gas) xenon time projection chamber currently puts the strongest limit on the spin-independent WIMP-nucleon interaction cross section for WIMP masses above $10$ GeV/c$^2$ with a minimum of $7.7 \times 10^{-47}$ cm$^2$ for $35$ GeV/c$^2$ WIMPs at 90% confidence level [69, 70]. The upgrade experiment XENONnT, with a 6.5-ton liquid-xenon target, is in planning. Another future

large direct detection project, DARWIN, is aiming at a target mass up to 40-ton [71]. Spin-dependent direct search experiments have also been widely pursued. The leading experiments searching for the WIMP-neutron interaction are again using liquid xenon. The lowest published cross-section limit is $10^{-41}$ cm$^2$ at 33 GeV/c$^2$ from the LUX collaboration [72]. More recently, the PandaX-II experiment reported a more stringent limit [73]. It is also important to note that, the sensitivity of WIMP nucleon interaction will soon hit 'neutrino floor' as shown in Fig. 2.9 by the orange band, where the recoil spectrum due to solar, atmospheric and supernova neutrinos will be identical with that of DM-nucleon interaction. In such situations, distinguishing DM signal becomes even more harder and requires a different experimental strategy altogether (typically detectors that can measure the annual modulation of DM flux coming from a particular direction). Before closing this section, we should briefly comment on the fact that the detection of sub-GeV DM requires a somewhat different approach compared to conventional direct detection via nuclear recoils as it becomes less effective due to the much smaller recoil energies [74–86]. In this thesis we focus on DM of $\sim \mathcal{O}(100)$ GeV and conventional direct search bound.

**Indirect Detection**

Residual DM annihilations DM, DM $\rightarrow$ SM, SM may still occur at late universe where the relative velocity $\sim 10^{-3}$, particularly in the Galactic centres. Therefore any excess to SM final states from these regions can also hint to the presence of DM. Among the final states of interest, photon and neutrinos, being neutral and stable, can reach the detectors without getting much affected by the intermediate space. In case of WIMP annihilation, the photon energy lies within an energy range that is well within the reach of space-based telescopes like Fermi-LAT (gamma rays in the energy range from 20 MeV to more than 300 GeV) or ground based telescopes like MAGIC (in the range of $\sim$ 50 GeV to $\sim$ 50 TeV). Detectable gamma-rays can be tested at the instruments like the Fermi Large Area Telescope (LAT)[2] in space or the ground-based Cherenkov telescopes like MAGIC [3]. The differential gamma ray flux produced due to WIMP-like DM annihilation in a given region of the sky ($\Delta\Omega$) and observed at the Earth reads [87–91]:

$$\frac{d\Phi}{dE}(\Delta\Omega) = \frac{1}{4\pi}\frac{\langle\sigma v\rangle J(\Delta\Omega)}{2m_{\rm DM}^2}\frac{dN}{dE}, \tag{2.30}$$

where $dN/dE$ is the average gamma-ray spectrum per annihilation and

$$J(\Delta\Omega) = \int_{\Delta\Omega} d\Omega' \int_{LOS} dl\rho^2\left(l, \Omega'\right), \tag{2.31}$$

is the well-known $J$-factor which encodes all of the relevant astrophysical information with $\rho$ being the DM density profile, and the integrals running over $\Delta\Omega$ and the line-of-sight (LOS) through the DM distribution. Since the DM can annihilate into charged fermion final states: $\mu^+\mu^-, \tau^+\tau^-, b\bar{b}$ etc, all such final states can

[2] http://fermi.gsfc.nasa.gov
[3] https://magic.mpp.mpg.de/

give rise to gamma rays. Therefore, one can constrain the DM annihilations to different charged final states from non observations of gamma ray excess [92–95]. At all energies, the cosmic ray (CR) spectrum is dominated by matter over antimatter. However, in most of the cases, DM annihilating (or decaying) to SM in the halo of the Milky Way would produce equal amounts of matter and antimatter. This would naturally lead to an excess of antimatter relative to that predicted by standard astrophysical mechanisms. Thus, the indirect DM search strategies exploiting CR look mostly for anti-proton or positron excess [96–107]. In addition to gamma rays and cosmic rays, DM annihilation can also produce highly energetic neutrinos that are potentially detectable by neutrino telescopes such as IceCube [108] or at low energies, Super-K [109]. DM annihilation products can also alter the abundance of light elements during BBN or change the inonization history of the universe at the time of formation of the CMB. The measurements of BBN and CMB put robust constraints on DM annihilation [36]. Similar to DM annihilation, indirect search for DM decaying to gamma-rays [110–112], $X$-rays [113, 114], neutrinos [115] and CR [116] also provide stringent limits on DM mass, coupling etc. However, for WIMP and FIMP like CDM cases we explore, the bounds from indirect search are milder than the one from relic density.

**Collider Searches**

In this section we review the experimental strategies relevant for DM searches at the collider (for example, at the Large Hadron Collider (LHC)). As emphasized earlier, the same DM+DM $\rightarrow$ SM+SM interaction that governs the freeze-out in the early universe giving rise to observed relic abundance today, can also produce DM at high energy collider through the reverse process: SM+SM $\rightarrow$ DM+DM. When dark sector consists of a single DM particle, one can only rely on mono-$X$ searches, which are concerned with the production of a single SM particle in association with missing transverse momentum produced by the DM. Here $X$ can be a gluon (jet), $V \in W, Z, \gamma$ or Higgs [117–122]. It is always possible to produce DM particles in association with one or more QCD jets from initial state radiation in proton-proton collisions. In a similar manner as in mono-jet events, DM may also be produced together with a vector boson $V \in \gamma, W, Z$ which is radiated off a quark in the initial state. While the corresponding production cross section is significantly smaller than for QCD radiation, the process is much cleaner and can therefore be searched for with higher sensitivity. Mono-photon searches are among the simplest searches for DM, requiring only a high $p_T$ photon [123, 124]. SM-like Higgs boson, in association with missing transverse momentum also turns out to be a promising signal both when Higgs decays in $\gamma\gamma$ and $b\bar{b}$ final state [123, 125–127]. Also, if the DM couples dominantly to heavy quark flavors, a promising signal at the LHC is a top-quark pair in association with missing transverse momentum [125, 128–131]. In all such cases, missing energy (momentum) is the key variable to segregate the DM signal, which can be defined as

$$\text{typical DM Signal : mono-X} + \not{E}_T; \quad X \in \{j, H, W, Z\};$$
$$\not{E}_T = -\sqrt{(\sum_{\ell,j,unc.} p_x)^2 + (\sum_{\ell,j,unc.} p_y)^2}, \tag{2.32}$$

where the sum runs over all visible objects at collider detector that include the leptons, jets, and the unclustered components. A multipartite dark sector, consisting of heavy charged fields can produce a signal like

$$\text{atypical DM signal} : n.\ell + m.j + \not{E}_T;\ \ell = \{e^{\pm}, \mu^{\pm}\}, \tag{2.33}$$

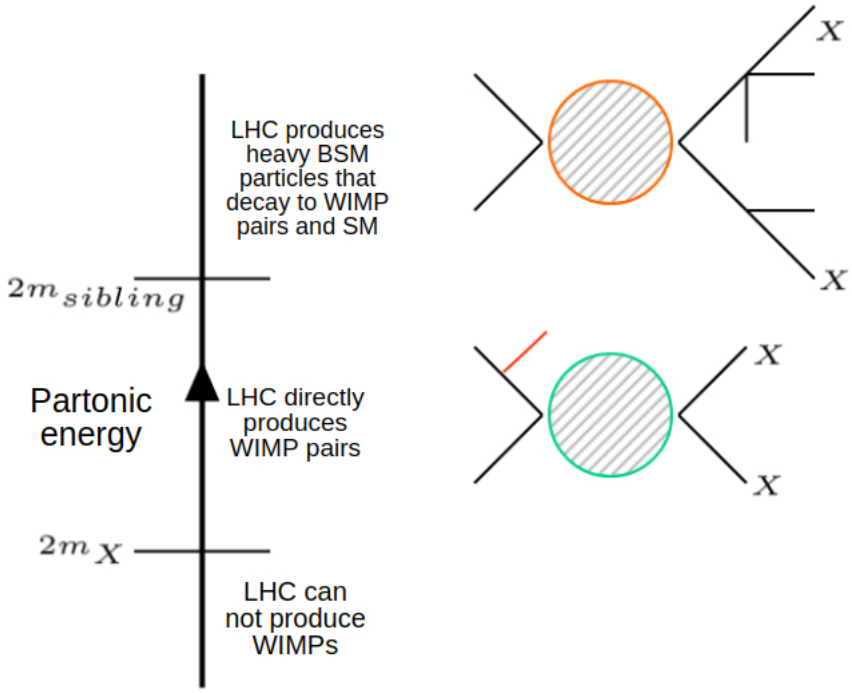


**Figure 2.10:** Possible DM Signals at Collider (LHC).

where $n$ and $m$ are real numbers. Fig. 2.10 nicely encapsulates both of these possibilities where the DM can either leave a simple mono-$X$ signal or can also give rise to more complicated signatures. The figure clearly tells us that if the center of mass (CM) energy of the collider (say, the LHC) is just above twice the DM mass $2m_X$, then LHC can directly produce a pair of WIMPs, and hence it is possible to probe the mono-$X$ signature with missing energy. If the CM energy goes beyond twice the mass of the heavier particles in the dark sector *i,e.*, $2m_{\text{sibling}}$ then it is possible to produce those heavier multiplets in the collider which can further decay to WIMP-pairs in association with SM leptons and jets. It is worth mentioning that if the DM mass is less than half of the mass of the SM Higgs boson, it may be possible to produce pairs of DM particles in Higgs decays, and therefore invisible Higgs decays can also be a good probe for DM signal at collider, although heavily constrained by current data [132–135]. While the searches in the context of complete theoretical frameworks such as Supersymmetry (SUSY) remain a focus of the LHC, over the years DM search program has been augmented by a model agnostic approach [118, 120, 136–144]. DM searches at colliders play an important role in complementing the search programme of non-collider searches. Especially, a non-observation of DM at the LHC would have important implications for our understanding of the nature of DM. We will discuss in detail the specific signal and simulation strategy in context of our model framework.

## 2.3 Non-thermal dark matter: Freeze-in & FIMPs

The basic idea of freeze-out is based on the assumption that the DM was in thermal equilibrium with the visible sector in the early universe. However, if the coupling between the visible sector and DM particles is very small $\sim \mathcal{O}(10^{-10})$ the interactions are not strong enough for the DM to remain in thermal equilibrium. Instead the observed DM abundance can be produced from particles in the thermal bath, called the *freeze-in* production. The particle undergoing freeze-in is (naturally) termed as feebly interacting massive particle (FIMP). In the simplest case, the initial number density of DM particles is either zero or negligibly small, and the observed abundance is produced by bath particle decays or annihilation. As the DM production takes place from the decay (or annihilation) of the bath particle, hence the freeze-in yield is active until the number density of the mother particle becomes Boltzmann-suppressed $\sim e^{-m/T}$. The comoving number density of DM particles then becomes a constant and the DM abundance freezes in after the temperature drops below the DM mass.

### 2.3.1 Boltzmann Equation (BEQ) for FIMP

Consider the case where the FIMP $X$ is the DM particle itself. If $\chi$ has a coupling to two bath particles via $\lambda\chi\mathcal{B}_1\mathcal{B}_2$, then for $m_{\mathcal{B}_1} > m_{\mathcal{B}_2} + m_\chi$, the freeze-in production of $\chi$ is via decay of the heavier bath particle $\mathcal{B}_1$. The relic abundance can be obtained by solving the Boltzmann equation (BEQ) for the number density of $\chi$ as

$$\dot{n}_\chi + 3Hn_\chi = \int d\Pi_\chi\, d\Pi_{\mathcal{B}_1}\, d\Pi_{\mathcal{B}_2} (2\pi)^4 \delta^4(p_{\mathcal{B}_1} - p_{\mathcal{B}_2} - p_\chi) \times \left[ |\mathcal{M}|^2_{\mathcal{B}_1 \to \chi + \mathcal{B}_2} f_{\mathcal{B}_1}(1 + f_\chi)(1 + f_{\mathcal{B}_2}) - |\mathcal{M}|^2_{\mathcal{B}_2 + \chi \to \mathcal{B}_1} f_{\mathcal{B}_2} f_\chi (1 + f_{\mathcal{B}_1}) \right]. \tag{2.34}$$

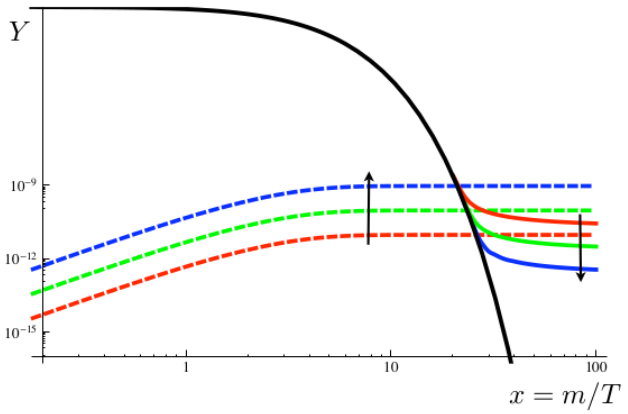


**Figure 2.11:** Plot of the evolution of the relic yields for conventional freeze-out (solid coloured) and freeze-in via a Yukawa interaction (dashed coloured) as a function of $x = m/T$. The black solid line indicates the yield assuming equilibrium is maintained, while the arrows indicate the effect of increasing coupling strength for the two processes. The figure is taken from [145].

The second term in the above expression involving the back-reaction can be approximated to be $f_\chi \approx 0$ in the early universe. Using the definition of decay width $\Gamma_{\mathcal{B}_1\to\mathcal{B}_2+\chi}$ of $\mathcal{B}_1 \to \mathcal{B}_2\chi$:

$$\Gamma_{\mathcal{B}_1\to\chi+\mathcal{B}_2} = \int \frac{1}{2m_{\mathcal{B}_1}} \frac{|\mathcal{M}|^2_{\mathcal{B}_1\to\chi+\mathcal{B}_2}}{g_{\mathcal{B}_1}} (2\pi)^4 \delta^4(p_{\mathcal{B}_1} - p_{\mathcal{B}_2} - p_\chi) d\Pi_\chi \, d\Pi_{\mathcal{B}_2}, \tag{2.35}$$

and neglecting Pauli-blocking/stimulated emission effects *i.e*, approximating $(1 + f_{\mathcal{B}_1}) \simeq 1$ we can re-cast Eq. (2.34) in terms of the yield $Y_\chi = \frac{n}{s}$ (using $\dot{T} \approx -H.T$) as [145]:

$$Y_\chi \simeq \int \frac{g_{\mathcal{B}_1} m^2_{\mathcal{B}_1} \Gamma_{\mathcal{B}_1}}{2\pi^2} \frac{K_1(x)}{s.H} dx, \tag{2.36}$$

where $x = \frac{m_{\mathcal{B}_1}}{T}$ and $s$ and $H$ are comoving entropy density and Hubble constant respectively. Performing the $x$ integral one can obtain:

$$Y_\chi \approx \frac{135 g_{\mathcal{B}_1}}{8\pi^3 (1.66) g_{\star s} g_{\star\rho}} \frac{M_{\rm pl}\Gamma_{\mathcal{B}_1}}{m^2_{\mathcal{B}_1}}. \tag{2.37}$$

Thus the abundance of the species in question can be obtained via:

$$\Omega_\chi h^2 = \frac{m_\chi Y_\chi(T_0)}{\rho_c} \approx \frac{1.09\times 10^{27} g_{\mathcal{B}_1}}{g_{\star s} g_{\star\rho}} \frac{m_\chi \Gamma_{\mathcal{B}_1}}{m^2_{\mathcal{B}_1}}. \tag{2.38}$$

The DM $\chi$ can also have a freeze-in production from the scattering/annihilation of the bath particle. In the simplest case, for a $2 \to 2$ process of the form $\lambda\chi\mathcal{B}_1\mathcal{B}_2\mathcal{B}_3$ where $\mathcal{B}_{1,2,3}$ are the bath particles, the BEQ for the freeze-in yield for $\chi$ can be written as

$$\dot{n}_\chi + 3Hn_\chi = \int \sum_{i=1}^{4} d\Pi_i \, (2\pi)^4 \, \delta^{(4)}\left(p_{\mathcal{B}_1} + p_{\mathcal{B}_2} - p_{\mathcal{B}_3} - p_\chi\right) |\mathcal{M}|^2_{\mathcal{B}_1\mathcal{B}_2\to\mathcal{B}_3\chi} \, f_{\mathcal{B}_1} f_{\mathcal{B}_2}. \tag{2.39}$$

The BEQ can be re-casted in terms of the bath temperature $T$ as

$$\dot{n}_\chi + 3Hn_\chi = \frac{T}{512\pi^6} \int_{s=m^2_\chi}^{\infty} ds d\Omega \, |\vec{p}|_{\mathcal{B}_1\mathcal{B}_2} \, |\vec{p}|_{\mathcal{B}_3\chi} \, |\mathcal{M}|^2_{\mathcal{B}_1\mathcal{B}_2\to\mathcal{B}_3\chi} \frac{K_1(\sqrt{s}/T)}{\sqrt{s}}, \tag{2.40}$$

with

$$|\vec{p}|_{ij} = \frac{1}{2\sqrt{s}} \sqrt{s - (m_i + m_j)^2} \sqrt{s - (m_i - m_j)^2},$$

where $m_{i,j}$ are the masses of the incoming/outgoing states. Since the matrix element is nothing but $|\mathcal{M}|^2_{\mathcal{B}_1\mathcal{B}_2\to\mathcal{B}_3\chi} = \lambda^2$, on changing variable to $Y_\chi$ one obtains [145]

$$Y_X \simeq \frac{135\lambda^2 M_{\rm pl}}{256\pi^7 g_{\star s}\sqrt{g_{\star\rho}}\,(1.66)\, m_\chi} \int_0^\infty dx x K_1(x) = \frac{135\lambda^2 M_{\rm pl}}{512\pi^7 g_{\star s}\sqrt{g_{\star\rho}}\,(1.66)\, m_\chi}. \tag{2.41}$$

As before, one can then easily obtain the relic abundance of $X$. From above relations, one can easily that freeze-in yield is proportional to the decay or annihilation cross-sections, therefore it is proportional to the interaction rate between the visible sector and DM particles. This is exactly opposite to that of the freeze-out scenario, where larger interaction rate implies smaller final abundance. In fact this is the reason, why the required coupling for freeze-in turns out that feeble to satisfy correct relic. However, the required coupling values and assumptions of the initial abundance are not the only differences between the freeze-in and freeze-out scenarios, as also the relation between the relevant mass scale and the bath temperature at the time of DM production is different. In the freeze-out mechanism the relic abundance is produced at $m/T = 10...30$, whereas for the freeze-in mechanism it arises during the epoch $m/T = 1...5$. This is depicted in Fig. 2.11, where we can clearly see how the yield of a relic behaves exactly opposite to each other in WIMP vs FIMP scenario.

Despite these opposite features, freeze-out and freeze-in share crucial common aspects: the final out-of-equilibrium abundance, given the relevant particle masses and couplings, can be computed solely from an initial state of bath particles that are in thermal equilibrium, and the resulting abundance is dominated by IR physics. Prospects of freeze-in production of DM via renormalizable interactions has widely been studied [145–156]. One can, however, consider an alternate possibility, where the freeze-in production proceeds via non-renormalizable operators. In such cases observed DM abundance usually becomes sensitive to the maximum temperature, arguably the reheat temperature ($T_{RH}$) of the universe. DM yield in such cases becomes maximum during reheat temperature itself. This is dubbed as *UV freeze-in* [157–159], as the DM abundance is set by the UV physics, in contrast to *IR freeze-in*, where DM abundance piles up at much lower temperature. We will come back to this feature in the context of a specific effective operator formalism.

**Signatures of FIMP**

As opposed to the WIMPs, the coupling of the FIMP to the thermal bath is very feeble, so a crucial question is whether the freeze-in mechanism can be tested by measurements at accelerators or by cosmological observations. Following are some of the possible observational aspects for freeze-in scenario.

- **Collider signatures:** A unique signature of a feebly coupled dark sector is the appearance of particles with macroscopic lifetimes. In many cases, the frozen-in DM is coupled to the SM via a mediator particle with dark charge, which itself is not necessarily feebly coupled to the visible sector. This mediator particle could then be produced in collider experiments [160] which decays to DM producing displaced signatures: tracks appearing away from the collision axis, long-lived particles decaying in the calorimeter, or disappearing tracks. Searches for long-lived particles have been done both by ATLAS and CMS [161–164]. There are also dedicated collaborations which search for long-lived and millicharged particles [164–168].

- **Astrophysical and cosmological signatures:** A potential solution to the small scale problems is given by warm DM, where structure formation is suppressed below the free-streaming scale of the light DM particles in the early Universe. However, warm DM is severely constrained by the Lyman-$\alpha$ forest data. This

discrepancy could be alleviated if the DM velocity distribution is non thermal, which is possible if DM is produced via freeze-in. Self-interacting DM produced via the freeze-in mechanism has also been considered in [169, 170]. In such cases it is possible to probe the strongly interacting FIMP by virtue of several astrophysical effects. As mentioned earlier, due to the feeble couplings generically present in the freeze-in set-up, long lived particles are a rather common feature in these models. If they decay into the SM, the energy deposited into the SM photon bath between BBN and photon decoupling eras can lead to observable effects in the light element abundances or in the CMB.

## 2.4 Dark Matter *à la* Vector Boson

Vector bosons (spin one particles) as fundamental particles play a significant role in the known SM physics. Vector bosons like photon, gluon, $W^{\pm}$, $Z$ are force carriers of electromagnetic, strong and weak interactions respectively. In the gauge theory construct of the SM they are called the 'gauge bosons' transforming under the adjoint representation of the corresponding gauge group, as discussed before. For explaining the nature of DM we already pointed out that there is absolute ignorance about its intrinsic spin. Therefore, a scalar, a fermion, a vector boson or even more complex spin structure can be assumed for particle DM. However, vector bosons, as they appear in quantum gauge theories, are somewhat special as DM candidates and are of interest for this thesis. It is therefore legitimate that we discuss some features that vector boson DM (VDM) frameworks inherit before we dig deep into specific model frameworks.

Compared to fermionic (spin-1/2) or scalar (spin-0) candidates, vector bosons are relatively unexplored DM candidates. Absent any vector boson in the SM having the credentials of DM, VDMs can appear in the models with extended SM gauge symmetry. One may note here that when stability and charge neutrality are concerned, VDM need not necessarily appear as a gauge vector boson. However, as discussed above, DM production in the universe either via WIMP or FIMP mechanism relies on the coupling of DM with the visible sector, which is difficult to achieve for a vector boson transforming under a global symmetry. In this thesis, we are not going to make an exception to that and consider the VDM as a massive gauge boson coming from an extended gauge sector that breaks via spontaneous symmetry breaking. Depending on the nature of the gauge extension, the vector boson can either be abelian or non-abelian.

An *abelian* VDM arises in a simple $U(1)$ extension of the SM, where simplest possibility is to assume all the SM particles to be neutral under that $U(1)_X$. In a phenomenologically viable set up, the symmetry must be broken completely to avoid the existence of massless fields. A discrete symmetry, say $Z_2$, is thus required on top of the $U(1)_X$ under which the new vector boson is odd to keep it stable. Note that, imposition of this symmetry is necessary to prevent kinetic mixing of the dark $U(1)$ with SM $U(1)_Y$ which can lead to the decay of the $U(1)_X$ gauge boson. The model also needs new complex scalar field which are singlet under the SM gauge symmetry, but transform under the new $U(1)_X$. The non-zero VEV of this scalar will lead to massive gauge boson via spontaneous breaking of $U(1)_X$. Hence a spin-0 scalar mediator is always present in all these cases that connects the dark sector with the

visible sector. The gauge boson transforming under the new $U(1)_X$ symmetry can still remain stable due to the unbroken $Z_2$ symmetry, and thus can be identified as a potential DM candidate. The extended scalar sector also helps to improve the vacuum stability by making the electroweak vacuum stable upto the Planck scale for $m_t \sim 173$ GeV. Within the framework of abelian gauge theory, one may also consider 'Stueckelberg mechanism' to generate mass term for the new gauge boson without introducing new scalar degrees of freedom [171, 172], but in that case one also needs additional fields so that the dark sector can communicate with the visible sector. For non-abelian cases, however, Higgs mechanism in spontaneous symmetry breaking remains the only presently known way to give masses to non-Abelian vector fields in a renormalizable and unitary theory. Due to the inherent simplicity and minimal particle content, such 'Higgs portal' model for abelian vector DM has been extensively studied in many different contexts [150, 173–189] both in UV complete and effective theories. Abelian gauge boson DM also appears in the context of more exotic theories like the large extra dimension [190] or the little Higgs model [191]. In this thesis we shall address abelian vector DM scenario within an effective theory framework where the dark and the visible sector is connected via an operator of mass dimension five.

A *non-abelian* VDM, on the other hand, in its simplest form, can appear from an $SU(2)_X$ extension of the SM gauge symmetry. Following the abelian case, one also needs a complex scalar that transforms under the same gauge group to initiate the spontaneous symmetry breaking. As before, the scalar field that breaks the gauge symmetry may be used as a portal to the visible sector by mixing with the SM Higgs; the amount of mixing controls the signal at direct detection experiments or at colliders. In the absence of any new fields transforming under the dark $SU(2)_X$, the DM is naturally stable due to the emergence of a custodial symmetry giving rise to degenerate, massive spin-1 particles as shown in [192–195]. In cases where the $SU(2)_X$ is broken by dark scalar multiplets of larger representations *e.g.*, a triplet or a quadruplet or a quintet, the remnant unbroken symmetry helps in stabilizing the DM [177, 196–198]. The situation becomes a bit complicated in the presence of new fields (*e.g.*, fermions) that transform under the $SU(2)_X$. In such cases, depending on the particle content, one needs to impose a discrete or global symmetry to ensure the stability of the DM [199–201]. Also, an extended scalar sector is required in order to generate masses for all the fermions. A particularly interesting aspect of non-abelian vector boson DM is the presence of self-interaction which naturally leads to a class of DM called the strongly interacting massive particles (SIMP) [202–204]. Non-abelian vector DM that self-interacts through low-mass, spin-1 mediators (dark photons) has recently been studied in [205]. Finally, one may equivalently consider a massive vector boson DM candidate emerging from a gauged hidden $SU(3)$ sector [206, 207]. A recent exploration with $SU(3)$ gauge group may resolve the tension in the Hubble constant measurement and give rise to a smaller $\sigma 8$ for structure growth [208]. However, in this thesis we shall stick to UV complete theory of non-abelian VDM (WIMP and FIMP) in the context of gauged $SU(2)$ extension of the SM.

## 2.5 The origin of Neutrino Mass

Existence of non-zero but tiny neutrino mass has been well established via short and long baseline neutrino oscillation experiments [209–216]. On the other hand, it is not possible to construct a renormalizable mass term for the neutrinos with the fermionic content and gauge symmetry of the SM. The obvious consequence is that in order to introduce a neutrino mass in the theory one must extend the particle content of the model, depart from gauge invariance and/or renormalizability, or do both. Although the mass of the lightest neutrino is unknown, but the sum of masses is bounded from above: $\sum_i m_{\nu_i} < 0.23$ eV by cosmological data from CMB observations [45] with PLANCK satellite. A stronger bound: $\sum_i m_{\nu_i} < 0.12$ eV can be derived if other cosmological observations are included [36].

Since in the SM neutrinos are massless, one is compelled to transcend beyond the realms of the SM. All fermions in the SM with the exception of neutrinos have two properties in common: They are Dirac fermions, and their masses are generated by the Higgs mechanism. It is not clear whether this also applies to neutrinos. Since they are neutral, they could in principle be their own antiparticles (Majorana fermions), and it may be that their mass is not solely generated by the Higgs mechanism. In this section we would like to briefly go through some known mass generation mechanisms for neutrinos.

### Dirac masses

We first consider the possibility that neutrinos are Dirac particles. This necessarily requires the existence of right handed (RH) neutrinos $N_R$ to construct mass term via Yukawa interaction:

$$-\mathcal{L}_{\text{Dirac}} = Y_\nu \overline{\ell_L} \widetilde{H} N_R + H.c., \tag{2.42}$$

where $\widetilde{H} = i\sigma^2 H^\star$ with $H$ being the SM Higgs doublet, and $l_L$ denotes the left-handed lepton doublet. After SSB, from Eq. (2.42) we can write:

$$-\mathcal{L}^{'}_{\text{Dirac}} = \overline{\nu_L} m_D N_R + H.c., \tag{2.43}$$

with $m_D = Y_\nu \langle H \rangle$ and $\langle H \rangle = 246$ GeV being the SM Higgs VEV. This mass matrix can then be diagonalized by a bi-unitary transformation to obtain the light neutrino mass. But, as one can see, since the mass term is generated from a Yukawa interaction (Eq. (2.43)) in the way as all other SM fermion masses, the Yukawa coupling then has to be very small $Y_\nu \sim 10^{-10}$ in order to be consistent with the observed light neutrino mass. This is one reason why this possibility of neutrino mass generation is somewhat "unnatural." A salient feature of massive Dirac neutrinos is lepton number conservation, while lepton flavours are violated in this process of mass generation. However, the observed phenomena of neutrino oscillations hint towards the existence of neutrino flavor violation, while oscillation can happen for neutrinos either of Dirac or Majorana nature.

**Majorana masses**

The LH neutrino field $\nu_L$, together with its charge conjugate partner $(\nu_L)^c$ can in principle form a neutrino mass term as $(\nu_L)^c$ is actually right-handed:

$$-\mathcal{L}_{\text{Majorana}} = \frac{1}{2}\overline{\nu_L}\,(\nu_L)^c\, m_L + H.c. \tag{2.44}$$

But such a kind of term is forbidden by the SM gauge symmetry, which contains only one $SU(2)_L$ Higgs doublet and preserves lepton number. However, it is possible to generate such a mass term in a gauge invariant way from the dimension-5 Weinberg operator:

$$Y_\nu \frac{1}{\Lambda}\,(\ell_L H)\,(H\ell_L)\,, \tag{2.45}$$

where $\Lambda$ is some high scale in the theory, and is the messenger of some new physics. Thus, the small Majorana mass is obtained from $\Delta L = 2$ operator after SSB:

$$m_\nu = \frac{Y\langle H\rangle^2}{2\Lambda} = \frac{Yv^2}{2\Lambda}. \tag{2.46}$$

Note that, if $\Lambda$ is large enough ($\Lambda \sim 10^{14}$ GeV), light neutrino mass in the correct ballpark can be generated even with $Y \sim \mathcal{O}(1)$ unlike the case in Sec. 2.5 which requires an "unnatural" Yukawa coupling. This effective description can be turned to UV complete model set ups called Seesaw models (obviously to address that a heavy new physics generates a light neutrino mass) as we discuss next. However, such a large new physics scale is difficult to probe. TeV scale $\Lambda$ can be assumed, for which $Y$ is again very small and the situation is fine tuned.

**Hybrid mass term**

The right handed neutrino (RHN) $N_R$, together with its charge conjugate counterpart $(N_R)^c$ can also form a Majorana mass term just as in Sec. 2.5. Hence, it is possible to write the following neutrino mass matrix in terms of $\nu_L, (\nu_L)^c$ and $N_R, (N_R)^c$ fields:

$$\begin{aligned} -\mathcal{L}_{\text{hybrid}} &= \overline{\nu_L} m_D N_R + \frac{1}{2}\overline{\nu_L}\,(\nu_L)^c\, m_L + \frac{1}{2}\overline{(N_R)^c} N_R m_R \\ &= \frac{1}{2}\begin{pmatrix}\overline{\nu_L} & \overline{(N_R)^c}\end{pmatrix}\begin{pmatrix} m_L & m_D \\ m_D^T & m_R\end{pmatrix}\begin{pmatrix}(\nu_L)^c \\ N_R\end{pmatrix} + H.c., \end{aligned} \tag{2.47}$$

where $m_{L,R}$ are the Majorana mass matrices corresponding to LH and RH neutrinos. There are two particularly interesting limits Eq. (2.47):

- If the mass $m_L$ is absent, one will be left with the canonical or **type-I seesaw** relation: $m_\nu \approx -m_D m_R^{-1} m_D^T$.

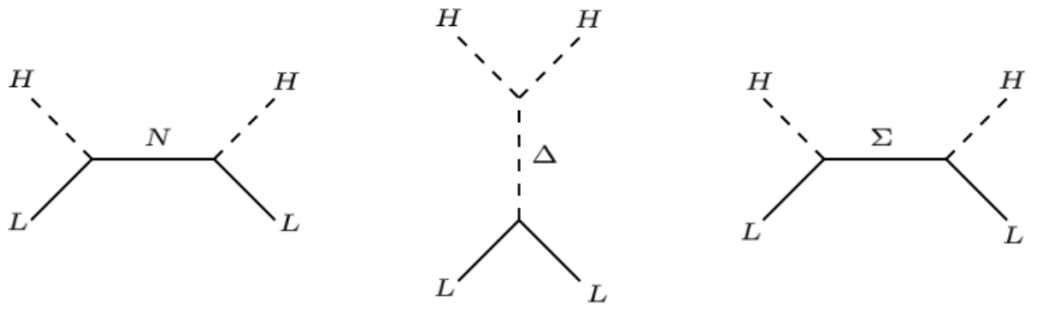


*Type-I seesaw* *Type-II seesaw* *Type-III seesaw*

$$m_\nu = Y_N^T \frac{1}{m_N} Y_N v^2 \qquad m_\nu = Y_\Delta^T \frac{\mu_\Delta}{m_\Delta^2} v^2 \qquad m_\nu = Y_\Sigma^T \frac{1}{m_\Sigma} Y_\Sigma v^2$$

**Figure 2.12:** Different types of seesaw mechanisms.

- If only the mass term $m_L$ is present, one will be left with the **type-II seesaw** relation: $m_\nu = m_L$.

Without loss of the gauge symmetry and Lorentz invariance, the essential spirit of seesaw mechanisms is to add a few new particles into the SM. Tiny masses of three known neutrinos are attributed to the existence of heavy degrees of freedom and lepton number violation. There are three celebrated seesaw mechanisms that are available in the literature:

- **Type-I seesaw:** Three heavy right-handed neutrinos are added into the SM and the lepton number is violated by their Majorana mass term [217–219]:

$$-\mathcal{L}_{\text{type-I}} \supset y_\nu \overline{\ell_L} \widetilde{H} N_R + \frac{1}{2} \overline{(N_R)^c} N_R m_N + H.c. \tag{2.48}$$

- **Type-II seesaw:** one heavy Higgs triplet is added into the SM and the lepton number is violated by its interactions with both the lepton doublet and the Higgs doublet [220–224]:

$$-\mathcal{L}_{\text{type-II}} \supset \frac{1}{2} y_\nu \overline{\ell_L} \Delta i\sigma^2 \ell_L^c - y_\Delta \mu_\Delta H^T i\sigma^2 \Delta H + H.c., \tag{2.49}$$

where $\Delta = \begin{pmatrix} \Delta^- & -\sqrt{2}\Delta^0 \\ \sqrt{2}\Delta^{--} & -\Delta^- \end{pmatrix}$ is the $SU(2)_L$ scalar triplet.

- **Type-III seesaw:** Three heavy triplet fermions are added into the SM and the lepton number is violated by their Majorana mass term [225–229]:

$$-\mathcal{L}_{\text{type-III}} \supset \sqrt{2} y_\nu \overline{\ell_L} \Sigma^c \widetilde{H} + \frac{1}{2} \text{Tr}\left(\overline{\Sigma} m_\Sigma \Sigma^c\right) + H.c., \tag{2.50}$$

with $\Sigma = \begin{pmatrix} \Sigma^0/\sqrt{2} & \Sigma^+ \\ \Sigma^- & -\Sigma^0/\sqrt{2} \end{pmatrix}$ is the $SU(2)_L$ fermion triplet

where $\widetilde{H} = i\sigma_2 H^\star$. Fig. 2.12 gives a nice pictorial description of all the seesaw mechanisms discussed above. Not to mention that there are a number of variations or combinations of these three typical seesaw mechanisms in the literature [230–236]. In context with a particular model we shall discuss one of the variants of seesaw mechanism, namley the 'inverse seesaw', which is interesting possibility of generating tiny neutrino masses at the TeV scale. The very fact that neutrinos have similar charge neutrality and weak interaction as similar to WIMP DM, it is intriguing to study DM and neutrino under the same umbrella of physics beyond the SM.

## 2.6 A theory of Grand Unification

As elaborated in Sec. 1.1, the SM is a product of three gauge groups: $SU(3)_c \otimes SU(2)_L \otimes U(1)_Y$ and so involves three independent couplings: $\{g_s, g_2, g_1\}$ corresponding to $SU(3)_c$, $SU(2)_L$ and $U(1)_Y$ respectively. The values of these couplings are different at Electroweak scale, which is one of the reasons that we see the nature the way it is. However, the question why they are so different leads to the idea of a possible gauge coupling unification, where we ideate that three SM gauge forces might have a common origin at some high scales, where they are described by a single unified gauge group, characterized by a single gauge coupling. The Grand Unified Theory (GUT) [217, 219, 237–241], thus, aims for the unification of the three couplings. Hence GUT is argued to be a complete and unique theory of all fundamental forces except gravity. The running of gauge couplings with energy stems from a sacred principle called renormalization, leading to renormalization group equations (RGE). GUT not only aims for a coupling unification, but family unification as well. Hence it also ensures the presence of quarks and leptons in a common multiplet of a single gauge group. Thus the fermions all originate from a single irreducible representation (irrep) of some larger gauge group, like $SU(5)$, $SO(10)$, $E(6)$ etc.

Though $SU(5)$ was found to be the simplest GUT group, it has been ruled out by the proton decay lifetime measurements [243]. GUT models are also supported by the fact that the running of the three SM gauge couplings makes them approach each other at some high scale (artifact of the gauge groups and corresponding RGEs), which approximately happens at $\sim 10^{14}$ GeV in the SM. However, as shown in Fig. 2.13, SM particle content do not allow the couplings to unify at one point. This might be taken as another reason for believing in physics beyond the SM. The other two main drawbacks of the SM like dark matter and neutrino mass, which we already have discussed in some details, can be well be addressed within unified gauge theories. For example, the 16 dimensional spinorial representation of $SO(10)$ can accommodate the 15 SM fermions per generation. The extra fermion can be the right

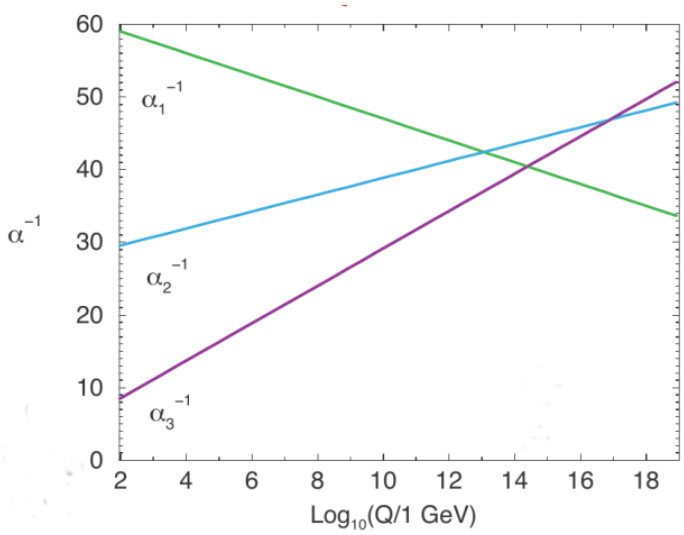


**Figure 2.13:** Running of the SM gauge couplings $\alpha_{1,2,3}$ corresponding to the gauge groups $U(1)_Y$, $SU(2)_L$ and $SU(3)_c$ with the renormalization scale $Q$. As it can be seen, gauge unification dos not work within the SM particle content. This figure is taken from [242].

handed neutrino (RHN) needed for mass generation of the SM neutrinos and can also be a potential DM candidate. The thesis explores one such possibilities where a non-abelian DM model is derivable from a decomposition of $E(6)$ or its maximal subgroup $[SU(3)]^3$.

## 2.7 Objective of the Thesis

The purpose of this thesis is to investigate models of vector boson DM and their phenomenological implications mainly in direct and collider searches. Vector bosons, as DM, require a gauge extension of the SM and in order to have a massive vector boson DM (by maintaining the gauge invariance of the underlying theory) the new gauge symmetry has to be spontaneously broken as explained before. This also demands an extended scalar sector to serve the purpose, together with a remnant symmetry that keeps the DM stable. As a result, vector boson DM models are difficult to construct, while they offer very rich phenomenology. One may have an abelian vector boson DM with $U(1)$ gauge group extension, or non-abelian vector boson DM with at least $SU(2)$ extension of the SM gauge symmetry. As mentioned in Sec. 2.4, the idea of an abelian extension being comparatively easier to conceive, has been addressed in the literature in profound detail. While the non-abelian construction is less explored. The thesis elaborates upon different possibilities of non-abelian vector boson DM within UV complete framework where the DM emerges from a gauged $SU(2)_X$ extension of the SM. An abelian DM prescription is also being addressed in a model-independent manner from the effective theory perspective where the SM is augmented with a gauged $U(1)_X$ symmetry that is broken spontaneously by a very heavy decoupled scalar such that the DM communicates with the SM exclusively through suppressed operator of dimension five.

Due to its simplicity and predictability with less fine tuning, we primarily focus on the WIMP paradigm. We show, for a single-component non-abelian WIMP-like

VDM it is possible to evade stringent spin-independent direct search bounds via: (a) co-annihilation and (b) unique $s$-channel direct search in presence of other exotic heavy fermions. The later has not been pointed out in the literature so far to the best of our knowledge. To this end, a multipartite WIMP scenario can also provide a cushion to disentangle annihilation cross-section to SM from direct search interaction, where the DM-DM conversion, *viz.*, heavier DM component annihilating to the lighter one can produce adequate thermal relic, and do not contribute to direct search cross-sections. The presence of exotic fermions and heavy scalars give rise to several interesting collider signatures, including multilepton plus missing energy signature for such WIMP-like VDM models, which can provide complementary search strategies to those due to direct search and serves as a key distinctive feature of a WIMP like vector boson DM framework.

As an alternate prescription to the WIMP paradigm, the thesis also sheds light on FIMP scenario where the VDM is produced via freeze-in from the decay of a bath particle. In case the interaction of the DM with the thermal bath is renormalizable, the resulting DM abundance is determined by "IR" freeze-in, where the dominant DM production occurs at low temperature, more accurately, around the mass of the decaying particle. The incredibly tiny coupling strength of the DM with the visible sector, which is required to keep the DM out of equilibrium, automatically saves the DM from direct search or collider search bounds. However, such scenarios are very tightly constrained from early universe measurements like the abundance of light elements during BBN or the observed pattern of CMB spectrum. The thesis explores the non-negligible contribution of the so-called 'late' decay of the bath particle to the observed DM abundance, which has not been pursued before. It is important to note how a FIMP-like non-abelian VDM gives rise to exclusive collider signal that is strikingly distinguishable from WIMP-like case. A comparison of the same model set up in WIMP and FIMP limit provides a clearer picture of the difference in allowed parameter space of the model. This may be helpful in reconstructing a DM model given a signal excess.

Finally, an effective theory formalism for vector boson DM is also analysed. This allows us to explore the advantages and limitations of a model independent approach to study vector boson DM. We adhere to the freeze-in mechanism where the VDM is feebly coupled to the visible sector via dimension five operator. In this case, the DM abundance is usually sensitive to the reheat temperature and reaches maximum. However, we show that once the reheat temperature is close to the mass scale of DM, the "IR" nature of the freeze-in re-surfaces. Thus, depending on the choice of scale of the reheat temperature, it is possible to have a pure UV freeze-in, an assorted set-up consisting both UV and IR or a pure IR freeze-in.

To summarize, the main idea of the thesis is to portray different phenomenological aspects of vector boson DM from collider and direct detection perspective encompassing both single or multi-component WIMP-like or FIMP-like DM in UV complete and effective model set ups and relate to other important issues like neutrino mass generation, grand unification etc.

Chapter 3

# Non-Abelian Vector Boson Dark Matter with quark connection

## Contents



## 3.1 Introduction

In this chapter we will analyze the phenomenology of a non-abelian vector boson DM which arises in an $SU(2)_N$ extension of the SM. $SU(2)_N$ is broken subsequently and results in massive gauge bosons. The $SU(2)_N$ is *dark* in the sense that the $SU(2)_N$ charges do not contribute to the hypercharge. Thus, all three $SU(2)_N$ gauge bosons are electromagnetic charge neutral and the lightest one can in principle be a DM. The stability of the DM is ensured by an extra global symmetry $U(1)_P$, breaking of which explicitly breaks the generalized lepton number $L = P + T_{3N}$ to $(-1)^L$ leading to a discrete $R-$parity as in supersymmetric theory. One of the main motivations of such a framework is to envisage a unified theory, $E(6)$ [200], which subsequently breaks to $SM \otimes SU(2)_N$. In the process of $E(6) \to SM \otimes SU(2)_N$, $D$-parity is broken in presence of an $SU(2)_N$ scalar triplet which allows $g_N$ to be different from $SU(2)_L$ gauge coupling. A non-zero vacuum expectation value (VEV) of this triplet scalar breaks the degeneracy of the dark gauge bosons and ensures a single component DM. Absence of the $SU(2)_N$ triplet ($D$-parity even case), on the other hand, leads to a constrained degenerate DM scenario which is ruled out from direct detection exclusion limits. Intermediate symmetry breaking takes care of the fact that hypercharge is determined without $SU(2)_N$ contribution, ensuring charge neutrality of the $SU(2)_N$ gauge bosons.

Phenomenology of the non-abelian vector boson DM in a similar framework was taken up in [201], but was not elaborate. In particular, non observation of DM in the direct search experiments is putting a huge constraint on the single component DM parameter space, eventually ruling out a large class of WIMP models from spin-independent direct search cross-sections. However, the model discussed here survives in a large region of relic density allowed parameter space from WMAP [29]/PLANCK [244] data satisfying current direct search bounds from LUX [66]. This is mainly due to its $t$-channel annihilation along with co-annihilation with heavier gauge boson and dominant $s$-channel direct search interaction. This has been validated through elaborate parameter space scan, assuming $SU(2)_N$ coupling as an independent parameter (and obeying unification prescription) [245].

The presence of exotic fermions lead to interesting signatures at the Large Hadron Collider (LHC). These fermions subsequently decay to DM providing a variety of signals of multilepton/jets final states that can testify such a framework in future runs of LHC. Two most promising signals of this model are leptonic: 'opposite sign dilepton' and 'hadronically quiet four lepton' with large missing energy. It has been explicitly shown, by analyzing different benchmark points, the 'hadronically quiet four lepton' signal is a smoking-gun signature for this model, typically because of less SM background.

This chapter is organized as follows: the model and the basic formalism is discussed in Sec. 3.2; DM phenomenology is discussed elaborately in Sec. 3.3 including relic density and direct search constraints. In Sec. 3.4, we study unified framework under $E_6$ and subsequent constraints on the model parameters. Some benchmark points, identified thereafter, are studied for collider signatures in Sec. 3.5. We finally conclude in Sec. 3.6.

## 3.2 Dark vector multiplet and exotic particles

The theory under consideration is $SU(2)_N \otimes SU(2)_L \otimes U(1)_Y \otimes SU(3)_C$ gauge symmetric. An additional global abelian symmetry $U(1)_P$ has also been introduced. This redefines the lepton number of the particles as $L = P + T_{3N}$. Explicit breaking of $U(1)_P$ breaks $L$ to $(-1)^L$ and results in conservation of a discrete symmetry $R = (-1)^{3B+L+2J}$ (very similar to $R$-parity in supersymmetry). This stabilizes the lightest particle odd under $R$-parity and serves as DM. $SU(2)_N$ charges do not contribute to the hypercharge ($Y$) and thus to electromagnetic charge, defined as $Q = T_{3L} + Y$. Hence, $SU(2)_N$ gauge bosons $X_{1,2,3}$ are electromagnetic charge neutral and the lightest of them, $X_1$ (odd under $R$), aptly fits into the criterion of a DM. Once $SU(2)_N$ symmetry is broken completely, the gauge bosons acquire masses of the scale of TeV. We adopt the same particle configuration as in [200, 201] to realise its high-scale origin, DM constraints, and collider signatures through elaborate analysis. Following is the particle content of the model, where the quantum numbers are mentioned under $SU(2)_L \otimes SU(2)_N \otimes U(1)_Y \otimes SU(3)_C \otimes U(1)_P$:

*Fermions:*

$$\begin{aligned}
&\begin{pmatrix} u \\ d \end{pmatrix} = [2,1,1/6,3;0]\,,\ u^c = [1,1,-2/3,\bar{3};0]\,,\\
&(h_q^c \ \ d^c) = [1,2,1/3,\bar{3};-1/2]\,, h_q = [1,1,-1/3,3;1]\\
&\begin{pmatrix} N & \nu \\ E & e \end{pmatrix} = [2,2,-1/2,1;1/2]\,,\ (E^c \ \ N^c) = [2,1,1/2,1;0]\\
&(\nu^c \ \ n^c) = [1,2,0,1;-1/2]
\end{aligned} \tag{3.1}$$

*Scalars:*

$$\begin{aligned}
&\begin{pmatrix} \phi_1^0 & \phi_3^0 \\ \phi_1^- & \phi_3^- \end{pmatrix} = [2,2,-1/2,1;1/2]\,,\ (\chi_1^0 \ \ \chi_2^0) = [1,2,0,1;-1/2]\\
&\begin{pmatrix} \phi_2^+ \\ \phi_2^0 \end{pmatrix} = [2,1,1/2,1;0]\,, \quad \begin{pmatrix} \Delta_2^0/\sqrt{2} & \Delta_3^0 \\ \Delta_1^0 & -\Delta_2^0/\sqrt{2} \end{pmatrix} = [1,3,0,1;1]\,.
\end{aligned} \tag{3.2}$$

Vertical parentheses indicate doublet under $SU(2)_L$ and the horizontal ones indicate doublet under $SU(2)_N$. For brevity, we mention one family of the particle spectrum and assume that gauge and Yukawa interactions are flavour diagonal. The fermion sector is augmented by an exotic quark $h_q$, an exotic electron $E$ and two exotic neutrinos $N, n$. The scalar sector consists of one $SU(2)_L$ doublet, one $SU(2)_N$ doublet, a bi-doublet and an $SU(2)_N$ triplet. With this scalar sector at hand, the most general scalar potential of the model can be written as:

$$\begin{aligned}
V =\ & \mu_1^2\,\mathrm{Tr}\left(\phi_{13}^\dagger\phi_{13}\right) + \mu_2^2\left(\phi_2^\dagger\phi_2\right) + \mu_\chi^2\left(\chi\chi^\dagger\right) + \mu_\Delta^2\,\mathrm{Tr}\left(\Delta^\dagger\Delta\right) + \left(\mu_3^2\,det\Delta + h.c.\right)\\
&+ \left(\mu_{22}\widetilde{\chi}\phi_{13}^\dagger\widetilde{\phi}_2 + \mu_{12}\chi\Delta\widetilde{\chi}^\dagger + \mu_{23}\widetilde{\chi}\Delta\chi^\dagger + h.c.\right) + \frac{1}{2}\lambda_1\left(\mathrm{Tr}\left(\phi_{13}^\dagger\phi_{13}\right)\right)^2 + \frac{1}{2}\lambda_2\left(\phi_2^\dagger\phi_2\right)^2\\
&+ \frac{1}{2}\lambda_3\,\mathrm{Tr}\left(\phi_{13}^\dagger\phi_{13}\phi_{13}^\dagger\phi_{13}\right) + \frac{1}{2}\lambda_4\left(\chi\chi^\dagger\right)^2 + \frac{1}{2}\lambda_5\left[\mathrm{Tr}\left(\Delta^\dagger\Delta\right)\right]^2\\
&+ \frac{1}{4}\lambda_6\,\mathrm{Tr}\left(\Delta^\dagger\Delta - \Delta\Delta^\dagger\right)^2 + \widetilde{\lambda}_1\chi\phi_{13}^\dagger\phi_{13}\chi^\dagger + \widetilde{\lambda}_2\chi\widetilde{\phi}_{13}^\dagger\widetilde{\phi}_{13}\chi^\dagger + \widetilde{\lambda}_3\phi_2^\dagger\phi_{13}\phi_{13}^\dagger\phi_2\\
&+ \widetilde{\lambda}_4\phi_2^\dagger\widetilde{\phi}_{13}\widetilde{\phi}_{13}^\dagger\phi_2 + \widetilde{\lambda}_5\left(\phi_2^\dagger\phi_2\right)\left(\chi^\dagger\chi\right) + \widetilde{\lambda}_6\left(\chi\chi^\dagger\right)\ \mathrm{Tr}\left(\Delta^\dagger\Delta\right)\\
&+ \widetilde{\lambda}_7\chi\left(\Delta^\dagger\Delta - \Delta\Delta^\dagger\right)\chi^\dagger + \widetilde{\lambda}_8\left(\phi_2^\dagger\phi_2\right)\mathrm{Tr}\left(\Delta^\dagger\Delta\right) + \widetilde{\lambda}_9\mathrm{Tr}\left(\phi_{13}^\dagger\phi_{13}\right)\mathrm{Tr}\left(\Delta^\dagger\Delta\right)\\
&+ \widetilde{\lambda_{10}}\,\mathrm{Tr}\left(\phi_{13}\left(\Delta^\dagger\Delta - \Delta\Delta^\dagger\right)\phi_{13}^\dagger\right).
\end{aligned} \tag{3.3}$$

$SU(2)_N$ gauge bosons $X_{1,2,3}$, are not assigned any global $U(1)_P$ charge as they transform under adjoint representation. Their respective $T_{3N}$ quantum numbers are $[1,0,-1]$, leading to $R$-charges for $X_{1,2}$ as (-1), and $X_3$ as (+1) (since $J=1$). The odd $R$-charged dark gauge bosons are stable as they cannot decay to a pair of SM

particles or to other heavier (by construction) exotic particles. Thus, in our scenario, the lightest of $X_{1,2}$ qualifies to be DM and in case of a degeneracy, both may serve as DM candidates. We shall elaborate upon this point later. We would also like to mention that with the given particle content (particularly in presence of $n^c, \nu^c$) the model is capable of generating light neutrino mass via usual seesaw mechanism through Yukawa interaction as explained in [199, 201], but the choice of parameters for the neutrino sector does not affect the DM sector, hence we do not elaborate on neutrino mass generation here.

## 3.3 $X_1$ as Vector Boson Dark Matter

In this section we explore the allowed parameter space of the vector boson DM through detailed parameter scan. In our scenario, the neutral scalars that acquire vacuum expectation values (VEV) are $\chi^0_{1,2}, \phi^0_{1,2}$, and $\Delta^0_{1,3}$. $SU(2)_N$ and electroweak symmetry is spontaneously broken through the VEV of $\chi^0_2$ $(\kappa_2)$ and $\phi^0_{1,2}$ $(v_{1,2})$ respectively. Due to the presence of a bi-doublet and an $SU(2)_L$ Higgs doublet, the physical Higgs field $(h)$ can be written as a linear combination of CP-even neutral components $(\phi_{1,2})$ $(h = (v_1 \ \phi^0_1 \ + v_2 \ \phi^0_2)/v$; where $v = \sqrt{v_1^2 + v_2^2} = 246$ GeV is the electroweak symmetry breaking scale). Physical scalar fields and their masses after spontaneous symmetry breaking of the model has been elaborated in [201]. VEV of the $SU(2)_N$ triplet components $\Delta^0_{1,3}$ $(\delta_{1,2})$ contribute to the $SU(2)_N$ gauge boson masses and causes the mass splitting between two lighter dark gauge bosons as [200, 201]:

$$m^2_{X_{1,2}} = \frac{1}{2} g_N^2 \left[\kappa_2^2 + v_1^2 + 2(\delta_1 \mp \delta_2)^2\right] \tag{3.4}$$

where the '-' sign corresponds to the mass of $X_1$ and the '+' sign is for the mass of $X_2$.

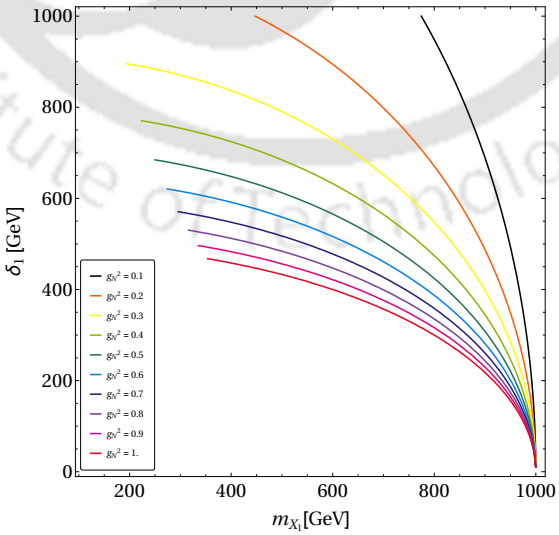


**Figure 3.1:** Contours of triplet VEV $\delta_1$ with DM mass $m_{X_1}$ is shown for $m_{X_3} = 1$ TeV for different choices of $SU(2)_N$ coupling $(g_N)$ in the maximum splitting scenario $(\delta_1 = \delta_2)$. All the points below these lines are ruled out as they predict $X_3$ lighter than TeV.

Therefore, the absence of the triplets (with $\delta_1 = \delta_2 = 0$) will make $X_{1,2}$ degenerate: $m^2_{X_1} = m^2_{X_2} = \frac{1}{2} g_N^2 [\kappa_2^2 + v_1^2]$. The other gauge boson $X_3$ (even under $R$) mixes with the usual SM neutral gauge boson $Z$ [200, 201]:

$$m^2_{Z,X_3} = \frac{1}{2} \begin{pmatrix} (g_1^2 + g_2^2)(v_1^2 + v_2^2) & -g_N \sqrt{g_1^2 + g_2^2}\, v_1^2 \\ -g_N \sqrt{g_1^2 + g_2^2}\, v_1^2 & g_N^2 [\kappa_2^2 + v_1^2 + 4(\delta_1^2 + \delta_2^2)] \end{pmatrix} . \tag{3.5}$$

The mass term for $X_3$ can then be assumed as: $m^2_{X_3} \approx \frac{1}{2} g_N^2 [\kappa_2^2 + v_1^2 + 4(\delta_1^2 + \delta_2^2)]$ as $Z - X_3$ mixing is very much constrained [246]. Now, it is also evident from Eq. (3.4) that the maximum splitting between $X_1,\ X_2$ can be achieved for $\delta_1 = \delta_2 = \delta$, where

$$m^2_{X_1} = \frac{1}{2} g_N^2 \left[\kappa_2^2 + v_1^2\right] ,\ \ m^2_{X_2} = m^2_{X_3} = \frac{1}{2} g_N^2 \left[\kappa_2^2 + v_1^2 + 8\delta^2\right] . \tag{3.6}$$

In this framework, using the exclusion limit of $m_{Z'} \sim \mathcal{O}(\text{TeV})$ from heavy neutral gauge boson search [247], we can put tentative lower limits on DM mass $(m_{X_1})$ depending on the choice of $\delta_1$. For different values of $SU(2)_N$ gauge coupling $(g_N)$, the lower limit on $m_{X_1}$ is shown in Fig. 3.1 which essentially follows from Eq. (3.6) as

$$m^2_{Z'} \equiv m^2_{X_3} = m^2_{X_1} + 4\delta^2 \gtrsim (1\ \text{TeV})^2 \tag{3.7}$$

.

When the triplet is absent or the VEV is zero, all three gauge bosons are degenerate, yielding a multipartite DM framework, which necessarily requires to be heavier than $\sim 1$ TeV as $m_{Z'} \gtrsim 1$ TeV.

### 3.3.1 DM Annihilation channels

Here we assume the VDM $(X_1)$ to remain in thermal equilibrium in early universe and therefore a WIMP like candidate. This is natural for this particular scenario, as SM particles also share dark $(SU(2)_N)$ charge. Relic density of DM is then evaluated through thermal freeze out of $X_1$ that is governed by the number changing processes for the DM. $X_1$ being odd under $R$-charge, can not directly couple to a pair of SM particles, but can connect to them via the exotic fermions odd under $R$. For example, one can have couplings like $\bar{d}\ h_q\ X_1$ or $\bar{E}\ e\ X_1$. Hence, there are different channels through which $X_1$ can annihilate to SM particles which eventually help the DM to freeze out:

- Annihilations to fermion pairs $d\bar{d};\ e\bar{e};\ \nu\bar{\nu}$ by exchanging $h_q,\ E,\ N$ respectively as shown in Fig. 3.2,
- Annihilation to pair of Higgs by exchanging $\phi_3,\ h$ and through four point contact term shown in Fig. 3.3,

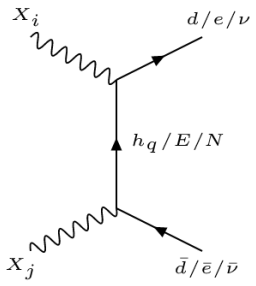


**Figure 3.2:** Annihilations (Co-annihilations with $i \neq j,\ \{i,j\} = \{1,2\}$) to SM fermion pairs by exotic quark exchange.

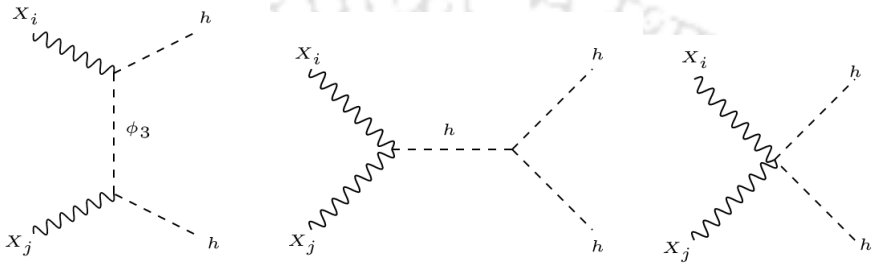


**Figure 3.3:** Annihilations (Co-annihilations with $i \neq j,\ \{i,j\} = \{1,2\}$) to SM Higgs pair.

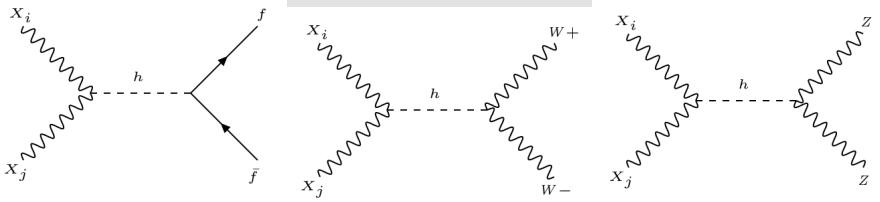


**Figure 3.4:** Annihilations (Co-annihilations with $i \neq j,\ \{i,j\} = \{1,2\}$) to SM fermions and gauge bosons through Higgs exchange

- Annihilation to pair of SM fermions and gauge bosons through Higgs exchange as in Fig. 3.4.

Total annihilation cross-section (in $s$-wave limit), computed from diagrams in Figs. (3.2), (3.3) and (3.4), can be found in Appendix. B.0.1 (Eq. (B.1)). Now, the independent parameters which control the phenomenological outcome of this model are: $SU(2)_N$ gauge coupling $g_N$ [1] and the masses of the exotic non-SM particles. This results in an effective four dimensional parameter space characterizing the DM sector of the model:

$$\{g_N, m_{X_1}, m_{h_q}, m\}, \tag{3.8}$$

where we simplify the situation by assuming the uncoloured exotic masses to be

[1]This, in principle, is not equal to SM $SU(2)_L$ coupling $g_L$ (except for $D$-parity conserving scenario as discussed later). The freedom of choosing $g_N$ was not considered in earlier analysis [200, 201].

the same: $m_E = m_N = m_{\phi_3} = m$. This still keeps phenomenological implications of the model intact.

### 3.3.2 Boltzmann Equation and thermal freeze out

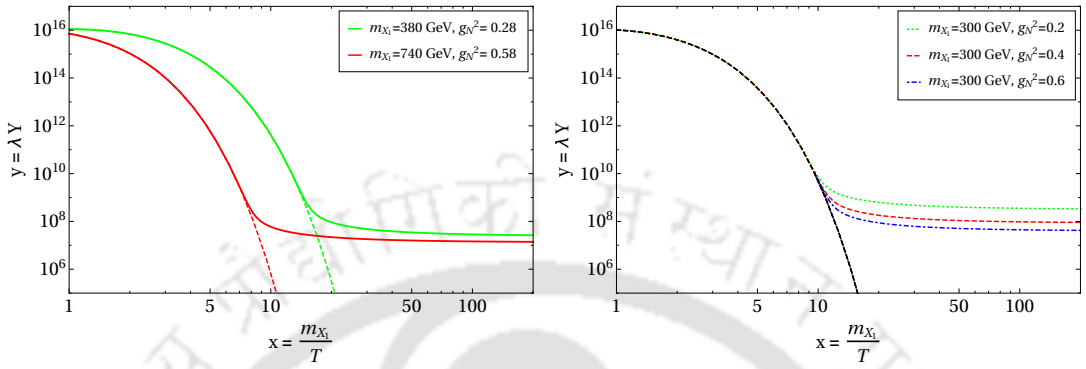


**Figure 3.5:** Patterns of thermal freeze out of $X_1$ has been framed in $y = \lambda\, Y$ vs $x = m_{X_1}/T$ plane. Left-panel: $\{m_{X_1},\ g_N\} = \{380\ \text{GeV}, 0.28\},\ \{740\ \text{GeV}, 0.58\}$ are chosen as illustration. Dashed lines show the respective equilibrium distributions. Right-panel: different values of $g_N = \{0.2, 0.4, 0.6\}$ are chosen for DM mass $m_{X_1} = 300$ GeV.

To compute thermal freeze out of the DM we need to solve Boltzmann equation (BEQ) [44] that can be written in a compact form following Sec. 2.2.1 as

$$\frac{dy}{dx} = -\frac{m_{X_1}}{x^2}\left[\sigma_0(y^2 - y^{EQ^2})\right], \tag{3.9}$$

where $y = \lambda Y$ with $\lambda = (0.264\, m_{Pl}\frac{g_{*s}}{\sqrt{g_*}})$, $\sigma_0 = \langle\sigma v_{\text{rel}}\rangle_{X_1X_1\to SMSM}$ given in Eq. (B.1). We demonstrate the patterns of DM freeze out in Fig. 3.5. Left panel shows two different combinations of $\{m_{X_1}, {g_N}^2\} = \{380\ \text{GeV}, 0.28\},\ \{740\ \text{GeV}, 0.58\}$; right panel shows freeze out for three different values of ${g_N}^2 = \{0.2, 0.4, 0.6\}$ for same DM mass $m_{X_1} = 300$ GeV. In the left plot, due to different choices of the DM masses, the equilibrium distributions (shown by dashed lines) are different, lighter ($m_{X_1} = 380$ GeV shown by the green line) appears above the heavier one ($m_{X_1} = 740$ GeV shown by the red line). Decoupling for these two cases occur at $x = 20$ ($T \sim 19$ GeV) and $x = 7$ ($T \sim 105$ GeV). Heavier component still has a smaller yield due to significantly larger coupling (${g_N}^2 = 0.58$), thanks to larger annihilation cross section.

### 3.3.3 Relic Density and allowed parameter space

After freeze-out, relic density for the DM is obtained from the yield following Eq. (2.16):

$$\Omega h^2 = \frac{m_{X_1} s_0 \sqrt{g_*}}{3H_0^2\ m_{pl}^3\ 0.26 g_{*s}} y(x_\infty), \tag{3.10}$$

where $y(x_\infty)$ is the solution of Eq. (3.9) at large values of $x$. This can be written in terms of annihilation cross-section under $s$-wave approximation as [44]:

$$\Omega h^2 \simeq \frac{2.4 \times 10^{-10}\text{GeV}^{-2}}{\langle \sigma v_{\text{rel}} \rangle_{X_1 X_1 \to SMSM}}. \tag{3.11}$$

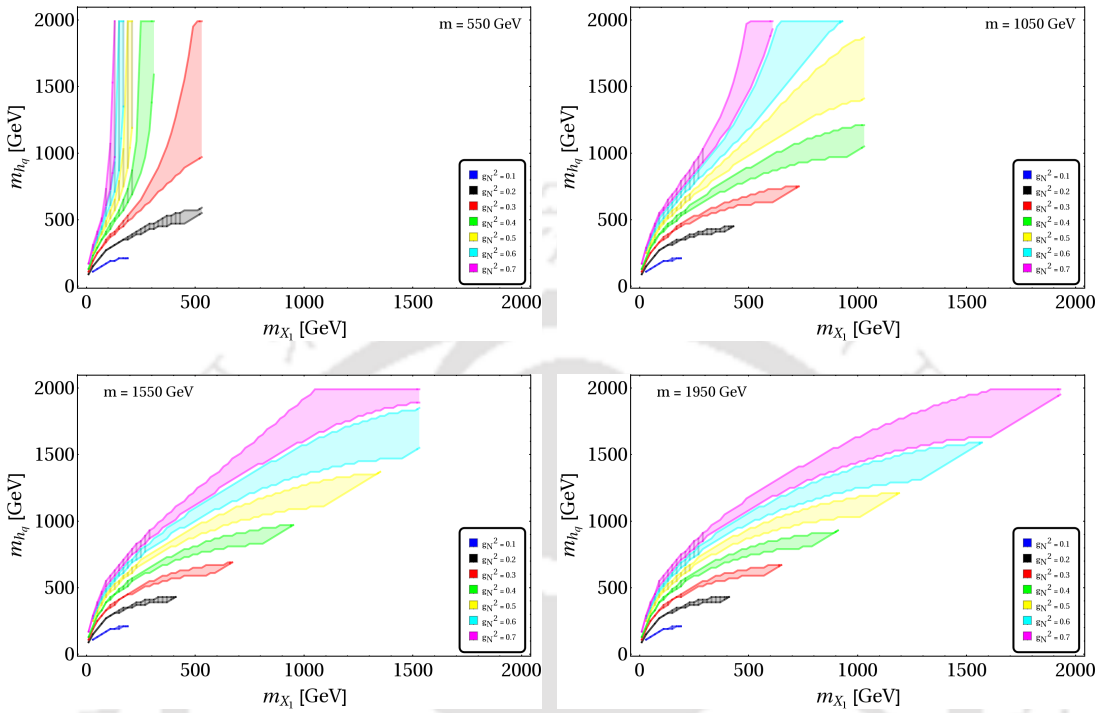


**Figure 3.6:** Relic density allowed parameter space in $m_{X_1} - m_{h_q}$ plane for four different values of $m = m_E = m_N$: 550 GeV (top left), 1050 GeV (top right), 1550 GeV (bottom left), 1950 GeV (bottom right) for different values of $g_N^2 \to \{0.1-0.7\}$. The hatched region is excluded by the VEV constraints.

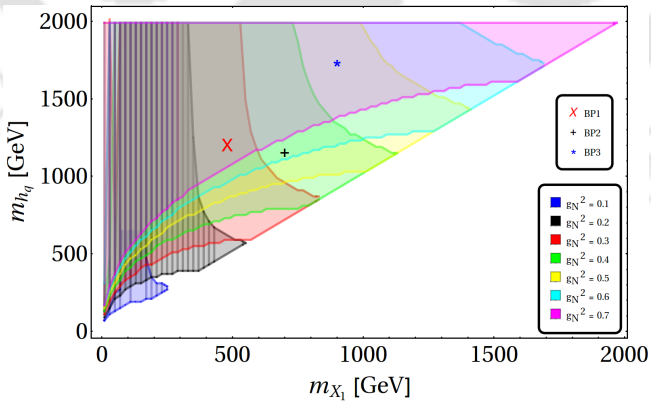


**Figure 3.7:** Relic density allowed parameter space in $m_{X_1}$-$m_{h_q}$ plane when $m = m_N = m_E$ is varied between $\{20 - 2000\}$ GeV for different $g_N^2 \to \{0.1 - 0.7\}$. The hatched region is discarded by VEV limit. Benchmark points (BP1, BP2, BP3) as discussed in Tab. 3.1 of the next section are also indicated in the plot.

To find the allowed region of parameter space satisfying Eq. (3.11) we vary the parameters $\{g_N, m_{h_q}, m_N = m_E = m, m_{X_1}\}$ as discussed earlier. In $m_{X_1}$-$m_{h_q}$ plane, the allowed parameter space is shown in Fig. 3.6 for different $g_N^2$ and $m$. Each figure

is for a specific value of $m$ and contains different colour coded regions corresponding to different values of $g_N^2$. For each of these regions, upper and lower boundaries correspond to maximum and minimum allowed values of $m_{h_q}$. This pattern is expected as relic density is closed from both sides. Annihilation cross-section decreases for larger $m_{h_q}$, causing more contribution to the relic density. Thus, for a given $g_N^2$, a cut-off in $m_{h_q}^{max}$ corresponds to the maximum allowed relic density. Similarly, the lower cut-off in $m_{h_q}$ corresponds to the maximum annihilation cross-section i.e, minimum relic density. From different figures in Fig. 3.6, we observe that for small values of $m$ only a small part of $m_{X_1}$ is allowed. This is a consequence of the constraint: $m_{X_1} \leq m$. Now, there exists a lower limit of $m_{X_1}$ for a given value of $g_N$ allowed by the VEV constraints as depicted in Fig. 3.1. The hatched regions on the left hand side of each figure in Fig. 3.6 shows the parameter space disallowed by VEV. In addition, using PLANCK limit shrinks the allowed region but keeps the interpretations same. Fig. 3.7 summarizes the allowed parameter space in $m_{X_1}$ vs $m_{h_q}$ plane when $m$ is varied upto 2 TeV. Three benchmark points (BP1, BP2, BP3), identified after imposing all constraints, are indicated in this plot which we shall use further for collider analysis.

### 3.3.4 Direct detection of VBDM

Spin-independent direct search cross-section for vector boson DM scattering off nuclei can be expressed as [248, 249]:

$$\sigma_{DD}^{SI} = \frac{1}{\pi}\left(\frac{m_{nu}}{m_{X_1}+m_{nu}}\right)^2 \left|\frac{Zf_p+(A-Z)f_n}{A}\right|^2, \tag{3.12}$$

where $Z$ and $(A-Z)$ are the number of protons and neutrons in Xe nucleus respectively. The mass of nucleus is given as $m_{nu} = Zm_p + (A-Z)m_n$. Here, $m_{p(n)}$ and $f_{p(n)}$ are the mass and form factor for proton (neutron). The ratios of the form factors of proton and neutron *w. r. t.* their respective masses are computed using the diagrams in Fig. 3.8 by incorporating the gluonic contributions along with the twist-2 operators. Here also the sub-dominant $t$-channel contribution due to Higgs mediation has been taken into account which was ignored in earlier analysis [201]. The ratios therefore read:

$$\begin{aligned}\frac{f_i}{m_i} = (I_i)\left[-\frac{g_N^2}{4m_h^2}\left(\frac{v_1}{v}\right)^2 - \frac{g_N^2}{16}\frac{m_{h_q}^2}{(m_{h_q}^2-m_{X_1}^2)^2}\right] + \frac{3}{4}(J_i)\left[-\frac{g_N^2}{4}\frac{m_{X_1}^2}{(m_{h_q}^2-m_{X_1}^2)^2}\right] \\ -(K_i)\left((1.19)\frac{g_N^2}{54m_h^2}\left(\frac{v_1}{v}\right)^2 + \frac{g_N^2}{36}\left[(1.19)\frac{m_{h_q}^2}{6(m_{h_q}^2-m_{X_1}^2)^2} + \frac{1}{3(m_{h_q}^2-m_{X_1}^2)}\right]\right)\end{aligned} \tag{3.13}$$

where $i$ stands either for proton $(p)$ or neutron $(n)$ and their respective form factors are $I_{p(n)} = 0.052\ (0.061);\ J_{p(n)} = 0.222\ (0.330);\ K_{p(n)} = 0.925\ (0.922)$.

Variation of $\sigma_{DD}^{SI}$ with $m_{X_1}$ is summarized in Fig. 3.9. In the upper panel, different colour coded regions correspond to different $g_N^2$ scanned over $m_{h_q}$ upto 2 TeV, allowed by relic density. Again, the maximum and minimum $m_{h_q}$ boundaries of each $g_N^2$ region correspond to maximum and minimum relic density for a given DM mass. $\sigma_{DD}$ has $s$-channel contribution from $h_q$ as shown in Fig. 3.8, where $m_{h_q}$

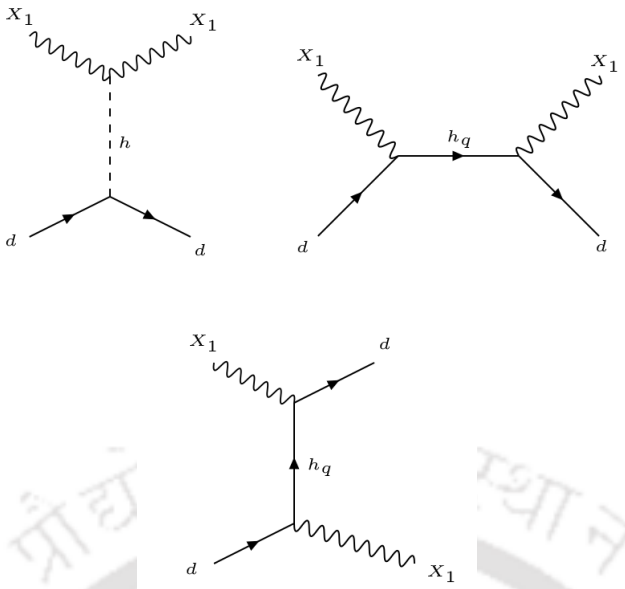


**Figure 3.8:** Relevant interactions of dark matter $(X_1)$ with quarks (nucleons) for direct-search experiments.

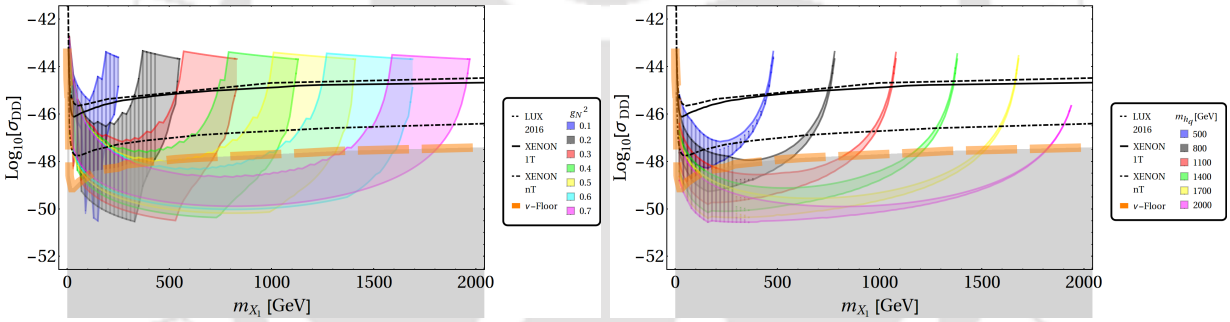


**Figure 3.9:** Spin independent direct search cross-section for the vector boson DM $X_1$ with respect to DM mass $(m_{X_1})$ for relic density allowed parameter space. Top: Different values of $g_N^2$ is shown by different colours where $m_{h_q}$ is varied appropriately to yield correct relic density. Bottom: Different $m_{h_q}$ values are shown by different coloured regions where $g_N^2$ is varied to yield correct relic density. Limits from LUX2016, XENON1T and XENONnT predictions are depicted by the dashed, solid and dot-dashed black lines respectively. The orange thick dashed line shows the background limit from solar, atmospheric and diffuse supernovae neutrinos while the grey shaded region below shows the neutrino floor. VEV constraints are shown by hatched regions.

appears in the propagator and therefore, smaller $\sigma_{DD}$ indicates larger $m_{h_q}$. The t-channel Higgs mediation yields sub-dominant contribution to the direct search cross-section. The VEV disallowed points are shown by hatched regions which almost entirely discard low DM masses for small $g_N^2 = \{0.1, 0.2\}$. In the bottom-panel, different coloured regions depict relic density allowed parameter space for fixed $m_{h_q}$ and for $g_N^2 : 0.1 - 0.6$. LUX and XENON1T exclusion limits as well as the future prediction from XENONnT are shown in both the figure. The main outcome of this analysis is to observe a huge region of parameter space still allowed by direct search limits. This can be attributed to the direct search cross-section of the DM guided by $m_{h_q}$ mediation in $s$-channel.

### 3.3.5 Co-annihilation of $X_1$ with $X_2$

One of the important aspects of the model under consideration is the co-annihilation effect, which further helps it to evade direct search bounds. There are two $R$-charge odd gauge bosons $(X_{1,2})$ present in this model. With $m_{X_2} > m_{X_1}$, the lightest one $(X_1)$ is stable and serves as DM candidate as discussed so far. The heavier one $(X_2)$ can contribute to the relic density of $X_1$ by co-annihilation to a pair of SM particles. The possible co-annihilation channels are already depicted in Figs. 3.2, 3.3, 3.4 (with $i = 1, j = 2$). Total effective cross-section, including co-annihilation, can be written following Eq. (2.19) as:

$$\langle\sigma v\rangle_{eff} = \langle\sigma v\rangle_{X_1X_1\to SM\ SM} + \langle\sigma v\rangle_{X_1X_2\to SM\ SM}\left(1+\frac{\Delta m}{m_{X_1}}\right)^{\frac{3}{2}}\exp\left(-\Delta m/m_{X_1}\right) \quad (3.14)$$

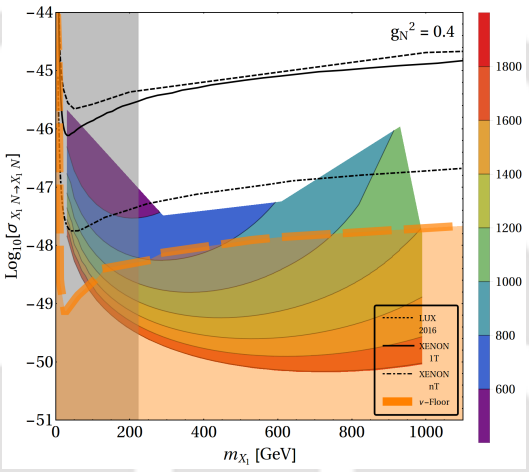


**Figure 3.10:** Direct search (spin independent) cross-section for relic density allowed parameter space for $X_1$ with co-annihilation taken into account. Different colour codes indicate different values of $m_{h_q}$. LUX 2016 and XENON 1T exclusion limits are shown along with XENONnT sensitivity by the dashed, solid and dot-dashed black lines respectively. Orange thick dashed line shows the background limit estimated from solar, atmospheric and diffuse supernovae neutrinos while the orange shaded region below indicates the neutrino floor. VEV exclusion limit is represented by the grey region.

where $\Delta m = m_{X_2} - m_{X_1}$. Co-annihilation cross sections are significant for small $\Delta m$ $(m_{X_1} \sim m_{X_2})$, or has a Boltzmann suppression otherwise. Following previous arguments, co-annihilation cross-sections are also computed at the threshold $s_0 = (m_{X_1} + m_{X_2})^2$ considering only the dominant $s$-wave contribution. A scan of the relic density allowed parameter space of the model after incorporating co-annihilation effects is shown in Fig. 3.10. Here we have chosen a specific $g_N^2(= 0.4)$ for illustration. Different values of $m_{h_q}$ are shown by different coloured regions. VEV exclusion limit is shown in the left hand side by the grey band, which puts a limit on the low DM mass $\sim$ 200 GeV. The orange thick dotted line points to the neutrino background (3-10 neutrino events), with the shaded region below depicting the neutrino floor. Noteworthy feature of Fig. 3.10 is that the relic-density allowed parameter space lies safely much below the current direct search exclusion limits, a

significant part of it going even lower than the XENONnT proposed limit. To summarize, the model predicts that direct search of this DM is going to be difficult and direct search exclusions will not be able to rule out a significant part of this model.

## 3.4 Road to unification

Here we have analyzed in detail how the gauge symmetry of our interest, $SU(2)_L \otimes SU(2)_N \otimes U(1)_Y \otimes SU(3)_C$, can be realized within an unified scenario. To understand this, we have adopted $E(6)$ as the unified group that has already been outlined in [200, 201]. We consider the following breaking patterns to achieve the low scale theory:

$$\begin{aligned} E(6) &\xrightarrow{M_U} SU(3)_L \otimes SU(3)_R \otimes SU(3)_C \xrightarrow{M_I'} SU(2)_L \otimes U(1)_L \otimes SU(2)_R \otimes U(1)_R \otimes SU(3)_c \\ &\xrightarrow{M_I} SU(2)_L \otimes U(1)_Y \otimes SU(2)_N \otimes SU(3)_c \xrightarrow{M_I^N} SU(2)_L \otimes U(1)_Y \otimes SU(3)_c \\ &\xrightarrow{EWSB} SU(3)_c \otimes U(1)_{EM}. \end{aligned} \tag{3.15}$$

In this section, we will first discuss the spontaneous symmetry breaking of $E(6)$ to the SM through multiple intermediate scales. We have computed the beta-function coefficients [250] for gauge coupling evolutions[2] for different intermediate scales. In the process, we have also used the extended survival hypothesis (ESH) [251] to allow the minimal fine tuning in the scalar potential. All contributing field representations and the beta coefficients for different scales are appended below:

- **From $M_{I'} \to M_U$:**

  $E(6)$ can be spontaneously broken to $SU(3)_L \otimes SU(3)_R \otimes SU(3)_C \equiv \mathcal{G}_{333}$ through the vacuum expectation value (VEV) of $650_H$ ($650_H^{'}$) scalar keeping $D$-parity intact (broken). The scalar and fermion fields that contribute to the running of the gauge couplings $\{g_{3L}, g_{3R}, g_{3C}\}$, associated with $SU(3)_L, SU(3)_R, SU(3)_C$ respectively, are[3]:

  $$\begin{aligned} &27_F = [\bar{3}, 3, 1] + [3, 1, 3] + [1, \bar{3}, 3], \quad 650_H^{'} \supset [8, 8, 1] + [1, 8, 1], \\ &27_H \supset [\bar{3}, 3, 1]. \end{aligned}$$

  Here we would like to mention, when this breaking occurs via VEV of $650_H$, then only $[8, 8, 1]$ contributes to the beta-functions and $D$-parity remains conserved. This can be understood intuitively as one can see, the fields contributing to the beta-coefficients in the running of $g_{3L}$ and $g_{3R}$ are identical. Thus $g_{3L} = g_{3R}$ will be maintained as long as $\mathcal{G}_{333}$ is unbroken. We compute the beta-coefficients as:

[2] We have considered the running of gauge couplings only, and ignored the contributions from Yukawa couplings.

[3] We have relied on extended survival hypothesis (ESH) which tells that only those scalars are light which are participating in the symmetry breaking. Thus, even if we start with an unified $E(6)$ group, only relevant submultiplets are considered.

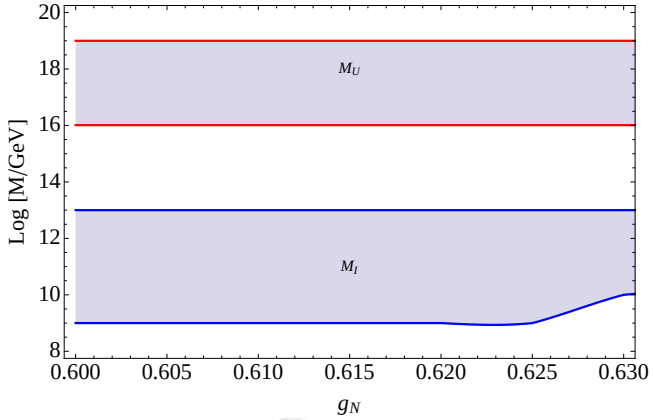


**Figure 3.11:** The unification within $D$-parity odd scenario has been encapsulated. The range of $SU(2)_N$ gauge coupling, $g_N$, and one of the intermediate scales $(M_I)$ have been explored with allowed unification scale $(M_U)$, i.e., within $\{10^{18} - 10^{19}\}$ GeV. Here, $M_I^{'}$ is considered to be degenerate with $M_I$, and $M_I^N$ is chosen to be TeV scale.

$$b_{3L} = 7/2,\, b_{3R} = 7/2\ (9/2),\, b_{3c} = -5,$$

where the value of $b_{3R}$ in parenthesis denote the $D$-odd case.

- **From $M_I \to M_{I'}$:**

  $SU(3)_L \otimes SU(3)_R \otimes SU(3)_C$ is further broken to $SU(2)_L \otimes U(1)_L \otimes SU(2)_R \otimes U(1)_R \otimes SU(3)_C (\equiv \mathcal{G}_{21213})$ through VEV of $(\bar{3}, 3, 1)$. The particles that contribute in the beta-functions are:

  $$27_F = [2, -1/2\sqrt{3}, 1, -1/\sqrt{3}, 1] + [2, 1/2\sqrt{3}, 1, 0, 3] + [1, 1/\sqrt{3}, 2, 1/2\sqrt{3}, 1]$$
  $$+[1, 0, 2, -1/2\sqrt{3}, \bar{3}] + [2, -1/2\sqrt{3}, 2, 1/\sqrt{3}, 1] + [1, 0, 1, 1/\sqrt{3}, \bar{3}] +$$
  $$[1, -1/\sqrt{3}, 1, 0, 3] + [1, 1/\sqrt{3}, 1, -1/\sqrt{3}, 1]$$
  $$27_H \supset [2, -1/2\sqrt{3}, 1, -1/\sqrt{3}, 1] + [1, 1/\sqrt{3}, 2, 1/2\sqrt{3}, 1] + [2, -1/2\sqrt{3}, 2, 1/2\sqrt{3}, 1]$$
  $$650_H \supset [1, 0, 3, 0, 1],$$

  under the symmetry group $\mathcal{G}_{21213}$. The corresponding beta-coefficients are given by:

  $$b_{2L} = -5/6,\, b_{2R} = -5/6\ (1/6),\, b_{LL} = b_{RR} = 115/18,\, \widetilde{b}_{RL} = \widetilde{b}_{LR} = 1/9,\, b_{3c} = -5.$$

- **From $M_I^N \to M_I$:**

  $\mathcal{G}_{21213}$ is broken to $SM \otimes SU(2)_N$ in such a way that the hypercharge generator is originated as one of the linear combination of $U(1)_L$ and $U(1)_R$ generators. The fermion and scalar fields that contribute to the evolutions of the gauge couplings, $\{g_{2L}, g_{2N}, g_1, g_{3C}\}$, are:

$$27_F = [2,1,1/6,3] + [1,1,-2/3,\bar{3}] + [1,2,1/3,\bar{3}] + [1,1,-1/3,3] + [2,2,-1/2,1]$$
$$+[2,1,1/2,1] + [1,1,1,1] + [1,2,0,1]$$

$$27_H \supset [2,2,-1/2,1] + [2,1,1/2,1] + [1,2,0,1]$$

$$650'_H \supset [1,3,0,1],$$

under the symmetry group $SU(2)_L \otimes SU(2)_N \otimes U(1)_Y \otimes SU(3)_C$. Corresponding beta-coefficients are:

$$b_{2L} = -5/6, b_{2R} = 1/6, b_{1Y} = 21/2, b_{3c} = -5,$$

respectively.

The sub-multiplet $650'_H \supset [1,8,1] \supset [1,3,0,1]$ is considered for $D$-parity breaking case only. This $SU(2)_N$ triplet $\Delta \equiv [1,3,0,1]$ plays a crucial role in this analysis. The VEV of this triplet breaks the mass degeneracy of the $SU(2)_N$ gauge bosons, leading to one component dark matter scenario. Otherwise, for $D$-parity conserving case where this triplet is absent, this framework will have two degenerate dark matter candidates.

- **From $M_{EW} \to M_I^N$:**
  In the next step, $[1,2,0,1] \in 27_H$, singlet under $SU(2)_L \otimes U(1)_Y \otimes SU(3)_c$, acquires VEV and causes spontaneous braking of $SU(2)_N$ leading to SM gauge symmetry. The fermion and scalar fields which participate in the evolution of gauge couplings are (under $SU(2)_L, U(1)_Y, SU(3)_c$):

$$27_H \supset [2,-1/2,1] + [2,1/2,1]$$
$$27_F \supset [2,1/6,3] + [1,-2/3,\bar{3}] + [1,1/3,\bar{3}] + [2,-1/2,1] + [1,1,1],$$

  and the corresponding beta-coefficients are:

$$b_{2L} = -3, b_{1Y} = 21/5, b_{3c} = -7,$$

  associated with $\{g_{2L}, g_{1Y}, g_{3C}\}$ respectively[4].

In the breaking pattern of $E(6) \to SU(2)_N \otimes SM \to SM$, we have considered both $D$-parity conserving and non-conserving cases. For $D$-parity broken case, we will have one extra $SU(2)_N$ triplet at the TeV scale, and its respective parent multiplet will be present at high scales. We have introduced three intermediate symmetry groups in between $E(6)$ and SM. In principle, these intermediate scales are different. But we have noted, as almost all the fermions (27-dimensional) stick till $SU(2)_N$ breaking scale, beta coefficients for $U(1)_L$ and $U(1)_R$ are quite large ($\sim 115/18$). This results

[4] $g_1$ is GUT normalized $U(1)_Y$ coupling and normalization factor 3/5 is used to fit within this framework.

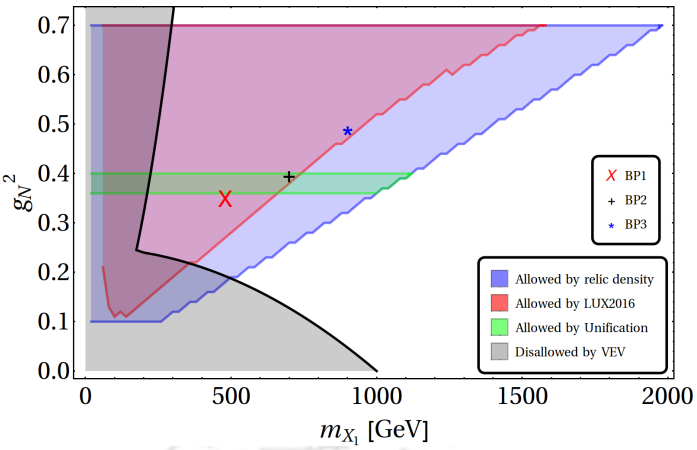


**Figure 3.12:** Relic density (blue shaded), direct search (red shaded) and unification (green shaded) allowed parameter space in $g_N^2 - m_{X_1}$ plane. Three chosen benchmark points BP1, BP2 and BP3 (see Tab. 3.1) are also shown.

in rapid growth of the respective gauge couplings, making them non-perturbative. Thus, to avoid such catastrophe, we have assumed that $\mathcal{G}_{333}$ is broken directly to $SM \otimes SU(2)_N$, i.e. $M_I$ coincides with $M_I^{'}$. Hence, in our scenario, $M_I^N$ and $M_I$ are the free parameters. In order to estimate the freedom of choosing $g_N$ different from $g_{2L}$ in $D$-parity odd scenario, we restrict $M_I^N$ to be around TeV scale for phenomenological considerations, while unification scale to be within $[10^{19} : 10^{16}]$ GeV. The allowed range of $g_N$ therefore turns to be $[0.60 : 0.63]$, as shown in Fig. 3.11.

For $D$-parity even case, $g_N$ is no more a free parameter and equals to $g_{2L}$. Here also, we find consistent solutions for unification with $M_I$ ranging between $[10^{19} : 10^{16}]$ GeV. The $D$-parity even case will lead to degenerate mass $(m_{X_1} = m_{X_2})$, as the triplet VEV is absent. Thus, we will have a degenerate two component dark matter scenario which is itself an interesting possibility. However, in that case we found that the DM has to be less than a TeV in order to satisfy the relic abundance and direct search. Since this is in conflict with our choice $m_{Z'} > 1$ TeV, hence the situation is phenomenologically nonviable and $D$-parity even case with degenerate DM does not work for this model.

Before we proceed further, we would like to summarize the outcome of DM phenomenology in the light of relic density, direct search and unification constraints. As we have argued to stick to the $D$-parity broken scenario, $g_N$ is not identical to $SU(2)_L$ coupling, and in principle, a free parameter. Hence DM mass $(m_{X_1})$ is a function of $g_N$ and $SU(2)_N$ symmetry breaking VEVs $(\kappa_2, \delta_{1,2})$. In Fig. 3.12, on top of relic density allowed (blue) and VEV disallowed (grey) parameter space, we incorporate direct detection constraint provided by LUX in (red) region and unification constraint (green). For further phenomenological exploration in context of LHC, we have chosen three benchmark points (BP): BP1 ($\times$), BP2 ($+$) and BP3 ($\star$). The details of these benchmark points are listed in Tab. 3.1.

## 3.5 Signals at the LHC

Collider signatures of this model yield a lot of interesting possibilities due to the presence of a number of beyond SM particles, which interact with the SM through

| Benchmark Points | $g_N$ | $m_{X_1}$ (GeV) | $m_{X_2}$ (GeV) | $m_{h_q}$ (GeV) | $m$ (GeV) | $\Omega h^2$ | $\sigma_{DD}$ (cm$^2$) |
|---|---|---|---|---|---|---|---|
| $BP1$ | 0.59 | 480 | 1000 | 1200 | 600 | 0.09 | $10^{-50}$ |
| $BP2$ | 0.63 | 700 | 1000 | 1160 | 860 | 0.1 | $10^{-49}$ |
| $BP3$ | 0.70 | 900 | 1000 | 1740 | 920 | 0.09 | $10^{-49}$ |

**Table 3.1:** Three benchmark points (BP1, BP2, BP3) of the model are identified with input parameters $\{g_N, m_{X_1}, m_{h_q}, m = m_N = m_E\}$. Relic density and direct detection cross-sections for these points are also mentioned. We have set $m_{X_2}$ at 1000 GeV to obey maximum splitting scenario.

the $SU(2)_N$ or Yukawa interactions. We will particularly highlight two multi-leptonic final states:

- Opposite sign dilepton plus a single jet and missing energy (OSD: $\ell^+\ell^- + 1\, j + \not{E}_T$),
- Hadronically quiet four lepton and missing energy (HQ4l: $2\ell^+2\ell^- + \not{E}_T$).

Leptonic final states are interesting for study at LHC as the SM background contribution is relatively less. Unfortunately no excess has been reported from the existing data yet. In this section, we will predict signal events in the aforementioned channels at $\sqrt{s} = 14$ TeV. The excess of signal is subject to the final state event selection criteria and we will discuss corresponding SM background contributions in each of the cases accordingly. The details of the simulation methodology and definition of re-constructed leptons, jets etc can be found in Appendix. C.

### 3.5.1 Opposite sign dilepton signal

LHC being a proton-proton collider, exotic particles with colour charge ($h_q$ in our case) can be produced copiously. Opposite sign dilepton (OSD) with $1j + \not{E}_T$ arises in the model from two different production processes: (i) $pp \to h_q X_1$, through the Feynman graphs shown in the top panel of Fig. 3.13, and (ii) $pp \to h_q \bar{h_q}$, as shown by the Feynman graphs in the top panel of Fig. 3.14. Variation in production cross-sections of these processes with exotic quark mass $m_{h_q}$ is shown in the bottom panels of Fig. 3.13 and Fig. 3.14 respectively.

Now $h_q$, once produced through $SU(2)_N$ gauge interactions, can only decay via $h_q \to X_{1,2}\, d$ (Fig. 3.15), depending on the availability of phase space. The branching fractions are plotted with respect to $m_{X_1}$ in the bottom panel of Fig. 3.15. Given a specific $m_{X_2}$ and $m_{h_q}$, the branching fraction to $X_1\, d$ reduces and $X_2\, d$ increases with $m_{X_1}$. In the limiting case, when $m_{X_1} = m_{X_2}$, the branching fractions of $h_q$ are same for both the final states. When $h_q$ decays to $dX_1$, the production of $pp \to h_q X_1$ will end in single jet plus missing energy events and $pp \to h_q \bar{h_q}$ will end with two

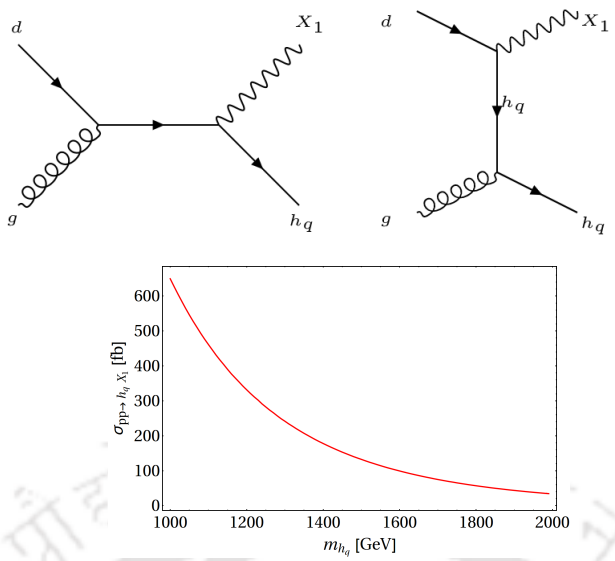


**Figure 3.13:** Top panel: Feynman diagrams for producing $pp \to h_q X_1$ at the LHC. Bottom panel: Production cross-section of $pp \to h_q X_1$ is plotted as a function of $m_{h_q}$ (GeV) at LHC for $\sqrt{s} = 14$ TeV, keeping the DM mass fixed at $m_{X_1} = 700$ GeV and $g_N^2 = 0.4$.

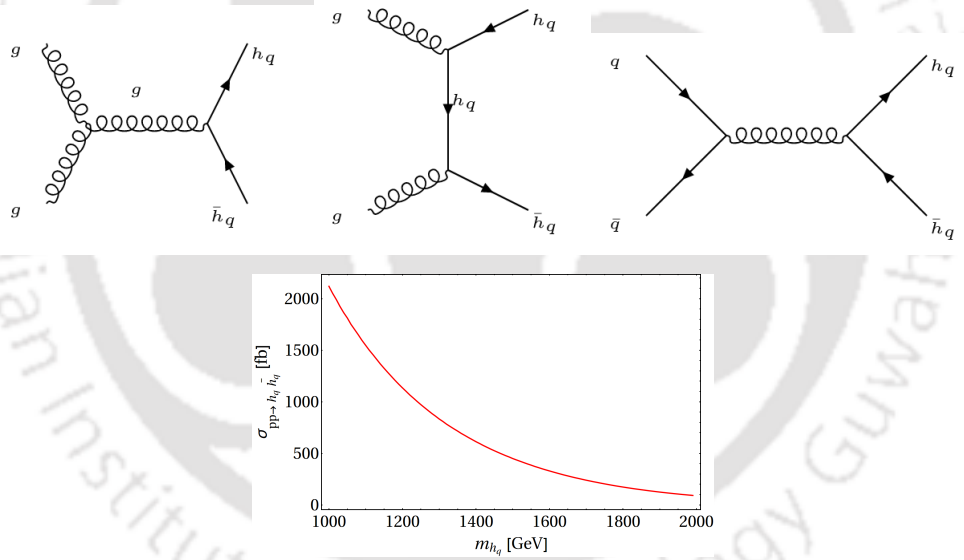


**Figure 3.14:** Top panel: Feynman diagram for producing $pp \to h_q \bar{h}_q$ at the LHC. Bottom panel: Production cross-section of $pp \to h_q \bar{h}_q$ is plotted as a function of $m_{h_q}$ (GeV) at LHC for $\sqrt{s} = 14$ TeV with $g_N^2 = 0.4$.

jets plus missing energy events, which are standard signatures of many DM models including those of minimal scalar singlet extensions. SM background for such final states are also huge and hence reducing the background for a possible excess in the signal is difficult if not impossible. However, $h_q \to dX_2$ may yield some interesting possibilities if we choose the following mass hierarchy in the spectrum:

$$m_{h_q} > m_{X_2} > m = m_E = m_N > m_{X_1} \,. \tag{3.16}$$

$X_2$ can then decay to $N\bar{\nu}$, $E^+e^-$ (see Fig. 3.16). The branching fraction of $X_2$

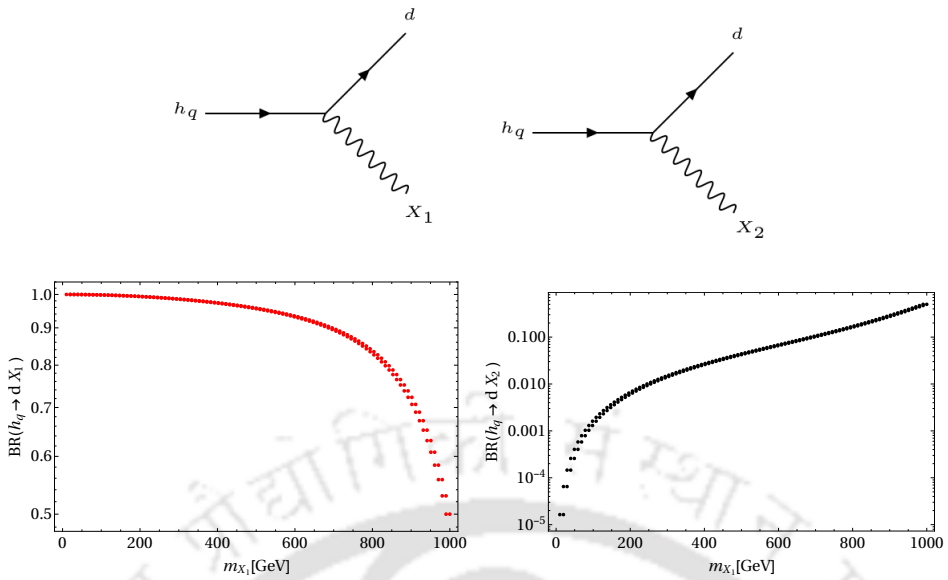


**Figure 3.15:** Top panel: Feynman diagrams for possible decay modes of $h_q$. Bottom panel: Decay branching fractions of $h_q$ as a function of $m_{X_1}$, Br$(h_q \to dX_1)$ on the left and Br$(h_q \to dX_2)$ on the right. We have chosen $m_{h_q} = 1160$ GeV and $m_{X_2} = 1000$ GeV for illustration.

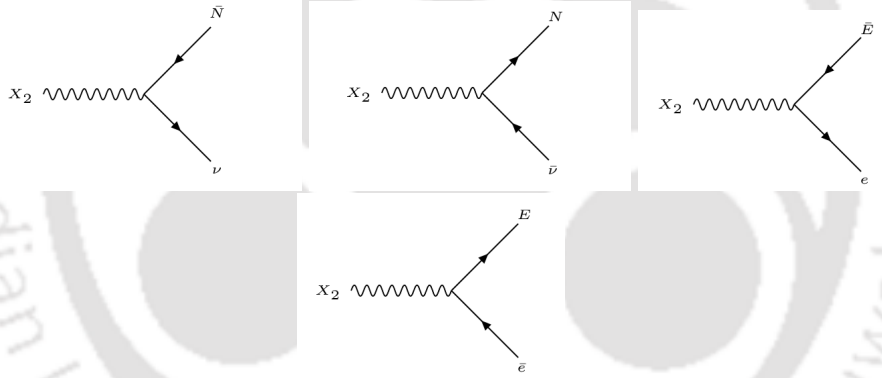


**Figure 3.16:** Feynman diagrams showing decays of $X_2$ to $N\ \bar{\nu},\ E^+e^-$ and their conjugate final states.

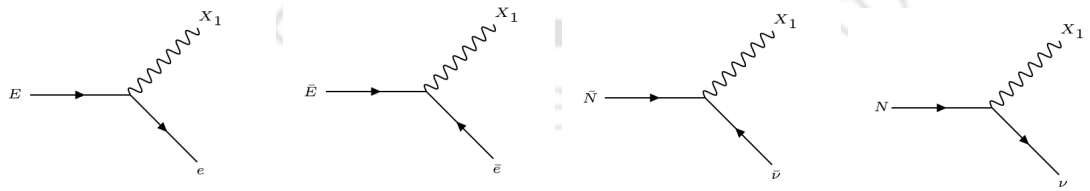


**Figure 3.17:** Feynman diagrams showing decays of $E$ and $N$ to $X_1$ and SM particles.

to neutrino and charged lepton final states are equal in the limit of $m_N = m_E$, which is assumed throughout the analysis. Now, exotic leptons will decay to DM with 100% branching fraction: $N \to \nu X_1,\ E \to eX_1$ as shown in Fig. 3.17. Hence, $pp \to h_q X_1,\ h_q \to dX_2,\ X_2 \to E^+e^-$ will lead to opposite sign same flavour dilepton, a soft jet, and missing energy in the final state. Similarly, $pp \to h_q\bar{h_q},\ h_q \to dX_2,\ X_2 \to E^+e^-$ will also mostly yield opposite sign same flavour dilepton, two

| Benchmark Points | $m_{X_1}$ | $m_{X_2}$ | $m_{h_q}$ | Br$(h_q \to dX_1)$ | Br$(h_q \to dX_2)$ |
|---|---|---|---|---|---|
| $BP1$ | 480 | 1000 | 1200 | 94.8 | 5.2 |
| $BP2$ | 700 | 1000 | 1160 | 89.7 | 10.3 |
| $BP3$ | 900 | 1000 | 1740 | 57.7 | 42.3 |

**Table 3.2:** Branching ratio of $h_q \to dX_{1,2}$ for three benchmark points: BP1, BP2 and BP3.

| Benchmark Points | $\sigma_{pp\to h_q X_1}$ (in pb) | $\sigma_{pp\to h_q \bar{h}_q}$ (in pb) | $\not{E}_T$ (in GeV) | $\sigma^{OSD}_{pp\to h_q X_1}$ (in pb) | $\sigma^{OSD}_{pp\to h_q \bar{h}_q}$ (in pb) | $N$ (100 fb$^{-1}$) |
|---|---|---|---|---|---|---|
| $BP1$ | 0.331 | 1.13 | $> 100$ | $1.77 \times 10^{-3}$ | $8.37 \times 10^{-4}$ | 260 |
| | | | $> 200$ | $1.53 \times 10^{-3}$ | $7.26 \times 10^{-4}$ | 225 |
| | | | $> 300$ | $9.70 \times 10^{-4}$ | $5.95 \times 10^{-4}$ | 156 |
| $BP2$ | 0.172 | 0.758 | $> 100$ | $1.62 \times 10^{-3}$ | $1.58 \times 10^{-3}$ | 320 |
| | | | $> 200$ | $1.04 \times 10^{-3}$ | $1.23 \times 10^{-3}$ | 227 |
| | | | $> 300$ | $5.45 \times 10^{-4}$ | $7.81 \times 10^{-4}$ | 132 |
| $BP3$ | 0.0199 | 0.102 | $> 100$ | $2.73 \times 10^{-4}$ | $1.42 \times 10^{-5}$ | 28 |
| | | | $> 200$ | $2.47 \times 10^{-4}$ | $1.36 \times 10^{-5}$ | 25 |
| | | | $> 300$ | $2.10 \times 10^{-4}$ | $1.20 \times 10^{-5}$ | 22 |

**Table 3.3:** OSD ($\ell^+\ell^- + 1jet + \not{E}_T$) events at LHC for chosen benchmark points with $p_{T_\ell} > 20$, $p_{T_j} > 40$ and $|m_Z - 15| \not\leq m_{ll} \not\leq |m_Z + 15|$ at $\sqrt{s} = 14$ TeV. Number of events predicted for $\mathcal{L} = 100$ fb$^{-1}$ luminosity.

jets, and missing energy events. In the second case, many of those two jet events qualify for single jet case as the jets are soft due to their production in association with a sufficiently heavy particle $X_2$, which carries away most of the momentum in the decay chain. We will perform collider analysis only for the selected benchmark points BP1, BP2, and BP3 (Tab. 3.1). Branching fractions of $h_q$ at those benchmark points are specified in Tab. 3.2.

The dominant SM processes which can mimic OSD signal and can serve as potential background are identified as $t\bar{t}$+jets, $WW$+jets, $WZ$+jets, $ZZ$+jets, and the $Drell\text{-}Yan$. The cross-section of the background is much larger than that of the signal and one needs to judicially choose the cuts on the final state observables to retain the signal and reduce the background. Missing energy ($\not{E}_T$) signature of the signal is characteristically different from that of the SM background. For background, $\not{E}_T$ dominantly comes from neutrinos and energy mismatch (due to smearing and detector inefficiency). $\not{E}_T$ distributions for the signal for the BPs are plotted along with the dominant SM backgrounds in Fig. 3.18. $\not{E}_T$ peaks at a larger value for the signal and at a smaller value for the background, thus allowing us to distinguish between the model(signal) from the background. This is done by putting a sufficiently large $\not{E}_T$.

Cross-sections for OSD events at the LHC with $\sqrt{s} = 14$ TeV and integrated luminosity $\mathcal{L} = 100$ fb$^{-1}$ are listed in Tab. 3.3 in terms of actual number of events [5]. On top of the basic cuts (as discussed in C), we have used following cuts to effectively

[5] Actual number of events $N$ for luminosity $\mathcal{L}$ can be obtained for seed simulation points $N_1$ and final state events $N_2$ as $N = (\sigma_p \times N_2 \times \mathcal{L})/N_1$, where $\sigma_p$ is the corresponding production cross-section.

| Process | $\sigma_p$ (in pb) | $\not{E}_T$(in GeV) | $\sigma^{OSD}$ (in pb) | $N(100\ \text{fb}^{-1})$ |
|---|---|---|---|---|
| $t\bar{t}+j$ | 809.79 | $>100$ | $137.66\times10^{-3}$ | 13766 |
| | | $>200$ | $<8.09\times10^{-3}$ | $<1$ |
| | | $>300$ | $<8.09\times10^{-3}$ | $<1$ |
| $WW+j$ | 60.58 | $>100$ | 64.82 | 6482 |
| | | $>200$ | $5.45\times10^{-2}$ | 545 |
| | | $>300$ | $1.81\times10^{-2}$ | 181 |
| $WZ+j$ | 0.15 | $>100$ | $2.16\times10^{-4}$ | 21 |
| | | $>200$ | $5.55\times10^{-5}$ | 5 |
| | | $>300$ | $2.40\times10^{-5}$ | 2 |
| $ZZ+j$ | 7.63 | $>100$ | $2.28\times10^{-4}$ | 22 |
| | | $>200$ | $<7.63\times10^{-5}$ | $<1$ |
| | | $>300$ | $<7.63\times10^{-5}$ | $<1$ |
| $Drell-Yan$ | 879.19 | $>100$ | $<8.79\times10^{-3}$ | $<1$ |
| | | $>200$ | $<8.79\times10^{-3}$ | $<1$ |
| | | $>300$ | $<8.79\times10^{-3}$ | $<1$ |

**Table 3.4:** OSD $(\ell^+\ell^- + 1jet + \not{E}_T)$ events for dominant SM background at LHC with $p_{T_\ell} > 20$, $p_{T_j} > 40$ and $|m_Z - 15| \not\leq m_{ll} \not\leq |m_Z + 15|$ at $\sqrt{s} = 14$ TeV and $\mathcal{L} = 100\ \text{fb}^{-1}$ luminosity. Appropriate $K-$factors are used for different processes to match to the NLO-NLL cross-sections available in literature (see text for details).

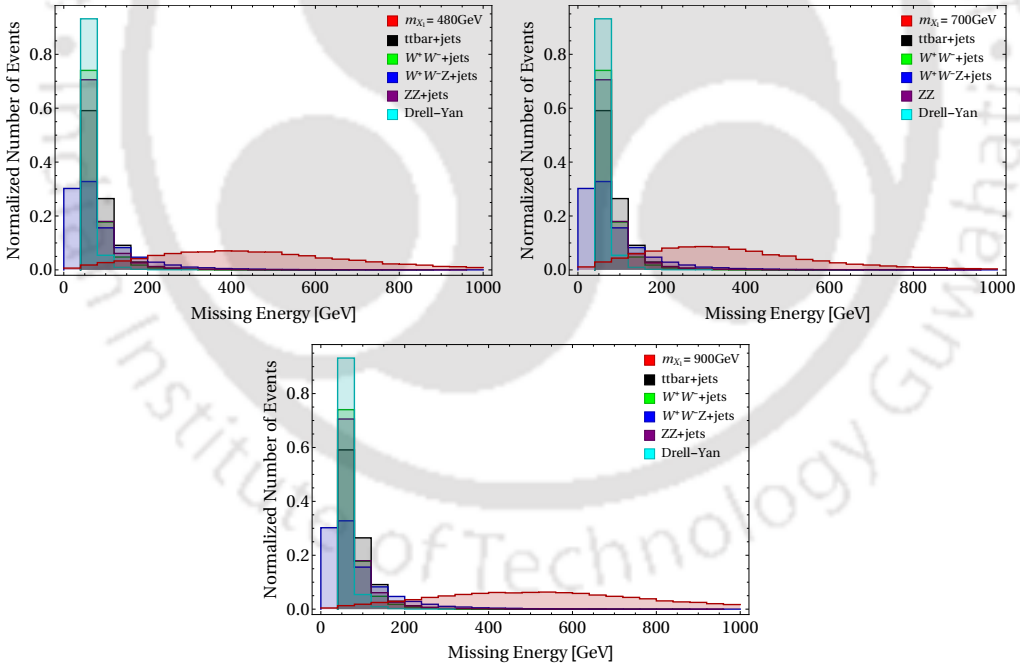


**Figure 3.18:** Missing energy distribution for $(\ell^+\ell^- + 1j + \not{E}_T)$ events at the LHC from $pp \to h_q X_1$ production for the benchmark points BP1 (top left), BP2 (top right) and BP3 (bottom) with dominant SM background.

separate signal from background:

- Missing Energy cut $(\not{E}_T)$: $\not{E}_T > 100$, 200, 300 GeV are used. Large $\not{E}_T$ retains the signal due to large DM masses of the benchmark points and reduces background.

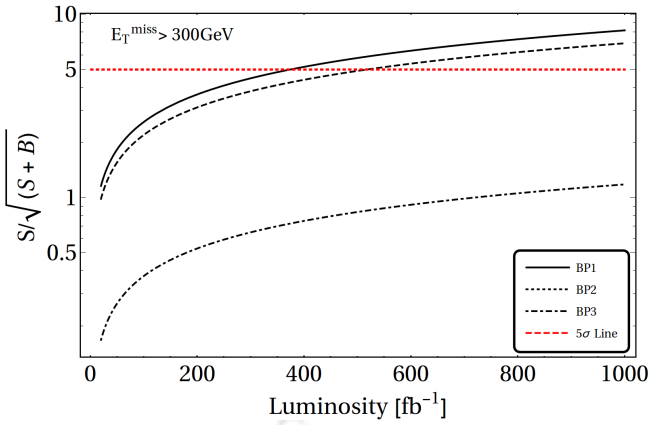


**Figure 3.19:** Significance plot of OSD ($\ell^+\ell^- + 1jet + \not{E}_T$) events at the benchmark points with $\not{E}_T$> 300 GeV versus luminosity (in fb$^{-1}$).

- Invariant mass cut: Invariant mass is defined as $m_{\ell\ell}{}^2 = (p_{\ell^-} + p_{\ell^+})^2$ for opposite sign same flavour dileptons. We require invariant mass not to lie within the Z mass window ($|m_z - 15| \nleq m_{\ell\ell} \nleq |m_z + 15|\ GeV$) to reduce background events from $Z$ production.
- For jets, a moderate cut $p_T > 40$ GeV is demanded. This is particularly because of the fact that the jets produced in the signal events carry only a small fraction of the momentum and are mostly soft.

Cross-sections for the dominant SM background processes contributing to OSD events at LHC is tabulated in Tab. 3.4. We have multiplied the production cross-sections generated at leading order (LO) by appropriate $K$ factors to match the NLO cross-section available in the literature. For example, for $t\bar{t}:\ K = 1.31, WWj:\ K = 1.30, WZj:\ K = 1.27, ZZj:\ K = 1.31, Drell\text{-}Yan:\ K = 1.2$ [252]. We estimate a limit on the final state event cross-section ($\sigma_e$) as $\sigma_e < \sigma_p/N$ where $N$ events are simulated with production cross section $\sigma_p$. A discovery significance for OSD events is shown in Fig. 3.19 in terms of luminosity (in fb$^{-1}$). Thus, there is a possibility to see an excess in BP1 and BP2 benchmark points in OSD final states at the LHC for high luminosity, while BP3 might be a little harder to explore.

### 3.5.2 Hadronically quiet four lepton signal

One of the unique collider signatures that this model offers, is the hadronically quiet four lepton (HQ4l). This can arise from the production of the heavier $SU(2)_N$ gauge boson $X_2$ following the Feynman graph in left panel of Fig. 3.20. $X_2$ further decays through the exotic leptons following Fig. 3.16 and Fig. 3.17 and produces two pairs of same flavour opposite sign dilepton with large missing energy ($\ell^\pm\ell^\mp\ell'^\pm\ell'^\mp + \not{E}_T$). The corresponding signal can have any of the following combinations: $e^\pm e^\mp e^\pm e^\mp$,$e^\pm e^\mp \mu^\pm \mu^\mp$, $\mu^\pm\mu^\mp\mu^\pm\mu^\mp$. We however choose final states inclusive of both the flavours. The production cross-section of $pp \to X_2X_2$ is much smaller as it is an $SU(2)_N$ gauge interaction process. With heavier $m_{X_2}$, the cross-section falls off sharply to a vanishingly small value as shown in the right panel of Fig. 3.20. We again note here that $pp \to h_q\bar{h_q}$ also contributes to HQ4l events, where in both legs $h_q$ decays via $h_q \to dX_2$ with $X_2 \to e^+e^-X_1$ through exotic charged leptons. The signal

event rates at the benchmark points are mentioned in Tab. 3.5. The lepton selection criteria remains similar to OSD search, while we demand the absence of jets with $p_T$ >20 GeV. Although the number of signal events is small in this case, SM background is even more rare. Dominant contributions come from $ZZ$, $WWWW$ and $Zt\bar{t}$ as estimated in Tab. 3.6. Again we show that missing energy is one of the main discriminators for separating signal and background. This is shown in Fig. 3.21 for three benchmark points and for the dominant SM backgrounds.

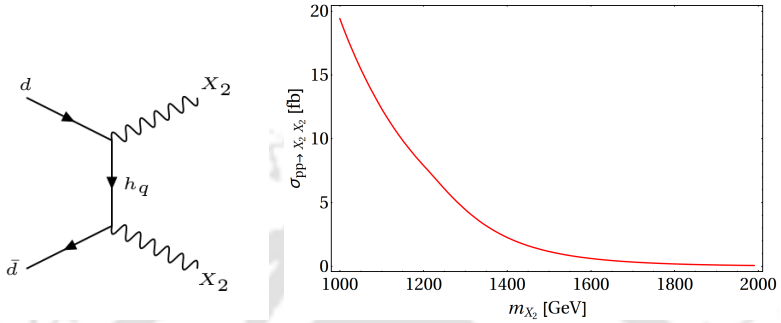


**Figure 3.20:** Left: Feynman diagram for producing a pair of $X_2$ at the LHC. Right: Cross-section of $pp \to X_2X_2$ as a function of $m_{X_2}$ at 14 TeV LHC.

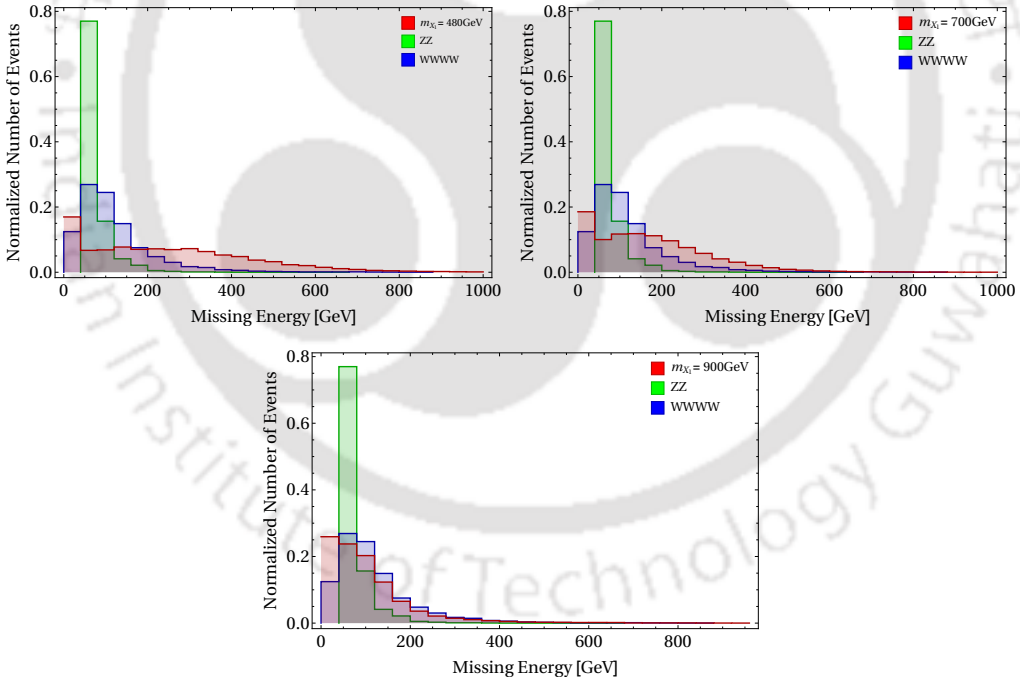


**Figure 3.21:** Missing energy ($\not{E}_T$) distribution for HQ4l events for the benchmark points BP1 (top left), BP2 (top right) and BP3 (bottom) with dominant SM background.

We have also checked the efficiency of invariant mass ($m_{\ell\ell}$) cut employed in the analysis and explicitly demonstrated the $m_{\ell\ell}$ distributions in Fig. 3.22. In the left panel, we plot $m_{\ell\ell}$ for OSD ($\ell^+\ell^- + 1jet + \not{E}_T$) events for signal from BP2 and dominant SM background from $ZZ$+jets, $W^+W^-Z$+jets. On the right-panel we plot $m_{\ell\ell}$ of any two same flavour opposite sign dilepton pair of HQ4l events for signal at BP2 with dominant SM backgrounds from $ZZ$,$Zt\bar{t}$. For OSD, both the backgrounds

| Benchmark Points | $\sigma_{pp\to X_2X_2}$ (in pb) | $\sigma_{pp\to h_q\bar{h}_q}$ (in pb) | $E_T^{miss}$ | $\sigma^{HQ4l}_{pp\to X_2X_2}$ (in pb) | $\sigma^{HQ4l}_{pp\to h_q\bar{h}_q}$ (in pb) | $N$ $(100fb^{-1})$ |
|---|---|---|---|---|---|---|
| $BP1$ | 0.0193 | 1.13 | $> 100$ | $1.88 \times 10^{-3}$ | $3.32 \times 10^{-4}$ | 221 |
| | | | $> 200$ | $1.53 \times 10^{-3}$ | $2.82 \times 10^{-4}$ | 181 |
| | | | $> 300$ | $1.07 \times 10^{-3}$ | $2.01 \times 10^{-4}$ | 127 |
| $BP2$ | 0.0264 | 0.758 | $> 100$ | $2.27 \times 10^{-3}$ | $5.99 \times 10^{-4}$ | 286 |
| | | | $> 200$ | $1.36 \times 10^{-3}$ | $4.11 \times 10^{-4}$ | 177 |
| | | | $> 300$ | $5.43 \times 10^{-4}$ | $2.15 \times 10^{-4}$ | 75 |
| $BP3$ | 0.0205 | 0.102 | $> 100$ | $1.73 \times 10^{-4}$ | $2.61 \times 10^{-4}$ | 43 |
| | | | $> 200$ | $3.93 \times 10^{-5}$ | $2.47 \times 10^{-4}$ | 27 |
| | | | $> 300$ | $1.56 \times 10^{-5}$ | $2.23 \times 10^{-4}$ | 23 |

**Table 3.5:** HQ4l ($\ell^+\ell^-\ell^{'+}\ell^{'-} + \not{E}_T$ ) events at LHC for chosen benchmark points with $p_{T_\ell} > 20$ and $|m_Z - 15| \not\leq m_{ll} \not\leq |m_Z + 15|$ for all opposite sign same flavour dilepton at $\sqrt{s} = 14\,TeV$ and $\mathcal{L} = 100fb^{-1}$ luminosity.

| Process | $\sigma_{production}(in\ pb)$ | $E_T^{miss}$ | $\sigma_{HQ4l}(in\ pb)$ | $N(100fb^{-1})$ |
|---|---|---|---|---|
| $ZZ$ | 0.024 | $> 100$ | $1.68 \times 10^{-5}$ | 1 |
| | | $> 200$ | $< 1.2 \times 10^{-6}$ | $< 1$ |
| | | $> 300$ | $< 1.2 \times 10^{-6}$ | $< 1$ |
| $W^+W^-W^+W^-$ | $1.17 \times 10^{-6}$ | $> 100$ | $< 7.8 \times 10^{-12}$ | $< 1$ |
| | | $> 200$ | $< 7.8 \times 10^{-12}$ | $< 1$ |
| | | $> 300$ | $< 7.8 \times 10^{-12}$ | $< 1$ |
| $Zt\bar{t}$ | 0.90 | $> 100$ | $1.8 \times 10^{-4}$ | 18 |
| | | $> 200$ | $4.5 \times 10^{-5}$ | 4 |
| | | $> 300$ | $< 4.5 \times 10^{-5}$ | $< 1$ |

**Table 3.6:** HQ4l ($\ell^+\ell^-\ell^{'+}\ell^{'-} + \not{E}_T$ ) events for dominant SM background at LHC with $p_{T_\ell} > 20$ and $|m_Z - 15| \not\leq m_{ll} \not\leq |m_Z + 15|$ for all opposite sign same flavour dilepton at $\sqrt{s} = 14\,TeV$ and $\mathcal{L} = 100fb^{-1}$ luminosity. Appropriate $K-$factors are used for different processes to match to the NLO-NLL cross-sections available in literature (see text for details).

$ZZ$+jets, $W^+W^-Z$+jets have $m_{\ell\ell}$ peaks around $Z$ mass window and reduce drastically with the invariant mass cut. For HQ4l, we can form dilepton invariant mass $m_{\ell\ell}$ depending upon same flavour or two different flavour leptons in the final state respectively. The $m_{\ell\ell}$ distribution for HQ4l events are shown for highest $m_{\ell\ell}$ obtained in the events. As can easily be seen that for $ZZ$ events, the distribution peaks at Z-mass, while signal events for BP2 peaks at a larger value. We therefore employ $|m_Z - 15| \not\leq m_{ll} \not\leq |m_Z + 15|$ cut for all the opposite sign same flavour invariant mass pairs formed in HQ4l events, which retains the signal to a large extent while the background drops significantly.

It is clear that hadronically quiet four lepton channel provides a smoking gun signature of the model as the significance plot suggests in Fig. 3.23. Such a signature is not often studied and should be analyzed with existing data for a possible excess.

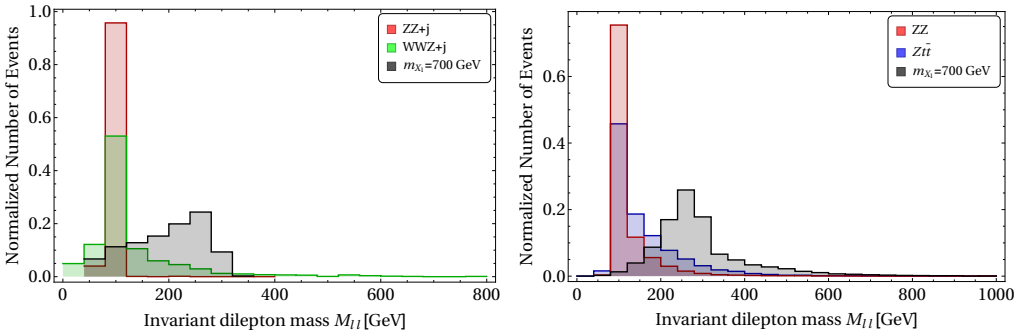


**Figure 3.22:** Invariant mass $(m_{ll})$ distribution for OSD (left) and HQ4l channel (right) for BP2 compared with $Z$ background.

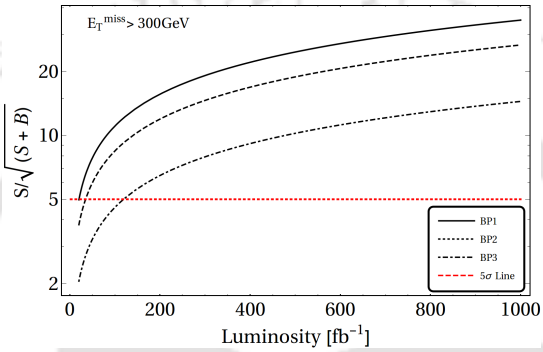


**Figure 3.23:** Significance plot for hadronically quiet four lepton final state (HQ4l) events for benchmark points at LHC for $\not{E}_T$> 300 GeV with luminosity (in fb$^{-1}$).

## 3.6 Summary

In this chapter we have analyzed the phenomenology of one possible variant of a non-abelian vector boson DM that appears as an $SU(2)_N$ extension of the SM. We elaborate on relic abundance and direct search outcome of the DM through detailed parameter space scan taking care of the freedom in choosing the $SU(2)_N$ gauge coupling. Several new features have emerged from this analysis including the crucial effects of co-annihilation.

The unification of the low scale model into gauge group $E(6)$ with consistent intermediate symmetries and breaking scheme has been discussed in this context. The breaking adopted here suggests that in $D$-parity conserved case, $SU(2)_N$ and $SU(2)_L$ couplings are equal $(g_N = g_L)$ with two degenerate vector boson DM, while for $D$-parity broken scenario we may have non-universality through $g_N \neq g_L$ and a single component DM emerges. The spread in the gauge coupling for $D$-odd case is determined by explicit calculation and the freedom is utilized for phenomenological analysis. Relic density constraint of the model correlates coupling and mass of the DM to the exotic quark mass $m_{h_q}$ and exotic lepton mass $m$. Dominant annihilation processes are $t$-channel diagrams through exotic fermion exchange. This allows a large range of DM masses above ∼200 GeV, lower than that is discarded from the bound on $Z - Z^{'}$ mixing.

Direct search interaction for this model is mainly $s$-channel process and mediates only via exotic quarks. Hence, except for those regions where $m_{h_q} \sim m_{DM}$, the model is very loosely constrained by spin independent direct search bounds. Co-

annihilation of DM with $X_2$ helps the DM to evade direct search constraints and the detection may go beyond the reach of XENONnT sensitivity. This is simply because co-annihilation only contributes to relic density and does not take part in direct search due to kinematical constraints. We also analyzed degenerate DM scenario in $D$-parity even case, where the DM mass has to be at least $m_{X_3} = m_{Z'} \gtrsim 1$ TeV, as three of the gauge bosons (including the DM) become degenerate. But this situation is ruled out because of relic density constraints.

The exotic particles present in the model can be produced at the LHC and their subsequent decays yield multi-lepton signatures with large missing energy. Opposite sign dilepton and hadronically quiet four lepton channels are discussed in context of the present LHC data through detailed simulations. We note that the presence of only one soft jet in two lepton channel can help to distinguish this model from SM background events like $t\bar{t}$ and also from other supersymmetric signals. Large missing energy cuts are shown to be effective to reduce the backgrounds and a possibility of seeing such a signal at 14 TeV emerges, albeit with large luminosity. A strong $H_T$ cut, as provided in the current LHC analysis of the data, washes away signal cross-section of this model. We therefore propose a minimal or no $H_T$ cut for seeing opposite sign dilepton signature of this particular scenario. However, a more crucial signal appears in the form of hadronically quiet four lepton with a provision to be probed at future LHC runs due to much less SM background.

Chapter 4

# Multipartite Dark Matter in $SU(2)_N$ extension of the Standard Model

## Contents



## 4.1 Introduction

A multi-particle dark matter (DM) framework consisting of non-abelian vector boson (VBDM) and scalar components is addressed in this chapter []. As before, the vector boson DM arises in an $SU(2)_N$ extension of the SM. An unbroken $U(1)$ symmetry is also imposed in order to ensure the stability of the new electromagnetic charge neutral gauge bosons. The key feature of this model is to assume that SM particles do not transform under additional $SU(2)_N$ symmetry unlike the case in previous chapter. Therefore, the VBDM lacks a direct search cross-section except for the Higgs portal which is constrained from Higgs data to avoid large mixing. This indeed helps the model to be allowed in a large parameter space from non-observation of DM in direct searches, for example in PANDA data [67]. Another interesting aspect of this analysis is to show the presence of scalar triplet as additional DM component apart from the VBDM as pointed out in [253]. The scalar DM will again have interactions to SM via Higgs portal and has direct search prospect. The analysis explores such a two-component DM parameter space of the model in the presence of non-zero DM-DM interactions [254].

The model also permits not-so-heavy neutrinos to generate light neutrino masses through *inverse seesaw* mechanism. This allows, in one hand, the heavy neutrinos to be stable and contribute as DM, while on the other hand, they can be produced in

the Large Hadron Collider (LHC) via hadronically quiet single lepton and hadronically quiet opposite sign dilepton (OSD) channel with missing energy. This is one of the important features of this analysis that was not addressed in the earlier proposal of the model [253]. The SM background can be tamed down to some extent by large missing energy cut ($\not{E}_T$) and $H_T$ cut ($\not{H}_T$). The discovery potential thus can be reached with a high luminosity. Generation of light neutrino masses (with not-so-heavy neutrinos ($\sim \mathcal{O}(500)\text{GeV}$)) also necessitates the VBDM $(X, \bar{X})$ to be degenerate with the third gauge boson component $X_3$. Therefore, co-annihilations play a crucial part on top of annihilation for VBDM and bridges a connection between the neutrino and the dark sector.

This chapter is organized as follows: we discuss the model in Sec. 4.2, neutrino mass generation mechanism in Sec. 4.3, followed by the vector boson DM analysis in Sec. 4.4. The multipartite DM set-up is elaborated in subsection. 4.4.3. Possible collider signatures are analysed in Sec. 4.5. Finally we summarize in Sec. 4.6.

## 4.2 Fields and interactions

The particle content for this model is chosen minimally in order to have a spontaneous symmetry breaking (SSB) of the extended $SU(2)_N$ gauge group to produce massive gauge bosons, and also to have a successful neutrino mass generation [253]. An important difference from the $SU(2)_N$ model discussed in last chapter [200, 201], is that all of the SM fermions here are singlet under $SU(2)_N$. The stability of DM is ensured by an added global $U(1)$ symmetry ($S^{'}$), imposed on the new particles (as in [253]), so that $S = S^{'} + T_{3N}$ remains unbroken. The stability of DM under an unbroken global continuous symmetry may however be broken by the presence of a possible quantum theory of gravity [255], which will therefore have observable effects in gamma ray, $X$-ray, neutrino and CMB data through DM decay, thus constraining such a case. The analysis in [255] shows that the limits on DM mass scale can be as stringent as few MeVs, by assuming dimension five effective operators suppressed by Planck scale, which explicitly breaks the DM symmetry. However, due to the lack of our knowledge of a possible quantum theory of gravity, and the fact that $S$ is generated by a combination of global symmetry $S^{'}$ together with $T_{3N}$ (isospin of a broken gauge symmetry), we assume $S$ to be unbroken up to Planck scale and avoid such constraints.

The new particles and their charges under $SU(3)_C \otimes SU(2)_L \otimes U(1)_Y \otimes SU(2)_N \otimes S'$ are given as:

$$\text{Three SU}(2)_N \text{ gauge bosons:} \qquad X_{1,2,3} \equiv (1,1,0,3,0),$$

$$\text{Three Dirac fermion doublets:} \qquad n = (n_1, n_2)_{L,R} \equiv (1,1,0,2,\frac{1}{2}),$$

$$\text{One scalar doublet:} \qquad \chi = (\chi_1, \chi_2) \equiv (1,1,0,2,\frac{1}{2}),$$

$$\text{One scalar bi-doublet:} \qquad \zeta = \begin{pmatrix} \zeta_1^0 & \zeta_2^0 \\ \zeta_1^- & \zeta_2^- \end{pmatrix} \equiv (1,2,-\frac{1}{2},2,-\frac{1}{2}),$$

where $\zeta$ transforms (vertically) under $SU(2)_L$ and (horizontally) under $SU(2)_N$. Furthermore, an $SU(2)_N$ scalar triplet ($\Delta$) is introduced:

$$\Delta = \begin{pmatrix} \Delta_2/\sqrt{2} & \Delta_3 \\ \Delta_1 & -\Delta_2/\sqrt{2} \end{pmatrix} \equiv (1,1,0,3,-1),$$

for generating neutrino masses, which will be discussed in the next section. The crucial construct of the model lies in the choice of $S'$ charges, which will be clear in a moment.

The scalar potential of this model reads [253]:

$$\begin{aligned} V = {} & \mu_\zeta^2 \text{Tr}(\zeta^\dagger\zeta) + \mu_\Phi^2 \Phi^\dagger\Phi + \mu_\chi^2 \chi^\dagger\chi + \mu_\Delta^2 \text{Tr}(\Delta^\dagger\Delta) + (\mu_1 \tilde{\Phi}^\dagger \zeta\chi + \mu_2 \tilde{\chi}^\dagger \Delta\chi + H.c.) \\ & + \frac{1}{2}\lambda_1[\text{Tr}(\zeta^\dagger\zeta)]^2 + \frac{1}{2}\lambda_2(\Phi^\dagger\Phi)^2 + \frac{1}{2}\lambda_3 \text{Tr}(\zeta^\dagger\zeta\zeta^\dagger\zeta) + \frac{1}{2}\lambda_4(\chi^\dagger\chi)^2 + \frac{1}{2}\lambda_5[\text{Tr}(\Delta^\dagger\Delta)]^2 \\ & + \frac{1}{4}\lambda_6 \text{Tr}(\Delta^\dagger\Delta - \Delta\Delta^\dagger)^2 + f_1 \chi^\dagger\tilde{\zeta}^\dagger\tilde{\zeta}\chi + f_2 \chi^\dagger\zeta^\dagger\zeta\chi + f_3 \Phi^\dagger\zeta\zeta^\dagger\Phi + f_4 \Phi^\dagger\tilde{\zeta}\tilde{\zeta}^\dagger\Phi \\ & + f_5(\Phi^\dagger\Phi)(\chi^\dagger\chi) + f_6(\chi^\dagger\chi)\text{Tr}(\Delta^\dagger\Delta) + f_7 \chi^\dagger(\Delta\Delta^\dagger - \Delta^\dagger\Delta)\chi + f_8(\Phi^\dagger\Phi)\text{Tr}(\Delta^\dagger\Delta) \\ & + f_9 \text{Tr}(\zeta^\dagger\zeta)\text{Tr}(\Delta^\dagger\Delta) + f_{10}\text{Tr}[\zeta(\Delta^\dagger\Delta - \Delta\Delta^\dagger)\zeta^\dagger]. \end{aligned} \tag{4.1}$$

Spontaneous symmetry breaking of $SU(2)_N \otimes S'$ to $S = S' + T_{3N}$ happens via the non-zero vacuum expectation value (VEV) of $SU(2)_N$ scalar doublet: $\langle\chi_2\rangle = u_2$. $S$ charge assignment for the new particles is given as:

$$n_1, \chi_1 \sim +1, \qquad n_2, \chi_2, \zeta_2, \Delta_3 \sim 0, \qquad \zeta_1, \Delta_2 \sim -1, \qquad \Delta_1 \sim -2,$$
$$X(\overline{X}) = \frac{X_1 \mp iX_2}{\sqrt{2}} \sim \pm 1, \qquad Z' = X_3 \sim 0.$$

All the SM particles have zero $S$ charge. Therefore, particles with non-zero $S$ charge will be protected from decaying into the SM. We can assume $X$ to be the

lightest of the particles with non-zero $S$ charge, and therefore a possible DM candidate. Furthermore, $\Delta_{1,2,3}$ scalars can become kinematically stable in certain regions of parameter space [253], and be part of a multi-component DM framework. We will investigate this possibility in details. The three other scalars which acquire VEV are: $\langle\zeta_2^0\rangle = v_2$, $\langle\Delta_3\rangle = u_3$, and $\langle\phi^0\rangle = v_1$. Note that the VEV assignment is different here from the $SU(2)_N$ extension considered in Chapter 3, where $\langle\Delta_1^0\rangle$ is also non-zero. Therefore, the $X_{1,2}$ bosons will have equal masses in this model, and more importantly $S = S' + T_{3N}$ global symmetry remains unbroken unlike in [201]. The masses of the gauge bosons are given by:

$$m_W^2 = \frac{1}{2}g_2^2\left(v_1^2+v_2^2\right), \qquad m_X^2 = \frac{1}{2}g_N^2\left(u_2^2+v_2^2+2u_3^2\right), \qquad m_{Z'}^2 \simeq \frac{1}{2}g_N^2\left(u_2^2+v_2^2+4u_3^2\right), \tag{4.2}$$

where $Z - Z'$ mixing matrix is given by:

$$m_{Z,Z'}^2 = \frac{1}{2}\begin{pmatrix} \left(g_1^2+g_2^2\right)\left(v_1^2+v_2^2\right) & -g_N\sqrt{g_1^2+g_2^2}\,v_2^2 \\ -g_N\sqrt{g_1^2+g_2^2}\,v_2^2 & g_N^2\left(u_2^2+v_2^2+4u_3^2\right)\end{pmatrix}. \tag{4.3}$$

To ensure small $Z$-$Z^{'}$ mixing [246], we assume $v_2 \ll u_2$. Furthermore, $u_3$ is assumed to be small which breaks the lepton number global symmetry $(L)$ to lepton parity $((-1)^L)$ as explained in Sec. 4.3. Therefore, the $X$ boson masses are nearly degenerate, i.e. $m_{Z'}(m_{X_3}) \simeq m_X$. This still makes the model phenomenologically viable in a large parameter space as $Z'$ doesn't have a tree level coupling to SM. This hides $Z'$ of this model from being observed at the LHC, and adds to the the freedom of choosing $m_{Z'}$ as a free parameter. This should again be contrasted to the case in [245], where there is a minimum limit on $m_{X_{1,2,3}} \geqslant 1$ TeV, for the degenerate vector boson DM case to respect the bound from $Z^{'}$ search data.

## 4.3 Neutrino Mass

One of the important features of the model is to generate neutrino mass successfully and thus addressing dark matter and neutrinos under one umbrella. The scalar bi-doublet $(\zeta)$, which acts as a mediator between the dark and visible sectors, also helps in generating masses for the neutrinos. The relevant Yukawa terms are:

$$f_\zeta \quad \left[\left(\overline{\nu}_L\zeta_1^0 + \overline{e}_L\zeta_1^-\right)n_{1R} + \left(\overline{\nu}_L\zeta_2^0 + \overline{e}_L\zeta_2^-\right)n_{2R}\right] \tag{4.4}$$

$$f_\Delta \quad \left[n_1 n_1\Delta_1 + \left(n_1 n_2 + n_2 n_1\right)\Delta_2/\sqrt{2} - n_2 n_2\Delta_3\right], \tag{4.5}$$

where in the second line $nn$ includes both of $n_L n_L$ and $n_R n_R$. The lepton number is conserved in (4.4) with $n$ carrying $L = 1$, and is broken to lepton parity, i.e. $(-1)^L$ by the $nn$ terms in (4.5). After SSB this turns out to be:

$$f_\zeta\, v_2\, \overline{\nu}_L n_{2R} - f_\Delta^L\, u_3\, n_{2L}n_{2L} - f_\Delta^R\, u_3\, n_{2R}n_{2R} + \text{h.c.} \tag{4.6}$$

where $f_\zeta$ and $f_\Delta$ are $3\times3$ matrices, and the neutrino mass matrix in the $(\overline{\nu}_L, n_{2R}, \overline{n}_{2L})$ basis is given by:

$$M_\nu = \begin{pmatrix} 0 & m_D & 0 \\ m_D & m_2' & M \\ 0 & M & m_2 \end{pmatrix}, \tag{4.7}$$

where each entry is a $3 \times 3$ matrix with $m_D = f_\zeta\, v_2$, $m_2' = f_\Delta^R\, u_3$, $m_2 = f_\Delta^{L^*}\, u_3$, and $M$ is a free Dirac mass term in $M\,(\overline{n}_{2L} n_{2R} + \overline{n}_{2R} n_{2L})$. The inverse seesaw neutrino mass is thus generated and given by:

$$m_\nu \simeq \frac{m_D^2\, m_2}{M^2} = f_\zeta^2 f_\Delta \left(\frac{v_2}{M}\right)^2 u_3. \tag{4.8}$$

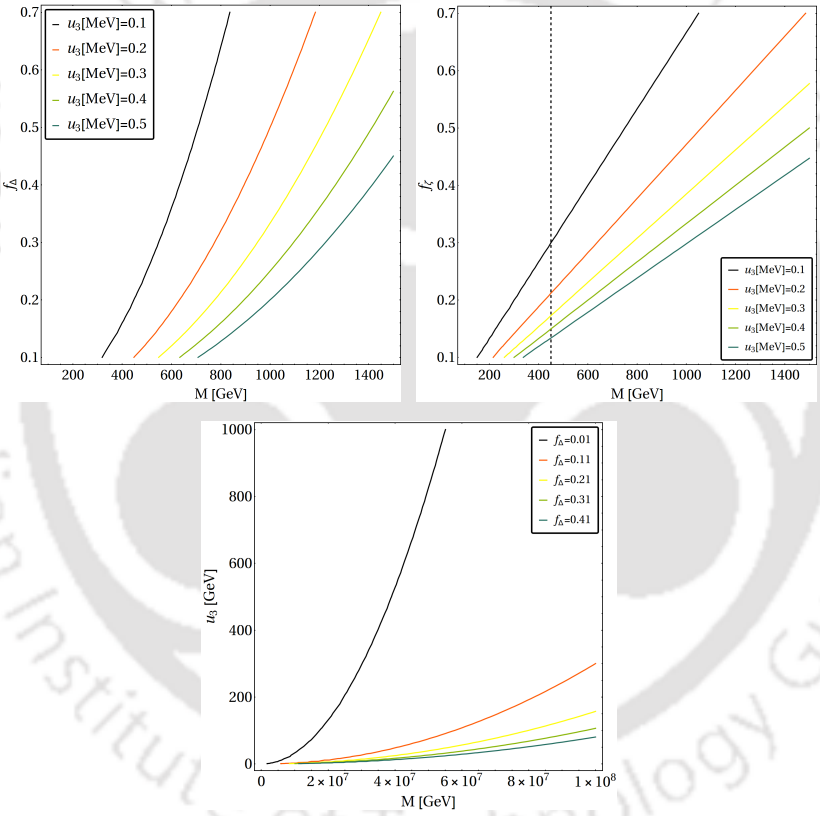


**Figure 4.1:** Top Left: $f_\Delta$ versus heavy neutrino mass $M$ ($\sim \mathcal{O}$ (hundreds of GeVs)) for different choices of $u_3$ ($\sim$ MeV) to keep $m_\nu \sim 0.1\ eV$ with $f_\zeta \sim \mathcal{O}(1)$; Top Right: $f_\zeta$ versus heavy neutrino mass $M(\sim \mathcal{O}$ (hundreds of GeVs)) corresponding to different values of the VEV $u_3$ to obtain right neutrino mass for $f_\Delta \sim \mathcal{O}(1)$. The black dashed line shows the mass of the heavy neutral chosen for selecting the BPs (Tab. 4.1). Bottom: $u_3$ (in GeV) versus $M$ ($\sim \mathcal{O}(10^7)$ GeV) for different values of coupling $f_\Delta$, where each contour satisfies $m_\nu \sim 0.1\ eV$.

Assuming $m_2, m_2', m_D \ll M$, $n$ remains pseudo-dirac with $m_n \simeq M$. Since, $\zeta$ is the portal between the SM and the hidden sector, the collider signatures of this model involve processes with $n$ in the final states. Therefore, a phenomenologically interesting choice of parameters would be $M \sim \mathcal{O}$(TeV), with $f_\zeta \sim 1$. Furthermore, we assume $v_2 \simeq 1$ GeV in order to have a small $Z - Z'$ mixing. Using $\sum m_\nu < 0.17$ eV [45], we take $m_\nu \simeq \mathcal{O}(0.1$ eV) such that:

$$u_3 \sim \frac{0.1}{f_\Delta}\,\text{MeV}. \tag{4.9}$$

A contour plot for correct neutrino mass $m_\nu \simeq \mathcal{O}(0.1\,\text{eV})$, following Eq. (4.8), is depicted in Fig. 4.1. The contours in $M - f_\Delta$ plane has been shown for $f_\zeta \sim \mathcal{O}(1)$ for different choices of $u_3$ in the LHS of top panel in Fig. 4.1. The same exercise is done in $M - f_\zeta$ plane for $f_\Delta \sim \mathcal{O}(1)$ [1] in top RHS graph for different $u_3$. The other possible regime is to assume $M \sim \mathcal{O}(10^7)$ GeV, which allows larger $u_3$ ($\sim$ hundreds of GeVs). This is shown on the bottom panel of Fig. 4.1 for $f_\zeta \sim \mathcal{O}(1)$ and $f_\Delta : \{0.01, 0.9\}$. The mass degeneracy between $X, X_3$ is broken in such a scenario and thus co-annihilations become subdominant to the annihilation processes for $X$ DM. For $M \sim 500$ GeV, the heavy neutrinos are stable and can be DM candidate, while heavy neutrinos with $M \sim 10^7$ GeV will decay and will not contribute as DM. Therefore such heavy neutrinos are also viable from neutrino mass and DM constraints, but will complicate the model in collider detection. We will therefore choose lighter $n_{1,2}$ scenario (as in the top panel of Fig. 4.1) and show that it plays a crucial role in yielding possible leptonic signature at the LHC.

## 4.4 Dark Matter Phenomenology

In this chapter also we assume all DM candidates to be present in the thermal bath and acquire correct relic via thermal freeze out. In particular, we highlight a couple of interesting features regarding DM phenomenology of the model : (i) The alteration to the single component vector boson DM freeze-out and its relic density due to co-annihilation contribution, which was not taken into account in the earlier analysis [253] and (ii) the presence of a second DM candidate ($\Delta$) in a large region of parameter space of the model, which is significantly influenced by DM-DM interactions. The heavy neutrinos $(n_1, n_2)$, assumed in this framework, can also be kinematically stable and serve as DM. However, for generating correct neutrino masses, the contribution of these particles to DM relic density will be very small.

### 4.4.1 Possible DM candidates of the model

At the very outset, we will sketch the parameter space of the model, where we can have different DM components coexisting together.

$\Delta_1$ and $\Delta_2$ component of the $SU(2)_N$ scalar triplet have non-zero $S$ charges. As they are charge neutral, they can qualify as DM if their stability is ensured. $\Delta_3$ having zero $S$ charge, mixes with the SM Higgs due to non-zero VEV (instigated by $f_8\Phi^\dagger\Phi\text{Tr}(\Delta^\dagger\Delta)$ term in the scalar potential) and decaying to SM. Therefore, $\Delta_3$ does not qualify as DM. On the other hand, $\Delta_1$ and $\Delta_2$ have the following interaction vertices with the vector boson $X$:$\Delta_1\Delta_2^* X$, $\Delta_2\Delta_3^* X$, $\Delta_1 XX$, $\Delta_2 XX_3$. As a result, possible decay of $\Delta_2$ to SM can occur via off-shell $\Delta_3$ as shown in left hand side (LHS) of Fig. 4.2. Similarly, $\Delta_1$ can also decay to SM via off-shell $\Delta_2$ and $\Delta_3$, shown in right hand side (RHS) of Fig. 4.2. So, $\Delta_1$ and/or $\Delta_2$ can be potential DM candidates if we

[1] While a large Yukawa may cause trouble to vacuum stability, the extended scalar sector is expected to save it.

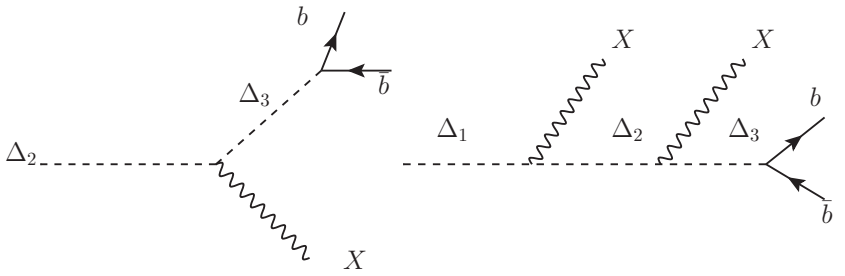


**Figure 4.2:** Decay of the triplet scalars to vector boson $X$ for $m_{\Delta_{1,2,3}} > m_X$. Left: Decay of $\Delta_2$ to SM via $\Delta_3$; Right: Decay of $\Delta_1$ to SM and $X$ via off-shell $\Delta_3$ and $\Delta_2$.

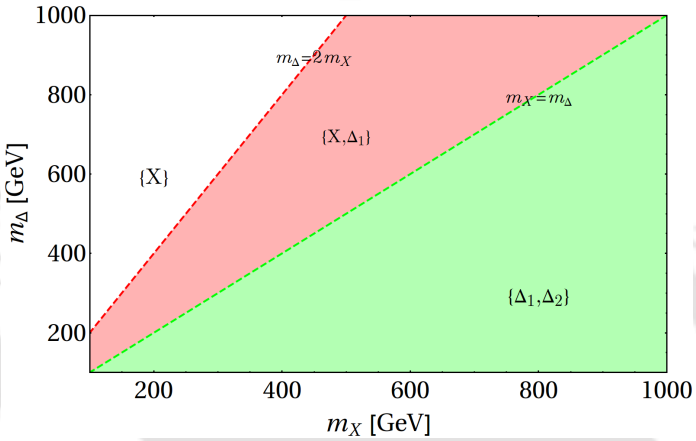


**Figure 4.3:** Regions of $m_X - m_\Delta$ (in GeV) parameter space, where single component and multi-component DM frameworks can be realised for degenerate scalar triplet masses $m_{\Delta_1} = m_{\Delta_2} = m_{\Delta_3} = m_\Delta$. In the white region ($2m_X < m_\Delta$), only $X$ can be a single component DM. In the pink region ($m_\Delta/2 < m_X < m_\Delta$), two component DM with $\{X, \Delta_1\}$ is operative. In the green region ($m_X > m_\Delta$), $\{\Delta_1, \Delta_2\}$ forms degenerate two-component DM.

can stop the decays shown in Fig. 4.2. The viability of $\Delta_1$ and $\Delta_2$ as DM are discussed in two possible scenarios: (i) Degenerate triplet scalar ($m_{\Delta_1} = m_{\Delta_2} = m_{\Delta_3} = m_\Delta$), (ii) Non-degenerate triplet scalar ($m_{\Delta_1} \neq m_{\Delta_2} \neq m_{\Delta_3}$).

(a) **Degenerate triplet scalar**: The triplet scalar components can be degenerate in the limit of $f_7 = 0$ [253]. In this limit,

- when $m_\Delta > m_X$:
  - i) $X$ is stable and a DM.
  - ii) $\Delta_2 \to X b\bar{b}$ is always possible with $m_X < m_\Delta$, hence $\Delta_2$ can never be a DM.
  - iii) If $m_\Delta < 2m_X$ then $\Delta_1$ is stable and becomes second DM component.
  - iv) If $m_\Delta > 2m_X$, then $\Delta_1$ decays and is not a DM candidate.
- when $m_\Delta < m_X$:
  - i) By default this implies $m_\Delta < 2m_X$ and hence $\Delta_1$ is stable and a DM.
  - ii) $\Delta_2$ is also stable and acts as second degenerate DM component with $\Delta_1$.

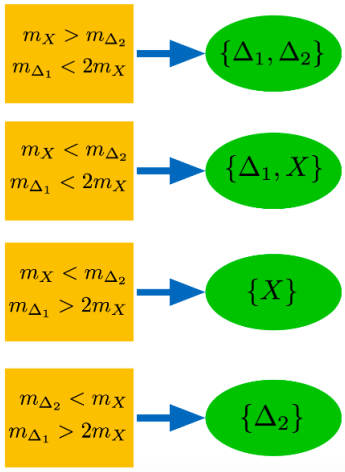


**Figure 4.4:** Main kinematic regions for single and two component DMs for non-degenerate scalar triplet scenario. They are: $\{\Delta_1, \Delta_2\}, \{\Delta_1, X\}, \{X\}, \{\Delta_2\}$.

iii) $X$ can decay into $\Delta_2$ (and subsequently to $\bar{b}b$) so it can not be a DM candidate.

Therefore, when $m_\Delta > m_X$, we can have both two-component (for $m_\Delta < 2m_X$ : $\{X, \Delta_1\}$) and one-component DM scenario (for $m_\Delta > 2m_X$ : $\{X\}$). On the other hand, when $m_\Delta < m_X$, we will have a degenerate 2-component DM scenario comprising of $\Delta_1$ and $\Delta_2$. The above situation for degenerate scalar triplet case is summarised in Fig. 4.3.

(b) **Non-Degenerate triplet scalar**: Non-degenerate scalar triplet scenario ($f_7 \neq 0$) can have four possible DM framework depending on the hierarchy of $m_{\Delta_1}$, $m_{\Delta_2}$, $m_X$. It is quite understood from Figure 4.2, between $\Delta_2$ and X, we can have one of them as a DM, while the possibility of $\Delta_1$ as DM will be guided by the hierarchy between $m_{\Delta_1}$ $vs$ $2m_X$. Therefore, the situations of interest are:

1. $\Delta_1, \Delta_2$ forming non-degenerate DM components : when $m_X > m_{\Delta_2}$ and $m_{\Delta_1} < 2m_X$,
2. $\Delta_1, X$ forming non-degenerate DM components : when $m_X < m_{\Delta_2}$ and $m_{\Delta_1} < 2m_X$
3. $X$ as single component DM: when $m_{\Delta_2} > m_X$, $m_{\Delta_1} > 2m_X$
4. $\Delta_2$ as single component DM: when $m_{\Delta_2} < m_X$, $m_{\Delta_1} > 2m_X$

This is also summarised in Fig. 4.4. We will analyze the degenerate scalar triplet model here for simplicity and economy of parameters. This itself offers a variety of single component $(X)$ or a multi-component interacting DM set-up (in the form of $\{\Delta_1, X\}$ or $\{\Delta_1, \Delta_2\}$).

### 4.4.2 $X$ as single component vector boson DM

$X$ can appear as a single component DM in degenerate scalar triplet case when $m_\Delta > m_X$ and $m_\Delta > 2m_X$. It can also be a single component DM for non-degenerate

scalar triplet case when $m_{\Delta_2} > m_X$ and $m_{\Delta_1} > 2m_X$. The dominant annihilation channels for $X$, shown in Fig. 4.5 are: (i) annihilation to heavy scalars ($\zeta$), (shown in the upper panel) and (ii) annihilation to the SM through Higgs portal (shown in the lower panel). Throughout the analysis, all the annihilation cross sections are calculated on threshold: $s_0 = 4m_X^2$ as the $s$-wave contribution is non-zero. The total annihilation cross section of $X$ can be found in Appendix. B.0.1 (Eq. (B.2)).

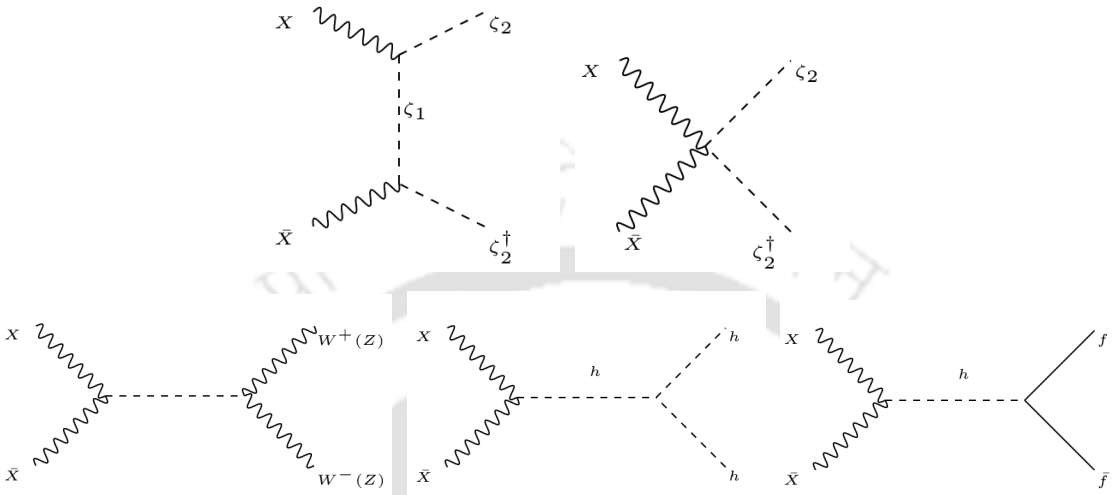


**Figure 4.5:** Top: Annihilation of $X$ DM into heavy scalar $\zeta_2, \zeta_2{}^\dagger$ via $t$-channel mediation of $\zeta_1$ and four pint interaction assuming $m_{\zeta_2} < m_X < m_{\zeta_1}$. Bottom: Annihilation of $X$ into SM via Higgs mediation in $s$-channel.

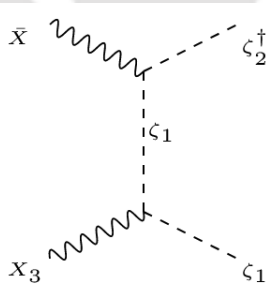


**Figure 4.6:** Co-annihilation of $X$ with $X_3$ to $\zeta_1\zeta_2^\dagger$ for $\frac{1}{2}(m_{\zeta_1} + m_{\zeta_2}) < m_X < m_{\zeta_1} + m_{\zeta_2}$ (see text for details).

Importantly, $X$ can undergo co-annihilation with $X_3$ via the diagram shown in Fig. 4.6. The effective cross section in this case can be written as:

$$\langle\sigma v\rangle_{\text{eff}} = \langle\sigma v\rangle_{X\bar{X}\to SM,\ \zeta_2\zeta_2^\dagger} + \langle\sigma v\rangle_{\bar{X}X_3\to\zeta_1\zeta_2^\dagger+hc}\left(1+\frac{\Delta m}{m_X}\right)^{\frac{3}{2}}\exp(-\Delta m\, x/m_X), \quad (4.10)$$

where $\Delta m = m_{X_3} - m_X$ and $x = \frac{m_X}{T}$. For co-annihilation to occur:

$$m_{\zeta_1} + m_{\zeta_2} < m_X + m_{X_3} \implies m_X > \frac{1}{2}(m_{\zeta_1} + m_{\zeta_2}),$$

in the limit $m_X \sim m_{X_3}$. Again, for stability of $X$:

$$m_X < m_{\zeta_1} + m_{\zeta_2}.$$

Together, we have the following condition:

$$\frac{1}{2}\left(m_{\zeta_1} + m_{\zeta_2}\right) < m_X < m_{\zeta_1} + m_{\zeta_2}. \tag{4.11}$$

We would once again remind that co-annihilation contributions become very important in this model as $\Delta m = m_{X_3} - m_X \to 0$. This happens for small $u_3$ ($\sim$ MeV), which is required for neutrino mass generation with heavy neutrinos of the order of hundreds of GeVs, as discussed earlier.

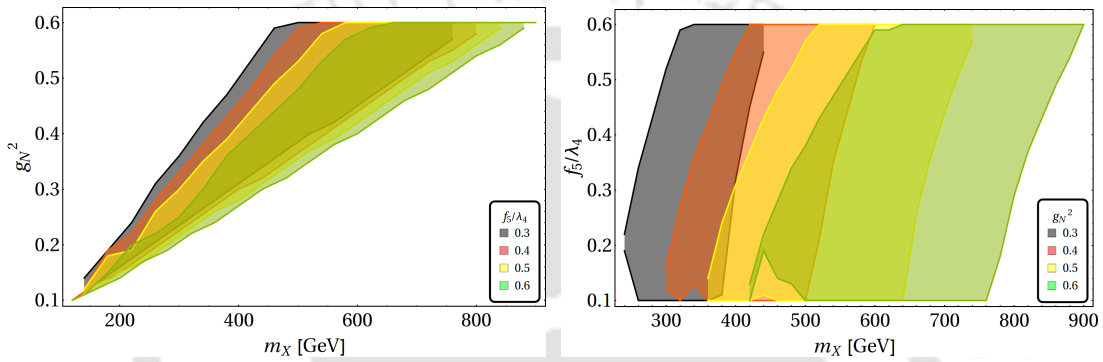


**Figure 4.7:** Relic density allowed parameter space for $X$ as a single component DM. On the left panel, allowed $m_X - g_N^2$ parameter space is shown for different $f_5/\lambda_4$; and on the right panel, $m_X - f_5/\lambda_4$ allowed parameter space is shown for different choices of $g_N^2$.

With these kinematic conditions, we will now proceed to scan the relic density allowed parameter space of single component $X$ in two different regions: (i) $m_{\zeta_1} > m_X > m_{\zeta_2}$ and (ii) $m_X < m_{\zeta_{2,1}}$. In the first case, annihilation occurs to the heavy scalar $\zeta_2$ and to SM, while in the second the annihilation occurs only to SM. The free parameters for the DM analysis can be chosen as:

$$\left\{g_N^2, \frac{f_5}{\lambda_4}, m_X, m_{\zeta_1}, m_{\zeta_2}\right\}. \tag{4.12}$$

Both the couplings are varied in the range $\{g_N^2$: 0.01-0.6$\}$ and $\{\frac{f_5}{\lambda_4}$: 0.01-0.6$\}$ for scanning the parameter space. The relic density (PLANCK data: $0.1165 \leq \Omega h^2 \leq 0.1227$) allowed parameter space for X is shown in Fig. 4.7. On the left panel, we have shown the allowed parameter space in terms of $m_X$ (in GeV) versus $g_N^2$ for different choices of $\frac{f_5}{\lambda_4}$. On the right panel, we show it in terms of $m_X$ (in GeV) versus $\frac{f_5}{\lambda_4}$ for different choices of $g_N^2$. First of all, we see that for larger $g_N^2$, we obtain a larger range of DM mass, that can satisfy relic density constraints. On the other hand, we see that the effect of $\frac{f_5}{\lambda_4}$ is milder than $g_N^2$. Essentially this is due to the fact that the t-channel annihilation of the DM to the heavy scalars ($\zeta_2$) is larger than the s-channel annihilation to SM particles through Higgs mediation. Low DM mass is favored by smaller $\{g_N^2, \frac{f_5}{\lambda_4}\}$. For the same reason, $g_N^2$ or $f_5/\lambda_4$ need to be as large as $\sim 0.6$ for DM mass $\sim 1$ TeV.

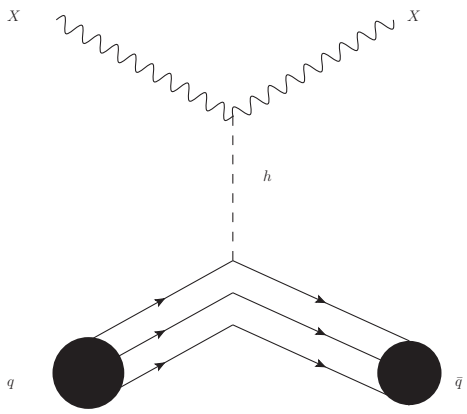


**Figure 4.8:** Direct search diagram for vector boson DM X.

The direct detection interaction for $X$ occurs via $t$-channel Higgs mediation as shown in Fig. 4.8. The spin-independent direct detection cross section scattering off a nucleus with $Z$ protons and $A - Z$ neutrons normalized to one nucleon is given by:

$$\sigma^{\rm SI} = \frac{1}{\pi}\left(\frac{m_N}{m_X + Am_N}\right)^2 \left(\frac{Zf_p + (A-Z)\,f_n}{A}\right)^2, \tag{4.13}$$

where $f_p$ and $f_n$ are the form factors given by [256]

$$\frac{f_p}{m_p} = -0.152\left[\frac{g_N^2\,(f_5/\lambda_4)}{4m_h^2}\right] - 0.848\left[\frac{g_N^2\,(f_5/\lambda_4)}{54m_h^2}\right] \tag{4.14}$$

$$\frac{f_n}{m_n} = -0.155\left[\frac{g_N^2\,(f_5/\lambda_4)}{4m_h^2}\right] - 0.845\left[\frac{g_N^2\,(f_5/\lambda_4)}{54m_h^2}\right] \tag{4.15}$$

where we used:

$$\frac{f_N}{m_N} = \left[\sum_{u,d,s} f_q^N + \frac{2}{27}\left(1 - \sum_{u,d,s} f_q^N\right)\right]\left[\frac{g_N^2\,(f_5/\lambda_4)}{4m_h^2}\right] \tag{4.16}$$

The above equations yield a bound on $f_5/\lambda_4$ from non-observation of $X$ in direct search experiment for a given $g_N^2$. Spin independent direct search cross-section for relic density allowed parameter space for the single component $X$ DM is shown in Fig. 4.9, as a function of DM mass, where $m_{\zeta_1} > m_X > m_{\zeta_2}$. On the upper panel, we show $g_N^2$ dependence through different colour shades, while on the lower panel, we show the dependence on $\frac{f_5}{\lambda_4}$ through different colour shades. The exclusion limit from PandaX is shown by the black dashed line and future limit from XENONnT [257] is also shown by the black dot-dashed line. We see that single component $X$ DM fits nicely between these two curves, giving this model a chance to be discovered by future direct search experiments. Note that $g_N^2$ has low sensitivity to the direct search cross-sections as the constant $g_N^2$ planes are placed horizontally along larger DM mass. On the other hand, constant $\frac{f_5}{\lambda_4}$ planes are stacked vertically, yielding larger direct search cross-sections for larger $\frac{f_5}{\lambda_4}$.

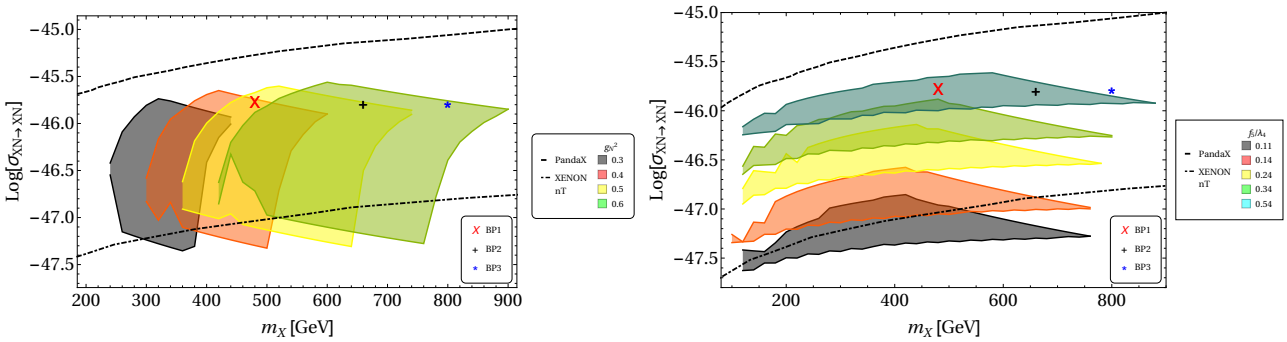


**Figure 4.9:** Spin independent direct search cross-section for relic density allowed parameter space for a single component $X$. Top: different $g_N^2$ regions are shown with different colours. Bottom: different $f_5/\lambda_4$ regions are shown. The exclusion limit from PandaX and future limit from XENONnT are shown through black dashed and black dot-dashed lines respectively.

Finally, we tabulate some benchmark points (BP) in Tab. 4.1, which satisfy both relic density and direct search constraints. These BPs will be used further for the collider analysis in section 4.5.

| Benchmark Point | $g_N$ | $\frac{f_5}{\lambda_4}$ | $m_X$ (GeV) | $m_{\zeta_2}$ (GeV) | $m_{\zeta_1}$ (GeV) | $m_{n_{1R}}$ (GeV) | $\Omega_X h^2$ | $\sigma^X_{DD}$ $(cm^2)$ | $\Omega_{n_{1,2}} h^2$ |
|---|---|---|---|---|---|---|---|---|---|
| BP1 | 0.64 | 0.56 | 480 | 330 | 620 | 450 | 0.12 | $10^{-45.7802}$ | 0.004 |
| BP2 | 0.70 | 0.60 | 660 | 350 | 700 | 450 | 0.12 | $10^{-45.7918}$ | 0.004 |
| BP3 | 0.77 | 0.59 | 800 | 410 | 820 | 450 | 0.12 | $10^{-45.7839}$ | 0.004 |

**Table 4.1:** Choices of the benchmark points used for collider analysis. Masses, couplings, relic density and direct search cross-sections for the DM candidates are tabulated where $2m_\Delta > m_X > m_\Delta$. $X$ has dominant contribution to relic density, while a subdominant contribution comes from $n_{1,2}$.

### 4.4.3 $\Delta_1$ and $X$ as two component DM

$X$ and $\Delta_1$ can form two component DM when $m_X < m_\Delta < 2m_X$ (see Fig. 4.3) in degenerate triplet scenario. First of all here $\Delta_1$ can additionally annihilate to $X\bar{X}$ (upper panel of Fig. 4.10), which was not accessible earlier when $m_\Delta < m_X$. This DM-DM conversion will play a crucial role in this region of the parameter space as we will elaborate. The annihilation cross-section for $\Delta_1$ will include the contributions from these additional graphs that appear in Appendix. B.0.1 (Eq. (B.3)).

The parameters for DM analysis in this case are given by:

$$\{g_N^2, f_8, m_\Delta, m_X\}. \tag{4.17}$$

As we have already elucidated before, the BEQ can be expressed in terms of the dimensionless quantity $x = m/T$, where $m$ is the mass of the DM. However, in the two-component case, we have a coupled Boltzmann equation, due to DM-DM interactions. Here, using a common $x$ is problematic since now there are two DM

candidates with different masses: $\{m_\Delta, m_X\}$. This issue did not arise in the previous case of $\Delta_1, \Delta_2$ as they were degenerate and did not have an effective DM-DM interactions. The way-out for this non-degenerate scenario is to introduce a reduced mass: $\mu = \frac{m_\Delta m_X}{m_\Delta + m_X}$, in terms of which the BEQs read [258]:

$$\frac{dy_1}{dx} = A\left[\langle\sigma v_{\Delta\Delta^*\to SMSM}\rangle\left(y_1^2 - y_1^{EQ^2}\right) + \langle\sigma v_{\Delta\Delta^*\to X\bar{X}}\rangle\left(y_1^2 - \frac{y_1^{EQ^2}}{y_2^{EQ^2}}y_2^2\right)\right],$$

$$\frac{dy_2}{dx} = A\left[\langle\sigma v_{X\bar{X}\to SMSM}\rangle\left(y_2^2 - y_2^{EQ^2}\right) - \langle\sigma v_{\Delta\Delta^*\to X\bar{X}}\rangle\left(y_1^2 - \frac{y_1^{EQ^2}}{y_2^{EQ^2}}y_2^2\right)\right], \tag{4.18}$$

where $A = -0.264\, M_{PL}\sqrt{g_*}\frac{\mu}{x^2}$ and the equilibrium distribution, recast in terms of $\mu$ has the form:

$$y_i^{EQ}(x) = 0.145\frac{g}{g_*}x^{3/2}\left(\frac{m_i}{\mu}\right)^{3/2} e^{-xm_i/\mu}, \tag{4.19}$$

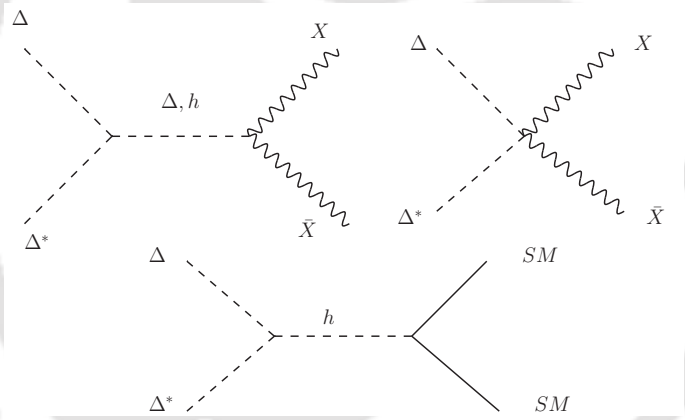


**Figure 4.10:** Annihilation of $\Delta_1$ to $X$ and SM when $m_X < m_\Delta < 2m_X$.

with $i \in (X, \Delta)$. The relic density allowed parameter space of this two component model is shown in Fig. 4.11. In the left panel, we show the allowed region in $m_X - g_N^2$ plane while the colour shades indicate $\Omega_X/\Omega_T$. The right panel shows a similar graph in $m_\Delta - g_N^2$ plane while the colour shades indicate the fraction of $\Delta$ DM in total abundance $\Omega_\Delta/\Omega_T$. The main take from these two graphs are that, the relic density is dominated here by the $X$ component. This can be explained simply as $X$ is the lighter component, it has less annihilations to the SM. On the contrary, larger annihilations of $\Delta$ compared to $X$, depletes the abundance of this component down to $20\%$ of the total.

In the LHS of Fig. 4.12 we show the fate of $\Delta$ in direct search plane, where in the x-axis we have $m_\Delta$ (GeV) and along y-axis we have effective spin-independent direct search cross section $\left(\frac{\Omega_\Delta}{\Omega_T}\right)\times\sigma_{\Delta N\to\Delta N}$ in log-scale. Here different colour shades represent different values of $f_8 : \{0.01, 0.03, 0.05, 0.09\}$ chosen for the scan. We can see that except for the low mass region of $\Delta$ ($m_\Delta \leq 250$ GeV) for $f_8 = 0.09$, the whole

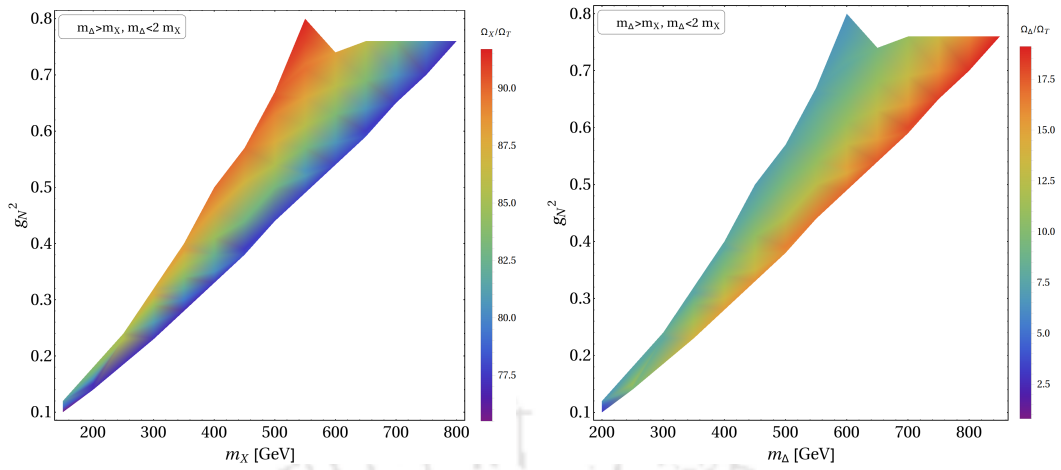


**Figure 4.11:** Left: Relic density allowed parameter space for two component DM set-up in $m_X - g_N^2$ plane, where the colour shades indicate $\Omega_X/\Omega_T$. Right: Same in $m_\Delta - g_N^2$ plane, where the colour shades indicate $\Omega_\Delta/\Omega_T$.

relic density allowed parameter space is available through direct search constraints. It is easy to understand that the higher the values of $f_8$, the higher is the effective direct search cross-section is. Therefore, direct search crucially tames the coupling $f_8 \leq 0.1$.

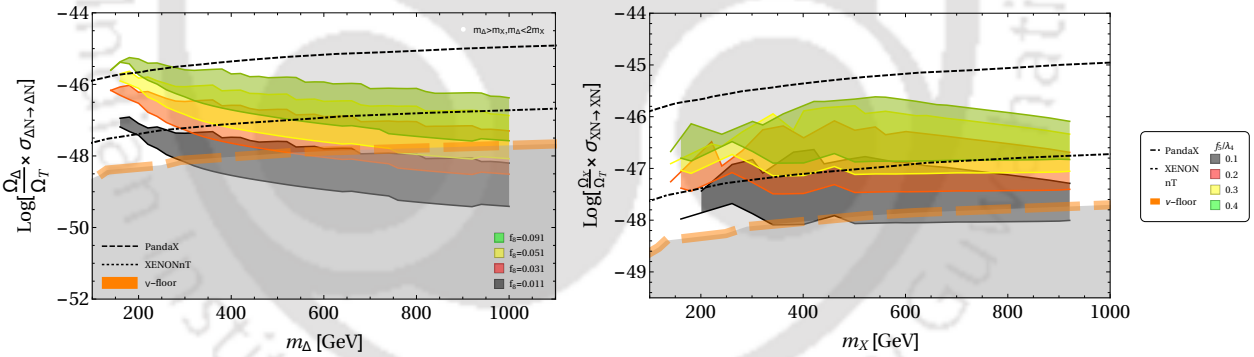


**Figure 4.12:** LHS: Spin independent effective direct search cross-section for $\Delta$, in terms of $m_\Delta$ vs. $Log(\frac{\Omega_\Delta}{\Omega_T} \times \sigma_{\Delta N \to \Delta N})$, when it is a part of two component dark matter scenario with DM : $\{\Delta, \mathrm{X}\}$. Allowed region of relic density parameter space have been divided into different $f_8$ values. RHS: Same for $X$ in terms of $m_X$ vs. $Log\,(\frac{\Omega_X}{\Omega_T} \times \sigma_{XN \to XN})$, where different coloured regions correspond to different values of $f_5/\lambda_4$. In both the plots the bound from PANDA, future sensitivity of XENONnT and neutrino floor are depicted.

In the RHS of Fig. 4.12 we show the parameter space allowed by relic density and direct search for $X$ in the two-component DM scenario. All of the parameter space allowed by relic density lies below the PandaX limit and a part of it even goes below the neutrino floor [64]. Different coloured regions in this plot correspond to different values of $f_5/\lambda_4$, which typically controls the direct detection cross-section of $X$ as discussed earlier. As expected, smaller values of $f_5/\lambda_4$ (shown for example by the black region) produces smaller cross-section, while a larger $f_5/\lambda_4$ is ruled out by XENONnT.

| Benchmark Point | $g_N$ | $\frac{f_5}{\lambda_4}$ | $m_X$ (GeV) | $m_{\zeta_2}$ (GeV) | $m_{\zeta_1}$ (GeV) | $m_\Delta$ (GeV) | $\Omega_X h^2$ | $\Omega_\Delta h^2$ | $\sigma^\Delta_{DD}$ $(cm^2)$ | $\sigma^X_{DD}$ $(cm^2)$ |
|---|---|---|---|---|---|---|---|---|---|---|
| BP4 | 0.63 | 0.30 | 481 | 320 | 621 | 500 | 0.077 | 0.043 | $10^{-50}$ | $10^{-46.35}$ |
| BP5 | 0.70 | 0.10 | 541 | 380 | 701 | 560 | 0.079 | 0.037 | $10^{-50}$ | $10^{-47.20}$ |
| BP6 | 0.83 | 0.20 | 681 | 540 | 821 | 700 | 0.087 | 0.033 | $10^{-50}$ | $10^{-46.47}$ |

**Table 4.2:** Choices of the benchmark points (BPs) for two-component $\{X,\Delta\}$ DM scenario. Masses, couplings, relic density and direct search cross-sections for both the DM candidates are tabulated.

In Tab. 4.2 we have tabulated possible values of masses of the dark gauge boson and triplet scalar for different couplings satisfying relic density and direct search for two-component DM scenario $\{\Delta_1,X\}$. As the collider signature of the model is independent of the choice of $m_\Delta$ and dependent only on the masses of the charged scalars $\{\zeta_1^\pm,\zeta_2^\pm\}$, the model would give rise to the same final states as that of single component vector boson DM framework as the mass hierarchy between $X$ and $\zeta$ remains unaltered.

## 4.5 Collider Phenomenology

Out of all the BSM particles introduced in the model, only the scalar bi-doublet $\zeta$ transforms under SM $SU(2)_L$, and one can produce both the charged $(\zeta^\pm_{1,2})$ and neutral components $(\zeta^0_{1,2})$ at the collider. The Feynman graphs for the production of such particles in the Large Hadron Collider (LHC) is shown in Fig. 4.13. These processes involve derivative couplings arising from the gauge kinetic term. Here we have elucidated two different processes which yield leptonic final states. One possibility is the charged current production of $\zeta_1^\pm,\zeta_1^0$ shown in the left panel of Fig. 4.13, and the other possibility is to have a neutral current production of $\zeta_1^\pm,\zeta_1^\mp$. Subsequent decays of these scalars to SM fermions and to RHN $n_{1R}$ via the Yukawa interactions enlisted in Eq. (4.5), are also shown in the figure. Here we assume the same mass hierarchy as chosen for DM phenomenology: $m_{\zeta_2} < m_X < m_{\zeta_1}$ and $m_{n_{1R}} < m_{\zeta_1}$. In such a hierarchy, the decay of the scalar bi-doublet components occur with 100 % branching ratios to the final states: $\zeta_1^\pm \to \ell^\pm n_{1R}$ and $\zeta_1^0 \to \nu n_{1R}$.

### 4.5.1 Signals at the LHC

Following the mass hierarchy, the production of the scalar bi-doublets at LHC will end up with two different leptonic final states:

- Single lepton plus missing energy $\left(1\ell^\pm + \not{E}_T\right)$ due to charged current interaction, as shown in the left panel of Fig. 4.13.
- Opposite sign di-lepton plus missing energy (OSD+$\not{E}_T$) due to neutral current interaction, as shown in the right panel of Fig. 4.13.

These channels are essentially hadronically quiet, as they contain no jets at the parton level, except for those which may arise due to initial state radiation (ISR). We will therefore focus only on the leptonic final states with zero jet veto, as we

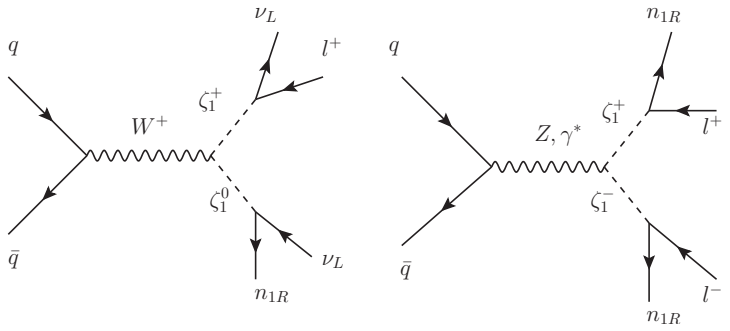


**Figure 4.13:** Figure showing production of heavy charged scalars and their subsequent decays into a hadronically quiet single lepton $\ell^\pm + \not{E}_T$ channel (on left) and hadronically quiet opposite sign dilepton channel $\ell^+\ell^- + \not{E}_T$ on right.

know, they are cleaner and suffer less from SM background contamination. We will analyze these two hadronically quiet lepton channels in details for the chosen benchmark points (BPs) as in Tab. 4.1. We also note here, that the right handed neutrinos are stable for the chosen hierarchy, and hence contribute to missing energy. As has already been stated, given the interactions proposed in this model, the other two DMs, namely $\Delta, X$ are harder to produce, if not impossible. Before proceeding further we would also like to note, since both $\zeta_1$ and $\zeta_2$ belong to the same bi-doublet, $\zeta_2^\pm, \zeta_2^0$ can also be produced in the collider via similar diagrams. But since $\zeta_2^0$ mixes with SM Higgs, it decays to $b\bar{b}$, while the charged companion will decay $\zeta_2^\pm \to \zeta_2^0 \ell^\pm \nu$ through off-shell $W$.

### 4.5.2 Event selection criteria

The details of the simulation methodology and the definition of re-constructed leptons and jets, along with different observables are elaborated in Appendix. C. For the backgrounds, the contribution to MET comes from the neutrinos, while for the signal, it comes dominantly from the stable RHN (as shown in Fig. 4.13). The MET distribution for the chosen BPs are plotted in the upper panel of Fig. 4.14 for single lepton and in Fig. 4.15 for OSD final states. Corresponding $H_T$ distributions are also shown in the lower panel of the same figures. In both cases, the dominant SM backgrounds are also shown. As it is clear from both Fig. 4.14 and Fig. 4.15, a high MET cut can reduce SM background, while retaining some of the signal strength in both single and two lepton channels. This is also true for $H_T$-cut as well. Therefore, the final state event selection required to have the following selection criteria on top of the trigger level cuts:

- Missing energy cut of $\not{E}_T > 100$, 200 and 300 GeV have been employed in both single and two-lepton cases to reduce SM backgrounds.
- $H_T$ cut of 200 and 300 GeV are also applied on top of MET cut to reduce the backgrounds further.
- For OSD events, an invariant mass cut over the $Z$-window $|m_z - 15| < m_{ll} < |m_Z + 15|$ has been applied to get rid-off the $ZZ$ background to a significant extent.

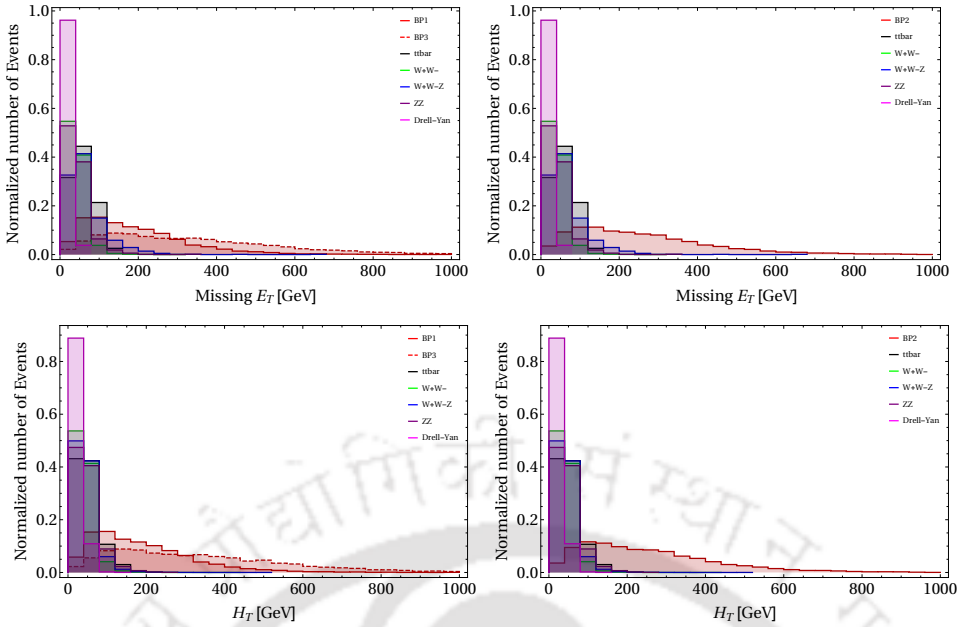


**Figure 4.14:** Top: Missing energy distribution for $1\ell^{\pm} + \not{E}_T$ final state for the benchmark points (BP1, BP2, BP3) are shown in red. Those of the dominant SM backgrounds are also shown. Bottom: $H_T$ distribution for the same. The simulation is done assuming LHC with $\sqrt{s} = 14$ TeV.

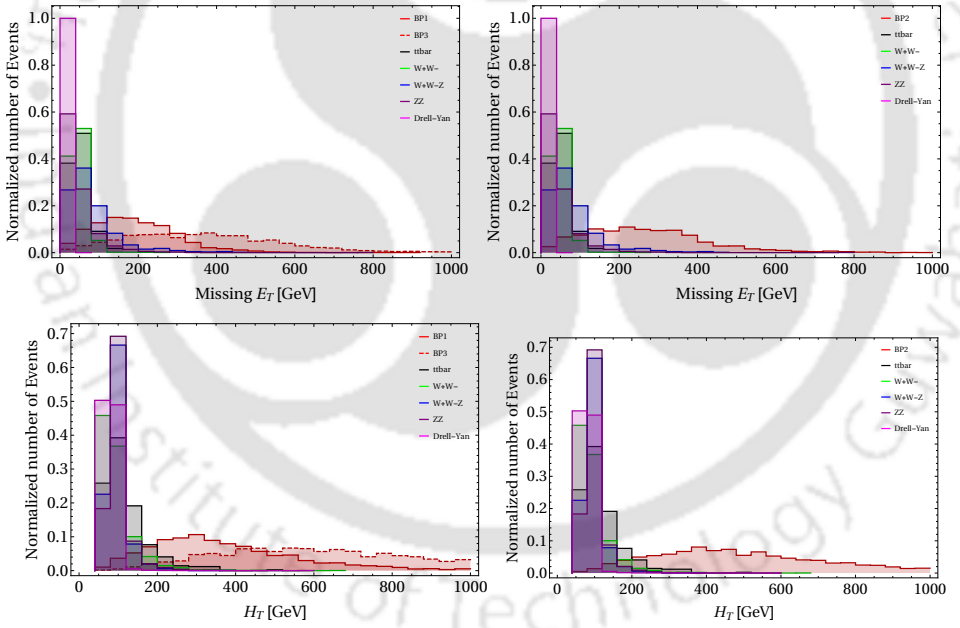


**Figure 4.15:** Top: Missing energy distribution for $\ell^{\pm}\ell^{\mp} + \not{E}_T$ final state for the benchmark points (BP1, BP2, BP3) are shown in red. Those of the dominant SM backgrounds are also shown. Bottom: $H_T$ distribution for the same. The simulation is done assuming LHC with $\sqrt{s} = 14$ TeV.

### 4.5.3 Event rates for the signal and the SM background

Cross sections of $1\ell^{\pm} + \not{E}_T$ and $\ell^{\pm}\ell^{\mp} + \not{E}_T$ channels and corresponding number of events at a luminosity $\mathcal{L} = 100\ fb^{-1}$ for $E_{CM} = 14$ TeV at the LHC are listed in Tab. 4.3 for the Benchmark points (BP1, BP2, BP3). Here, the production cross-sections are also mentioned, so that we see the sensitivity of the missing energy cut as has been used with $\not{E}_T > 100,\ 200,\ 300$ GeVs.

| Benchmark Point | $\sigma_{\zeta_1^\pm\zeta_1^0}$ (fb) | $\sigma_{\zeta_1^0\bar{\zeta}_1^0}/\sigma_{\zeta_1^+\zeta_1^-}$ (fb) | $\not{E}_T$ (GeV) | $H_T$ (GeV) | $\sigma^{\ell\pm}$ (fb) | $N_{\rm eff}^{\ell\pm}$ | $\sigma^{\rm OSD}$ | $N_{\rm eff}^{\rm OSD}$ |
|---|---|---|---|---|---|---|---|---|
| BP1 | 1.89 | 1.29 | >100 | > 100 | 0.25 | 25 | 0.04 | 4 |
| | | | | > 200 | 0.14 | 14 | 0.04 | 4 |
| | | | | > 300 | 0.06 | 6 | 0.03 | 3 |
| | | | >200 | > 100 | 0.15 | 15 | 0.02 | 2 |
| | | | | > 200 | 0.14 | 14 | 0.02 | 2 |
| | | | | > 300 | 0.06 | 6 | 0.01 | 1 |
| | | | >300 | > 100 | 0.06 | 6 | 0 | 0 |
| | | | | > 200 | 0.06 | 6 | 0 | 0 |
| | | | | > 300 | 0.06 | 6 | 0 | 0 |
| BP2 | 1.16 | 0.81 | >100 | > 100 | 0.17 | 17 | 0.03 | 3 |
| | | | | > 200 | 0.12 | 12 | 0.03 | 3 |
| | | | | > 300 | 0.07 | 7 | 0.02 | 2 |
| | | | >200 | > 100 | 0.12 | 12 | 0.02 | 2 |
| | | | | > 200 | 0.11 | 11 | 0.02 | 2 |
| | | | | > 300 | 0.07 | 7 | 0.02 | 2 |
| | | | >300 | > 100 | 0.07 | 7 | 0.01 | 1 |
| | | | | > 200 | 0.07 | 7 | 0.01 | 1 |
| | | | | > 300 | 0.07 | 7 | 0.01 | 1 |
| BP3 | 0.59 | 0.43 | >100 | > 100 | 0.09 | 9 | 0.02 | 2 |
| | | | | > 200 | 0.07 | 7 | 0.02 | 2 |
| | | | | > 300 | 0.05 | 5 | 0.02 | 2 |
| | | | >200 | > 100 | 0.07 | 7 | 0.01 | 1 |
| | | | | > 200 | 0.07 | 7 | 0.01 | 1 |
| | | | | > 300 | 0.05 | 5 | 0.01 | 1 |
| | | | >300 | > 100 | 0.05 | 5 | 0.01 | 1 |
| | | | | > 200 | 0.05 | 5 | 0.01 | 1 |
| | | | | > 300 | 0.05 | 5 | 0.01 | 1 |

**Table 4.3:** Signal events with $\sqrt{s} = 14$ TeV at the LHC for luminosity $\mathcal{L} = 100\ fb^{-1}$ for benchmark points (BP1, BP2, BP3). The variation of number of final state signal events with $\not{E}_T$ and $H_T$ cut-flow are also tabulated.

The first obvious thing to notice is, with heavier masses for the charged bi-doublet scalars for the BPs, the cross-section in both the final states diminishes accordingly due to larger phase space suppression. Secondly, the number of events in OSD is smaller than that of single lepton ones, owing to (i) the hierarchy of the charge current and neutral current production cross-section itself and (ii) those cases, where the neutral current production may also yield an effective single lepton event, if one of the leptons is soft and fails to register with the desired $p_T$ cut. The production cross-section is small for all the BPs, and so is the numbers of expected events at a luminosity as high as $\sim 100\,\text{fb}^{-1}$. We define the effective number of final state events as:

$$N_{\rm eff} = \frac{\sigma_{\rm p} \times n}{N} \times \mathcal{L}, \tag{4.20}$$

where $n$ is the simulated number of events obtained by simulating $N$ events corresponding to production cross-section of $\sigma_p$ and $\mathcal{L}$ is the integrated luminosity. Using the same selection criteria, the number of final state events for dominant SM backgrounds are tabulated in Tab. 4.4. Here we have multiplied the cross section in leading order (LO) with the appropriate $K$-factors to obtain the cross section

| Process | $\sigma_{\text{production}}$ (pb) | $\not{E}_T$ (GeV) | $H_T$ (GeV) | $\sigma^{\ell^\pm}$ (fb) | $N_{\text{eff}}^{\ell^\pm}$ | $\sigma^{\text{OSD}}$ | $N_{\text{eff}}^{\text{OSD}}$ |
|---|---|---|---|---|---|---|---|
| $t\bar{t}$ | 814.64 | >100 | >100 | 22.80 | 2280 | 17.10 | 1710 |
| | | | >200 | 1.62 | 162 | 2.44 | 244 |
| | | | >300 | $< 0.81$ | $< 1$ | $< 0.81$ | <1 |
| | | >200 | $>100$ | 1.62 | 162 | $< 0.81$ | $< 1$ |
| | | | >200 | 0.81 | 81 | $< 0.81$ | $< 1$ |
| | | | >300 | $< 0.81$ | $< 1$ | $< 0.81$ | $< 1$ |
| | | >300 | $>100$ | $< 0.81$ | $< 1$ | $< 0.81$ | $< 1$ |
| | | | >200 | $< 0.81$ | $< 1$ | $< 0.81$ | $< 1$ |
| | | | >300 | $< 0.81$ | $< 1$ | $< 0.81$ | $< 1$ |
| $W^+W^-$ | 99.98 | >100 | $>100$ | 54.48 | 5448 | 20.49 | 2049 |
| | | | >200 | 3.99 | 399 | 9.99 | 999 |
| | | | >300 | 0.49 | 49 | 1.99 | 199 |
| | | >200 | $>100$ | 1.99 | 199 | 1.99 | 199 |
| | | | >200 | 0.49 | 49 | 1.99 | 199 |
| | | | >300 | 0.49 | 49 | 0.49 | 49 |
| | | >300 | $>100$ | 0.49 | 49 | $< 0.49$ | $< 1$ |
| | | | >200 | 0.49 | 49 | $< 0.49$ | $< 1$ |
| | | | >300 | 0.49 | 49 | $< 0.49$ | $< 1$ |
| $W^\pm Z$ | 0.15 | >100 | $>100$ | 0.14 | 14 | 0 | 0 |
| | | | >200 | 0.01 | 1 | 0 | 0 |
| | | | >300 | 0 | 0 | 0 | 0 |
| | | >200 | >100 | 0.012 | 1 | 0 | 0 |
| | | | >200 | 0 | 0 | 0 | 0 |
| | | | >300 | 0 | 0 | 0 | 0 |
| | | >300 | $>100$ | 0 | 0 | 0 | 0 |
| | | | >200 | 0 | 0 | 0 | 0 |
| | | | >300 | 0 | 0 | 0 | 0 |
| $ZZ$ | 14.01 | >100 | >100 | 7.07 | 707 | 0.21 | 21 |
| | | | >200 | 0.35 | 35 | 0.14 | 14 |
| | | | >300 | $< 0.07$ | $< 1$ | 0.07 | 7 |
| | | >200 | $>100$ | 0.35 | 35 | $< 0.07$ | $< 1$ |
| | | | >200 | 0.28 | 28 | $< 0.07$ | $< 1$ |
| | | | >300 | $< 0.07$ | $< 1$ | $< 0.07$ | $< 1$ |
| | | >300 | >100 | $< 0.07$ | $< 1$ | $< 0.07$ | $< 1$ |
| | | | >200 | $< 0.07$ | $< 1$ | $< 0.07$ | $< 1$ |
| | | | >300 | $< 0.07$ | $< 1$ | $< 0.07$ | $< 1$ |

**Table 4.4:** SM background events at $\sqrt{s} = 14$ TeV for luminosity $\mathcal{L} = 100\ fb^{-1}$ at the LHC. The cross sections have been multiplied by the appropriate $K$-factors to match with their NLO order cross-section (see text for details). The variation of number of final state background events with $\not{E}_T$ and $H_T$ cut-flow are also tabulated.

in the NLO approximation. The $K$-factors for the different SM processes are chosen as [252]: for $t\bar{t}:\ K = 1.47, WW:\ K = 1.38, WZ:\ K = 1.61, ZZj:\ K = 1.33, Drell\text{-}Yan:\ K = 1.2$. Again, in Tab. 4.4, we show that we can reduce SM backgrounds to a significant extent, by employing the MET cut. However, for $\not{E}_T > 100, 200$ GeV, a significant number of events are still left from $W^+W^-$ final state. This can only

be reduced with $\not{E}_T > 300$ GeV for two lepton but single lepton case will still be submerged under a large $W^+W^-$ background events.

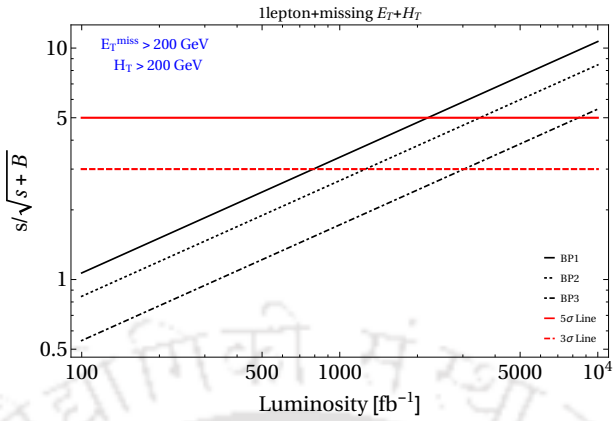


**Figure 4.16:** Significance plot for the signal $1\ell^{\pm} + \not{E}_T$ events for the chosen benchmark points in terms of luminosity. The red solid (dashed) line shows the $5\sigma$ $(3\sigma)$ discovery limit.

From this analysis it is evident that, although it is possible to eliminate or at least reduce the SM background with judicious choice of different cuts, but as the production cross section for the signals itself is very low, it is only possible to see such a signal at the LHC at a very high integrated luminosity for both single lepton and opposite-sign-dilepton cases. And as it is evident from Tab. 4.3, the OSD case is even harder to probe at LHC. In Fig. 4.16, we show the significance for the single lepton channel only. As it is seen, with $\not{E}_T > 200$ GeV and $\not{H}_T > 200$ GeV (which removes most of the backgrounds), the significance reaches the discovery limit $(5\sigma)$ at a luminosity of $\gtrsim 1000\ fb^{-1}$. As the OSD case fails to reach at least $3\sigma$ confidence even at $\gtrsim 1000$ fb$^{-1}$ luminosity, we are not showing its discovery potential.

## 4.6 Summary

The model of our interest in this chapter is an $SU(2)_N$ gauge extension of the SM, where the lightest vector boson $X$ is stabilized by an unbroken $S$ charge arising from $SU(2)_N \times S' \to S$ through spontaneous symmetry breaking. We assume symmetry $S$ remains intact up to the Planck scale to avoid constraints coming from CMB, Gamma ray, neutrino flux etc due to the DM decay. The model offers a multipartite DM framework, involving the scalar triplet $\Delta$ and heavy neutrinos, depending on the kinematics. We highlighted the role of DM-DM interactions to govern thermal freeze-out of the heavier component. For example, when $\{\Delta, X\}$ can both be DM, we show that $X$ always has the larger part of relic density while obeying DD bound (thanks to its annihilation to non-SM particles). $\Delta$ being heavier in such a case, can annihilate to $X$ yielding a larger annihilation cross-section and smaller relic density. However, as the freeze-out is mainly governed by DM-DM interaction, it is saved from direct search.

We have explored the collider signal of this model framework and see that this model might manifest itself through hadronically quiet leptonic final states along with missing energy at LHC. We note here, that as no SM particle are charged under the additional $SU(2)_N$, the phenomenology is in sharp contrast to what we discussed

in previous chapter [245]. The leptonic signals arise from the production and subsequent decays of the scalar bi-doublets present in the theory. Although, the missing energy (MET) and $H_T$ allows us to separate the signal from the SM background, the small strength of EW production cross-section does only allow it to be explored at large luminosity regime.

The model also addresses the generation of neutrino masses through inverse see-saw mechanism by assuming the presence of heavy chiral neutrinos $(n_1, n_2)$. The proportionality of neutrino mass to the vev $\langle\Delta_3\rangle$, requires it to have a small value thus making the vector boson $(X)$ degenerate with $X_3$. This predicts additional contribution to the thermal freeze-out of $X$ DM through $X - X_3$ co-annihilation. Hence the model offers a very interesting connection between the neutrino sector and DM phenomenology.

Chapter 5

# Non-Abelian Vector Boson Dark Matter via freeze-in

## Contents



## 5.1 Introduction

So far we have discussed the freeze-out aspects of WIMP-like vector boson DM. However, FIMP-like situation is equally probable and offers new phenomenology to explore. This chapter, thus, aims to address the non-thermal *freeze-in* production of a non-abelian vector boson dark matter (DM) in the context of a UV complete model. The particle content and symmetry assignment of the model [253] is exactly same as that appeared in the last chapter where we performed the analysis in the context of freeze-out. Thus, the DM arises in an $SU(2)_N$ extension ($N$ stands for neutral) of the Standard Model (SM) where an additional $U(1) = S^{'}$ global symmetry stabilizes the lightest of the vector boson $(X, \bar{X})$ as DM through unbroken $S = T_{3N} + S^{'}$. The DM $(X, \bar{X})$ in this model is produced from the decay of a scalar bi-doublet $\zeta_1^{0,\pm}$, owing to $SU(2)_N$ interaction[1]. Naturally, the correct relic density of $X, \bar{X}$ via freeze-in indicates that the $SU(2)_N$ gauge coupling needs to be $\sim \mathcal{O}(10^{-10})$. One of the salient features of this study is to show that the contribution to DM production from the decay of $\zeta_1^{0,\pm}$ remains significant even after the freeze-out of $\zeta_1^{0,\pm}$. We point out that such a feature is inevitable whenever the decay is slow enough,

[1] If the decay is kinematically forbidden, then annihilation of $\zeta_1^{0,\pm}$ to produce $(X, \bar{X})$ becomes important.

although not much elaborated in FIMP literature. Moreover, our formulae for computing the yield of the DM from the decay of a decoupled species is actually model-independent, and can be applied to any scenario where the freeze-in production of the DM is taking place via the decay of a heavy particle, which shared a common temperature with the thermal bath in the early universe. The subsequent change in the allowed parameter space due to the 'late decay' turns out to be quite noteworthy [259]. The $SU(2)_N$ scalar triplet ($\Delta$) required for neutrino mass generation also provides with additional DM components in this model. The neutral components of $\Delta$ turn out to be stable at the scale of the universe life time, thanks to the small $SU(2)_N$ gauge coupling in the freeze-in mechanism advocated here. Therefore the model also serves as a multipartite FIMP DM set up, although the DM components do not have sizable interaction with each other. As mentioned in the beginning, the same model from WIMP perspective, has already been thoroughly explored in the last chapter. The present exercise therefore provides an opportunity to compare two different realizations (freeze out versus freeze in) of the same model.

The chapter is organised as follows: in Sec. 5.2 we have provided the details of the model including the symmetry breaking and spectrum of the physical particles that are important for the present phenomenology. Then in Sec. 5.3 we have shown how light neutrino mass can be generated via inverse seesaw mechanism in this framework. Sec. 5.4 contains the main DM analysis under which in subsection 5.4.1 and 5.4.1 we have discussed in detail the yield for $X$ and $\Delta$ by solving the Boltzmann equation (BEQ). In Sec. 5.5 we have shown the possible signatures that this model may yield at the colliders. Finally in Sec. 5.6 we have summarized our findings.

## 5.2 Particle content

| Particles | $SU(3)_c$ | $SU(2)_L$ | $U(1)_Y$ | $SU(2)_N$ | $S'$ |
|---|---|---|---|---|---|
| $X_{1,2,3}$ | 1 | 1 | 0 | 3 | 0 |
| $n = (n_1, n_2)_{L,R}$ | 1 | 1 | 0 | 2 | 1/2 |
| $\chi \equiv (\chi_1, \chi_2)$ | 1 | 1 | 0 | 2 | 1/2 |
| $\zeta \equiv \begin{pmatrix} \zeta_1^0 & \zeta_2^0 \\ \zeta_1^- & \zeta_2^- \end{pmatrix}$ | 1 | 2 | -1/2 | 2 | -1/2 |
| $\Delta \equiv \begin{pmatrix} \Delta_2/\sqrt{2} & \Delta_3 \\ \Delta_1 & -\Delta_2/\sqrt{2} \end{pmatrix}$ | 1 | 1 | 0 | 3 | -1 |
| $\Phi \equiv \begin{pmatrix} \phi^+ \\ \phi^0 \end{pmatrix}$ | 1 | 2 | 1/2 | 1 | 0 |

**Table 5.1:** Relevant particle content of the model and their charges under $SU(3)_c \otimes SU(2)_L \otimes U(1)_Y \otimes SU(2)_N \otimes S'$. $SU(2)_L$ doublets are indicated by vertical parenthesis with $T_{3L} = \pm 1/2$ for up and down components respectively. $SU(2)_N$ doublet is depicted by entries in horizontal parenthesis with $T_{3N} = \pm 1/2$ to left and right fields respectively.

| Particles | $S'$ | $S = S' + T_{3N}$ |
|---|---|---|
| $X(\bar{X})$ | 0 | +1(-1) |
| $X_3$ | | 0 |
| $n_{1L,R}$ | 1/2 | +1 |
| $n_{2L,R}$ | | 0 |
| $\chi_1$ | 1/2 | +1 |
| $\chi_2$ | | 0 |
| $\zeta_1$ | -1/2 | -1 |
| $\zeta_2$ | | 0 |
| $\Delta_1$ | | -2 |
| $\Delta_2$ | -1 | -1 |
| $\Delta_3$ | | 0 |

**Table 5.2:** $S$ charge assignment for the new particles added in the model as introduced in Tab. 5.1.

As mentioned in the beginning, the particle content of the model considered in this chapter is exactly same as that in Chapter. 4. Therefore we refrain from repeating all the details here once more. However, for the reader's ease, the charges of different fields appearing in this model under the prescribed symmetry are mentioned in Tab. 5.1 and Tab. 5.2. The choice of the VEVs and couplings required in the present scenario is mainly dictated by the DM phenomenology. Since in this work we are interested to see the freeze-in aspect of the $SU(2)_N$ vector bosons (as mentioned in Sec. 6.1), we require the gauge coupling $g_N$ to be extremely small ( $\lesssim \mathcal{O}(10^{-10})$) in order to keep the lightest gauge boson out of equilibrium. We will carefully evaluate the correct order of the coupling and explore effects of such small coupling in the DM phenomenology. An immediate consequence of this is that $g_N \lesssim \mathcal{O}(10^{-10})$ results in a very large $u_2 \sim \mathcal{O}(10^{10})$ GeV for $m_X \sim \mathcal{O}(\text{TeV})$. Therefore $v_2 \ll u_2$ and $g_N \ll g_{1,2}$, which ensures small $Z$-$Z^{'}$ mixing [246]. As before, due to the absence of any tree-level coupling of the $Z^{'}$ with the SM, one has the freedom of choosing $m_{Z'}$ as a free parameter. Furthermore, owing to $u_3 \ll u_2$, it is clear that the $X$ boson masses are nearly degenerate, i.e. $m_{Z'}(m_{X_3}) \simeq m_X$.

The minimization conditions corresponding to the VEV hierarchy $u_3, v_1, v_2 \ll u_2$ can be found in Appendix. B.0.2. The VEV $u_2$ being very large, dictates the scalar masses predominantly. Note that $\chi_2$ and $\Delta_{1,2,3}$ are at the same scale as $u_2$. For other scalars, dominant contribution arises from the presence of terms proportional to $\mu_1 u_2 v_1/v_2$ (except the SM Higgs). If we require the masses of these new scalars to be at TeV scale, we should have $m \sim 10\sqrt{\mu_1 u_2} \sim 1$ TeV, which requires $|\mu_1| \lesssim 10^{-9}$ GeV. In that case, $H^+, \eta^0, \xi_2^0$ can all be at $\mathcal{O}(1$ TeV) scale. Without any further assumptions $\Delta_{1,2,3}$, $\xi_1^0$, $\zeta_1^-$, $\chi_2^R$ are all around the $u_2$ scale and very heavy: $\mathcal{O}(10^{13}$ GeV). However, as we will demonstrate, the freeze-in of $X$ is mainly dictated by $\zeta_1^{0,-}$ decays, and

| Scale | $\lvert\mu_1\rvert \lesssim 10^{-9}$ GeV | $\lvert\mu_1\rvert \lesssim 10^{-9}$ GeV, $f_1 = f_2$ |
|---|---|---|
| $\mathcal{O}(10^{13}$ GeV$)$ | $\Delta_{1,2,3}, \zeta_1^-, \xi_1^0, \chi_2^R$ | $\Delta_{1,2,3}, \chi_2^R$ |
| $\mathcal{O}(1$ TeV$)$ | $H^+, \eta^0, \xi_2^0, n_1, n_2$ | $H^+, \eta^0, \xi_1^0, \xi_2^0, \zeta_1^-, n_1, n_2$ |
| $\mathcal{O}(100$ GeV$)$ | $W^\pm, Z, H, t$ | |
| $\mathcal{O}(1$ GeV$)$ | $X, Z', b, c, \tau$ | |
| $\mathcal{O}(< 1$ GeV$)$ | $e, \mu, \nu_e, \nu_\mu, s, u, d$ | |

**Table 5.3:** Spectrum of physical particles appearing at different scales assuming $g_N \sim 10^{-13}$, compatible with freeze-in requirement of $X(\bar{X})$. In the dark matter analysis we will further assume $f_1 \approx f_2$, such that both $\zeta_1^{-,0}$ are brought down to $\sim$ TeV scale.

a large $m_{\zeta_1^{0,-}}$ mass will produce over abundance of the DM. In order to avoid the overabundance of $X$, we need $m_{\zeta_1^{0,-}} \lesssim 10$ TeV; which can be achieved by setting $f_2 = f_1$ and cancelling the over powering $u_2$ term (see Eq. (B.21)). In Tab. 5.3 we have listed the physical particles in our model (including SM) with their corresponding mass scales that fit the freeze-in requirement for the vector boson DM. It is also important to mention here that the correct DM relic density via freeze in of $X$ allows $m_X$ to vary in a large range between few GeV's to few hundred GeV's, but the heavier DM masses are constrained by BBN data. Therefore we have listed them in the range of $\mathcal{O}(1$ GeV$)$ in Tab. 5.3. Similarly, $n_{1,2}$ masses can also be as large as $\sim \mathcal{O}(10^5)$ GeV depending on the Yukawa coupling as we demonstrate in the next section although they have been classified to lie in $\mathcal{O}(1$ TeV$)$ in the Tab. 5.3.

## 5.3 Neutrino mass

As already elaborated in chapter 4, the generation of light neutrino mass is a novel feature of this model addressed together with DM. In principle, the light neutrino mass generation mechanism is independent of DM phenomenology. However, we will take a quick tour of the neutrino sector here and advocate a subtle phenomenological connection to the freeze-in prospect of the DM, in the light of mass scales introduced in Tab. 5.3.

The gauge and $S$ invariant Yukawa terms responsible for neutrino mass generation in this model are given by:

$$f_\zeta \quad \left[\left(\overline{\nu}_L \zeta_1^0 + \overline{e}_L \zeta_1^-\right) n_{1R} + \left(\overline{\nu}_L \zeta_2^0 + \overline{e}_L \zeta_2^-\right) n_{2R}\right] \tag{5.1}$$

$$f_\Delta \quad \left[n_1 n_1 \Delta_1 + \left(n_1 n_2 + n_2 n_1\right) \Delta_2/\sqrt{2} - n_2 n_2 \Delta_3\right]. \tag{5.2}$$

The lepton number is conserved in (5.1) with $n$ carrying $L = 1$, and is broken to lepton parity, i.e. $(-1)^L$ by the $nn$ terms in (5.2). After SSB we have the following mass terms for the neutrinos:

$$f_\zeta \, v_2 \, \overline{\nu}_L n_{2R} - f_\Delta^L \, u_3 \, n_{2L} n_{2L} - f_\Delta^R \, u_3 \, n_{2R} n_{2R} + \text{h.c.}, \tag{5.3}$$

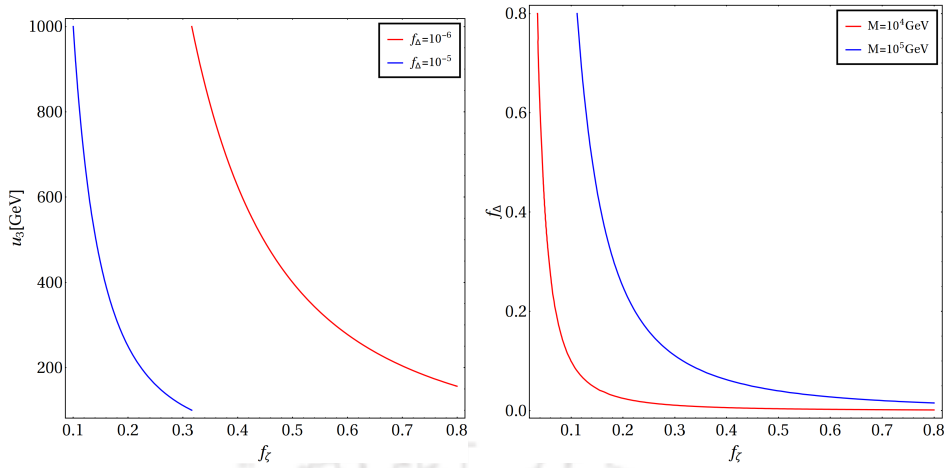


**Figure 5.1:** LHS: Contours showing light neutrino mass $m_\nu \sim 0.1$ eV for different choices of the Yukawa coupling $f_\Delta = \{10^{-5}, 10^{-6}\}$ (in blue and red respectively) in $f_\zeta - u_3$ plane when $u_3 \sim \mathcal{O}(100\text{ GeV})$ and $M \sim \mathcal{O}(\text{TeV})$. RHS: Contours satisfying light neutrino mass ($m_\nu \sim 0.1$ eV) in $f_\zeta$-$f_\Delta$ plane for two different choices of $n_{1,2}$ masses $M : \{10^4, 10^5\}$ GeV (in red and blue curves respectively) with $u_3 = 100$ GeV.

where $f_\zeta$ and $f_\Delta$ are $3\times3$ matrices and $f_\Delta$ is further classified to address left handed ($f_\Delta^L$) and right handed ($f_\Delta^R$) Yukawa couplings separately. The neutrino mass matrix in the $(\overline{\nu}_L, n_{2R}, \overline{n}_{2L})$ basis is then given by:

$$M_\nu = \begin{pmatrix} 0 & m_D & 0 \\ m_D & m_2' & M \\ 0 & M & m_2 \end{pmatrix}, \tag{5.4}$$

where each entry is a $3 \times 3$ matrix with $m_D = f_\zeta\, v_2$, $m_2' = f_\Delta^R\, u_3$, $m_2 = f_\Delta^{L*}\, u_3$, and $M$ is a free Dirac mass term in $M\,(\overline{n}_{2L} n_{2R} + \overline{n}_{2R} n_{2L})$. Thus, the inverse seesaw neutrino mass is given in the form (assuming $f_\Delta^R \simeq f_\Delta^L \simeq f_\Delta$):

$$m_\nu \simeq \frac{m_D^2\, m_2}{M^2} = f_\zeta^2 f_\Delta \left(\frac{v_2}{M}\right)^2 u_3. \tag{5.5}$$

From here we see that if we assume $u_3 \sim \mathcal{O}\,(100\text{ GeV})$ and $M \sim \mathcal{O}\,(1\text{ TeV})$, we can generate light neutrino mass in the correct ballpark for $f_\Delta \sim \mathcal{O}\,(10^{-6})$ and $f_\zeta \sim \mathcal{O}(1)$. This is shown in the LHS of Fig. 5.1 where the two contours correspond to light neutrino mass $m_\nu \sim 0.1$ eV for smaller values of $f_\Delta : \{10^{-5}, 10^{-6}\}$ in blue and red respectively. One can however, choose a less fine-tuned $f_\Delta \sim \mathcal{O}\,(1)$ at the expense of making the RHNs super heavy $\sim 10^5$ GeV. This is depicted in the RHS of Fig. 5.1 where we have chosen a fixed $u_3 = 100$ GeV and obtained contours of correct neutrino mass ($m_\nu \sim 0.1$ eV) for two different choices of $M : \{10^4, 10^5\}$ GeV (red and blue curves respectively) in the plane of $f_\zeta - f_\Delta$. We would like to mention here that the second choice of heavy $n_{1,2}$ is more desirable as it does not require the Yukawa couplings to be extremely fine-tuned, i.e. $\sim \mathcal{O}(10^{-6})$ and secondly will help us in addressing the freeze-in of $X(\bar{X})$ as the only possible decay mode of $\zeta_1^{\pm,0}$. More interestingly, it will also distinguish the collider signature of this model from that of the WIMP example [254].

## 5.4 Dark sector

| | Degenerate $\Delta$ ($f_7 = 0$) | | Non-degenerate $\Delta$ ($f_7 \neq 0$) | |
|---|---|---|---|---|
| Production mechanism of $\Delta$ | Freeze-Out | Freeze-In | Freeze-Out | Freeze-In |
| Scalar quartic coupling $f_8$ | $\mathcal{O}(1)$ | $\mathcal{O}(10^{-12})$ | $\mathcal{O}(1)$ | $\mathcal{O}(10^{-12})$ |

**Table 5.4:** Different production scenarios for $\Delta$'s, and their dependence on $f_{7,8}$ couplings. Throughout this study the freeze-in of $X$ is assumed.

In this set-up we assume $X$ to be the lightest non-zero $S$ charge particle and hence a DM candidate as stated in Sec. 5.2. This choice is even more natural when $g_N$ is considered small as we have here for the freeze-in of $X$. Because of this, $X$ is not in thermal equilibrium in the early universe and is produced via the decay or annihilation of an odd-$S$ particle that can be in thermal bath. Therefore, in our model, $X$ can be produced via freeze-in from the decays of the scalar triplet $\Delta$ (Fig. 5.2) and the bi-doublet scalar components $\zeta_1^{0,\pm}$ (Fig. 5.3) when kinematically accessible. The mass hierarchy among different components of the $\Delta$ (namely, $\Delta_{1,2,3}$) is controlled by the parameter $f_7$. If we assume $f_7 = 0$ then all three components have the same mass. $\Delta$'s can be produced from the Higgs quartic interaction, which is a function of $f_8$. Therefore, freeze-in production of $\Delta$ requires $f_8 \sim 10^{-12}$, while for freeze-out: $f_8 \sim 1$. The Feynman graph for the production of $\Delta$ is shown in Fig. 5.4. For simplification, we assume $f_{9,10} \ll f_8$ so that the $\Delta \leftrightarrow \zeta$ mixing and conversions can be neglected. We will show that $\Delta$'s are naturally stable in the freeze-in scenario (for $g_N \sim 10^{-15} - 10^{-10}$, $f_8 \sim 10^{-12}$), and we have $\{\Delta_{1,2,3}\}$ as long-lived relics that contribute to the DM abundance in addition to $X(\bar{X})$. Different production possibilities of $\Delta$, depending on the choice of the model parameters and possible degeneracy is classified in Tab. 5.4. We primarily focus on the degenerate scalar triplet scenario with $f_7 = 0$ and calculate the yield of the DM components ($\{X, \Delta_{1,2,3}\}$) via freeze-in by solving Boltzmann equations (BEQ) in subsection. 5.4.1.

### 5.4.1 Degenerate $\Delta$'s with $f_8 \sim \mathcal{O}(10^{-12})$

The masses of particles in $\Delta$ triplet are degenerate if $f_7 = 0$. In this case, $\Delta_{1,2,3}$ can decay via the tree level diagram on the LHS of Fig. 5.2. This diagram is only possible after the EWSB when $\Delta_3$ mixes with the Higgs via $f_8 \left(\Phi^\dagger \Phi\right) tr\left(\Delta^\dagger \Delta\right)$. The effective vertex for $\Delta_3 \to t\bar{t}$ decay is $\sim f_8 m_t u_3 / m^2_{\Delta_3}$. Since $m_{\Delta_3} \sim \mathcal{O}(10^{13}\ \text{GeV})$ and $f_8 \sim \mathcal{O}(10^{-12})$ in the freeze-in scenario, the decay vertex factor is tiny. This results in a very large lifetime for $\Delta_3$. As an estimate, if we set $m_{\Delta_3} = 10^{13}$ GeV, $f_8 = 10^{-12}$ and $u_3 = 100$ GeV, this decay width turns out to be $2 \times 10^{-57}$ GeV, which dubs into $\sim 6 \times 10^{32}$ sec in terms of decay lifetime. This is of course much larger than lifetime of the universe, which is $\sim 10^{17}$ sec. This makes all of the $\Delta$'s stable [2].

[2] If we calculate the lifetime of $\Delta_1$ from the decay $\Delta_1 \to \bar{X}\bar{X}t\bar{t}$ turns out to be $6 \times 10^{34}$ sec for similar choices of $g_N = 10^{-13}$, $f_8 = 10^{-12}$ and $m_X = 5$ GeV.

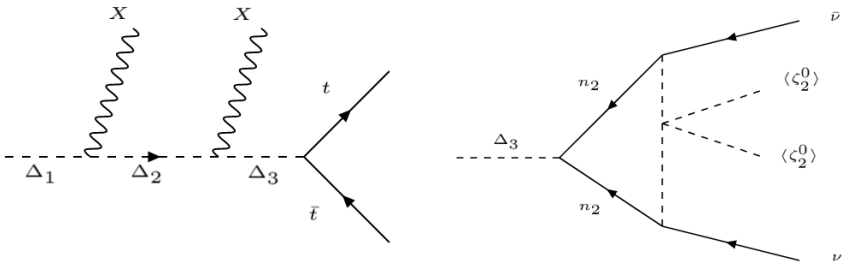


**Figure 5.2:** Decay of $\Delta$'s at tree level to $t\bar{t}$ (left) and decay of $\Delta_3$ via 1-loop to SM neutrinos (right).

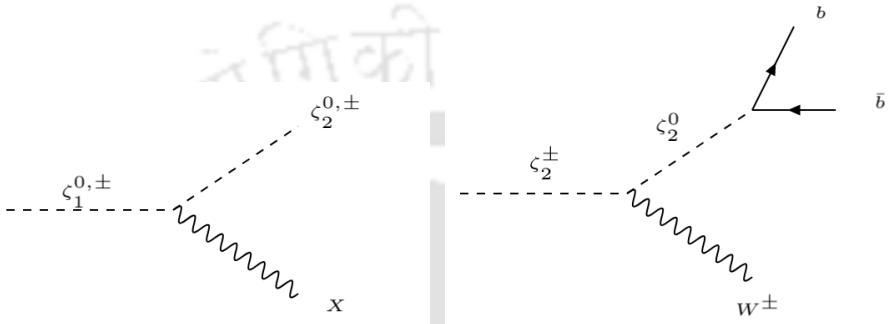


**Figure 5.3:** Left: Decay of $\zeta_1^{0,\pm}$ to $\zeta_2^{0,\pm}$ and $X$ resulting in production of $X$ via freeze-in for $g_N \sim \mathcal{O}\left(10^{-13}\right)$. Right: Decay of $\zeta_2^{\pm}$ to SM final states after $SU(2)_N$ is broken.

On the other hand, the loop-induced decay of $\Delta_3$ to SM neutrinos (RHS of Fig. 5.2), is possible even before the EWSB mediated by Yukawa couplings with $n_2$. The decay width for this process is understandably small as it is proportional to the SM neutrino mass. Even if we assume the Yukawa couplings involved in this decay to be $f_\zeta \sim \mathcal{O}(1)$ and $f_\Delta \sim \mathcal{O}(10^{-6})$, the decay width turns out to be $\sim 4.75 \times 10^{-65}$ GeV for $m_{n_2} \sim 1$ TeV and $m_{\zeta_2} \sim 200$ GeV. Therefore, with a lifetime of $10^{41}$ sec, we conclude that $\Delta_3$ (and hence $\Delta_{1,2}$) is always a long-lived relic. $X$ is kinematically stable and the prime DM candidate of the model with $m_X < m_{\zeta_1}, m_{\Delta_2}$. If we further assume $g_N \sim \mathcal{O}(10^{-13})$, then $\zeta_1^{0,-} \to \overline{X} + \zeta_2^{0,-}$ will produce $X$ via freeze-in mechanism (LHS of Fig. 5.3). Note that after spontaneous breakdown of $SU(2)_N$, bi-doublet $\zeta$ breaks into two doublets, i.e. $\left(\zeta_1^0, \zeta_1^-\right)$ & $\left(\zeta_2^0, \zeta_2^-\right)$. After the electroweak SSB, $\zeta_2^{0,-}$ components will decay as shown in the RHS of Fig. 5.3. As mentioned above, we are assuming $f_{9,10} \ll f_8$ for simplicity, such that $\Delta \leftrightarrow \zeta$ conversion is negligible. In the following subsection we calculate abundance for both $X$ and $\Delta$ using appropriate BEQ.

### Computation of yield for $\Delta$ and $X$

Let us first estimate the yield of $\Delta$, which become stable due to small $f_8$ and contribute to DM relic density as elaborated in the last section. The rate of change of number density of $\Delta$ is governed by the following BEQ:

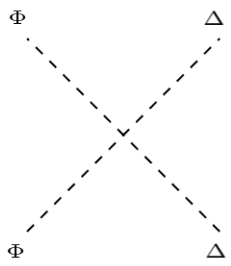


**Figure 5.4:** Production of $\Delta$ via contact interaction from the annihilation of SM Higgs *before* EWSB. This channel is proportional to the coupling $f_8$.

$$\begin{aligned}\dot{n}_{\Delta_i} + 3Hn_{\Delta_i} = &\int d\Pi_\Phi\, d\Pi_{\Phi^*}\, d\Pi_{\Delta_i}\, d\Pi_{\Delta_i^*} (2\pi)^4 \delta^4(p_\Phi + p_{\Phi^*} - p_{\Delta_i} - p_{\Delta_i^*}) \\ &\times \Big[ |\mathcal{M}|^2_{\Phi\Phi^*\to\Delta_i\Delta_i^*}\, f_\Phi f_{\Phi^*}(1+f_{\Delta_i})(1+f_{\Delta_i^*}) \\ &\quad - |\mathcal{M}|^2_{\Delta_i\Delta_i^*\to\Phi\Phi^*}\, f_{\Delta_i} f_{\Delta_i^*}(1+f_\Phi)(1+f_{\Phi^*}) \Big] ,\end{aligned} \tag{5.6}$$

where $d\Pi_i \equiv d^3p_i/(2\pi)^3 2E_i$ is the Lorentz invariant phase space factor. Following Fig. 5.4, the only way of producing $\Delta$ or depleting its number density occurs through the quartic interaction with Higgs $(H)$. We are focusing on the freeze-in production of $\Delta$ before EWSB and after SSB of $SU(2)_N$. Higgs can then produce a pair of super-heavy $\Delta$ only beyond the threshold center-of-mass (C.O.M) energy $s \geq 4m_\Delta^2$.

Now, assuming negligible initial abundance for $\Delta_i$'s, we can set $f_{\Delta_i} = 0$. We can also neglect the Pauli-blocking/stimulated emission effects, i.e. $f_i \ll 1$. Then, following Eq. (2.41) one can simply write Eq. (5.6) as

$$Y_{\Delta_i} \simeq \frac{135 f_8^2 M_{\rm pl}}{256\pi^7 g_{\star s}\sqrt{g_{\star\rho}}\,(1.66)\, m_{\Delta_i}} \int_0^\infty dx x K_1(x) = \frac{135 f_8^2 M_{\rm pl}}{512\pi^7 g_{\star s}\sqrt{g_{\star\rho}}\,(1.66)\, m_{\Delta_i}}. \tag{5.7}$$

The total relic abundance of $\Delta$'s, i.e. $\Omega_\Delta = 3\Omega_{\Delta_i}$ owing to its degeneracy is given by

$$\Omega_\Delta \cdot h^2 = 3 \times \frac{2970\, m_\Delta\, Y^\infty_{\Delta_i}\, \text{cm}^{-3}}{1.88\times 10^{-29}\, \text{g}\cdot\text{cm}^{-3}} \approx 10^{21} f_8^2. \tag{5.8}$$

We see that for $f_8 \in 6.19 \times [10^{-13}, 10^{-12}]$ we get relic density in the correct ball park, when the corresponding relic density of $\Delta$ is $\Omega_\Delta \cdot h^2 \approx [\%1, \%100]$ of the observed DM relic density.

We now focus on $X$. The relic abundance of $X$ is coming from the $\zeta_1^{0,-}$ decays. We also assume that $n_{1,2}$ is heavier than $\zeta_1$, so that $\zeta_1 \to \zeta_2 + X$ constitutes 100% decay branching fraction of $\zeta_1$. The contributions from the $\Delta$ decays are exceedingly slow for small $f_8$. This makes $\Delta$ a DM candidate (as explained before) with negligible contribution to the freeze-in production of $X$. The production of $X$ from annihilation $(\zeta_1\zeta_1 \to XX)$ is much more suppressed due to the presence of $g_N^2$ in the amplitude and can be neglected. Therefore, the contribution to the number density of $X$ can then be written as:

$$\begin{aligned}\dot{n}_{\bar{X}} + 3Hn_{\bar{X}} =& 2\int d\Pi_{\bar{X}}\, d\Pi_{\zeta_1}\, d\Pi_{\zeta_2}(2\pi)^4\delta^4(p_{\zeta_1} - p_{\zeta_2} - p_{\bar{X}}) \\ &\times \left[|\mathcal{M}|^2_{\zeta_1\to\bar{X}+\zeta_2}\, f_{\zeta_1}(1+f_{\bar{X}})(1+f_{\zeta_2}) - |\mathcal{M}|^2_{\zeta_2+\bar{X}\to\zeta_1}\, f_{\zeta_2} f_{\bar{X}}(1+f_{\zeta_1})\right] \\ =& 2\int d\Pi_{\zeta_1}\, e^{-\left(E_{\zeta_1}-\mu_{\zeta_1}\right)/T'}\, e^{-(m_{\zeta_1}/E_{\zeta_1})\theta(t-t_D)\Gamma\cdot(t-t_D)}\, (2m_{\zeta_1} g_{\zeta_1})\, \Gamma_{\zeta_1\to\zeta_2+\bar{X}},\end{aligned} \tag{5.9}$$

where $\theta$ is the step function, $t_D$ is the $\zeta$ decoupling time from the SM particles, and the factor of 2 arises from same contribution of $\zeta_1^0$ and $\zeta_1^-$ decays to $X$ production. It is important to note that when $\zeta_1$ is in thermal equilibrium with the hot plasma, $T = T'$, but after $\zeta_1$ decouples: $T \neq T'$. We have set $f_{\bar{X}} = 0$ in accordance with freeze-in prescription and used:

$$\Gamma \equiv \Gamma_{\zeta_1\to\zeta_2+\bar{X}} = \int \frac{1}{2m_{\zeta_1}} \frac{|\mathcal{M}|^2_{\zeta_1\to\bar{X}+\zeta_2}}{g_{\zeta_1}} (2\pi)^4\delta^4(p_{\zeta_1} - p_{\zeta_2} - p_{\bar{X}})\, d\Pi_{\bar{X}}\, d\Pi_{\zeta_2}, \tag{5.10}$$

where $g_{\zeta_1} = 1$. Since $\zeta$ is a cold relic then $E_{\zeta_1} \approx m_{\zeta_1}$ for $t > t_D$, which simplifies Eq. (5.9):

$$\begin{aligned}\dot{n}_{\bar{X}} + 3Hn_{\bar{X}} =& 2e^{-\theta(t-t_D)\Gamma\cdot(t-t_D)} \int \frac{d^3p_{\zeta_1}}{(2\pi)^3\,\gamma_{\zeta_1}}\, e^{-\left(E_{\zeta_1}-\mu_{\zeta_1}\right)/T'}\, \Gamma_{\zeta_1\to\zeta_2+\bar{X}} \\ =& \frac{m^2_{\zeta_1}\,\Gamma_{\zeta_1\to\zeta_2+\bar{X}}}{\pi^2}\, T'\, K_1(m_{\zeta_1}/T')\, e^{\frac{\mu_{\zeta_1}}{T'}}\, e^{-\theta(t-t_D)\Gamma\cdot(t-t_D)},\end{aligned} \tag{5.11}$$

where $\gamma_{\zeta_1} = E_{\zeta_1}/m_{\zeta_1}$. Using the comoving yield $Y_{\bar{X}} = n_{\bar{X}}/\mathcal{S}$ and $\dot{T} \approx -T\cdot H$ we have:

$$\frac{dY_{\bar{X}}}{dT} = -\frac{m^2_{\zeta_1}\,\Gamma_{\zeta_1\to\zeta_2+\bar{X}}}{\pi^2}\, \frac{T'}{T\,H\,\mathcal{S}}\, K_1(m_{\zeta_1}/T')\, e^{\frac{\mu_{\zeta_1}}{T'}}\, e^{-\theta(t-t_D)\Gamma\cdot(t-t_D)}, \tag{5.12}$$

The presence of $T^{'}$ in BEQ segregates the equation to the cases (i) before decoupling and (ii) after decoupling of $\zeta_1$ from thermal bath. It is important to relate temperature $T^{'}$ to the decoupling temperature ($T_D$). Throughout our calculations we use:

$$T' = \left(\frac{R(t_D)}{R(t)}\right)^2 \cdot T_D, \qquad m - \mu(T') = \frac{T'}{T_D}\cdot(m - \mu_D), \tag{5.13}$$

for cold relics (see Appendix. D for the derivation). We now express $T'$ in terms of the temperature of the hot plasma ($T$) using the conservation of entropy, i.e. $S = \mathcal{S}\cdot R^3(t) = g_\star^S\, T^3\, R^3(t) = \text{const.}$[3]:

$$T \propto (g_\star^S)^{\frac{-1}{3}}\, R^{-1}. \tag{5.14}$$

[3] $g_\star^S$ and $g_\star^\rho$ are the effective number of relativistic degrees of freedom for entropy and energy respectively.

Now, since at the decoupling $T'_D = T_D$, we then have:

$$T' = \left(\frac{g^s_\star(T)}{g^s_\star(T_D)}\right)^{\frac{1}{3}} \left(\frac{g^\rho_\star(T)}{g^\rho_\star(T_D)}\right)^{\frac{1}{4}} \left(\frac{T^2}{T_D}\right). \tag{5.15}$$

The total $\bar{X}$ yield from $\zeta$ decays is then given by:

$$\begin{aligned} Y^\infty_{\bar{X}} =& \frac{90\,\Sigma_\zeta}{6.64\pi^4}\left(\int_0^{x_D} \frac{x^3 K_1(x)}{g^s_\star(x)\sqrt{g^\rho_\star(x)}}\,dx \right. \\ &\left. + \int_{x_D}^\infty e^{\frac{-0.3\,\Sigma_\zeta}{\sqrt{g^\rho_\star(x)}}(x^2-x_D^2)} \frac{x_D\cdot x^2}{\eta(x,x_D)} K_1\left[\alpha(x,x_D)\left(\frac{x^2}{x_D}\right)\right] e^{\frac{\alpha(x,x_D)x^2-x_D^2}{x_D}}\,dx\right). \end{aligned} \tag{5.16}$$

The second integral within the parenthesis (from $x_D$ to $\infty$) indicates the contribution of the late decays of $\zeta_1$ (after its decoupling from thermal bath) to the production of DM ($X$). We would like to point out that an elaborate estimation of such contribution has not been carried out before in literature. The relic abundance of $X$ and $\bar{X}$ is then given by

$$\Omega^X_{\rm DM}\cdot h^2 = 2\times\Omega_X\cdot h^2 = 2\times\frac{2970\,m_X\,Y^\infty_X\,{\rm cm}^{-3}}{1.88\times10^{-29}\,{\rm g}\cdot{\rm cm}^{-3}}, \tag{5.17}$$

where the factor of two is due to the contribution from both $X$ and $\bar{X}$. Note that, Eq. (5.16) is practically independent of the model concerned (except for the couplings and masses appearing in $\Sigma_\zeta$) as it solely involves the number of degrees of freedom $g^s_*$ and $g^\rho_*$ and the dimensionless quantity $x_D$ which for all practical purposes can be taken to be $x_D \sim 25$. Hence this is a generic expression for computing yield in all such cases where the DM is produced via freeze-in from the decay of a heavy species before and after its decoupling from the thermal bath.

In Fig. 5.5 we have plotted the evolution of the relic abundances of $\Delta$ and $X$ as a function of the dimensionless parameter $x = M_{\zeta_1}/T$. The parameters in Fig. 5.5 are chosen such that $\Omega_\Delta + \Omega_X = \Omega_{\rm DM}\cdot h^2 = 0.1198$. We have chosen four different values of $m_\zeta$, to generate four different relative contributions of $X$ and $\Delta$ to the total relic density as $\Omega_X/\Omega_{\rm DM} = \{\%25, \%50, \%75, \%99\}$ from top-left to bottom-right respectively. The evolution of yield for $\Delta$ (shown by solid blue line in each of the plots) follows the familiar pattern of freeze-in production, which initially increases with $x$, and finally becomes constant as the temperature of the universe falls below the mass of $\Delta$. For $X$ (the solid magenta curve), note that the first point where the relic abundance function flattens is around $x \gtrsim 10$, where the exponential suppression inside the Bessel function becomes dominant. However, the function then rises for a second time, and captures the contribution from the decay after decoupling of $\zeta$. First of all, the second rise in freeze-in curve for $X$ shows that the yield from decays after the decoupling can be as large as the yield before decoupling. This indicates the importance of the late decay to be considered for correct evaluation of freeze-in relic density. The effect of late decay can be understood in more details from Eq. (5.16). The share from the second integral ($x > x_D$) in Eq. (5.16) is at first suppressed by $K_1[x_D]$ and therefore it takes a long time (not until $x \sim 10^4$) for the yield to build up to an amount comparable to the yield before $x_D$. This happens because the asymptotic exponential suppression in $K_1(\alpha x^2/x_D)$ cancels out the increasing exponential

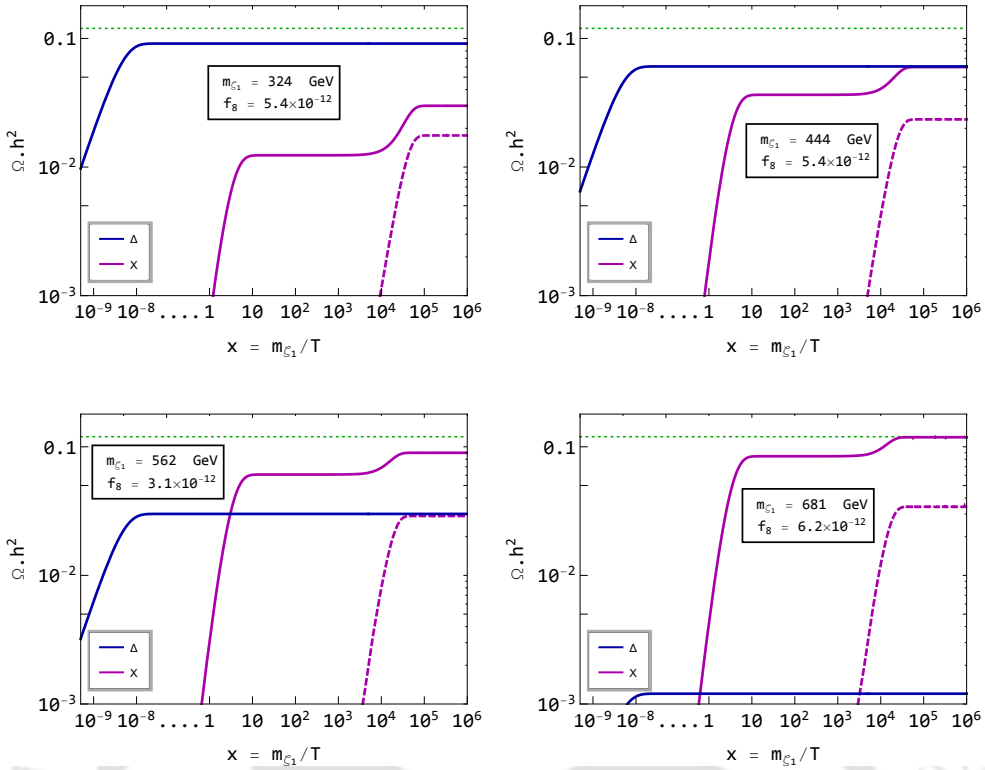


**Figure 5.5:** The evolution of the relic abundances $\Omega_\Delta \cdot h^2$ and $\Omega_X \cdot h^2$ as a function of $x = M_{\zeta_1}/T$ for four different cases with $\Omega_X/\Omega_{\rm DM} = \{\%25, \%50, \%75, \%99\}$ from top-left to bottom-right respectively. We have also assumed $g_N = 10^{-13}$, $M_\Delta = 10^{13}$ GeV, $M_{\zeta_2} = 200$ GeV, $m_X = 5$ GeV. The green dotted line corresponds to $\Omega_\Delta + \Omega_X = \Omega_{\rm DM} \cdot h^2 = 0.1198$, and the dashed magenta curve is the contribution just from the late $\zeta_1$ decays, i.e. after $\zeta_1$ decoupling for $x \geq x_D$.

term $\exp(\alpha x^2/x_D)$. This gain stops later as the exponential suppression from the decays becomes dominant around $x \sim 10 \cdot m_{\zeta_1}/\sqrt{M_{\rm Pl}\Gamma} \sim (5 \cdot 10^4 - 10^5)$[4]. The sole contribution of the late decays to the yield are separately plotted by dashed magenta curves in each plot in Fig. 5.5, to show the exact $x$ for the late rise of the yield. It is also clear that if the decay rate was much faster, the second integral would become suppressed and we wouldn't see any effect of late production.

### Bounds on decaying relic particles from BBN and CMB

Standard BBN may be significantly perturbed by the energy injections due to both neutral decays [260] $\zeta_1^0 \to \overline{X} + \zeta_2^0$ and charged decays [261] $\zeta_1^- \to \overline{X} + \zeta_2^-$. In the case of decaying electrically charged particles with $\tau > 100$ seconds, the existence of bound states between nuclei and the relics may significantly change nuclear reaction rates. Here, we analyze the decays with $0.05$ s $< \tau < 100$ s using the results from Ref. [260], and rule out the ones with $\tau > 100$ s for simplicity. As a result, this puts a lower bound on $g_N$, depending on different choices of DM masses. The hadronic branching ratio $(B_h)$ for $\zeta_1^0$ decays is $B_h^1 \approx 0.695$, and for $\zeta_1^-$ depends on parameters like $M_{n_2}, f_\zeta$. We can assume for heavy $n_2$ and/or small $f_\zeta$, the weak decays $\zeta_1^- \to \bar{X} + \zeta_2^- \to \bar{X} + \zeta_2^0 + W^-$ become dominant and so the hadronic branching ratio of

[4]Assuming $m_{\zeta_1} \sim 300$ - $700$ GeV, $m_{\zeta_2} = 200$ GeV, $m_X = 5$ GeV, we have $\Gamma \sim 10^{-23} - 10^{-21}$ GeV, where $g_\star^\rho \sim 10.75$.

the charged component is $B_h^2 \approx 0.9$. Therefore, for a conservative bound we assume hadronic branching for the both cases to be $B_h = 1$ throughout our analysis. We also assume that the mass difference $(m^-_{\zeta_1} - m^0_{\zeta_1})$ generated during the EWSB is negligible compared to their masses before EWSB. We then extrapolate the results in [260] for arbitrary $m_{\zeta_1}$. The total energy of the resulting quarks in these decays is taken to be the same as $m_{\zeta_1}$ following [260].

A decaying long-lived DM candidate can be constrained by various observations. For example, it can alter the ionization and heating history of the CMB and its power spectrum [255]. Decays to several decay modes *e.g.* $b\bar{b}$, $WW$, $\mu\bar{\mu}$ can also be constrained by the AMS-02 precise measurements of the antiproton/proton $(p/\bar{p}\,)$ fraction [262], as no evidence of new source of antiproton has been found in these data. This in turn, results in the following bounds on the hadronic decay life time of the DM [255]:

$$\text{CMB:} \qquad \tau(\text{DM} \to b\bar{b}) \gtrapprox 10^{24}\, s, \tag{5.18}$$

$$\text{AMS-02:} \qquad \tau(\text{DM} \to b\bar{b}) \gtrapprox 10^{27}\, s. \tag{5.19}$$

As we already have shown, the $\Delta$'s have lifetime comparable to that of the universe. Now, if we set $m_X = 5$ GeV, $g_N = 10^{-12}$ and $f_8 = 10^{-11}$ then for $u_3 = 100$ GeV we obtain the following decay width and corresponding decay lifetime for the $\Delta$'s:

$$\Gamma\left(\Delta_1 \to \bar{X}\bar{X}b\bar{b}\right) = 4.1 \times 10^{-60}\ \text{GeV} \quad \longrightarrow \quad \tau_{\Delta_1} \sim 10^{36}\ \text{sec} \tag{5.20}$$

$$\Gamma\left(\Delta_2 \to \bar{X}b\bar{b}\right) = 5.1 \times 10^{-59}\ \text{GeV} \quad \longrightarrow \quad \tau_{\Delta_2} \sim 10^{35}\ \text{sec} \tag{5.21}$$

$$\Gamma\left(\Delta_3 \to b\bar{b}\right) = 1.2 \times 10^{-58}\ \text{GeV} \quad \longrightarrow \quad \tau_{\Delta_3} \sim 10^{34}\ \text{sec}. \tag{5.22}$$

All these decay rates turn out to be much longer than the bounds mentioned in Eq. (5.18), and so only the bounds from the $\zeta_1$ decays are relevant for final estimate of allowed parameter space. Note that, since some of the energy of $\Delta_1$ goes into $\bar{X}$'s, the actual bounds are smaller, and these numbers are conservative.

**Summary of available parameter space**

The relic density allowed parameter space for $X$ is plotted in $m_{\zeta_1} - m_X$ plane in Fig. 5.6 for different choices of $g_N = \{10^{-12}, 10^{-13}, 10^{-14}, 10^{-15}\}$ (clockwise from top left). Each plot contains several contours corresponding to a specific percentage of the total DM density coming from $X$ (numbers inside parenthesis). Therefore, each curve corresponds to a specific value of $f_8$ such that the rest of the DM abundance ($100\%-$ the percentage in the parenthesis) is coming from $\Delta$. This is possible because the relic density of $X$ and that of $\Delta$ are uncorrelated in the model. We see from the plots that constant $\Omega_X$ curves rises in $m_{\zeta_1} - m_X$ plane for larger $m_X$ and then takes a sharp turn to decrease the required $m_{\zeta_1}$ to satisfy relic density and then rises again. In order to interpret the shape of the contours in Fig. 5.6, let's first take a look at the parameter space assuming the late decays are ignored. This is shown in Fig. 5.7 with the dashed upward moving faint lines in the background. These contours basically correspond to constant relic density $(\Omega_X h^2)$, which is mainly dictated by $\Omega_X \propto c \approx m_X \cdot \Sigma_\zeta$, since the second integral in Eq. (5.16) is to be ignored. Therefore, it is straightforward to see that the larger is the value of $m_X$, the smaller

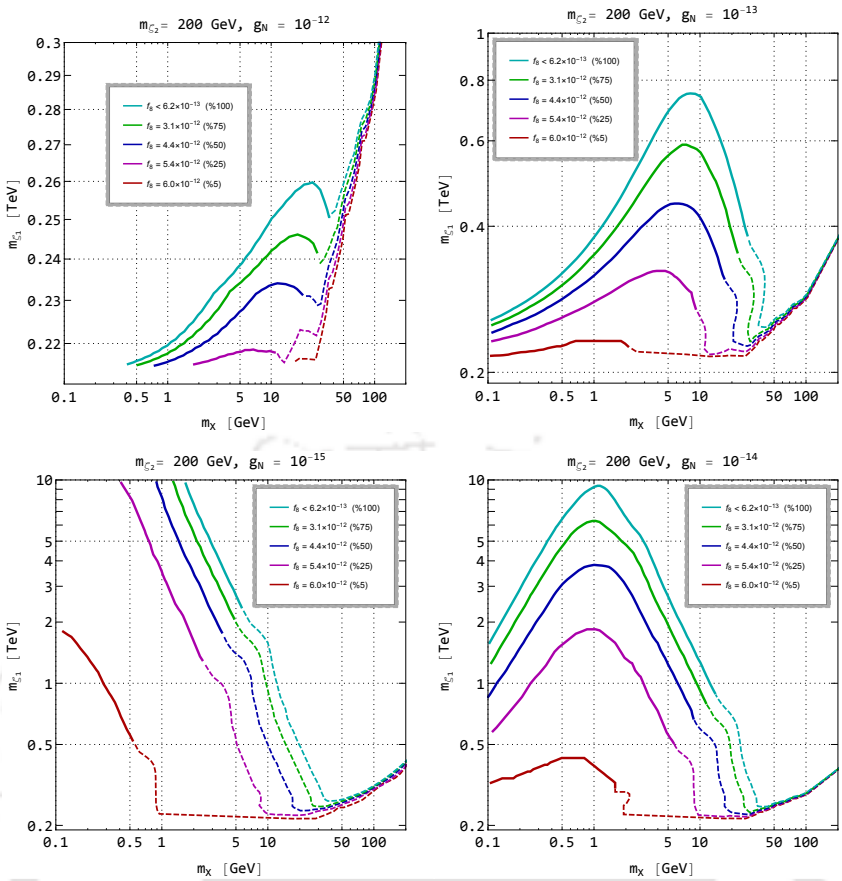


**Figure 5.6:** Parameter space of the model satisfying relic abundance constraint in $m_{\zeta_1}$-$m_X$ plane when $g_N = \{10^{-12}, 10^{-13}, 10^{-14}, 10^{-15}\}$ (clockwise from top left) and $M_{\zeta_2} = 200$ GeV are kept fixed for each plot. Each contour satisfies total relic abundance of $\Omega_{\rm DM} \cdot h^2 = 0.1198$ for different choices of the scalar quartic coupling $f_8$. The numbers inside the parentheses are the percentage of DM comprised of $X$. The dashed portion in each curve is ruled out by the BBN constraints.

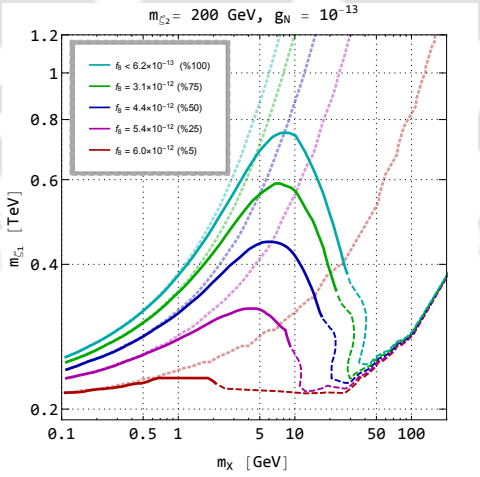


**Figure 5.7:** Parameter space of satisfying the relic abundance constraint for $g_N = 10^{-13}$ in $m_{\zeta_1}$-$m_X$ plane. The opaque dotted curves in the background are the corresponding contours if the late decays are ignored. The dashed regions are ruled out by the BBN constraints.

$\Sigma_\zeta$ has to be and therefore $m_\zeta$ will needs to be larger as $\Sigma_\zeta \propto 1/m_\zeta^2$. It is also clear, for small $m_X$ (as we require larger $\Sigma_\zeta$) the second integral in Eq. (5.16) has smaller con-

tribution due to exponential suppression from $\Sigma_\zeta$. This is reflected in Fig. 5.7 where the case with late decays and the case without them merge together at low $m_X$. As we trace these contours from low $m_X$ region (left) to high $m_X$ regions (right), we observe a departure for the curves where the late decays are involved. Now, with larger $m_X$, $\Sigma_\zeta$ decreases. This increases the contribution from the late decays as the second integral in Eq. (5.16) is proportional to $e^{-\Sigma_\zeta}$. Therefore, if we compare the case with late decay ($\Sigma^1_\zeta$) to that without late decay ($\Sigma^2_\zeta$), it is easy to see that:

$$\begin{aligned} &\Sigma^1_\zeta > \Sigma^2_\zeta; \\ \implies &m^1_{\zeta_1} < m^2_{\zeta_1}, \end{aligned} \tag{5.23}$$

which is reflected in the drop of the curve beyond certain $m_X$. Also note that as $m_{\zeta_1}$ is lowered and $m_X$ is increased, we get into a region where the decay rate is so slow that it violates the BBN bounds (dashed region). As $m_X$ is increased even further, all the contours converge to the kinematically forbidden boundary i.e. $m_{\zeta_1} = m_X + m_{\zeta_2}$. This characteristic feature is reflected in each plot in Fig. 5.6 for different choices of $g_N$ with $m_{\zeta_2}$ fixed at 200 GeV.

### 5.4.2 Degenerate $\Delta$'s with $2m_X < m_\Delta$ and $f_8 \sim \mathcal{O}(1)$

In this case let us first compute the lifetime of the $\Delta$'s assuming $f_8 \sim \mathcal{O}(1)$. We once again recall here that $m_\Delta \sim \mathcal{O}(10^{13})$ GeV. Let us choose $m_X = 5$ GeV and $g_N \sim \mathcal{O}(10^{-13})$ for which $X$ yields relic density in correct ballpark. We then find, $\Gamma_{\Delta_3 \to t\bar{t}} = 1.3 \times 10^{-35}$ GeV which dubs into a lifetime of $\sim 5 \times 10^{11}$ sec $\ll \tau_{\text{universe}}$. With the same set of parameters, we find $\Gamma_{\Delta_2 \to \overline{X} t\bar{t}} = 5.5 \times 10^{-36}$ GeV, which gives rise to a lifetime of $\sim 10^{11}$ sec. The decay width for $\Delta_1$ turns out ot be $\Gamma_{\Delta_1 \to \overline{X} X t\bar{t}} = 4.5 \times 10^{-37}$ GeV, with a lifetime of $\sim 10^{12}$ sec. Therefore, with $f_8 \sim \mathcal{O}(1)$ we end up with a situationwhere all of the triplet scalar components are unstable and don't contribute to the DM relic abundance. Therefore we end up with a single component $X$ DM set up.

## 5.5 Collider search

Possible collider signatures of this model in the context of usual freeze-out of $X$ was elaborated in [254]. It was pointed out that, the only field connecting the dark sector (having $SU(2)_N$ charge) with the SM is the scalar bi-doublet. Therefore, the charged and neutral components of the scalar bi-doublet can be produced at the LHC via the diagrams shown in the top panel of Fig. 5.8. The variation of production cross-section of the charged and neutral components of the scalar bi-doublet at the LHC with respect to its mass $m_{\zeta_1}$ for $E_{\text{CM}}$ =14 TeV is shown in the bottom panel of Fig. 5.8. It should be noted that charge current contribution is more pronounced than the neutral current contribution which we pointed out in our earlier analysis [254]. We have implemented the model in `CalcHEP` [263] and used `CTEQ6l` [264] as a representative parton distribution function for generating this process. The SM gauge coupling is mostly responsible for the production of the bi-doublet components at the LHC. The Higgs portal interactions are again assumed to be small to be compatible with the Higgs data.

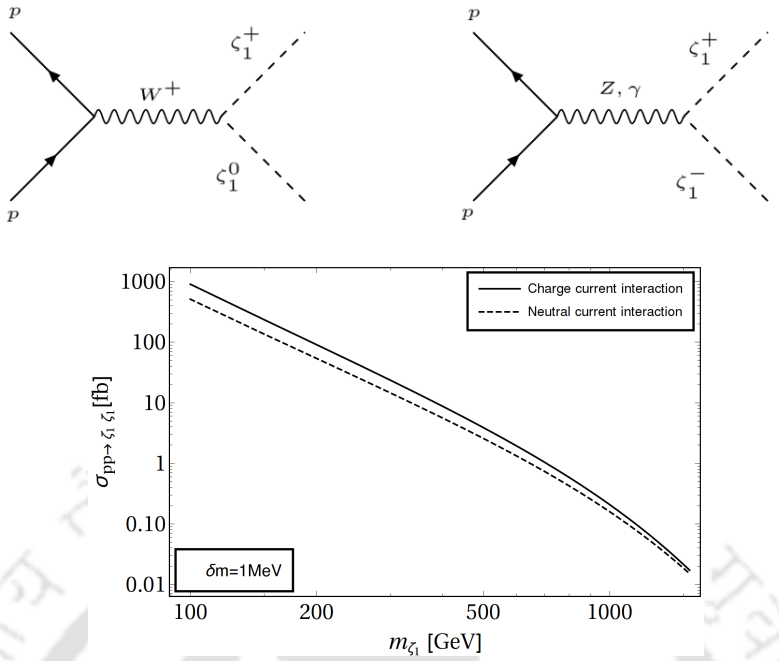


**Figure 5.8:** Top: Associated and pair production of heavy charged scalars at the LHC via charged current (LHS) and neutral current (RHS) interaction. Bottom: Variation of production cross section of $pp \to \zeta_1^{\pm}\zeta_1^0, \zeta_1^+\zeta_1^-$ at the LHC with $E_{\rm CM}$ =14 TeV. Contributions are from charged current (**solid**) and neutral current (**dashed**) interactions for $\delta m = 1$ MeV.

If the additional neutrinos $(n_1, n_2)$ are lighter than $\zeta_1^{\pm,0}$ (which is quite legitimate in WIMP scenario even after addressing correct neutrino mass generation), then these bi-doublet scalars can further decay to neutrinos and SM leptons ( $\zeta_1^+ \to \ell^+ + n_{1R}$) via Yukawa interaction given in Eq. (5.2), giving rise to the following signatures in colliders [254]:

- Single lepton with missing energy $(1\ell^{\pm} + \not{E}_T)$ due to charged current interaction.
- Opposite sign di-lepton with missing energy $(\ell^+\ell^- + \not{E}_T)$ due to neutral current interaction.

In the WIMP-like freeze-out scenario of $X$, therefore this model may leave an imprint of leptonic signal excess at the colliders. However, in the present framework, we assume that the DM production is from the decay of $\zeta_1 \to \zeta_2 + X$, and the additional neutrinos $(n_1, n_2)$ to be heavier than $\zeta_1$. It is understandable that the DM analysis will be modified by the corresponding decay branching ratio if $n_{1,2}$ are lighter than $\zeta_1$. It is also instructive to remind that heavier $n_{1,2}$ ($\sim 10^6$ GeV) arises naturally when we assume the Yukawa in a legitimate ball park $f_\Delta \sim 0.1$ via a large $u_3 \sim 100$ GeV to address the required neutrino mass (see Sec. 5.3). One may still assume the presence of lighter $n_{1,2}$ ($\sim$ TeV) with fine tuned $f_\Delta \sim 10^{-7}$ and $m_{n_{1R}} < m_{\zeta_1}$, yielding single lepton and di-lepton signature as before. In that case, the DM production will be further suppressed and appropriate decay branching ratios have to be assumed. Therefore, in the light of DM analysis performed here, the neutrinos $(n_{1,2})$ are heavier than the scalar bi-doublet $\zeta_{1,2}^{\pm}, \zeta_{1,2}^0$. As a result, these scalars can

not decay to RHN plus SM leptons. However, there can be a small mass splitting $\delta m$ between the charged and neutral components of the bi-doublet. As a result, the charged scalars, once produced, can undergo the decays shown in Fig. 5.9 via off-shell $W$ or via off-shell $n_{1,2R}$ to $\zeta_1^0 + \ell + \nu_\ell$.

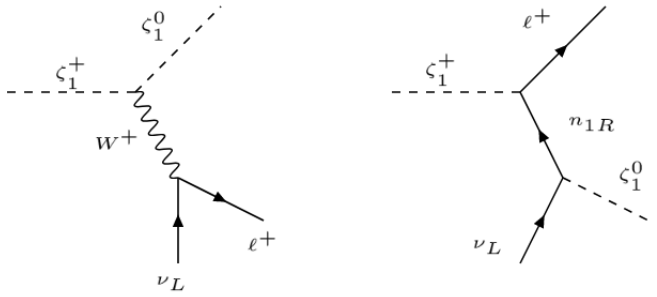


**Figure 5.9:** Decay of the charged components of the scalar bi-doublet which is kinematically possible since $m_{\zeta_1^+} - m_{\zeta_1^0} \equiv \delta m > 0$.

| $\delta m$ (GeV) | $Br(\zeta_1^\pm \to \zeta_1^0, \ell^\pm, \nu_L)$ (via $W$) | $Br(\zeta_1^\pm \to \zeta_1^0, \ell^\pm, \nu_L)$ (via $n_{1R}$) |
|---|---|---|
| 0.1 | 0.99 | 0.0007 |
| 0.5 | 0.99 | 0.0007 |

**Table 5.5:** Decay branching ratio of $\zeta_1^\pm \to \zeta_1^0, \ell^\pm$ via $W$ and via $n_{1R}$. Here we have chosen $m_{\zeta_1} = 1.2$ TeV and $\delta m = 100$ MeV with RHNs of mass $M = 10^5$ GeV.

| $\delta m$ (GeV) | $\Gamma$ (GeV) | $L = c\tau$ (m) |
|---|---|---|
| 0.1 | $3.12 \times 10^{-18}$ | 63.05 |
| 0.3 | $7.58 \times 10^{-16}$ | 0.26 |
| 0.5 | $9.76 \times 10^{-15}$ | 0.20 |

**Table 5.6:** Decay lengths for the three-body decay of $\zeta_1^\pm$ assuming maximum mass splitting $\delta m$ of 500 MeV for $m_{\zeta_1^\pm} = 1.2$ TeV, RHN mass $M = 10^5$ GeV and $f_\zeta \sim \mathcal{O}(1)$.

Note that the diagram in the LHS of Fig. 5.9 involves the vertex $\zeta_1^+ \zeta_1^0 W$, which is proportional to $g_L(p_1 + p_2)_\mu$ where $p_1$ and $p_2$ are the momenta of the incoming and outgoing scalars, while the other vertex involves only the SM gauge coupling $g_L$. The diagram on the RHS of Fig. 5.9, on the other hand, only depends on the Yukawa coupling $f_\zeta$, which we assume to be $\sim \mathcal{O}(1)$. Since $n_{1R}$ is heavy, these decays are dominated by the $W$-mediated process as in the LHS of Fig. 5.9. In Tab. 5.5, we show a couple of sample points with two different mass splitting, where 99% of the branching is carried away by the $W$-mediated decay as $m_W \ll m_{n_{1R}}$. Also

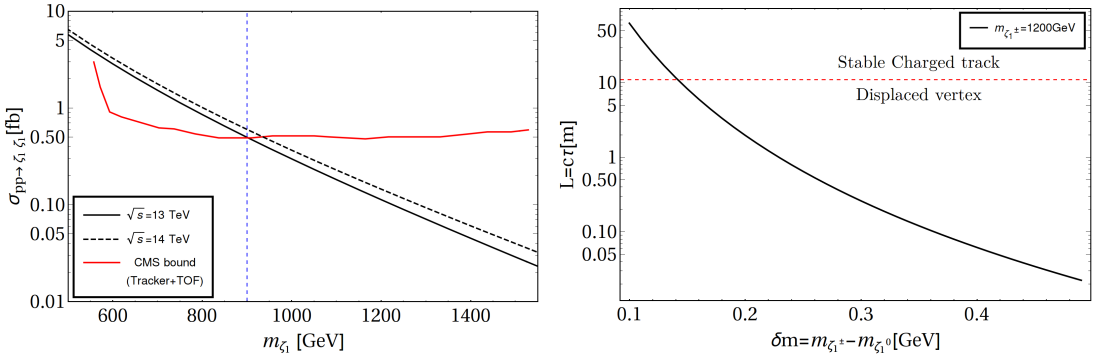


**Figure 5.10:** Left: The variation of production cross section of $pp \to \zeta_1^\pm \zeta_1^0, \zeta_1^+ \zeta_1^-$ at the LHC with $E_{\rm CM}$ =13 TeV (solid black curve) and $E_{\rm CM}$ =14 TeV (dashed black curve). The red solid curve shows the bound from CMS searches for HSCP at $\sqrt{s} = 13$ TeV and luminosity 12.9 fb$^{-1}$. The vertical dashed line shows the minimum mass that is allowed by the CMS exclusion limit; Right: Decay length of $\zeta_1^+ \to \zeta_1^0 + \ell^- + \bar{\nu}_\ell$ (in meter) in terms of mass splitting $\delta m \sim \mathcal{O}(100\,\text{MeV})$ (in GeV). We show the possibilities of displaced vertex or stable charged track segregated via dashed red line at collider assuming a legitimate $m_{\zeta_1^\pm} = 1.2$ TeV .

note that in the limit $\delta m \ll m_{\zeta_1}$, the decay width mostly depends on $\delta m$ (which controls the phase space) and not on $m_{\zeta_1^\pm}$. For example, if we fix $\delta m = 0.1$ GeV, then for $m_{\zeta_1^\pm} = 1.2$ TeV, the decay width is $3.127 \times 10^{-18}$ GeV, which changes to $3.126 \times 10^{-18}$ GeV for $m_{\zeta_1^\pm} = 1.5$ TeV. For $\delta m \sim \mathcal{O}(100\,\text{MeV})$ this model can give rise to charge track and/or displaced vertex [147] at the colliders that can be probed by current or future experiments [168, 265]. A heavy stable charged particle (HSCP) such as $\zeta_1^+$ in our model, will typically travel with a velocity $\beta \equiv \frac{v}{c} < 1$. Hence, as it passes through the silicon detectors, it produces an ionizing track with higher ionization energy loss rate (larger $dE/dx$) compared to the SM particles [266]. Also, if the HSCP decays outside the detectors, the time of flight (TOF) measured by the muon system will be longer than that of relativistic muons. These two features can distinguish non-standard HSCPs from the SM particles.

Typically, for $c\tau \lesssim \mathcal{O}(10\,\text{m})$ the searches for HSCPs are done via displaced vertex signatures, while for $c\tau > \mathcal{O}(10\,\text{m})$ a sizable fraction will decay only after crossing the tracker and/or muon chamber [266]. We use the CMS bound on HSCP production cross-section at the LHC [267] to constrain the mass of $\zeta_1$ in our model. The $\zeta_1$ production cross-section is plotted in the LHS of Fig. 5.10 with respect to $\zeta_1$ mass. We have also shown the limit from the CMS tracker+TOF analysis [267] (for luminosity of 12.9 fb$^{-1}$) with a solid red curve. As one can see, these constraints rule out $m_{\zeta_1^\pm} \lesssim 1$ TeV. We have tabulated the decay lengths for some selected values of $\delta m$ with $m_{\zeta_1^\pm} = 1.2$ TeV in Tab. 5.6. The same is also shown in RHS of Fig. 5.10 where we have plotted the variation of the decay length with respect to mass splitting $\delta m$ for $m_{\zeta_1^\pm} = 1.2$ TeV. As mentioned, the decay length decreases as the mass splitting $\delta m$ increases. We have indicated a red dashed line, above which ($c\tau > 10$ m) the model can give rise to stable charged track and below ($c\tau \lesssim 10$ m) displaced vertex signature.

## 5.6 Summary

In this chapter we have analysed FIMP realization of a non-abelian vector boson DM in $SU(2)_N$ extension of the SM. The model at hand also addresses neutrino mass generation and neutrino mass constraint plays an important role in identifying the allowed parameters of the model together with DM constraints. For example, this exercise has led us to conclude (i) scalar triplets are super heavy (of the scale of $SU(2)_N$ breaking), (ii) sterile neutrinos assumed in the model can also be naturally heavier than scalar bi-doublet. Now, both of these two conclusions have immense phenomenological consequence. Therefore, the exercise performed in this analysis can serve as a benchmark to address non-thermal DM production together with neutrino mass and Higgs phenomenology.

One of the important outcomes of this analysis turns out to be out-of-equilibrium decay of a heavier particle to DM. In the present context, scalar bi-doublet $\zeta_1^{0,\pm}$ decays into its lighter partner $\zeta_2^{0,\pm}$ plus DM $X$, and this is solely responsible for non-thermal production of the DM. The production of DM occurs after $SU(2)_N$ symmetry breaking ($\sim 10^{12}$ GeV) and before electroweak symmetry breaking. We find that, the decay of $\zeta_1^{0,\pm}$ provides a significant contribution to DM relic density even after the freeze-out of $\zeta_1^{0,\pm}$ from thermal bath. This results in a sharp deviation of relic density contour in $M_{\zeta_1} - m_X$ allowed plane compared to the case where the late productions are neglected. The impact of this conclusion can be made in a generic and model independent way, to demand that any particle in thermal bath whose decay is slow enough ($\sim 10^{-24}$ GeV) can contribute significantly after freeze out and alter the available parameter space to a significant extent. We provide with a generic expression for the DM yield including the late decays that may serve useful in identifying such contributions for any model. CMB data constrains the decay life time of long lived DM particles to hadronic final states ($\Delta \to b\bar{b}$ in our case) to be greater than $\tau(\text{DM} \to b\bar{b}) \gtrapprox 10^{24}\, s$. However, since the correct relic density is achieved for $\tau_\Delta \gtrapprox 10^{36}\, s$, this bound does not affect that part of the parameter space where $\Delta$ is a viable DM candidate. There are bounds from AMS-02 that constrains life time of hadronically decaying DM (again $\Delta \to b\bar{b}$ in our case), while BBN data constrains life time of semi-stable hadronically decaying charged and neutral particle ($\zeta_{1,2}^{0,\pm}$ in our case).

The same model has been studied for WIMP realization as mentioned before. It is therefore important to identify the difference in their phenomenological implication. While freeze-in makes the DM insensitive to direct search, the WIMP can be detected via future direct search experiments. It is important to note that WIMP-like $X$ is allowed upto ~TeV, but FIMP realization restricts it within $\sim 50$ GeV. The most crucial distinction however may arise from collider searches. While the WIMP realization could provide a signal excess in single or opposite sign di-lepton events associated with large missing energy, the FIMP case predicts stable charge track or displaced vertex signature.

Chapter 6

# Feebly coupled vector dark matter in effective theory

## Contents



## 6.1 Introduction

Effective DM-SM operators provide a model-independent framework to probe DM characteristics like relic density, direct search and collider search prospects. Such operators are usually written as $\mathcal{O} = \mathcal{O}_{SM}\mathcal{O}_{DM}$, where $\mathcal{O}_{SM}$ consists of SM fields and $\mathcal{O}_{DM}$ consists of additional DM fields (scalar, fermion or vector boson). The Lagrangian is assumed to be invariant under $\mathcal{G}_{SM} \times \mathcal{G}_{DM}$, where SM fields in $\mathcal{O}_{SM}$ transform only under SM gauge symmetry ($\mathcal{G}_{SM} = SU(3)_c \times SU(2)_L \times U(1)_Y$) and neutral under $\mathcal{G}_{DM}$, while DM fields transform only under dark symmetry ($\mathcal{G}_{DM}$, often assumed to be $Z_2$) and are singlets under $\mathcal{G}_{SM}$. A heavy mediator is assumed to couple to both dark and visible sector weakly and the operators are expected to vanish when the mass of the heavy mediator goes to infinity following decoupling theorem. A complete set of such operators have been written upto dimension six assuming $\mathcal{G}_{SM}$ to be SM gauge group [268, 269] as well as assuming $\mathcal{G}_{SM} \sim U(1)_{EM}$ after spontaneous electroweak symmetry breaking [136] keeping dark symmetry intact.

In this chapter we elaborate a model where the dark sector is coupled to visible sector *only* via effective dimension 5 (dim.5) operator [270]. We choose the simplest extension of the SM by Abelian $U(1)_X$ gauge group. The $U(1)_X$ vector boson is EM charge neutral and must be stable for becoming DM. The stability is guaranteed by

imposing an additional $Z_2$ symmetry under which the dark vector boson is odd, then the kinetic mixing $X^{\mu\nu}B_{\mu\nu}$ is forbidden. However a direct connection between DM and the visible sector (SM) still could be introduced if an extra real scalar ($\Phi$) odd under the stabilizing symmetry is present. Then an operator of mass dim.5, $X^{\mu\nu}B_{\mu\nu}\Phi/\Lambda$, is allowed. For dimensional reasons the interaction must be suppressed by an unknown new physics (NP) scale $\Lambda$. It is worthy to mention here, even without $X^{\mu\nu}B_{\mu\nu}\Phi$ term, dark sector can couple to the SM, via the mixing of scalar boson (call it $S$) that breaks $U(1)_X$ and the Higgs doublet ($H$) via a portal term $|S|^2|H|^2$ [150]. Here however, we will assume that the scalar $S$ is super heavy and decouples. In addition a quartic portal interaction of the scalar $\Phi$, $\Phi^2|H|^2$ is also allowed by the symmetry. The coupling is relevant for $\Phi$ being in thermal equilibrium with the SM, however fails to produce vector boson DM without the dim.5 operator. For the consistency of Effective Field Theory (EFT), the NP scale also requires to be larger than the maximum reheat temperature $\Lambda > T_{\rm RH}$. Together, it is more appealing to assume that the VDM is feebly connected to the SM and it freezes-in. We also demonstrate the limitation of *UV* freeze-in which is advocated in context of effective operators [157].

Finally we note that owing to feeble DM-SM interaction to account for correct relic density in FIMP like models, the possibility of detecting such DM candidates at direct or collider searches is limited. However, if one has an extended dark sector, like we have $\Phi$ having same $Z_2$ symmetry as of VDM ($X^\mu$), there can still be a possibility. We comment on observing mono-X (where X stands for jet, photon, $W, Z$ or $H$) plus missing energy signature in this framework at the upcoming run of Large Hadron Collider (LHC).

The chapter is arranged as follows. Sec. 6.1 contains an introduction to VDM models. In Sec. 6.2 the model considered here is described and its Stueckelberg formulation specified. Sec. 6.3 discusses properties of the Boltzmann equation relevant for the DM production. Sec. 6.4 contains our findings for the DM abundance via the freeze-in and shows regions of the parameter space consistent with the observed DM abundance. In Sec. 6.5 we comment on experimental constraints and collider signatures of the model. Sec. 6.6 shows summary and conclusions.

## 6.2 The Model

The minimal VDM model contains a $U(1)_X$ gauge boson denoted here by $X_\mu$. In order to establish direct interactions between $X_\mu$ and the SM one also requires presence of a real scalar $\Phi$. Both of them should be odd under a $Z_2$ which stabilises DM candidate, i.e. the vector boson ($m_X < m_\Phi$). Therefore the symmetry group of the model is $\mathcal{G} = SU(3)_C \times SU(2)_L \times U(1)_Y \times U(1)_X \times Z_2$. To generate a mass for the dark gauge boson we also introduce a complex scalar $S$ charged under $U(1)_X$, which acquires a vacuum expectation value to break $U(1)_X$ spontaneously. The $Z_2$ transformation acts on these fields as follows:

$$Z_2: \quad X_\mu \to -X_\mu, \; S \to S^\star, \; \Phi \to -\Phi\,. \tag{6.1}$$

The quantum numbers under $SU(3)_c \times SU(2)_L \times U(1)_Y \times Z_2$ of the new fields are tabulated in Tab. 6.1.

| Fields | $SU(3)_c$ | $SU(2)_L$ | $U(1)_Y$ | $Z_2$ |
|---|---|---|---|---|
| $\Phi$ | 1 | 1 | 0 | $-\Phi$ |
| $X$ | 1 | 1 | 0 | $-X$ |
| $S$ | 1 | 1 | 0 | $S^*$ |

**Table 6.1:** Charges of the new particles under $SU(3)_c \times SU(2)_L \times U(1)_Y \times Z_2$ symmetry.

With these fields and the charges, we can write the renormalizable $SU(3)_c \times SU(2)_L \times U(1)_Y \times Z_2$ invariant scalar potential as:

$$V(H,S,\Phi) = -\mu_H^2|H|^2 - \mu_S^2|S|^2 + \mu_\Phi^2\Phi^2 + \lambda_H|H|^4 + \lambda_S|S|^4 + \lambda_\Phi\Phi^4 + \lambda_{H\Phi}|H|^2\Phi^2 + \lambda_{S\Phi}|S|^2\Phi^2 + \lambda_{SH}|H|^2|S|^2, \tag{6.2}$$

The total renormalizable Lagrangian then reads:

$$\mathcal{L}_{\text{tot}} = -\frac{1}{4}X_{\mu\nu}X^{\mu\nu} + |D_\mu^X S|^2 + (D_\mu^{SM}H)^\dagger(D^{SM\,\mu}H) + \frac{1}{2}\partial_\mu\Phi\partial^\mu\Phi - V(H,S,\Phi) + \mathcal{L}_{\text{SM}}, \tag{6.3}$$

where $H$ is the $SU(2)_L$ SM Higgs doublet and $D_\mu^{SM}$ is the SM covariant derivative. The $X_\mu$ field tensor and corresponding covariant derivative are defined as

$$X_{\mu\nu} = \partial_\mu X_\nu - \partial_\nu X_\mu; \;\; D_\mu^X S = \partial_\mu S - ig_X S X_\mu; \tag{6.4}$$

where $g_X$ denotes $U(1)_X$ gauge coupling. Below we are going to investigate limit of the above model when the mass of one of the physical scalars contained in the spectrum becomes very large. We expect to reproduce a version of the Stueckelberg model coupled to the extra scalar $\Phi$ and the SM Higgs doublet $H$. The goal is to determine, among the degrees of freedom of the considered model, the Stueckelberg scalar introduced in order to make the Stueckelberg Lagrangian gauge symmetric.

### 6.2.1 Positivity criteria

In order to formulate conditions for asymptotic positivity (for large field strengths) of the potential in Eq. (6.2) we shall first write down the matrix of quartic couplings in the basis: $|S|^2, \Phi^2, |H|^2$:

$$W \equiv \begin{pmatrix} \lambda_S & \frac{\lambda_{S\Phi}}{2} & \frac{\lambda_{SH}}{2} \\ \frac{\lambda_{S\Phi}}{2} & \lambda_\Phi & \frac{\lambda_{H\Phi}}{2} \\ \frac{\lambda_{SH}}{2} & \frac{\lambda_{H\Phi}}{2} & \lambda_H, \end{pmatrix}. \tag{6.5}$$

Now, a scalar potential biquadratic in fields is bounded from below if the matrix $W$ is co-positive [271]. Thus, the vacuum stability conditions for the potential in Eq. (6.2) are given by the Sylvester criteria for the co-positivity of $W$ [271, 272]:

$$\lambda_S > 0, \quad \lambda_\Phi > 0, \quad \lambda_H > 0, \tag{6.6}$$

also,

$$\tilde{\lambda}_{S\Phi} \equiv \lambda_{S\Phi} + 2(\lambda_S\lambda_\Phi)^{1/2} > 0, \tag{6.7}$$
$$\tilde{\lambda}_{H\Phi} \equiv \lambda_{H\Phi} + 2(\lambda_\Phi\lambda_H)^{1/2} > 0, \tag{6.8}$$
$$\tilde{\lambda}_{SH} \equiv \lambda_{SH} + 2(\lambda_S\lambda_H)^{1/2} > 0, \tag{6.9}$$
$$\lambda_\Phi^{1/2}\lambda_{SH} + \lambda_S^{1/2}\lambda_{H\Phi} + \lambda_H^{1/2}\lambda_{S\Phi} + 2(\lambda_S\lambda_\Phi\lambda_H)^{1/2} + 2(\tilde{\lambda}_{S\Phi}\tilde{\lambda}_{H\Phi}\tilde{\lambda}_{SH})^{1/2} > 0. \tag{6.10}$$

We emphasize that these are necessary and sufficient conditions for vacuum stability [271].

### 6.2.2 Minimization conditions and spontaneous symmetry breaking

We parametrize the scalar fields as follows:

$$H = \begin{pmatrix} \phi^+ \\ \frac{h+i\phi^0}{\sqrt{2}} \end{pmatrix}; \quad S = \frac{\rho}{\sqrt{2}} e^{i\sigma_S/v_S}. \tag{6.11}$$

The extrema conditions for the potential in Eq. (6.2) read

$$\left.\frac{\partial V}{\partial h}\right|_{h=v_h} = 0, \quad \left.\frac{\partial V}{\partial \rho}\right|_{\rho=v_S} = 0, \quad \left.\frac{\partial V}{\partial \Phi}\right|_{\Phi=v_\Phi} = 0. \tag{6.12}$$

Hereafter we assume $\mu_H^2,\ \mu_S^2,\ \mu_\Phi^2 > 0$ in order to generate proper symmetry breaking. We will require that the above conditions are satisfied by non-zero vacuum expectation values (vevs) of $\langle H\rangle = v_h \neq 0$ and $\langle S\rangle = v_S \neq 0$, while for $\Phi$ we require zero-vev; $\langle\Phi\rangle = v_\Phi = 0$.

The following relations are implied by the minimization conditions (6.12):

$$\begin{aligned} &v_h(2\lambda_H v_h^2 + \lambda_{SH} v_S^2 - 2\mu_H^2) = 0 \\ &v_S(2\lambda_S v_S^2 + \lambda_{SH} v_h^2 - 2\mu_S^2) = 0 \\ &v_\Phi(2\mu_\Phi^2 + 4\lambda_\Phi v_\Phi^2 + \lambda_{H\Phi} v_h^2 + \lambda_{S\Phi} v_S^2) = 0. \end{aligned} \tag{6.13}$$

We will therefore expand $H$ and $S$ around the non-zero vevs as follows

$$H = \begin{pmatrix} \phi^+ \\ \frac{h+v_h+i\phi^0}{\sqrt{2}} \end{pmatrix}; \quad S = \frac{\rho + v_S}{\sqrt{2}} e^{i\sigma_S/v_S}, \tag{6.14}$$

where we have used the same notation for the fluctuations around the vacuum as earlier for the initial fields. In the expression above $\sigma_S$ is the Goldstone boson that constitutes the longitudinal component of the $X_\mu$, while the SM Goldstone

| # | $v_h^2$ | $v_S^2$ | $v_\Phi^2$ | $V\|_{\text{extr}}$ |
|---|---|---|---|---|
| 1 | 0 | 0 | 0 | 0 |
| 2 | 0 | $\frac{\mu_S^2}{\lambda_S}$ | 0 | $-\frac{1}{4}\frac{\mu_S^4}{\lambda_S}$ |
| 3 | $\frac{\mu_H^2}{\lambda_H}$ | 0 | 0 | $-\frac{1}{4}\frac{\mu_H^4}{\lambda_H}$ |
| 4 | $\frac{2\left(2\lambda_S\mu_H^2-\lambda_{SH}\mu_S^2\right)}{4\lambda_H\lambda_S-\lambda_{SH}^2}$ | $\frac{2\left(2\lambda_H\mu_S^2-\lambda_{SH}\mu_H^2\right)}{4\lambda_H\lambda_S-\lambda_{SH}^2}$ | 0 | $-\frac{\lambda_S\mu_H^4-\lambda_{SH}\mu_H^2\mu_S^2+\lambda_H\mu_S^4}{4\lambda_H\lambda_S-\lambda_{SH}^2}$ |

**Table 6.2:** The table shows possible extrema with $v_\Phi = 0$ and corresponding values of the potential 6.2.

bosons are $\phi^{\pm,0}$. Note that there is no potential for $\sigma_S$. We have adopted a Cartesian parametrization for the doublet $H$ together with a polar parametrization for the complex singlet $S$. The purpose was to find out the degree of freedom that corresponds to the Stueckelberg scalar, it will be discussed in details shortly.

In Table 6.2 we list all possible extrema that satisfy (6.13) for $v_\Phi = 0$ together with corresponding values of the potential. There may exist three other extrema with $v_\Phi \neq 0$, however for the stability of $\Phi$ we are going to choose parameters that ensure $v_\Phi = 0$. We are going to find conditions that guarantee the solution #4 to be the global minimum. First we must make sure that $v_\Phi = 0$ is the only possible vev for $\Phi$, for that purpose we will assume that for given quartic couplings we adjust $\mu_\Phi^2$ such that $2\mu_\Phi^2 + 4\lambda_\Phi v_\Phi^2 + \lambda_{H\Phi} v_h^2 + \lambda_{S\Phi} v_S^2 > 0$, then indeed $v_\Phi = 0$ is the only solution of (6.13). Next, we observe that

$$V_4 - V_2 = -\frac{(-2\lambda_S\mu_H^2 + \lambda_{SH}\mu_S^2)^2}{4\lambda_S(4\lambda_H\lambda_S - \lambda_{SH}^2)} \tag{6.15}$$

$$V_4 - V_3 = -\frac{(-2\lambda_H\mu_S^2 + \lambda_{SH}\mu_H^2)^2}{4\lambda_H(4\lambda_H\lambda_S - \lambda_{SH}^2)}\,. \tag{6.16}$$

As it will be seen, we assume $4\lambda_H\lambda_S - \lambda_{SH}^2 > 0$ in order to ensure positivity of masses squared, in addition $\lambda_{S,H} > 0$ for the positivity of the potential, therefore hereby we have shown that the extremum #4 is the deepest one, and it must be the global minimum regardless what is the nature of solutions #1, #2 and #3 (refer to tabl. 6.2).

The mass matrix squared corresponding to the solution #4 for physical degrees of freedom expressed in the basis $\{h, s, \Phi\}$ reads:

$$\mathcal{M}^2 = \begin{pmatrix} 2v_h^2\lambda_H & v_h v_S \lambda_{SH} & 0 \\ v_h v_S \lambda_{SH} & 2v_S^2\lambda_S & 0 \\ 0 & 0 & 2\mu_\Phi^2 + \lambda_{H\Phi} v_h^2 + \lambda_{S\Phi} v_S^2 \end{pmatrix}, \tag{6.17}$$

where it is clearly seen that only $\{h, \rho\}$ mixes (as they get non-zero vevs) while $\Phi$ (the (3,3) element of the matrix) only receives contribution proportional to the vev of the other two fields. The eigenvalues of the mass matrix read:

$$m_{\pm}^2 = \lambda_H v_h^2 + \lambda_S v_S^2 \pm \sqrt{(\lambda_H v_h^2 + \lambda_S v_S^2)^2 - (v_h v_S)^2(4\lambda_S\lambda_H - \lambda_{SH}^2)}, \quad (6.18)$$

$$m_{\Phi}^2 = 2\mu_{\Phi}^2 + \lambda_{H\Phi} v_h^2 + \lambda_{S\Phi} v_S^2 \,. \quad (6.19)$$

Hereafter we will adopt the convention that $h_1$ is always the 125 GeV SM-like Higgs boson discovered in 2012 at the LHC. Therefore $m_1 = m_{\pm}$ and $m_2 = m_{\mp}$ for $h_1$ heavier (upper sign) or lighter (lower sign) than $h_2$. Hereafter we are going to consider the case of very heavy $h_2$, i.e. $m_2 \gg m_1$. As it is seen from (6.18), for quartic couplings not exceeding perturbative limits $\sim 4\pi$, heavy $h_2$ requires large $v_S$, i.e. $v_S \gg v_h$. It is clear that the presence of a minimum at the extremum #4 requires:

$$4\lambda_S\lambda_H - \lambda_{SH}^2 > 0 \qquad \text{and} \qquad 2\mu_{\Phi}^2 + \lambda_{H\Phi} v_h^2 + \lambda_{S\Phi} v_S^2 > 0 \,. \quad (6.20)$$

The first condition above together with the potential positivity condition (6.9) implies $\lambda_{SH} < 2\sqrt{\lambda_S\lambda_H}$. Note also that $4\lambda_S\lambda_H - \lambda_{SH}^2 > 0$ guarantees positivity of $v_h^2$ and $v_S^2$, see tabl. 6.2.

Now we can now rotate the weak basis to get the mass basis via:

$$\begin{pmatrix} h_1 \\ h_2 \\ \Phi \end{pmatrix} = \mathcal{R}^{-1} \begin{pmatrix} h \\ s \\ \Phi \end{pmatrix}, \quad (6.21)$$

where $\mathcal{R}$ is the Euler rotation matrix of the form:

$$\mathcal{R} = \begin{pmatrix} \cos\alpha & -\sin\alpha & 0 \\ \sin\alpha & \cos\alpha & 0 \\ 0 & 0 & 1 \end{pmatrix}. \quad (6.22)$$

The mixing angle $\alpha$ is determined by the entries of the mass matrix as follows[1]:

$$\sin 2\alpha = \frac{\text{sign}(\lambda_{SM} - \lambda_H) 2\mathcal{M}_{12}^2}{\sqrt{(\mathcal{M}_{11}^2 - \mathcal{M}_{22}^2)^2 + 4(\mathcal{M}_{12}^2)^2}} \qquad \cos 2\alpha = \frac{\text{sign}(\lambda_{SM} - \lambda_H)(\mathcal{M}_{11}^2 - \mathcal{M}_{22}^2)}{\sqrt{(\mathcal{M}_{11}^2 - \mathcal{M}_{22}^2)^2 + 4(\mathcal{M}_{12}^2)^2}} \quad (6.23)$$

The potential (6.2) has 9 real parameters:

$$\{\mu_{H,S}, \mu_{\Phi}, \lambda_{H,S,\Phi}, \lambda_{H\Phi}, \lambda_{S\Phi}, \lambda_{SH}\}. \quad (6.24)$$

Amongst these, $\mu_{H,S}$ can be replaced by the vevs $v_h$ and $v_S$ following Eq. (6.13). Adopting (6.18) for $m_1 = m_-$ one can express $v_S$ through $\{m_1^2 = 2\lambda_{SM} v_h^2, \lambda_H, \lambda_S, \lambda_{SH}\}$ as follows:

$$v_S^2 = v_h^2 \frac{4\lambda_{SM}(\lambda_H - \lambda_{SM})}{4\lambda_S(\lambda_H - \lambda_{SM}) - \lambda_{SH}^2}. \quad (6.25)$$

This reduces the number of free parameters in the scalar sector to seven:

$$\{\mu_{\Phi}, \lambda_{H,S,\Phi}, \lambda_{SH}, \lambda_{H\Phi}, \lambda_{S\Phi}\}.$$

[1] See [183, 273] for a detailed discussion of the $H - S$ system.

### 6.2.3 Decoupling limit

Here we would like to explore the *decoupling* limit of a very heavy new scalar ($h_2$). From (6.18) it is clear that the limit $m_2 \to \infty$ requires $v_S \to \infty$. In order to do that, it is useful to define:

$$\Delta \equiv 4\lambda_S(\lambda_H - \lambda_{SM}) - \lambda_{SH}^2 \tag{6.26}$$

From (6.25) we find:

$$v_S^2 = v_h^2 \frac{4\lambda_{SM}(\lambda_H - \lambda_{SM})}{\Delta}, \tag{6.27}$$

from where we see that large $v_S^2$ corresponds to $\Delta \to 0$. From the parameters of the scalar potential (listed in Appendix. E) we obtain:

$$m_2^2 = v_h^2 \frac{8\lambda_S\lambda_{SM}(\lambda_H - \lambda_{SM})}{\Delta} + \mathcal{O}(\Delta^0). \tag{6.28}$$

So, clearly $\Delta \to 0$ implies $m_2 \to \infty$ unless $\lambda_H = \lambda_{SM}$. Now we can investigate the behavior of the mixing angle for $\Delta \approx 0^+$, it is easy to see that:

$$\sin 2\alpha = \text{sign}(\lambda_{SM} - \lambda_H) \left(\frac{\Delta}{\lambda_S \lambda_{SM}}\right)^{1/2} + \mathcal{O}(\Delta^{3/2}), \tag{6.29}$$

so it is evident that $\alpha \to 0$ as $\Delta \to 0$ ($m_2 \to \infty$). From now on we shall use the following set of parameters: [2]

$$(m_1, m_2, v_h, \lambda_S, \lambda_H) \qquad \text{and} \qquad (m_\Phi, \lambda_\Phi, \lambda_{H\Phi}, \lambda_{S\Phi}). \tag{6.30}$$

Using the relations in Eq. (E.11) and Eq. (E.12) assuming large $m_2$, we are now going to construct an effective residual theory in the limit of large $m_2$. Note that this leads to $\sin 2\alpha \to 0$, such that

$$h_1 = -\cos\alpha\, h + \sin\alpha\, \rho \longrightarrow h \tag{6.31}$$

$$h_2 = -\sin\alpha\, h + \cos\alpha\, \rho \longrightarrow \rho\,. \tag{6.32}$$

Therefore all we need to do is to expand the Lagrangian for the SM supplemented by $S$, $X_\mu$ and $\Phi$ around the vacuum adopting the parametrization (6.14) and drop the $h_2 \leftrightarrow \rho$ and rename $h_1$ by $h$. It turns out that the resulting effective Lagrangian reads:

$$\mathcal{L}_{\text{lim}} = -\frac{1}{4}X_{\mu\nu}X^{\mu\nu} + |D_\mu^X S|^2 + (D_\mu^{SM} H)^\dagger (D^{SM\,\mu} H) + \frac{1}{2}\partial_\mu\Phi\partial^\mu\Phi - V_{\text{lim}}(h,\Phi)\,, \tag{6.33}$$

where the potential is independent of $\sigma_S$ and given by:

$$\begin{aligned} V_{\text{lim}}(h,\Phi) \;=\; & \frac{1}{2}m_h^2 h^2 + \lambda_H v_h h^3 + \frac{1}{4}\lambda_H h^4 + \\ & + \frac{1}{2}m_\Phi^2\Phi^2 + \lambda_{H\Phi} v_h h\Phi^2 + \lambda_\Phi\Phi^4 + \frac{1}{2}\lambda_{H\Phi}h^2\Phi^2 + \text{const.} \end{aligned} \tag{6.34}$$

[2] We consider the case $m_2 > m_1$, so $\lambda_H > \lambda_{SM}$.

where $m_h = m_1$.

The kinetic terms in the limit $m_2 \to \infty$ should be written after expanding around the vacuum and decoupling/removing $\rho$ as follows:

$$\begin{aligned} |D_\mu S|^2 &= \frac{1}{2}(m_X X_\mu - \partial_\mu \sigma_S)(m_X X^\mu - \partial^\mu \sigma_S) \\ (D_\mu^{SM} H)^\dagger (D^{SM\,\mu} H) &= \frac{1}{2}\partial_\mu h \partial^\mu h + \cdots , \end{aligned} \tag{6.35}$$

where the ellipsis contain all the interaction terms.

### 6.2.4 Stueckelberg Lagrangian in decoupling limit

One can easily notice that the effective Lagrangian (6.33) coincides with the standard form of the Stueckelberg Lagrangian invariant under the following transformation:

$$\begin{aligned} X_\mu &\to X'_\mu = X_\mu + \partial_\mu \theta \\ \sigma_S &\to \sigma'_S = \sigma_S + m_X \theta \\ \Phi &\to \Phi' = \Phi \end{aligned} \tag{6.36}$$

In other words we have just proven that in the limit $m_2 \to \infty$ the theory defined by the Lagrangian (6.3) reduces to the Stueckelberg Lagrangian.

In addition our model is invariant under the $Z_2$:

$$X_\mu \to -X_\mu, \qquad \sigma_S \to -\sigma_S, \qquad \Phi \to -\Phi \tag{6.37}$$

There are various comments here in order. First, note that the Stueckelberg scalar is just the Goldstone boson $\sigma_S$. To see this, the polar parametrization of $S$ adopted in Eq. (6.14) was crucial. A consequence of that was also the disappearance of the potential for $\sigma_S$. Since our model is gauge invariant, the quantization requires fixing a gauge. We adopt the following gauge fixing term

$$\mathcal{L}_{gf} = -\frac{1}{2\xi}\left(\partial^\mu X_\mu + \xi m_X \sigma_S\right)^2 . \tag{6.38}$$

The advantage of the adopted gauge fixing is that it cancels mixing between $\partial^\mu X_\mu$ and $\sigma_S$. Expanding the Lagrangian one obtains eventually

$$\begin{aligned} \mathcal{L} \;=\; & \mathcal{L}_{\text{lim}} + \mathcal{L}_{gf} = -\frac{1}{4}X_{\mu\nu}X^{\mu\nu} + \frac{m_X^2}{2}X_\mu X^\mu - \frac{1}{2\xi}\left(\partial^\mu X_\mu\right)^2 + \frac{1}{2}\partial_\mu\sigma_S\partial^\mu\sigma_S - \frac{1}{2}\xi m_X^2\sigma_S^2 + \\ & + \frac{1}{2}\partial_\mu\Phi\partial^\mu\Phi + \frac{1}{2}\partial_\mu h\partial^\mu h - V_{\text{lim}}(h,\Phi) + \cdots . \end{aligned} \tag{6.39}$$

In order to gauge-fix away $\sigma_S$ one must adopt the unitary gauge, which corresponds to $\xi \to \infty$. In the Stueckelberg formalism, in the unitary gauge, in presence of $\Phi$, one could expect presence of a term like $X_\mu X^\mu \Phi^2$ since it is allowed by symmetries. However, it turns out that the operator $X_\mu X^\mu \Phi^2$ may only originate from dim.6 term $|D_\mu S|^2\Phi^2$ and therefore must be suppressed by $1/\Lambda^2$. This is the only gauge invariant way to generate an operator $\propto X_\mu X^\mu \Phi^2$. It explains why the operator $X_\mu X^\mu \Phi^2$

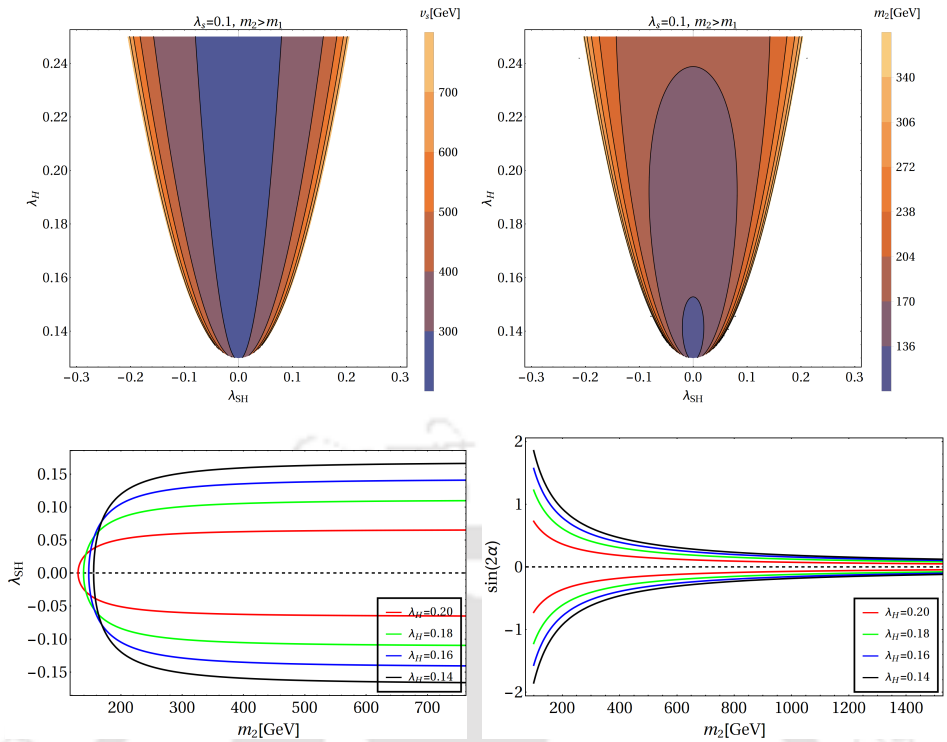


**Figure 6.1:** Top: The contours show allowed range of the vev $v_S$ and mass of the decoupled heavy scalar $m_2$ as a function of $\lambda_H$ and $\lambda_{SH}$ for fixed $\lambda_S = 0.1$. Bottom left: $\lambda_{SH}$ as a functions of $m_2$ for fixed values of $\lambda_H$. Bottom right: $\sin(2\alpha)$ as a functions of $m_2$ for fixed values of $\lambda_H$. Decoupling of the dark sector is clearly seen in the limit of large $m_2$.

can not appear as an unsuppressed dim.4 operator, even though naively it could be added within the Stueckelberg strategy.

The decoupling limit of the scalar potential consistent with all the theoretical constraints is illustrated in Fig. 6.1. In the top left panel, we show the allowed region in the $(\lambda_H, \lambda_{SH})$ plane for $m_2 > m_1$ where the colors varying from blue to yellow show larger $v_s$. Top right panel shows the same but coloring is with respect to $m_2$. Both these top panels show the decoupling limit at the outer edge of the allowed parameter space. In bottom left panel, we show $\lambda_{SH}$ as a function of $m_2$ at fixed values of $\lambda_H$. Similarly the bottom right figure shows $\sin(2\alpha)$ as a function of $m_2$, the convergence to zero-mixing angle is clearly shown. Summarizing, to reach the Stueckelberg limit starting from the Lagrangian (6.3) a carefully adjusted trajectory in the parameter space must be adopted. An important consequence of approaching the $m_2 \to \infty$ limit is the decoupling of the dark sector from the SM at dimension-4 operators by $\sin(2\alpha) \to 0$ and decoupling of $X_\mu$ from $S$ by $g_X \to 0$. It should also be recalled that to avoid instability of the potential $m_2$ must be finite (although can be large).

### 6.2.5 Higher dimensional operator to connect DM and SM sectors

Note that the coupling $\lambda_{H\Phi}$, which parametrizes the quartic portal interactions $\Phi^2|H|^2$, remains unsuppressed in the decoupling limit. Besides CP-violating operator $X_{\mu\nu}\tilde{X}^{\mu\nu}$ [3] this is the only renormalizable (dim-4) communication between the dark and visi-

[3] That is irrelevant for DM phenomenology considered in this paper.

ble sectors in the limit. Leading corrections to this communication will be provided by dim-5 operators that are invariant under transformations from $\mathcal{G} = SU(3)_C \times SU(2)_L \times U(1)_Y \times U(1)_X \times Z_2$ and under Lorentz transformations and which are made of the scalar $\Phi$, the vector $X_\mu$ and possibly combinations of SM fields. It is easy to see that there are only two non-trivial operators that satisfy required symmetry conditions [4]:

$$\mathcal{L}_{\text{dim-5}} = \frac{c}{\Lambda} B_{\mu\nu} X^{\mu\nu} \Phi + \frac{\tilde{c}}{\Lambda} B_{\mu\nu} \tilde{X}^{\mu\nu} \Phi. \tag{6.40}$$

This operator has already been introduced in [269], where it was mentioned that such an operator can be generated at the tree level only via antisymmetric tensor mediators. Finally, one can then write down the complete Lagrangian as:

$$\begin{aligned}
\mathcal{L}_{\text{tot}} &= \mathcal{L}_{\text{lim}} + \mathcal{L}_{gf} + \mathcal{L}_{\text{dim-5}} \\
&= -\frac{1}{4} X_{\mu\nu} X^{\mu\nu} + \frac{m_X^2}{2} X_\mu X^\mu - \frac{1}{2\xi} \left(\partial^\mu X_\mu\right)^2 + \frac{1}{2} \partial_\mu \sigma_S \partial^\mu \sigma_S - \frac{1}{2} \xi m_X^2 \sigma_S^2 + \\
&\quad + \frac{1}{2} \partial_\mu \Phi \partial^\mu \Phi + \frac{1}{2} \partial_\mu h \partial^\mu h - \left\{ \frac{1}{2} m_h^2 h^2 + \lambda_H v_h h^3 + \frac{1}{4} \lambda_H h^4 + \right. \\
&\quad \left. + \frac{1}{2} m_\Phi^2 \Phi^2 + \lambda_{H\Phi} v_h h \Phi^2 + \lambda_\Phi \Phi^4 + \frac{1}{2} \lambda_{H\Phi} h^2 \Phi^2 + \text{const.} \right\} + \cdots + \\
&\quad + \frac{c}{\Lambda} B_{\mu\nu} X^{\mu\nu} \Phi + \frac{\tilde{c}}{\Lambda} B_{\mu\nu} \tilde{X}^{\mu\nu} \Phi \,,
\end{aligned} \tag{6.41}$$

where ellipsis denote interactions of the SM Higgs boson $h$ with other SM components that are not relevant here. We note here that we necessarily assume $\Lambda > m_2$, otherwise higher dimensional operators (neglected in this work) would appear in the scalar potential. We also adopt the following notations hereafter: $\alpha(\tilde{\alpha}) = \frac{c(\tilde{c})}{\Lambda}$; $\beta = \frac{\tilde{\alpha}}{\alpha}$.

## 6.3 DM yield via freeze-in

It is clear from the preceeding section that the couplings $\Phi\Phi h_1 h_1$ and $\Phi\Phi h_1$ remain unsuppressed in the decoupling limit that we are exercising here. These interactions are $\propto \lambda_{H\Phi}$, which is not suppressed. This is the only renormalizable communication between the dark and visible sectors. So, it is quite likely to assume that in the early universe $\Phi$ is abundant being in equilibrium with the SM (i.e. with $h$). Since $\Phi$ is the next lightest $Z_2$-odd dark component its decays and annihilations may produce DM (i.e. $X$) non-thermally. This the mechanism (freeze-in) we will investigate hereafter. The Boltzmann equations governing $X$ production in the early universe are derived in Appendix. F.1. We will discuss the applicability of neglecting various masses while calculating the amplitudes for decays and annihilations. Before going into the details, we would like to clarify that in the following sections, in order to satisfy the EFT limit and also have a successful freeze-in, we will adopt the following hierarchy amongst the scales and masses involved in the model:

[4] Another dim-5 operator would require a presence of right-handed neutrinos $\nu_R$. This option will not be pursued hereafter.

$$\Lambda \gtrsim m_2 \gtrsim T_{RH} > m_\Phi > m_X, \tag{6.42}$$

where $T_{\rm RH}$ is the reheating temperature at which the inflation ends.

### 6.3.1 DM production: decay and annihilation channels

The processes that produce VDM, can easily be cooked up from interactions introduced in the preceding section and vertices collected in Appendix E.3. We classify all the DM number changing processes on the basis of their occurrences before electroweak (EW) symmetry breaking (EWSB) i.e. for thermal bath temperature $T > T_{\rm EW} \simeq 160\,{\rm GeV}$ or after EWSB, i.e. for $T < T_{\rm EW}$. Due to the presence of the $\Phi X B$ vertex the VDM $X$ can always be produced from the decay of the scalar $\Phi$ that maintains thermal equilibrium with the SM bath via the portal interaction $\lambda_{H\Phi}\,|H|^2\,\Phi^2$. This decay channel, shown in Fig. 6.2, is always present before and after EWSB as $m_\Phi > m_X$, which is anyway our prime assumption for the stability of the VDM. After EWSB, the decay occurs to $Z, \gamma$. Apart from the decay, we also have four $2 \to 2$ annihilation channels with one DM in the final state as shown in Fig. 6.3 before EWSB [5]. The processes include two $t$-channel and two $s$-channel graphs including Goldstone bosons ($\phi^{0,\pm}$). Note that, before EWSB all the SM states are massless and the Goldstone bosons (GB) are propagating degrees of freedom as the $SU(2)_L$ scalar has the form:

$$H = \begin{pmatrix} \phi^+ \\ \phi^0 \end{pmatrix}. \tag{6.43}$$

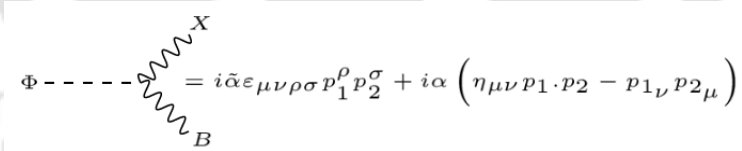


**Figure 6.2:** Decay of $\Phi \to XB$ before EWSB and $\Phi \to X\gamma(Z)$ after EWSB, which contributes to the freeze-in production of $X$. The vertex factor shown here is the one for $\Phi \to XB$.

The dark sector fields $\{\Phi, X\}$, on the other hand, are massive due to $U(1)_X$ breaking, which occurs at much higher energy scale. Due of the presence of totally antisymmetric rank four Levi-Civita symbol in the interaction vertex $\Phi X B$ and the momenta dependent interaction vertices for the GB's, all the processes involving Goldstone bosons in $t$-channel and $s$-channel identically become zero at the level of amplitude squared. Therefore, all those processes with GB's drop out leaving only the $\Phi \to X, B$ decay channel, along with the two $2 \to 2$ annihilation diagrams $f\Phi \to fX,\ ff \to X\Phi$ (the top right and bottom left diagram of Fig. 6.3) for DM production via freeze-in before EWSB. However, as we shall see in subsequent sections, the decay before EWSB is sub-dominant as compared to the annihilation processes for large reheat temperature ($T_{\rm RH} \gg m$).

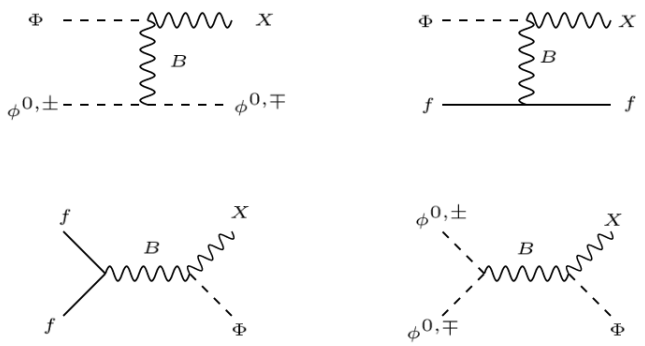


**Figure 6.3:** Annihilations via $t$-channel (top) and $s$-channel (bottom) leading to the production of VDM $X$ *before* EWSB. The diagrams with Goldstone bosons identically vanish, leaving only two diagrams with SM fermions.

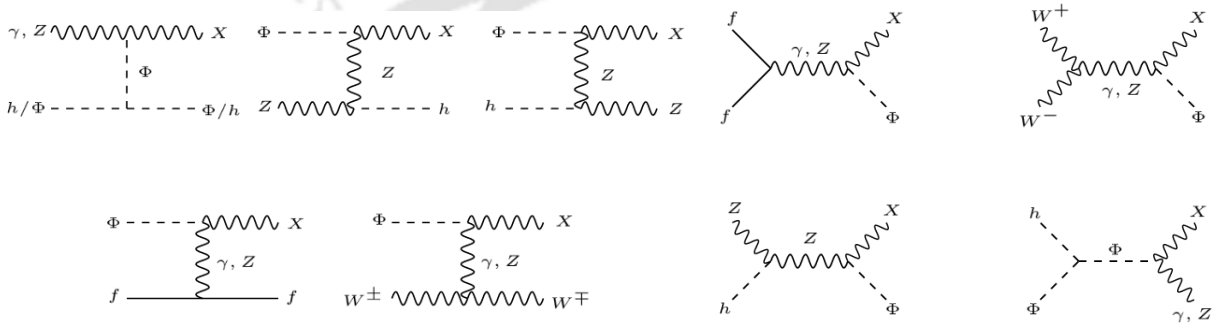


**Figure 6.4:** Annihilations via $t$-channel (left panel) and $s$-channel (right panel) leading to the production of $X$ *after* EWSB.

Once the EW symmetry is broken, the GB's are no more individual physical degrees of freedom, instead they become longitudinal polarizations of the charged and neutral SM gauge bosons with $v_h = 246$ GeV. Also, the physical gauge bosons can be obtained in the mass basis by rotating the weak basis as:

$$\begin{pmatrix} B_\mu \\ W_{3\mu} \end{pmatrix} = \begin{pmatrix} c_w & -s_w \\ s_w & c_w \end{pmatrix} \begin{pmatrix} A_\mu \\ Z_\mu \end{pmatrix}, \tag{6.44}$$

where $c(s)_w$ is the (co)sine of the Weinberg angle. Thus, after EWSB, the decay corresponds to $\Phi \to X, \gamma(Z)$, while all $2 \to 2$ annihilation channels giving rise to DM final states are shown in Fig. 6.4. Due to massive propagator contributions after EWSB, the decay becomes more relevant for the determination of the DM yield, as we will demonstrate and discuss later.

[5]All such processes with a pair of DM in the final state are suppressed by $\sim 1/\Lambda^2$ and hence sub-dominant.

### 6.3.2 Validity of UV freeze-in

In this section, we demonstrate the difference between massless and massive limit of DM production cross-section and therefore we will be able comment on limitations of the Ultra Violet (UV) freeze-in advocated in [157, 274]. Here we limit ourself to the period before EWSB so all the SM particles are massless. The masses of the dark sector $\Phi$ and $X$ are assumed to be of the same order, typically $m_\Phi \sim m_X \sim m \sim \mathcal{O}(1\text{TeV})$. Hereafter the "massless limit" refers to zero-mass approximations, i.e. both SM and dark masses are zero. Our task in this section is to estimate size of mass effects, i.e. contributions to the yield that depend on the dark masses. Since we limit ourself to the temperatures above $T_{\rm EW}$ therefore Eq. (F.12) can be simplified [6] as:

$$Y_X(T_{\rm EW}) = \frac{1}{4\cdot 512\pi^6}\int_{T_{\rm EW}}^{T_{\rm RH}} \frac{dT}{s(T)\,H(T)} \int_0^\infty ds \left\{\int d\Omega \left|\mathcal{M}^{\rm bEWSB}[s,\cos\theta]\right|^2_{i,j\to X,k}\right\} \sqrt{s} K_1\left(\frac{\sqrt{s}}{T}\right). \tag{6.45}$$

Here onward we shall refer to $\mathcal{M}^{\rm bEWSB}$ as $\mathcal{M}$. For strictly massless case the integration over $s$ can be performed analytically, so the result reads

$$Y_{m=0} = AI(\theta_{min})\frac{45T_{RH}}{512\pi^7}\frac{16M_{pl}}{1.66 g_{\star s}\sqrt{g_{\star\rho}}}, \tag{6.46}$$

where $A$ contains all the couplings and constant factors that arise in the computation of $|\mathcal{M}^{m=0}[s,\cos\theta]|^2_{i,j\to X,k}$, and it is defined through the following relation:

$$\left|\mathcal{M}^{m=0}[s,\cos\theta]\right|^2_{i,j\to X,k} = Asm(\cos\theta), \tag{6.47}$$

with $m(\cos\theta)$ containing all the angular dependance of the amplitude squared while

$$I(\theta_{\rm min}) \equiv \frac{1}{2}\int_{-1}^{\cos\theta_{\rm min}} d\cos\theta m(\cos\theta), \tag{6.48}$$

where $\theta_{\rm min}$ is an angular cutoff necessary to avoid singularities that appear in the forward direction for t-channel diagrams, in the following $\theta_{\rm min} = 10^{-2}$ will be adopted.

Now, we would like to estimate the difference between the massless and massive limit. For that, let us define:

$$\Delta Y(T) \equiv Y(T)|_{m=0} - Y(T)|_{m\neq 0}. \tag{6.49}$$

Also, note that,

$$\left|\mathcal{M}^{m\neq 0}[s,\cos\theta]\right|^2_{i,j\to X,k} = \left|\mathcal{M}^{m=0}[s,\cos\theta]\right|^2_{i,j\to X,k} + \mathcal{O}\left(\frac{m^2}{s}\right). \tag{6.50}$$

[6] The contribution from $\Phi$ decays are negligible here.

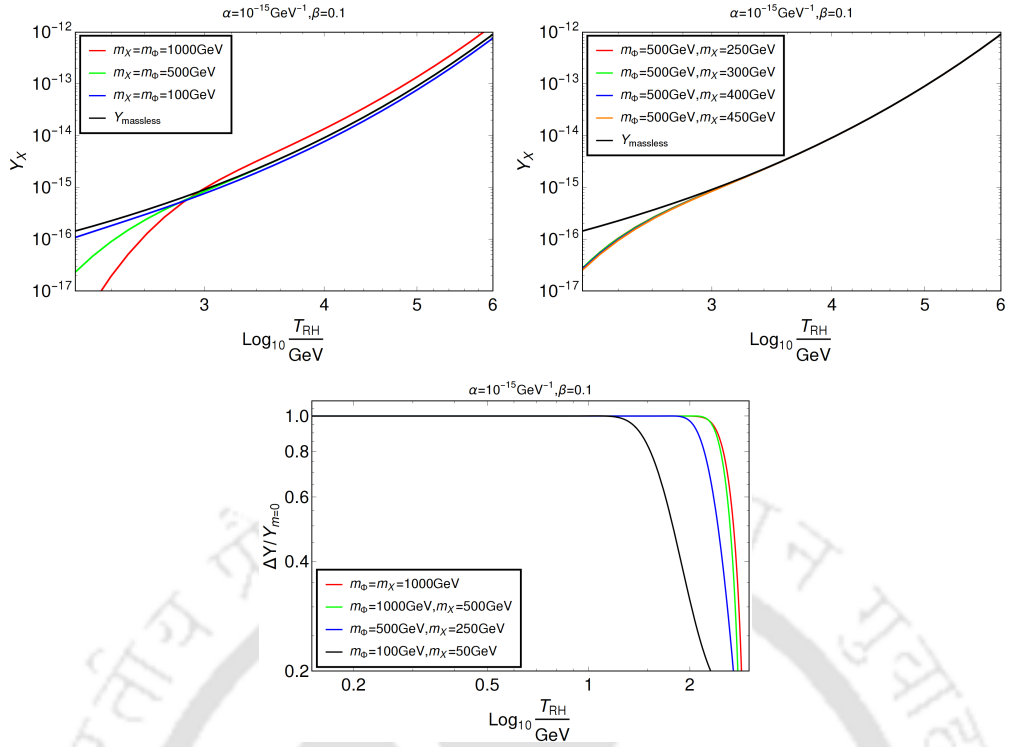


**Figure 6.5:** Top panels: Comparison of the yield at $T_{\rm EW}$ in the massive case versus that in the massless case with respect to the reheat temperature, where the red, green and blue curves correspond to the massive cases while the black curve represents the massless case. Bottom panel: Variation of $\Delta Y/Y_{m=0}$ with the reheat temperature for different choices of the masses shown in different colours. In all the plots "massless" refers to $\to m = 0$.

We assume here that the terms $\mathcal{O}\left(\frac{m^2}{s}\right)$ are negligible, note however that the mass dependance remains in $s_{\rm min} = m^2$. Then, for processes with amplitude squared of the form given in Eq. (6.47) we find:

$$\Delta Y(T_{\rm EW}) \approx A\frac{45}{512\pi^7}\frac{I(\theta_{\rm min})M_{\rm Pl}}{1.66\cdot(g_\star)^{1/2}g_\star^s}\int_{T_{\rm EW}}^{T_{\rm RH}}dT'\int_0^{\frac{m}{T'}}dx\,x^4K_1(x), \tag{6.51}$$

where $x \equiv \sqrt{s}/T$. As an example, let's consider a $t$-channel process $\Phi f \to X f$, where $f$ stands for the SM fermions. Then we find $I(\theta_{\rm min}) = 1/2\int_{-1}^{\cos\theta_{\rm min}} d\cos\theta(5+\cos\theta-\cos 2\theta)/(1-\cos\theta) \approx 75$. For $T_{\rm RH} \gg m, T_{\rm EW}$ we can estimate $\Delta Y(T_{\rm EW})$ as follows

$$\Delta Y(T_{\rm EW}) \approx AI(\theta_{min})\frac{45}{512\pi^7}\frac{M_{pl}}{1.66g_{\star s}\sqrt{g_{\star\rho}}}4.65m. \tag{6.52}$$

Note that $\Delta Y(T_{\rm EW})$ is linear in $m$ as it obviously should vanish in the limit $m \to 0$. We should also note that Eq. (6.52) is process independent and can be written in this particular form whenever the matrix element squared can be expressed in the form of Eq. (6.47).

Now, let us find out the condition under which $\Delta Y$ becomes as large as $Y_{\rm massless}$, as that will dictate the condition for which massless limit can be no longer adopted for the UV freeze-in scenario. This can simply be found out by equating Eq. (6.52) and Eq. (6.46):

$$\Delta Y = AI(\theta_{min})\frac{45}{512\pi^7}\frac{M_{pl}}{1.66 g_{\star s}\sqrt{g_{\star\rho}}}\left(m\int_0^{T_{\rm RH}/m} dug(u)\right) \lesssim Y_{m=0} \quad (6.53)$$
$$\implies m \lesssim 3.5\, T_{\rm RH}.$$

This implies that, as long as the masses involved in the freeze-in process are approximately less that three times of the reheat temperature, one can overlook the masses and the yield can be computed in the massless limit. This, in other words, justifies the fact that for large reheat temperature the massless limit is a good approximation for obtaining the UV freeze-in yield. In Fig. 6.5, we demonstrate the difference between the yield obtained for massive and massless case of DM production for all the processes before EWSB put together. We plot $Y_X(T = T_{EW})$ as a function of $T_{\rm RH}$ and see that massive case sharply differs from the massless case (black line) at small $T_{\rm RH}$, while they exactly merge as the reheat temperature becomes large. In the bottom panel we show the same feature in terms of $\frac{\Delta Y}{Y_{m=0}}$ for different choices of $m_{X,\Phi}$.

## 6.4 DM relic abundance via freeze-in

As described in details in the last section, within the freeze-in paradigm, the DM yield is controlled by the annihilation and/or decay of SM as well as dark sector particles. Following Eq. (F.13) in Appendix F.1 we write down the BEQ governing the DM yield as [150]:

$$xHs\frac{dY_X}{dx} = \gamma_{\rm ann} + \gamma_{\rm D}, \quad (6.54)$$

where $Y_X = n_X/s$. $H$ is the Hubble parameter given by $H = 1.66\sqrt{g_{\star\rho}}T^2/M_{pl}$ and $x = m_X/T$ is a dimensionless quantity to parametrize the temperature of the thermal bath. As mentioned earlier, the $\gamma$'s denote the so-called reaction density for different particles annihilating (decaying) to the DM. The detail expressions of the reaction densities for $2 \to 2$ annihilations and $1 \to 2$ decays are given in Appendix. F. In order to compute the DM yield, we solve Eq. (6.54) with the initial condition $Y_X \approx 0$ at large $T$ *i.e.*, small $x$ in accordance with the usual FIMP set-up [7]. By solving Eq. (6.54) one can obtain the total DM yield $Y_X$ at the present epoch *i.e.*, $Y_X(T_0)$. The relic abundance of $X$ at present temperature can then be obtained via:

$$\Omega_X h^2 = \left(2.75 \times 10^8\right)\left(\frac{m_X}{\rm GeV}\right) Y_X(T_0). \quad (6.55)$$

We must also remind that the PLANCK [36] allowed relic density reads:

$$\Omega h^2 = 0.11933 \pm 0.00091, \quad (6.56)$$

[7] The zero intial abundance of the DM could be a result of reheating itself when the inflaton decays preferentially to the visible sector without reheating the hidden sector, or may be due to some other mechanism.

which we will use to find the relic density allowed parameter space of the model.

Since in our case the connection between the dark and the visible sector proceeds via a non-renormalizable interaction, the DM abundance is usually characterized by UV freeze-in [157, 274] limit, where the DM abundance is sensitive to the reheat temperature $T_{\rm RH}$ of the universe and NP scale $\Lambda$ only. This is in sharp contrast to the Infra-Red or IR freeze-in scenario where the two sectors communicate via renormalizable operators, and the DM abundance is set by the IR physics *i.e.*, the yield becomes maximum at low temperature, typically at $T \sim m_X$ [145]. As we have already shown in the preceding section, when reheat temperature drops close to the masses involved in the annihilation or DM production process, massive kinematics start playing a key role in the yield and UV limit can not be trusted. Therefore our analysis will be divided into two regimes, depending on the scale of the reheat temperature ($T_{\rm RH}$):

- $T_{\rm RH} >> m_i$, where the reheat temperature lies way above different masses that appear in the model.
- $T_{\rm RH} \gtrsim m_i$, where the reheat temperature lies close to the masses in the theory.

In the following sub-sections we will take a closer look into above two cases.

### 6.4.1 Large reheat temperature: $T_{\rm RH} \gg m$

In this sub-section the reheat temperature is assumed to be much larger than the dark sector masses. We would like to mention that computing the reaction densities, we consider both $2 \to 2$ annihilation channels and $\Phi \to XB$ decay channel before EWSB, while after EWSB we only take into account the $\Phi \to XZ(\gamma)$ decays for reasons elaborated soon. Also note that, all the SM fields are massless before EWSB but the dark sector fields $(m_\Phi, m_X)$ are massive irrespective of the era, thanks to $U(1)_X$ breaking at very high scale. First we compare reactions densities for annihilation and the decay as a function of $x \equiv m_X/T$. Often we use a dimensionless variable $r = \frac{m_X}{m_\Phi} < 1$ to illustrate scan results.

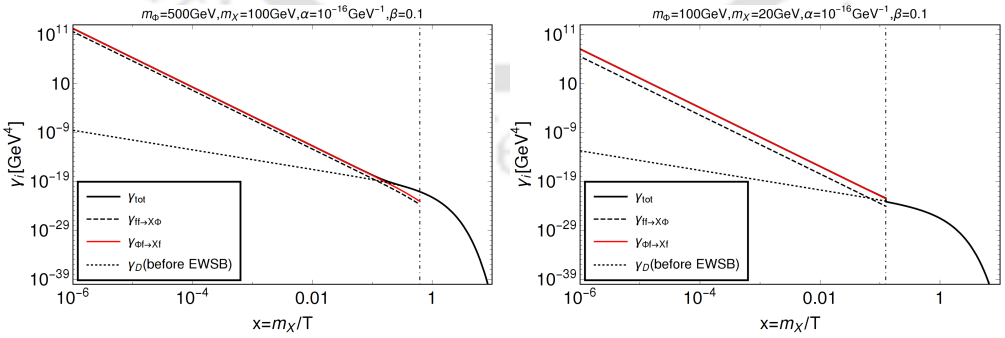


**Figure 6.6:** Comparison of reaction densities ($\gamma_{\rm ann,D}$) for annihilation and the decay. Before EWSB we show the $s$-channel $\bar{f}f \to X\Phi$ process (black dashed) and $t$-channel $\Phi f \to Xf$ (red) and also the decay contribution (black doted), while after EWSB we plot the density for the decay (solid black) only. The solid black line (hidden beneath the red line before EWSB) shows both contributions from the annihilation and the decay together. In the left panel we choose $m_\Phi = 500$ GeV, $m_X = 100$ GeV, while in the right, we choose $m_\Phi = 100$ GeV, $m_X = 20$ GeV. In both cases we have $\alpha = 10^{-16}$ GeV$^{-1}$, $\beta = 0.1$. The vertical dashed-dotted lines shows $x$ corresponding to EWSB.

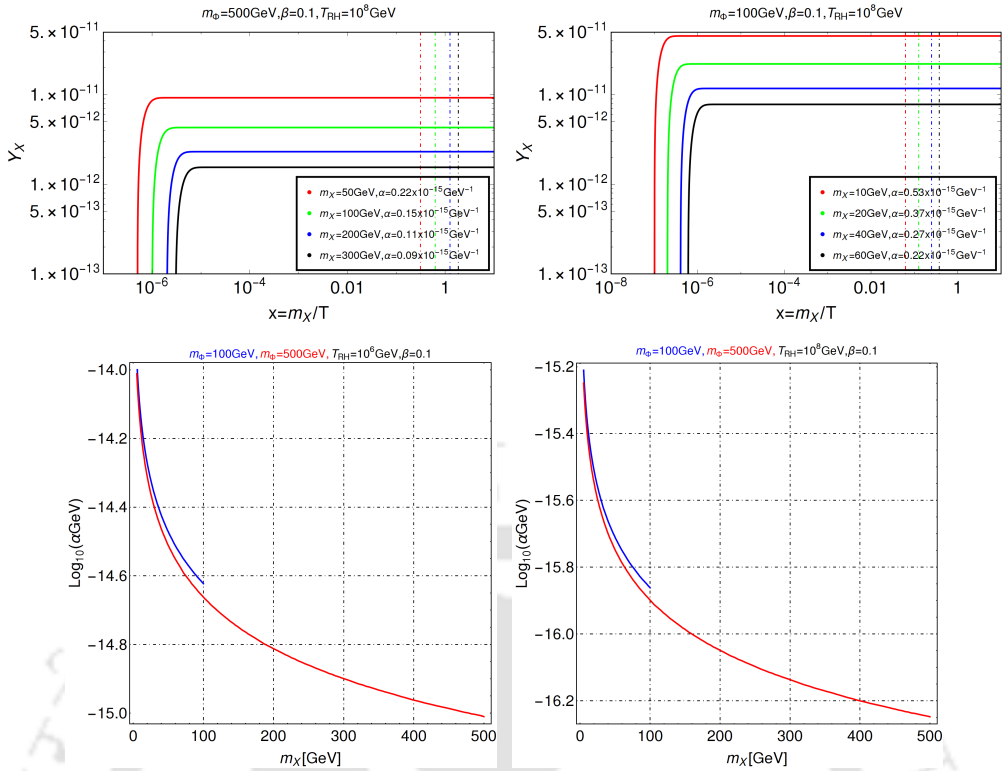


**Figure 6.7:** Top left: evolution of the DM yield $Y_X$ for parameters which imply correct relic DM abundance as a function of $x = m_X/T$ obtained by solving Eq. (6.54). Here different colored curves indicate different choices of $r = \frac{m_X}{m_\Phi} = \{0.1, 0.2, 0.4, 0.6\}$ in red, green, blue and black respectively for a fixed $m_\Phi = 100$ GeV, $\alpha = 10^{-16}$ GeV$^{-1}$, $\beta = 0.1$ and reheat temperature $T_{\rm RH} = 10^8$ GeV. The vertical dashed-dotted lines correspond to $x_{\rm EW} = m_X/T_{\rm EW}$ for different values of $m_X$. Top right: same as top left but with $m_\Phi = 500$ GeV. Bottom left: relic density allowed parameter space in terms of $m_X - \alpha$ where different colored contours correspond to $m_\Phi = 500$ GeV (red) and $m_\Phi = 100$ GeV (blue) for a fixed $\beta = \frac{\tilde{\alpha}}{\alpha} = 0.1$ and reheat temperature $T_{\rm RH} = 10^6$ GeV. Bottom right: same as bottom left but with $T_{\rm RH} = 10^8$ GeV.

In Fig. 6.6 we show individual contributions of annihilations and the decay to the reaction densities as a function of $x$ keeping the DM mass, the $\Phi$ mass, and the coupling $\alpha(\tilde{\alpha})$ fixed. The vertical dashed-dotted line represents EWSB $x_{EW} = m_X/T_{EW}$. Here we clearly see that the reaction densities due to the $s$-channel and $t$-channel annihilation processes are much larger than that due to decay before EWSB, while after EWSB the reaction density falls to a very small value. The suppression of the decay before EWSB can be understood comparing the analytical forms of reaction densities for annihilation (in massless limit) and decay as follows:

$$q \equiv \frac{\gamma_{\rm ann}}{\gamma_{\rm D}} \sim \frac{\int_0^\infty ds s^{3/2} \sigma_{ann}(s) K_1\left(\sqrt{s}/T\right)}{\alpha^2(1+\beta^2) m_\Phi^5 K_1\left(m_\Phi/T\right)} \sim \left(\frac{T}{m_\Phi}\right)^5 \frac{1}{K_1\left(m_\Phi/T\right)}, \tag{6.57}$$

where $\sigma_{ann}(s) \propto \alpha^2(1+\beta^2) \times$ const. was assumed. It then follows that for $T >> m_\Phi \implies q \gg 1$ and for $T \sim m_\Phi \implies q \sim 1$. We however, would like to caution the reader that above formula is not strictly valid at $T$ close to EWSB when massive kinematics become important for computing annihilation cross-sections as elaborated in Sec. 6.3.2. This implies that the DM is dominantly produced before EWSB, while the yield accumulated after EWSB is negligibly small. This is a typi-

cal feature of UV freeze-in where the maximum yield production happens at high temperature.

The effect of large reheat temperature and large reaction densities at high temperature is reflected in the DM yield shown in the top panels of Fig. 6.7. In both scans we keep $T_{RH} = 10^8$ GeV. In the top panel of Fig. 6.7 we see that the DM yield builds up quickly with $x$ (i.e. with lowering temperature) and reaches its maximal value already at very high temperature $T \sim T_{\rm RH}$. Then it freezes-in immediately producing an yield that remains constant till $T = T_0 \simeq 2.73$ K. The asymptotic value of the yield, $Y_0 \equiv Y(T_0)$, directly implies the PLANCK observed DM relic abundance via Eq. (6.55). As seen from Eq. (6.55) each choice of the DM mass requires appropriate $Y_0$ what results in the splitting of the colored curves at large $x$ observed in Fig. 6.7. On the other hand each $Y_0$ requires the couplings $\alpha, \tilde{\alpha}$ tuned appropriately, as shown in the legend of Fig. 6.7. The left top panel corresponds to $m_\Phi = 500$ GeV, while the top right panel to slightly smaller value $m_\Phi = 100$ GeV. The vertical dashed lines show the locations of EWSB, although its effect on the final yield is invisible. In the bottom panels of Fig. 6.7 we show contours corresponding to the central value of the PLANCK observed relic abundance ($\Omega h^2 \simeq 0.1199$) in the $\alpha - m_X$ plane for fixed $m_\Phi = 500$ GeV and 100 GeV and two different values of $T_{\rm RH}$. Since $\Omega_X \propto m_X$, we see for larger DM mass smaller $\alpha$ is required to compensate for the over abundance. Note, that in each panel the kinematical condition $m_\Phi \gtrsim m_X$ is obeyed. As expected, for the same DM mass, growing $T_{\rm RH}$ requires lower couplings. We would finally note that to find yield in such a scenario, the masses in all reactions can be safely neglected and the processes after EWSB contributes negligibly.

### 6.4.2 Low reheat temperature: $T_{\rm RH} \gtrsim m$

It turns out that when the reheat temperature drops down to $\sim$ TeV scale, then processes that take place after EWSB are relevant and contribute significantly to final yield making this scenario more interesting. In the upper left panel of Fig. 6.8 we have shown the DM yield as a function of $x$ for $T_{\rm RH} = 10$ TeV and varying DM masses. In order to satisfy the relic abundance, we need larger $\alpha$ as $Y_X \sim T_{\rm RH}\alpha^2$ as the reheat temperature is smaller than before. In the upper right panel we have shown the yield for even smaller reheat temperature $T_{\rm RH} = 1$ TeV. Note the visible enhancement of the yield caused by the after-EWSB decay contribution at $x \sim 1$. The enhancement is more prominent for smaller $T_{\rm RH}$. In the lower panel we have shown curves in the $m_X - \alpha$ plane that reproduce proper DM abundance for a fixed $T_{\rm RH}$. It is seen that in this low $T_{\rm RH}$ regime the required $\alpha$ is by two orders of magnitude larger in order to satisfy correct relic abundance (compare bottom panels of Fig. 6.8 with those of Fig. 6.7).

### 6.4.3 Summary of the parameter space

Effects of varying reheat temperature for DM yield evolution has been shown in the top panels of Fig. 6.9 for two different sets of dark sector masses. For $T_{\rm RH} = 10^8$ GeV (shown by the red curve) i.e. for the $T_{\rm RH} \gg m$, we observe yield that follows typical UV freeze-in pattern and becomes maximum at $T \sim T_{\rm RH}$. With gradual decrease in $T_{\rm RH}$, although the characteristic UV freeze-in is still visible at smaller $x$, however the yield also builds up at larger $x$ and final freeze-in occurs at $T \sim$

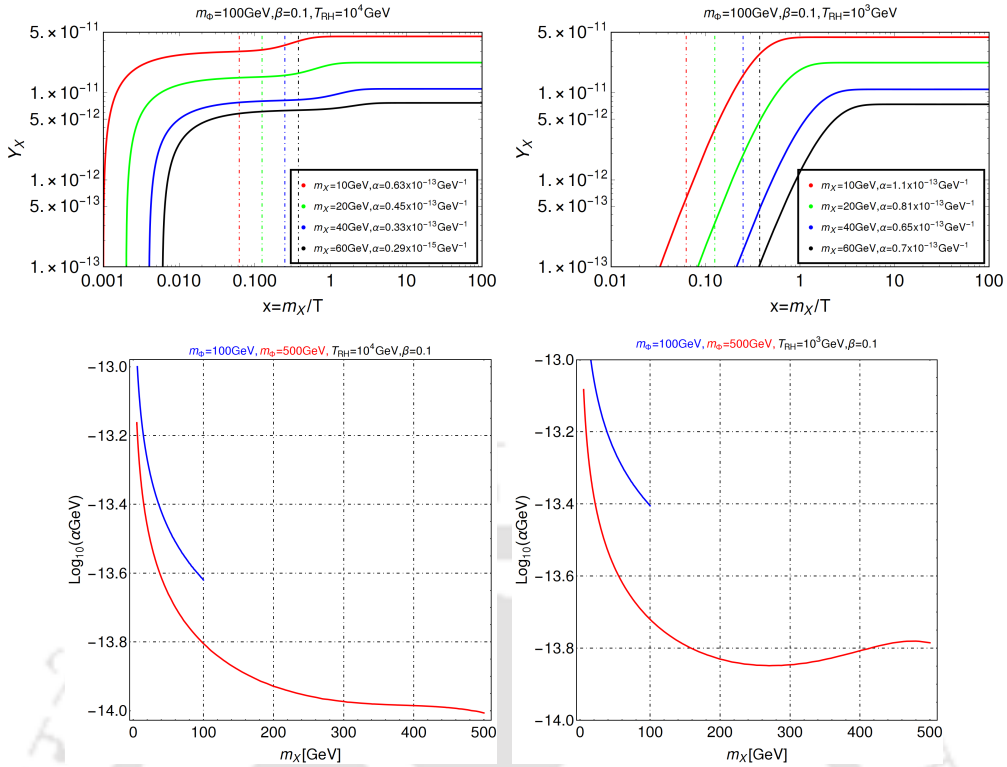


**Figure 6.8:** Top left: DM yield as a function of $x = m_X/T$ for a reheat temperature $T_{\rm RH} = 10$ TeV considering both annihilation and decay to be active before EWSB, while keeping only decay after EWSB. We choose $m_\Phi = 100$ GeV and $\beta = 0.1$ while for each value of $m_X$, $\alpha$ is adjusted to reproduce the central value of the measured relic abundance. Top right: Same as top left but with $T_{\rm RH} = 1$ TeV. In both of the plots the vertical dashed lines denote EWSB ($x_{EW}$). Bottom left: Relic density allowed parameter space in $m_X - \alpha$ plane for $T_{\rm RH} = 10$ TeV and $\alpha$ adjusted to reproduce the DM abundance. Bottom right: Same as bottom left but with $T_{\rm RH} = 1$ TeV.

$m_X$, as shown by the blue ($T_{\rm RH} = 10^4$ GeV) and black curves ($T_{\rm RH} = 10^3$ GeV). For $T_{\rm RH} = 1$ TeV the IR characteristic of freeze-in is more prominent. Note that, all the parameters chosen in these plots reproduce the observed relic abundance and hence the yields for the same $m_X$ at low $x$ converge to the same asymptotic value, as they indeed must do according to (6.55). Colorful curves in the upper panels correspond to different values of $\alpha$ adjusted so that in spite of varying $T_{\rm RH}$, the asymptotic value is the same and corresponds to the observed abundance. [8] For large $T_{\rm RH}$ one requires a smaller $\alpha$ to obtain the right abundance to compensate the effect of larger integration region. We also note that the yield $Y(x \to 0)$ values in these the two upper panels are different due to different choices of DM masses. In the middle panel of Fig. 6.9 we show curves in the $\alpha - T_{\rm RH}$ space that imply proper DM abundance. It is interesting to note that for $T_{\rm RH} \lesssim 1$ TeV, the relic density becomes independent of the reheat temperature as the IR freeze-in dominates over UV freeze-in. Beyond 1 TeV the effective coupling $\alpha$ must decreases with grow of $T_{\rm RH}$ for a fixed DM mass in order to satisfy the central value of the PLANCK observed relic abundance as $Y_X \propto T_{\rm RH}\alpha^2$. Also for a fixed $T_{\rm RH}$, larger DM mass requires smaller $\alpha$ simply because $\Omega_X \propto m_X$ following Eq. (6.55). In the bottom panel of Fig. 6.9, we

[8] The initial condition for all our solutions of the freeze-in BEQ assumes no DM at $T_{\rm RH}$, i.e. $Y_X(m_X/T_{\rm RH}) = 0$. On the other hand $\alpha$ is adjusted so that the observed abundance is satisfied, i.e. for the same $m_X$ the curves in upper panels of Fig. 6.9 converge to the same value for $x \to 0$.

illustrate the effect of $\tilde{\alpha}$ by varying $\beta = \frac{\tilde{\alpha}}{\alpha} = \{0.001, 0.1, 0.3, 0.5, 1.0, 3.0, 5.0\}$ (shown in different colors) on the resulting relic density allowed parameter space. Note that quantities like reaction rates, DM yields or $\Phi$-lifetime depend on $\alpha$ and $\beta$ via $\alpha^2 + \widetilde{\alpha}^2 = \alpha^2\,(1+\beta^2)$.

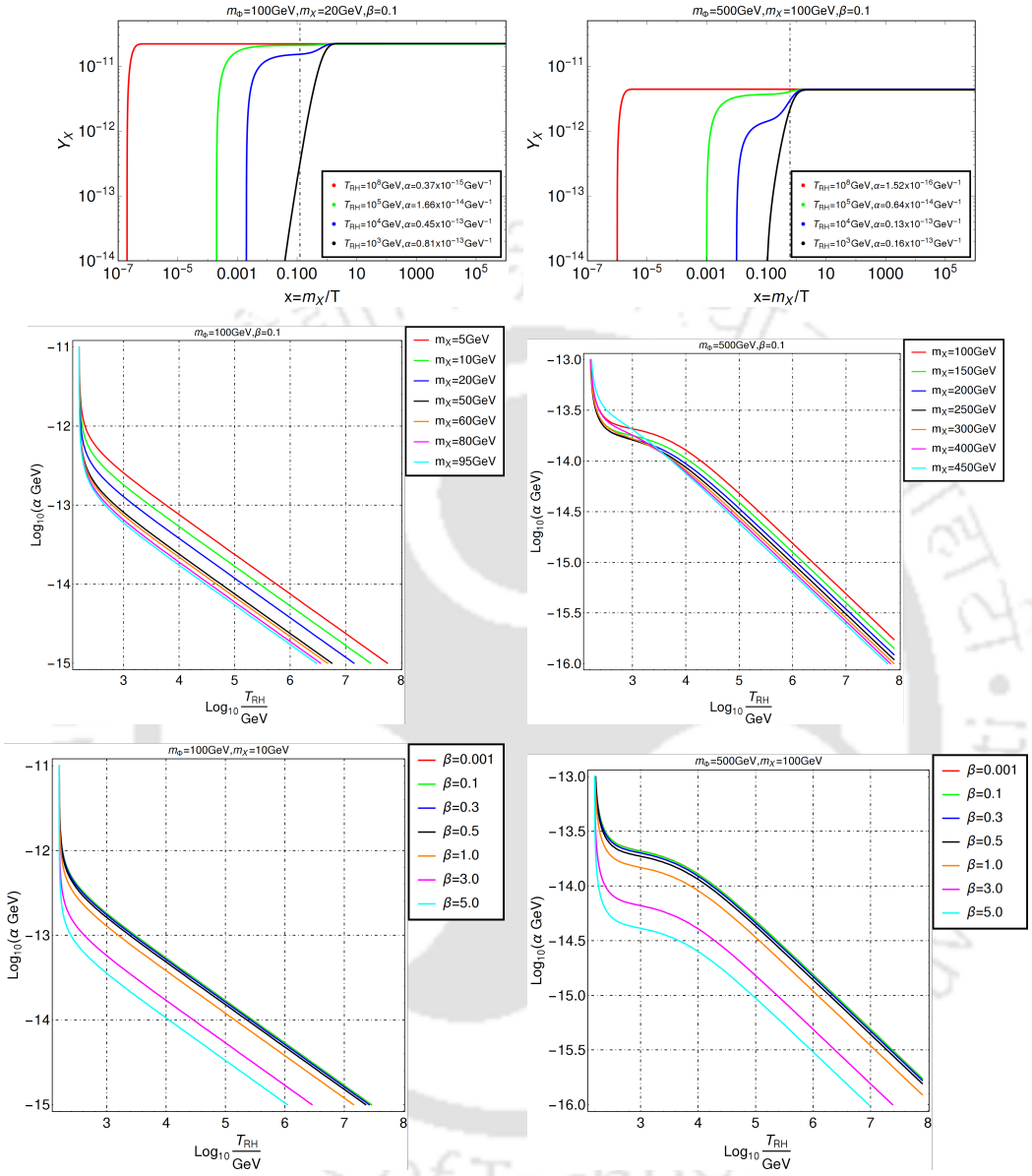


**Figure 6.9:** Top panel: DM yield as a function of temperature for different choices of the reheat temperature $T_{\rm RH}$ : $\{10^5, 10^2, 10, 1\}$ TeV shown in red, green, blue and black curves respectively. Here we have considered both annihilation and decay channels before EWSB where SM particles are massless while the dark particles are massive. In the post-EWSB scenario we have considered only the decays with massive states. The parameters chosen correspond to right relic abundance. In each of these plots the vertical dashed-dotted lines denote EWSB ($x_{EW}$). Middle left: Relic density allowed parameter space in terms of $\alpha - T_{\rm RH}$ where different colored contours correspond to different $m_X$ for a fixed $m_\Phi = 100$ GeV. Middle right: Same as middle left panel, but for a different fixed $m_\Phi = 500$ GeV. Bottom left: Same as middle panel but for different choices of $\beta : \{0.001, 0.1, 0.3, 0.5, 1.0, 3.0, 5.0\}$ for $m_\Phi = 100$ GeV and $m_X = 10$ GeV. Bottom right: Same as bottom left with $m_\Phi = 500$ GeV and $m_X = 100$ GeV.

We have decided to present those quantities for fixed $\beta = 0.1$ and various values

of $\alpha$. Equivalently the numbers shown in plots could be parametrized by $\alpha\,(1+\beta^2)^{1/2} = \alpha_{\rm old}\,(1+(0.1)^2)^{1/2}$, where $\alpha_{\rm old}$ is the parameter specified in our plots with $\beta = 0.1$. Clearly, larger $\beta$ requires smaller $\alpha$ and this is what we see in the orange ($\beta = 1.0$), magenta ($\beta = 3.0$) and cyan ($\beta = 5.0$) colored contours.

## 6.5 Signature of the model


**Figure 6.10:** Left: Inelastic DM scattering off the nuclei $N$ for direct search of DM; right: DM annihilating to photon final states via $\Phi$ mediation for indirect search of DM.

As we have already demonstrated, the dimensionful $\Phi - B - X$ vertex ($\alpha(\tilde{\alpha})$) is constrained by relic density of DM to be $\alpha(\tilde{\alpha}) \lesssim 10^{-12}$ GeV$^{-1}$ for $T_{\rm RH} \gtrsim 10^3$ GeV. Therefore, assuming $c \sim \mathcal{O}(1)$ [9], one can conclude that freeze-in of the VDM requires the NP scale $\Lambda \gtrsim 10^{12}$ GeV at least or higher for larger reheat temperature. If the effective operators (6.40) where $n$-loop generated, then we would roughly conclude that $\Lambda \gtrsim 10^{12-2n}$ GeV. Hereafter we assume that the Lagrangian (6.40) is indeed tree-level generated. Therefore, the phenomenology of the model is severely constrained. First of all, note that there is no $XX - SM$ vertex, therefore no elastic scattering of the DM against nuclei is possible. So, this model easily avoids stringent constraints from non-observation of DM scattering at direct search experiments. DM can only scatter off nuclei inelastically with $\Phi$ in the final state as shown in left panel of Fig. 6.10. Since $m_\Phi > m_X$, hence such an inelastic scattering is forbidden even if the mass difference $\delta m = m_\Phi - m_X \gtrsim \mathcal{O}(100)$ MeV [275]. On the other hand, due to the presence of $\Phi - X - \gamma$ vertex, the DM pair annihilation may give rise to monochromatic X-ray line (right panel of Fig. 6.10) but such photon flux will be hugely suppressed by $1/\Lambda^2$ and can not account for the, say, galactic-center gamma ray excess as observed. Hence this model in its freeze-in realization of DM can not be probed from either direct nor indirect DM search experiments.

However, since the portal coupling $\lambda_{H\Phi}$ is unconstrained by existing observations and as argued before this coupling can be as large as $\lambda_{H\phi} \sim \mathcal{O}(1)$, hence the non-standard scalar $\Phi$ can be produced at the collider via Higgs mediation (see Fig. 6.12). Once these $\phi$'s get produced at colliders they will eventually decay via Fig. 6.2 to DM and SM final states like $Z, \gamma$. This is the same channel that also gives rise to DM production via freeze-in. For particular choice of the effective coupling $\alpha$ that gives rise to right relic abundance, the $\Phi$ remain stable over the detector length. This is shown in Fig. 6.11, where we see that for $\alpha = 10^{-14} - 10^{-13}$ GeV$^{-1}$ the average decay length of $\Phi$ is $L_\Phi = c\tau_\Phi \gtrsim 100$ km, where $c = 3 \times 10^8$ m/sec. In such a case the $\Phi$'s basically escapes LHC detector and gives rise to missing energy ($\not{E}_T$), which can be

[9] As mentioned in ref. [269] the Lagrangian (6.40) can be generated at the tree-level by integrating out anti-symmetric tensor mediators, then indeed $c \sim \mathcal{O}(1)$.

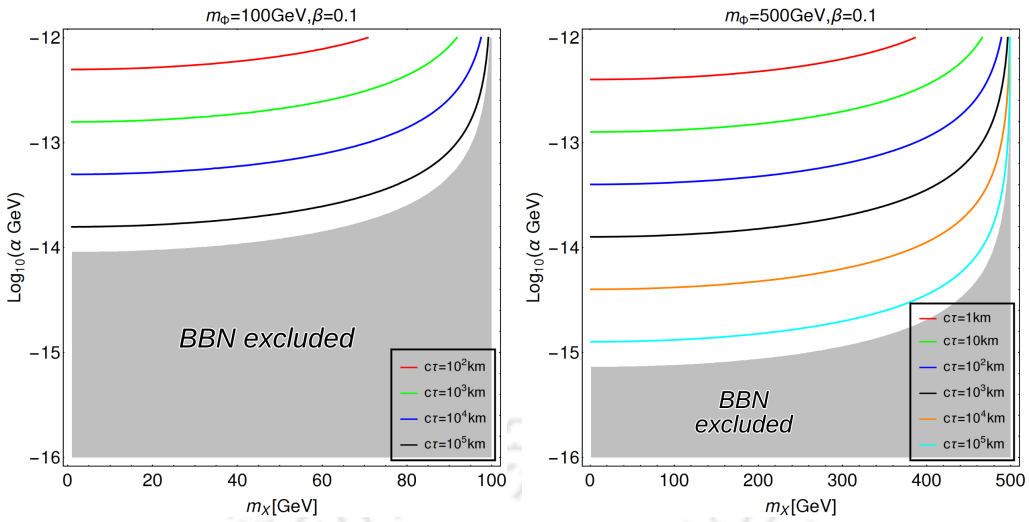


**Figure 6.11:** The contours show different decay lengths of $\Phi$ for particular choices of the parameters that can produce right relic abundance for the DM. This can result in missing energy signature within the collider. The gray shaded region is where $\tau_\Phi > \tau_{\rm BBN}$.

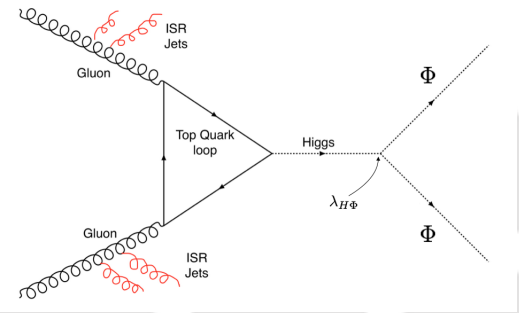


**Figure 6.12:** $\not{E}_T$ + jets signature that the model can produce at the collider.

constructed out of the recoil of an initial state radiation (ISR) of a gluon, $\gamma$, $W^\pm$, $Z$, $H$ as

$$\not{E}_T = -\sqrt{\left(\sum_{\ell,j} p_x\right)^2 + \left(\sum_{\ell,j} p_y\right)^2}, \tag{6.58}$$

where the sum runs over all visible objects that include leptons and jets, and unclustered components. Therefore, the model can finally produce monojet [10] plus missing energy signal that has extensively been searched at the LHC [123, 276, 277] as a vanilla DM signal particularly for Higgs portal DM models. However, usually, when one produces DM that is connected with the SM via a Higgs portal, then the coupling is tightly constrained from direct search. Therefore, such signals are pretty small and submerged into huge SM background. In our case, as mentioned, the coupling ($\lambda_{H\phi}$) can be large and can produce a significant number of such mono-X signal events, that may be of interest for next run of LHC. It is worth noting that decays of $\Phi$ have to be completed before the onset of Big Bang Nucleosynthesis

[10] Multijet final states will be infested with huge SM backgrounds.

(BBN) [44, 278], so that it does not alter the standard BBN picture. Therefore here we will require that $\tau_\Phi \lesssim \tau_{\rm BBN} \sim 1$ sec which, for fixed $m_\Phi$ and $m_X < m_\Phi$, puts a lower bound on $\alpha$ as illustrated by the gray shaded region in both the panels of Fig. 6.12.

## 6.6 Summary

In this chapter we have presented a vector boson DM that is weakly coupled to the visible SM sector via dim.5 operator. The advantage of the model is the absence of tree-level elastic DM scattering against nuclei and a double suppression of present time DM annihilation in, for instance, dwarf galaxies. Therefore this scenario easily and naturally satisfies existing experimental constraints. The model contains a dark sector composed, in a unitary gauge, of a massive vector $X_\mu$, and a real scalar $\Phi$. $X_\mu$ is a gauge boson of spontaneously broken extra $U(1)_X$ gauge symmetry. The vector $X_\mu$ and the scalar $\Phi$ are odd under a $Z_2$ symmetry introduced to stabilize the DM candidate, $X_\mu$. $\Phi$ is assumed to be heavier than $X_\mu$. The SM sector is extended by an extra heavy neutral Higgs boson that decouples when its mass goes to infinity, as we assume here. The lowest dimensional operator responsible for DM-SM interaction are $1/\Lambda\ X^{\mu\nu}B_{\mu\nu}\Phi$ and $1/\Lambda\ \tilde{X}^{\mu\nu}B_{\mu\nu}\Phi$.

We have investigated a possibility of DM production via a freeze-in mechanism through decays of $\Phi$ and annihilations including $\Phi$. It turned out to be convenient to consider two distinct regimes of the reheat temperature. The first one is when the reheat temperature is significantly higher than masses involved in the production process. This situation mimics the case of UV freeze-in, when the production happens mostly before EWSB and all processes after EWSB are insignificant. However the situation alters, when reheat temperature (which can be thought of a free parameter, being very loosely constrained by BBN) drops to lower values close to the mass scale $(m)$ typical for the dark sector. It has been shown that UV freeze-in, although advertised to describe the case of freeze-in production of DM in EFT formalism, is not fully correct, massive contributions start playing an important role and effects of IR freeze-in i.e. DM yield building even up to lower temperature $(T \sim m)$ starts showing up.

In order to predict properly the observed DM abundance, the scale of the dimension-5 operators must be large $\Lambda \sim 10^{12} - 10^{16}$ GeV depending on the DM mass $m_X$, the reheat temperature $T_{\rm RH}$ and an underlying mechanism for the generation of the relevant effective operators. The huge size of $\Lambda$ implies that at the lowest level of perturbative expansion neither elastic scattering off nuclei is allowed nor present time annihilations of DM in e.g. centers of galaxies are possible. However, it turns out that LHC collider signals mediated by Higgs boson exchange are possible, $gg \to H^* \to \Phi\Phi$. Since the scale of $\Lambda$ required by the DM abundance is large $\Lambda \sim 10^{12} - 10^{16}$ GeV the heavier scalar $\Phi$ is effectively stable at the detector length scale and hence can produce mono-jet, photon, $Z, W^\pm$ or $H$ events accompanied by missing energy drifted away by pairs of $\Phi$ bosons.The signal cross-section could be quite substantial as the portal coupling between $\Phi$ and the SM remains unconstrained.

Chapter 7

# Conclusion and future directions

The thesis describes possibilities of vector boson constituting DM content of the universe. Unlike scalar and fermion DM, vector boson DM models are not much abundant in the literature due to the requirement of non-trivial model extensions. A vector boson DM, in its simplest form, can be ideated to emerge from a gauged abelian extension of the Standard Model (SM) gauge symmetry where the extended symmetry can be spontaneously broken by the non-zero vacuum expectation value (VEV) of a scalar charged under the same symmetry. The DM, thus obtained, can be stabilized either by some additional symmetry or some remnant symmetry of the broken gauge group. Electromagnetic charge neutrality of the DM can be ensured by assigning zero hypercharge, provided it is also a singlet under SM $SU(2)_L$ gauge group. In the same spirit, a gauged non-abelian $SU(2)_X$ extension of the SM can give rise to minimal non-abelian vector boson DM (when the symmetry is spontaneously broken by a scalar, fundamental under $SU(2)_X$) that can be made naturally stable in the absence of extra fermions transforming under $SU(2)_X$. However, in that case, the model is a simple 'Higgs portal model' that although satisfies stringent direct search limits but loses its phenomenological richness. As we have illustrated in this thesis, in the presence of new fermions (coloured and/or uncoloured) and extended scalar sector, non-abelian vector boson DM models emerging from a $SU(2)_N$ extension ($N$ stands for electromagnetic charge neutrality) can have a plethora of interesting phenomenological outcome. But in all such cases one needs to impose an additional symmetry to ensure the stability of the DM. In the first case (Chapter 3), an additional $U(1)_P$ symmetry is assumed that generates generalized lepton number $L = P + T_{3N}$ which breaks to $(-1)^L$ to render DM stable, similar to $R$ parity in Supersymmetry. In the next model also (Chapter 4 and Chapter 5) an additional global $U(1)$ symmetry ($S^{'}$) is imposed on the new particles so that $S = S^{'} + T_{3N}$ remains unbroken and keeps the lightest particle (vector boson DM) stable. In the final chapter (Chapter 6), the effective theory realization of an abelian vector boson DM is considered with an unbroken additional $Z_2$ symmetry under which the DM transforms as $X^\mu \to -X^\mu$.

For a weakly interacting massive particle (WIMP) DM the most serious bound comes from non-observation of DM in spin-independent direct search interaction. Therefore, WIMP-like vector boson DM requires some way to disentangle its annihilation channels from direct search to achieve correct relic abundance satisfying direct search exclusion limits. In the simplest case, with no additional particle under dark

symmetry, this is difficult to achieve. One established way of evading this bound is to assume heavier particles in the dark sector with which DM can co-annihilate to efficiently deplete its number density. Direct search, on the other hand, being low energy process, can not up-scatter into such heavier states, and thus can address right abundance satisfying direct search constraint. In this thesis we highlight two more additional processes that may help to circumvent the direct search bound. One possibility is the presence of a $t$-channel DM annihilation and $s$-channel direct search graphs. Aided by heavy mediators in the $s$-channel, WIMP-like vector boson DM can evade rigorous spin-independent direct detection and survive over a huge parameter space satisfying relic abundance. Such a scenario is possible in the presence of heavy fermions which also transform under the SM gauge symmetry as demonstrated Chapter 3. The conclusion is generic and goes beyond the specific model construct. The other way is to exploit DM-DM interaction in multipartite frameworks as in Chapter 4, where the heavier DM component can dominantly annihilate to lighter DM component for acquiring relic under-abundance so that DM-SM coupling can be relaxed to obey the correct bound. Again, the feature is generic and pertinent to multipartite DM frameworks in general.

As advertised throughout the thesis, two concrete motivations to look for physics beyond the SM are DM and the generation of tiny neutrino mass. In the process of accommodating vector boson DM in the non-abelian extensions of the SM, we have simultaneously addressed both. In the first case (Chapter 3) the neutrino mass can be generated via the usual seesaw mechanism, but the two sectors namely neutrino and DM are mutually exclusive and the choice of parameters for one hardly affects the other. This is also true for the outcome of the collider analysis in this model. In the second (as well as in the third in Chapter 5) case in Chapter 4 , the generation of light neutrino mass occurs via inverse seesaw of type-III due to the presence of a $SU(2)_N$ scalar triplet in the theory. Neutrino mass constraints, typically the choice of the heavy neutrino mass, crucially dictates the phenomenology of the model as elaborated in Chapter 4 and Chapter 5.

The presence of exotic fermions and scalars in the theory paves the path of probing the vector boson DM models at the collider. For high luminosity and sufficient center of mass energy it is possible to produce those heavier multiplets in collider experiments which can further decay to WIMP-pairs in association with SM leptons (and jets) giving rise to distinctive missing energy signature that can be distinguished from the SM background with judicious cuts on missing energy, effective mass etc. For example, in the first model (Chapter 3), we have exotic leptonic signatures like opposite sign dilepton with jets and hadronically quiet four lepton channels with missing energy to probe due to the exotic quark production at LHC. In the second model (Chapter 4), absent heavy fermions with $SU(2)_L$ charge, one can produce the scalar bi-doublet which finally decays to single lepton and opposite sign dilepton with missing energy that can be separated from the SM background. The signature space of the model(s) have been explored with numerical event simulation in relic density and direct search allowed parameter space. Neutrino mass constraint plays a crucial role in choosing the mass hierarchy (particularly in the second and in the third model) which results in specific signal observables.

Beyond the WIMP-paradigm, one can also account for the observed DM abundance when DM is produced via the non-thermal 'freeze-in' process. Two Chapters of the thesis elaborates on it in context of a non-abelian vector boson DM (in Chap-

ter 5) and an abelian vector boson DM in effective theory (in Chapter 6). Although the generic freeze-in technology is well understood and immensely exploited in the literature in several contexts, we had two very important points to address. Firstly, we have estimated the contribution of late time decay of the mother particle to DM relic. Although, it has been explained for a non-abelian vector boson DM (Chapter 5), it is applicable for any *IR* freeze-in scenario where the dark sector and the visible sector communicate via some renormalizable interaction. In such cases the DM yield freezes in to the right abundance at a lower temperature. Secondly, in scenarios where the dark and visible sectors are conjoined through a non-renormalizable interaction (via operators with a minimum mass dimension of five), DM yield is usually assumed to be sensitive to the highest temperature of the thermal bath (arguably the reheat temperature of the universe) giving rise to usual *UV* freeze-in approximation. We however show that for a lower reheat temperature one can identify the DM yield builds slowly, bearing the signature of IR freeze-in. This, again, is a model-independent statement and points out the caveat of usual *UV* freeze-in approximation where, in general, masses of all the particles involved in the theory are ignored (compared to the reheat temperature and the NP scale) for the computation of the DM yield. For FIMP-like DM, due to the lack of strong enough coupling with the visible sector, the most common signatures are the presence of stable charged tracks, displaced vertices and disappearing tracks as explored in Chapter 5. Interestingly, for the FIMP like case as advocated in Chapter 6, we see there is a possibility of enhanced the mono-$X$ ($X \in$ jet, photon, gauge/Higgs boson) plus missing energy signature at colliders.

Finally, let us comment on some of the issues that have not been addressed in this thesis and can be pursued further. Even though the presence of several scalar multiplets makes the tree-level scalar potential a bit complicated, but it is understandable that such extended scalar sector can improve the vacuum stability of the theory. However, such analysis requires a detailed study of the vacuum structure of the scalar potential which the thesis does not address. Indirect search bounds on vector DM, which generally constraints DM annihilation cross-section to different hadronic/leptonic final states, may turn out to be important for WIMP-like DM. Even though such constraints are not discussed in the present context but understanding the complementarity and interplay of different search strategies can be the key to drawing robust conclusions on the fate of all these models. In this regard, the cosmological and astrophysical data are stupendously important in providing complementary search strategies for DM detection. Non-abelian vector boson DM can naturally be a good candidate for strongly self interacting DM (SIMP) that can have implications for structure formation, successfully addressing the so called 'core vs. cusp' and 'too big to fail' problems, not addressed in the thesis. Complementarity between direct and collider search strategies can be further pinned down specifically in context of generic vector boson DM in effective theory construct. The most important question however is how to decipher which one among a scalar, a fermion or a vector boson DM (if any) or a combination of several may constitute the unknown component of the universe. This perhaps can be addressed, given a specific signal observed either at direct or at collider searches, by a comparative analysis between class of models yielding similar final state together with other constraints taken under consideration.

Appendix A

# Thermally averaged cross-section

We define the thermally averaged annihilation cross section times velocity $\langle \sigma\, v \rangle$ as

$$\langle \sigma\, v \rangle = \frac{\int \sigma\, v\, \exp(-E_1/T)\, \exp(-E_2/T)\, d^3p_1\, d^3p_2}{\int \exp(-E_1/T)\, \exp(-E_2/T)\, d^3p_1\, d^3p_2}\,. \tag{A.1}$$

where $p_{1,2}$ are the three-momenta and $E_{1,2}$ the energies of the colliding particles in the cosmic comoving frame. The momentum-space volume element can be written as

$$d^3p_1\, d^3p_2 = 4\pi p_1 dE_1\, 4\pi p_2 dE_2\, \frac{1}{2}\, d\cos\theta\,, \tag{A.2}$$

where $\theta$ is the angle between $\vec{p}_{1,2}$. On changing the integration variables from $\{E_1, E_2\}$ to $\{E_+, E_-\}$, where

$$E_+ = E_1 + E_2\,,\, E_- = E_1 - E_2\,,\, s = 2m^2 + 2E_1E_2 - 2p_1p_2\cos\theta\,, \tag{A.3}$$

the Jacobian of the transformation turns out to be

$$J = \begin{vmatrix} \frac{1}{2} & -\frac{1}{2} & \otimes \\ \frac{1}{2} & \frac{1}{2} & \otimes \\ 0 & 0 & -\frac{1}{2p_1p_2} \end{vmatrix} = \frac{1}{4p_1p_2}\,. \tag{A.4}$$

Therefore, the volume element in Eq. (A.2) becomes

$$d^3p_1\, d^3p_2 = 2\pi^2\, E_1E_2\, dE_+\, dE_-\, ds\,. \tag{A.5}$$

Thus, the numerator in (A.1) can be computed as follows:

$$
\begin{aligned}
&\int \sigma\, v \exp(-E_1/T)\, \exp(-E_2/T)\, d^3p_1\, d^3p_2 \\
&= 2\pi^2 \int dE_+ \int_{-\sqrt{1-\frac{4m^2}{s}}\sqrt{E_+^2-s}}^{\sqrt{1-\frac{4m^2}{s}}\sqrt{E_+^2-s}} dE_- \int ds\, \sigma\, F\, \exp(-E_+/T) \\
&= 4\pi^2 \int ds\, \sigma\, F \sqrt{1-\frac{4m^2}{s}} \int dE_+ \exp(-E_+/T) \sqrt{E_+^2-s} \\
&= 2\pi^2 T \int ds\, \sigma\, (s-4m^2)\, \sqrt{s}\, K_1\left(\sqrt{s}/T\right) .
\end{aligned}
\tag{A.6}
$$

In the above, we have used the following integral representation of the *modified Bessel function*

$$
K_\nu(z) = \frac{\sqrt{\pi}\, z^\nu}{2^\nu\, \Gamma\left(\nu+\frac{1}{2}\right)} \int_1^\infty dt \exp\left(-zt\right)\, \left(t^2-1\right)^{\nu-\frac{1}{2}} , \tag{A.7}
$$

to calculate $K_1(z)$ as

$$
K_1(z) = z \int_1^\infty dt \exp\left(-zt\right)\, \left(t^2-1\right)^{\frac{1}{2}} . \tag{A.8}
$$

Similarly, the denominator in (A.1) becomes

$$
\begin{aligned}
&\int \exp(-E_1/T) \exp(-E_2/T)\, d^3p_1\, d^3p_2 = \left[\int \exp(-E_1/T)\, d^3p_1\right]^2 \\
&= \left[4\pi \int dE_1 \exp(-E_1/T)\, p_1 E_1\right]^2 \\
&= \left[4\pi \int dE_1 \exp(-E_1/T) \sqrt{E_1^2-m^2} E_1\right]^2 = \left[4\pi m^2 T\, K_2\left(m/T\right)\right]^2 .
\end{aligned}
\tag{A.9}
$$

Thus, the thermally averaged cross-section turns out to be

$$
\langle \sigma\, v \rangle = \frac{1}{8m^4 T\, K_2^2\left(m/T\right)} \int_{4m^2}^\infty ds\, \sigma\, (s-4m^2)\, \sqrt{s}\, K_1\left(\sqrt{s}/T\right) . \tag{A.10}
$$

Appendix B

# Annihilation cross-sections and minimization conditions

Here we gather relevant cross-sections for the DM annihilation processes that appear in Chapter. 3 and Chapter. 4, together with the physical scalar mass spectrum that appear in Chapter. 5 and relevant for Tab. 5.3.

### B.0.1 Annihilation cross-sections

The annihilation cross-section ($s$-wave) for the channel $X_1X_1 \to \text{SM, SM}$ in Chapter. 3 is given by

$$
\begin{aligned}
\langle \sigma v_{\text{rel}} \rangle_{X_1X_1 \to \text{SM,SM}} = \frac{g_N^4 m_{X_1}^2}{72\pi} \Bigg\{ & \sum_{h_q} \frac{N_c}{(m_{h_q}^2 + m_{X_1}^2)^2} + \sum_{E} \frac{1}{(m_E^2 + m_X^2)^2} + \sum_{N} \frac{1}{(m_N^2 + m_{X_1}^2)^2} \Bigg\} \\
& + \frac{g_N^2}{2\pi} \left(\frac{v_1}{v}\right)^2 \Bigg\{ \frac{1}{6} \frac{m_f^2}{(4m_{X_1}^2 - m_h^2)^2 + \Gamma_h^2 m_h^2} \left(1 - \frac{m_f^2}{m_{X_1}^2}\right)^{\frac{3}{2}} \\
& + \frac{1}{4m_{X_1}^2} \frac{m_Z^4}{(4m_{X_1}^2 - m_h^2)^2 + \Gamma_h^2 m_h^2} \left(1 - \frac{m_Z^2}{m_{X_1}^2}\right)^{\frac{1}{2}} \\
& + \frac{1}{4m_{X_1}^2} \frac{m_W^4}{(4m_{X_1}^2 - m_h^2)^2 + \Gamma_h^2 m_h^2} \left(1 - \frac{m_W^2}{m_{X_1}^2}\right)^{\frac{1}{2}} \Bigg\} \\
& + \frac{1}{32\pi m_{X_1}^2} \sqrt{1 - \frac{m_h^2}{m_{X_1}^2}} \Bigg\{ \frac{1}{3} g_N^4 \left(\frac{v_1}{v}\right)^4 + \frac{3\, g_N^2 m_h^4}{\left(4m_{X_1}^2 - m_h^2\right)^2 + \Gamma_h^2 m_h^2} \left(\frac{v_1}{v}\right)^2 \\
& + \frac{2 g_N^3 m_h^2 \left(4m_{X_1}^2 - m_h^2\right)}{(4m_{X_1}^2 - m_h^2)^2 + \Gamma_h^2 m_h^2} \left(\frac{v_1}{v}\right)^3 \Bigg\}.
\end{aligned}
\tag{B.1}
$$

For the process $X\overline{X} \to \zeta_2^\dagger \zeta_2$ appeared in Chapter. 4 the $s$-wave annihilation cross-section reads

$$\langle\sigma v_{\rm rel}\rangle_{X\bar{X}\to\zeta_2\zeta_2} = \frac{g_N^4}{576\pi m_X^2}\sqrt{1-\frac{m_{\zeta_2}^2}{m_X^2}}\left(2+\left[1+\frac{4\left(m_X^2-m_{\zeta_2}^2\right)}{m_{\zeta_1}^2+m_X^2-m_{\zeta_2}^2}\right]^2\right)$$
$$+\frac{m_{W,Z}^4}{48\pi m_X^2}\sqrt{1-\frac{m_{W,Z}^2}{m_X^2}}\left[\frac{g_N^4\left(f_5/\lambda_4\right)^2}{\left(4m_X^2-m_h^2\right)^2+\Gamma_h^2 m_h^2}\right]\left[3+4\left\{\left(\frac{m_X}{m_{W,Z}}\right)^4-\left(\frac{m_X}{m_{W,Z}}\right)^2\right\}\right]$$
$$+\frac{m_f^2}{24\pi}\left(1-\frac{m_f^2}{m_X^2}\right)^{3/2}\left(\frac{g_N^4\left(f_5/\lambda_4\right)^2}{\left(4m_X^2-m_h^2\right)^2+\Gamma_h^2 m_h^2}\right)+\frac{3m_h^4}{128\pi m_X^2}\sqrt{1-\frac{m_h^2}{m_X^2}}$$
$$\left[\frac{g_N^4\left(f_5/\lambda_4\right)^2}{\left(4m_X^2-m_h^2\right)^2+\Gamma_h^2 m_h^2}\right]. \tag{B.2}$$

The $s$-wave cross-section for the pair annihilation process $\Delta\Delta \to \text{SM},\text{SM}$ in Chapter 5 is given by

$$\langle\sigma v_{\rm rel}\rangle_{\Delta\Delta\to\text{SM,SM}} = \frac{g_N^4}{32\pi m_\Delta^2}\sqrt{1-\frac{m_X^2}{m_\Delta^2}}\left[2+\left(\frac{2m_\Delta^2}{m_X^2}-1\right)^2\right]$$
$$\left[1-\sqrt{2}f_8\left(\frac{f_5}{\lambda_4}\right)\frac{v^2\left(4m_\Delta^2-m_h^2\right)}{\left(4m_\Delta^2-m_h^2\right)^2+\Gamma_h^2 m_h^2}+\frac{1}{2}f_8^2\left(\frac{f_5}{\lambda_4}\right)^2\frac{v^4}{\left(4m_\Delta^2-m_h^2\right)^2+\Gamma_h^2 m_h^2}\right]$$
$$+\frac{f_8^2}{32\pi m_\Delta^2}\sqrt{1-\frac{m_h^2}{m_\Delta^2}}\left(\frac{\left(4m_h^2-m_\Delta^2\right)^2}{\left(4m_\Delta^2-m_h^2\right)^2+\Gamma^2 m_h^2}\right)+\frac{3f_8^2}{8\pi}\sqrt{1-\frac{m_f^2}{m_\Delta^2}}\frac{m_f^2}{\left(4m_\Delta^2-m_h^2\right)^2+\Gamma^2 m_h^2}$$
$$+\frac{f_8^2}{8\pi m_\Delta^2}\sqrt{1-\frac{m_W^2}{m_\Delta^2}}\frac{m_W^4}{\left(4m_\Delta^2-m_h^2\right)^2}\left(2+\frac{\left(2m_\Delta^2-m_W^2\right)^2}{m_W^4}\right)+$$
$$\frac{f_8^2}{8\pi m_\Delta^2}\sqrt{1-\frac{m_Z^2}{m_\Delta^2}}\frac{m_Z^4}{\left(4m_\Delta^2-m_h^2\right)^2}\left(2+\frac{\left(2m_\Delta^2-m_Z^2\right)^2}{m_Z^4}\right). \tag{B.3}$$

### B.0.2 Minimization conditions

The minimization conditions for the scalar potential appearing in Chapter. 5:

$$u_2^2 \approx -\frac{\mu_\chi^2}{\lambda_4} \tag{B.4}$$
$$v_1^2 \approx -\frac{\mu_\Phi^2+f_5 u_2^2}{\lambda_2} \tag{B.5}$$
$$v_2 \approx -\frac{\mu_1 v_1 u_2}{\mu_\zeta^2+f_1 u_2^2} \tag{B.6}$$
$$u_3 \approx -\frac{\mu_2 u_2^2}{\mu_\Delta^2+(f_6+f_7)u_2^2}, \tag{B.7}$$

where from the last line it follows that unless $u_2 \ll \mu_\Delta$, we should have $\mu_2 \approx u_3$.

The $SU(2)_N$ triplet scalars $\Delta_{1,2,3}$, remain complex with masses given by:

$$m^2_{\Delta_1} \approx -4f_7u_2^2 - \frac{2\mu_2 u_2^2}{u_3}, \tag{B.8}$$

$$m^2_{\Delta_2} \approx -2f_7u_2^2 - \frac{2\mu_2 u_2^2}{u_3}, \tag{B.9}$$

$$m^2_{\Delta_3} \approx 2\frac{u_2^2\,\mu_2}{u_3}. \tag{B.10}$$

The rest of the neutral physical scalars of our model are:

$$h = \frac{1}{\sqrt{v_1^2+v_2^2}}\left(v_1\text{Re}(\phi_2) + v_2\text{Re}(\zeta_2^0)\right), \tag{B.11}$$

$$\xi_2^0 = \frac{1}{\sqrt{v_1^2+v_2^2}}\left(-v_2\text{Re}(\phi_2) + v_1\text{Re}(\zeta_2^0)\right), \tag{B.12}$$

$$\xi_1^0 \approx \frac{1}{\sqrt{v_2^2+u_2^2}}\left(-u_2\zeta_1^0 + v_2\chi_1\right), \tag{B.13}$$

$$\eta^0 \approx \frac{-1}{\sqrt{v_1^2+u_2^2(1+v_1^2/v_2^2)}}\left(u_2\text{Im}\left(\phi_2^0\right) + \frac{u_2v_1}{v_2}\text{Im}\left(\zeta_2^0\right) + v_1\text{Im}\left(\chi_2\right)\right), \tag{B.14}$$

with masses

$$m_h^2 \approx 4\lambda_2 v_1^2, \tag{B.15}$$

$$m^2_{\xi_2^0} \approx -\frac{2\mu_1u_2v_1}{v_2}, \tag{B.16}$$

$$m^2_{\eta^0} \approx -\frac{2\mu_1u_2v_1}{v_2}\left(1+(v_2/v_1)^2\right), \tag{B.17}$$

$$m^2_{\xi_1^0} \approx 2\left(f_2-f_1\right)\left(u_2^2+v_2^2\right) - \frac{2\mu_1u_2v_1}{v_2} - 4f_{10}u_3^2, \tag{B.18}$$

$$m^2_{\chi_2^R} \approx 4\lambda_4 u_2^2. \tag{B.19}$$

From the two charged scalars, $\zeta_1^-$ does not mix and is physical, while $H^+$ is an admixture of $\phi^+$ and $\zeta_2^+$:

$$H^+ = \frac{1}{\sqrt{v_1^2+v_2^2}}\left(v_2\phi^+ + v_1\zeta_2^+\right). \tag{B.20}$$

The masses of the charged scalars:

$$m^2_{\zeta_1^-} \approx 2(f_2-f_1)u_2^2 - \frac{2\mu_1u_2v_1}{v_2} - 4f_{10}u_3^2, \tag{B.21}$$

$$m^2_{H^+} = 2\left(v_1^2+v_2^2\right)\left(f_3-f_4-\frac{\mu_1u_2}{v_1v_2}\right). \tag{B.22}$$

Appendix C

# Collider simulation methodology

For the LHC simulation describd in Chapter. 3 and 4 we adopted a general strategy. We implemented the model in `CalcHEP` [263] to generate the parton level events. These events are then fed into `PYTHIA` [279] for showering and hadronization. We have used `CTEQ6L` [264] parton distribution function with renormalization ($\mu_R$) and factorization ($\mu_F$) scales set to the sub-process center-of-mass-energy ($\sqrt{\hat{s}}$). To mimic the experimental environment at LHC, we use the following identification criteria:

- *Lepton* ($\ell = e, \mu$): They are identified with minimum transverse momentum ($p_T$) of 20 GeV, and with pseudorapidity $|\eta| < 2.5$ to identify them in the central region of the detector. Two leptons are treated as isolated objects if their mutual separation satisfy $\Delta R = \sqrt{(\Delta\eta)^2 + (\Delta\phi)^2} \geq 0.2$. Lepton-jet separation must satisfy $\Delta R \geq 0.4$. $\tau$ leptons are difficult to observe in electromagnetic and muon calorimeters due to their shorter lifetime and so they are not usually classified into lepton category.

- *Jet* ($jet$): We have used `PYCELL`, the cone jet formation algorithm built within `PYHTIA`, to define the clustered hadrons as $jet$s. The detector is assumed to span $|\eta| \leq 5$ and is segmented in 100-$\eta$ and 70-$\phi$ bins. The minimum transverse energy $E_T$ of each cell is taken as $0.5$ GeV, while we require $E_T \geq 2$ GeV for a cell to act as a jet initiator. All the partons within $\Delta R = 0.4$ from the jet initiator cell are included in the formation of the jet, and we require $E_T \geq 20$ GeV for a group to be considered as a jet. For isolation of the jets from the unclustered objects (see below), we also impose a cut of $\Delta R > 0.4$.

- *Unclustered Objects*: All the other final state particles, which are not isolated leptons and separated from jets, are considered as unclustered objects. This clearly means all the particles (electron/photon/muon) with $0.5 < E_T < 10$GeV and $|\eta| < 5$ and jets with $0.5 < E_T < 20$ GeV and $|\eta| < 5$, which leave their presence in the detector, are considered as unclustered objects.

- *Missing energy* ($\not{E}_T$) : Though the invisible particles produced in the decay chain of exotic particles will be missed in the detector, their transverse momentum can be estimated from the momentum imbalance in the associated visible particles (leptons and jets). This missing energy is thus defined as:

$$\not{E}_T = (p_T)_{mis} = -(p_T)_{vis},\ (p_T)_{vis} = \sqrt{(\sum_{\ell,j} p_x)^2 + (\sum_{\ell,j} p_y)^2}\,. \tag{C.1}$$

Note that the negative sign in the definition of missing energy do not carry any significance and we will always refer to the absolute value. We also note that missing energy identification takes the unclustered objects, which do not fall into the lepton or $jet$ category as defined by detector sensitivity, into account.

SM background for the corresponding signal events play a crucial role in identifying the signal significance and discovery potential of the underlying model. We generate dominant SM backgrounds using MADGRAPH [252] and shower them in PYTHIA. We have appropriately used $K$-factor to match the next-to-leading-order (NLO) cross-sections for the processes contributing to SM background.

Appendix D

# Evolution of chemical potential

Let $d^3p\, d^3x$ be the phase space element at temperature $T$ and $d^3p^{'}\, d^3x^{'}$ is that at temperature $T_D$. Since the distance scales as $R$ and the momentum (of a free particle) scales as $R^{-1}$, we can write:

$$d^3p^{'}d^3x^{'} = \left(\frac{R}{R_D}\right)^3 d^3p \left(\frac{R_D}{R}\right)^3 d^3x = d^3pd^3x. \tag{D.1}$$

Since $N = n.R^3$ is fixed we have

$$f(p)d^3pd^3x = f(p^{'})d^3p^{'}d^3x^{'} = f(p^{'})d^3pd^3x \implies \exp\left(\frac{E-\mu}{T}\right) = \exp\left(\frac{E^{'}-\mu_D}{T_D}\right) \tag{D.2}$$

We consider two cases:

(a) Hot Relic: If particles are *relativistic* at the time of decoupling ($E \simeq p$), then:

$$\exp\left(\frac{p-\mu}{T}\right) = \exp\left(\frac{p^{'}-\mu_D}{T_D}\right) = \exp\left(\frac{p-(R_D/R).\mu_D}{T_D.(R_D/R)}\right). \tag{D.3}$$

Hence, for hot relics: $T_D = \frac{R(t)}{R(t_D)}.T$ and $T_D = \frac{T_D}{T}.\mu$.

(b) Cold Relic: If the particles are *non-relativistic* at the time of decoupling, then: $E \simeq m + \frac{p^2}{2m}$.

$$\begin{aligned}\exp\left(\frac{E-\mu}{T}\right) &= \exp\left(\frac{p^2/2m+m-\mu}{T}\right) \equiv \exp\left(\frac{p^{'2}/2m+m-\mu_D}{T_D}\right) \\ &= \exp\left(\frac{p^2/2m+(R_D/R)^2.(m-\mu_D)}{T_D.(R_D/R)^2}\right).\end{aligned} \tag{D.4}$$

Comparing $T_D = T(\frac{R}{R_D})^2$ with $m-\mu = (\frac{R_D}{R})^2.(m-\mu_D)$ implies $\mu(t) = m + (\mu_D - m)\frac{T}{T_D}$.

Appendix E

# Parameters of the scalar potential & relevant vertices

## E.1 Scalar potential parameters

Here we collect useful relations between potential parameters corresponding to the scalar potential described in Chapter. 6:

$$\begin{aligned} m_1^2 &= \sec(2\alpha)\left(2\lambda_H v_h^2 \cos^2\alpha - 2\lambda_S v_S^2 \sin^2\alpha\right), \\ m_2^2 &= \sec(2\alpha)\left(2\lambda_S v_S^2 \cos^2\alpha - 2\lambda_H v_h^2 \sin^2\alpha\right), \\ m_\Phi^2 &= 2\mu_\Phi^2 + \lambda_{H\Phi} v_h^2 + \lambda_{S\Phi} v_S^2. \end{aligned} \tag{E.1}$$

The couplings, likewise, can be expressed in terms of the physical masses and mixing:

$$\begin{aligned} \lambda_H &= \frac{m_1^2 \cos^2\alpha + m_2^2 \sin^2\alpha}{2v_h^2}, \ \lambda_S = \frac{m_1^2 \sin^2\alpha + m_2^2 \cos^2\alpha}{2v_S^2}, \\ \lambda_{SH} &= \frac{\sin\alpha\cos\alpha\,(m_1^2 - m_2^2)}{v_h v_S}, \ \lambda_{S\Phi} = \frac{-2\mu_\Phi^2 + m_3^2 - \lambda_{H\Phi} v_h^2}{v_S^2}, \end{aligned} \tag{E.2}$$

with,

$$\sin(2\alpha) = \left(\frac{2v_h v_S}{m_1^2 - m_2^2}\right)\lambda_{SH}. \tag{E.3}$$

Now, from Eq. (E.1) we see:

$$m_1^2 + m_2^2 = 2\left(\lambda_H v_h^2 + \lambda_S v_S^2\right). \tag{E.4}$$

From Eq. (6.25)-(E.4) we find a useful expression for $m_2$:

$$m_2^2 = v_h^2 \frac{2(\lambda_H - \lambda_{SM})(4\lambda_H\lambda_S - \lambda_{SH}^2)}{4\lambda_S(\lambda_H - \lambda_{SM}) - \lambda_{SH}^2} \tag{E.5}$$

## E.2 Expansion of parameters in powers of $m_2$

The mass parameters, along with $v_S^2$, $\lambda_{SH}$ and $\sin 2\alpha$ can be calculated and expanded in powers of $m_2$ as follows:

$$v_S^2 = \frac{m_2^2}{2\lambda_S} + \frac{\lambda_{SM} - \lambda_H}{\lambda_S} v_h^2 \tag{E.6}$$

$$\lambda_{SH}^2 = 4\lambda_S \left[\lambda_H - \frac{\lambda_{SM} m_2^2}{m_2^2 + 2(\lambda_{SM} - \lambda_H) v_h^2}\right] = 4\lambda_S(\lambda_H - \lambda_{SM}) + \mathcal{O}\left(\frac{1}{m_2^2}\right) \tag{E.7}$$

$$\sin 2\alpha = -2\sqrt{2(\lambda_H - \lambda_{SM})}\frac{v_h}{m_2} + \mathcal{O}\left(\frac{1}{m_2^3}\right) \tag{E.8}$$

$$\mu_\Phi^2 = \frac{1}{2}\left[m_\Phi^2 + v_h^2\left(\frac{\lambda_{S\Phi}(\lambda_H - \lambda_{SM})}{\lambda_S} - \lambda_{H\Phi}\right) - \frac{\lambda_{S\Phi}}{2\lambda_S} m_2^2\right] \tag{E.9}$$

$$\mu_H^2 = \frac{1}{2}\left(2\lambda_H v_h^2 + \lambda_{SH} v_S^2\right) = \left(\frac{\lambda_H - \lambda_{SM}}{4\lambda_S}\right)^{1/2} m_2^2 + \mathcal{O}\left(\frac{1}{m_2^0}\right) \tag{E.10}$$

$$\mu_S^2 = \frac{1}{2}\left(2\lambda_S v_S^2 + \lambda_{SH} v_h^2\right) = \frac{m_2^2}{2} + \mathcal{O}\left(\frac{1}{m_2^0}\right). \tag{E.11}$$

Also one can note:

$$4\lambda_S(\lambda_H - \lambda_{SM}) - \lambda_{SH}^2 = 8\lambda_S\lambda_{SM}(\lambda_H - \lambda_{SM})\frac{v_h^2}{m_2^2} + \mathcal{O}\left(\frac{1}{m_2^4}\right). \tag{E.12}$$

## E.3 Relevant vertices

Adopting the Lagrangian of the model in Eq. (6.41) in Chapter. 6, one finds relevant vertices and propagators collected here.

| Vertex | Vertex factors |
|---|---|
| 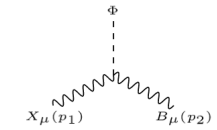  | $i\tilde{\alpha}\varepsilon_{\mu\nu\rho\sigma}p_1^\rho p_2^\sigma + i\alpha\left(\eta_{\mu\nu}p_1.p_2 - p_{1_\nu}p_{2_\mu}\right)$ |
| 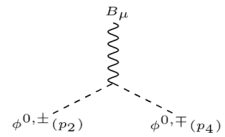  | $-\frac{ig_1}{2}\left(p_2 - p_4\right)_\mu$ |
| 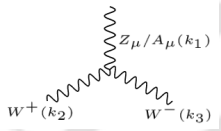  | $-ie\left[\left(k_1-k_2\right)_a g_{bc} + \left(k_2-k_3\right)_b g_{ac} + \left(k_1-k_3\right)_c g_{ab}\right]$ |
| | $-ig_2c_w\left[\left(k_1-k_2\right)_a g_{bc} + \left(k_2-k_3\right)_b g_{ac} + \left(k_1-k_3\right)_c g_{ab}\right]$ |
| $f\bar{f}B_\mu$ | $\frac{ig_1}{2}\gamma^\mu\frac{1}{2}\begin{cases}\left(Y_L^\ell + Y_R^\ell\right) - \gamma_5\left(Y_L^\ell - Y_R^\ell\right)\\ \left(Y_L^Q + Y_R^Q\right) - \gamma_5\left(Y_L^Q - Y_R^Q\right)\end{cases}$ |
| $h\Phi\Phi$ | $2i\lambda_{H\Phi}v_h$ |
| $hZZ$ | $\frac{iv_h}{4}\left(g_1^2+g_2^2\right)$ |
| $f\bar{f}Z_\mu$ | $-i\frac{g_2}{c_w}\gamma_\mu\frac{1}{2}\begin{cases}\left(c_v^\ell - c_a^\ell\gamma_5\right)\\ \left(c_v^Q - c_a^Q\gamma_5\right)\end{cases}$ |
| $f\bar{f}\gamma$ | $-ieQ_f\gamma_\mu$ |
| Propagator | $R_\xi$ gauge Feynman rules |
| $Z_\mu$ $k$ $Z_\nu$ | $\frac{i}{k^2-m_Z^2}\left[-g_{\mu\nu} + (1-\xi)\frac{k_\mu k_\nu}{k^2-\xi m_Z^2}\right]$ |
| $A_\mu$ $k$ $A_\nu$ | $\frac{i}{k^2}\left[-g_{\mu\nu} + (1-\xi)\frac{k_\mu k_\nu}{k^2}\right]$ |

**Table E.1:** Relevant DM-SM interaction vertices and vertex factors along with SM propagators. All momenta are assumed flowing towards the vertices. Here $\ell$ stands for SM leptons and $Q$ stands for the SM quark generations. $Y_{L,R}^{\ell(Q)}$ is the hypercharge for left and right-chiral leptons (quarks): $Y_L^\nu = -1, Y_L^e = -1, Y_R^e = -2; Y_L^Q = 1/3, Y_R^u = 4/3, Y_R^d = -2/3$.

Appendix F

# Reaction densities

For a $2 \to 2$ annihilation channel the reaction density is defined as:

$$\begin{aligned}\gamma\left(a, b \to 1, 2\right) &= \int \prod_{i=1}^{4} d\Pi_i \left(2\pi\right)^4 \delta^{(4)}\left(p_a + p_b - p_1 - p_2\right) f_a^{eq} f_b^{eq} \left|\mathcal{M}_{a,b\to 1,2}\right|^2 \\ &= \frac{T}{32\pi^4} g_a g_b \int_{s_{min}}^{\infty} ds \, \frac{\left[\left(s - m_a^2 - m_b^2\right)^2 - 4m_a^2 m_b^2\right]}{\sqrt{s}} \sigma\left(s\right)_{a,b\to 1,2} K_1\left(\frac{\sqrt{s}}{T}\right),\end{aligned} \tag{F.1}$$

where $a, b(1, 2)$ are the incoming (outgoing) states and $g_{a,b}$ are corresponding degrees of freedom. Here $f_i^{eq} \approx \exp^{-E_i/T}$ is the Maxwell-Boltzmann distribution. The Lorentz invarint 2-body phase space is denoted by: $d\Pi_i = \frac{d^3 p_i}{(2\pi)^3 2E_i}$. The amplitude squared (summed over final and averaged over initial states) is denoted by $\left|\mathcal{M}_{a,b\to 1,2}\right|^2$ for a particular $2 \to 2$ scattering process that lead to a scattering cross-section of $\sigma\left(s\right)$ defined as

$$\sigma\left(s\right) = \frac{1}{4\sqrt{s}\left|\vec{p_i}\right|} \int d\Pi_1 d\Pi_2 \left(2\pi\right)^4 \delta^{(4)}\left(p_a + p_b - p_1 - p_2\right) \left|\mathcal{M}_{a,b\to 1,2}\right|^2.$$

with

$$\left|\vec{p_i}\right| = \frac{1}{2\sqrt{s}} \sqrt{\left(s - m_a^2 - m_b^2\right)^2 - 4m_a^2 m_b^2}$$

being the 3-momenta of the initial state in the center of mass frame. The lower limit of the integration over $s$ is $s_{min} = \max\left[\left(m_a + m_b\right)^2, \left(m_1 + m_2\right)^2\right]$. For a $1 \to 2$ decay process the reaction density is given by:

$$\begin{aligned}\gamma\left(a \to 1, 2\right) &= \int \sum_{i=1}^{3} d\Pi_i \left(2\pi\right)^4 \delta^{(4)}\left(p_a - p_1 - p_2\right) f_a^{eq} \left|\mathcal{M}_{a\to 1,2}\right|^2 \\ &= \frac{g_a}{2\pi^2} m_a^2 \Gamma_{a\to 1,2} T K_1\left(\frac{m_a}{T}\right),\end{aligned} \tag{F.2}$$

where

$$n_a^{\text{eq}} = \int d\Pi_a f_a^{\text{eq}} \equiv \frac{T}{2\pi^2} m_a^2 K_2\left(m_a/T\right)$$

is the equilibrium number density of the state $a$.

## F.1 Boltzmann equations for freeze-in

For DM production via decay, such as $\Phi \to BX$ in Chapter. 6, the Boltzmann equation (BEQ) for the number density of $X$ can be written as:

$$\dot{n_X} + 3Hn_X = \int d\Pi_X d\Pi_B d\Pi_\Phi \left(2\pi\right)^4 \delta^4 \left(p_X + p_B - p_\Phi\right) |\mathcal{M}|^2_{\rm D} \, f_\Phi, \tag{F.3}$$

Similarly, the BEQ for DM $(X)$ production via generic annihilation process $i, j \to X, k$ reads

$$\dot{n_X} + 3Hn_X = \int d\Pi_X d\Pi_i d\Pi_j d\Pi_k \left(2\pi\right)^4 \delta^4 \left(p_X + p_k - p_i - p_j\right) |\mathcal{M}|^2_{i,j\to X,k} \, f_i f_j. \tag{F.4}$$

The BEQ in Eq. (F.4) can be rewritten as an integral over the CM energy as:

$$\dot{n_X} + 3Hn_X \approx \frac{T}{512\pi^6} \int_0^\infty ds d\Omega P_{ij} P_{Xk} \, |\mathcal{M}|^2_{i,j\to X,k} \, \frac{1}{\sqrt{s}} K_1 \left(\frac{\sqrt{s}}{T}\right), \tag{F.5}$$

where $P_{ab} = \frac{1}{2\sqrt{s}} \sqrt{s - (m_a + m_b)^2} \sqrt{s - (m_a - m_b)^2} \to \frac{\sqrt{s}}{2}$ in the limit $m_{a,b} \to 0$. The BEQ corresponding to the decay in terms of the yield $Y_X = n_x/s$ can be written in the differential form as:

$$-s(T)H(T)T \frac{dY_X^{\rm D}}{dT} = \frac{g_\Phi m_\Phi^2 \Gamma_{\Phi\to X,B}}{2\pi^2} T K_1 \left(m_\Phi/T\right), \tag{F.6}$$

where we have defined:

$$\Gamma_{\Phi\to X,B} = \int \frac{1}{2m_\Phi} \frac{|\mathcal{M}|^2_{\Phi\to X,B}}{g_\Phi} \left(2\pi\right)^4 \delta^4 \left(p_X + p_B - p_\Phi\right) d\Pi_X d\Pi_B \tag{F.7}$$

as the decay width of $\Phi$. It is possible to express Eq. (F.6) in terms of the $x \equiv m_X/T$ and the reaction density $\gamma_D$ (Eq. (F.2))

$$xHs \frac{dY_X^{\rm D}}{dx} = \gamma_D. \tag{F.8}$$

For the case of annihilation one can similarly write:

$$-s(T)H(T)T \frac{dY_X^{\rm ann}}{dT} = \frac{T}{512\pi^6} \int_0^\infty ds d\Omega P_{ij} P_{Xk} \, |\mathcal{M}|^2_{i,j\to X,k} \, \frac{1}{\sqrt{s}} K_1 \left(\frac{\sqrt{s}}{T}\right). \tag{F.9}$$

Again, in terms of the reaction density defined in Eq. (F.1), one can express the yield due to annihilation as:

$$xHs \frac{dY_X^{\rm ann}}{dx} = \gamma_{\rm ann}. \tag{F.10}$$

Following Eq. (F.6) and Eq. (F.9) the total yield:

$$\begin{aligned} Y_X^{\text{total}} &= Y_X^{\text{D}} + Y_X^{\text{ann}}, \\ &= \int_{T_{\text{min}}}^{T_{\text{max}}} dT \frac{m_\Phi^2 \Gamma_{\Phi\to X,B}}{2\pi^2} \frac{K_1\left(m_\Phi/T\right)}{s(T)H(T)} \\ &+ \frac{1}{512\pi^6} \int_{T_{\text{min}}}^{T_{\text{max}}} \frac{dT}{s(T)H(T)} \int_{s=0}^{\infty} ds d\Omega \left(\frac{\sqrt{s}}{2}\right)^2 |\mathcal{M}|^2_{i,j\to X,k} \frac{1}{\sqrt{s}} K_1\left(\frac{\sqrt{s}}{T}\right). \end{aligned} \tag{F.11}$$

Thus, the yield at temperature $T_0$ finally reads

$$\begin{aligned} Y_X^{\text{total}}\left(T_0\right) = &\left\{ \int_{T_{\text{EW}}}^{T_{\text{RH}}} dT \frac{m_\Phi^2 \Gamma_{\Phi\to X,B}}{2\pi^2} \frac{K_1\left(m_\Phi/T\right)}{s(T)H(T)} \right. \\ &\left. + \frac{1}{512\pi^6} \int_{T_{\text{EW}}}^{T_{\text{RH}}} \frac{dT}{s(T)H(T)} \int_0^{\infty} ds d\Omega \left(\frac{\sqrt{s}}{2}\right)^2 |\mathcal{M}^{\text{bEWSB}}|^2_{i,j\to X,k} \frac{1}{\sqrt{s}} K_1\left(\frac{\sqrt{s}}{T}\right) \right\} \\ &+ \left\{ \int_{T_0}^{T_{\text{EW}}} dT \frac{m_\Phi^2 \Gamma_{\Phi\to X,\gamma(Z)}}{2\pi^2} \frac{K_1\left(m_\Phi/T\right)}{s(T)H(T)} \right. \\ &\left. + \frac{1}{512\pi^6} \int_{T_0}^{T_{\text{EW}}} \frac{dT}{s(T)H(T)} \int_0^{\infty} ds d\Omega \left(\frac{\sqrt{s}}{2}\right)^2 |\mathcal{M}^{\text{aEWSB}}|^2_{i,j\to X,k} \frac{1}{\sqrt{s}} K_1\left(\frac{\sqrt{s}}{T}\right) \right\}, \end{aligned} \tag{F.12}$$

where $\mathcal{M}^{\text{(a)bEWSB}}$ stands for the amplitude for processes appearing (after) before EWSB. One can, equivalently, express the BEQ in a more general manner in terms of the reaction densities utilising Eq. (F.8) and Eq. (F.10) as:

$$xHs\frac{dY_X}{dx} = \gamma_{\text{ann}} + \gamma_{\text{D}}. \tag{F.13}$$

# Bibliography


[1] S. L. Glashow, *Partial Symmetries of Weak Interactions*, *Nucl. Phys.* **22** (1961) 579–588.

[2] S. Weinberg, *A Model of Leptons*, *Phys. Rev. Lett.* **19** (1967) 1264–1266.

[3] F. Englert and R. Brout, *Broken Symmetry and the Mass of Gauge Vector Mesons*, *Phys. Rev. Lett.* **13** (1964) 321–323.

[4] P. W. Higgs, *Broken Symmetries and the Masses of Gauge Bosons*, *Phys. Rev. Lett.* **13** (1964) 508–509.

[5] G. S. Guralnik, C. R. Hagen and T. W. B. Kibble, *Global Conservation Laws and Massless Particles*, *Phys. Rev. Lett.* **13** (1964) 585–587.

[6] CMS collaboration, S. Chatrchyan et al., *Observation of a new boson at a mass of 125 GeV with the CMS experiment at the LHC*, *Phys. Lett.* **B716** (2012) 30–61, [1207.7235].

[7] ATLAS collaboration, G. Aad et al., *Observation of a new particle in the search for the Standard Model Higgs boson with the ATLAS detector at the LHC*, *Phys. Lett.* **B716** (2012) 1–29, [1207.7214].

[8] Particle Data Group collaboration, M. Tanabashi et al., *Review of Particle Physics*, *Phys. Rev.* **D98** (2018) 030001.

[9] G. Isidori, G. Ridolfi and A. Strumia, *On the metastability of the standard model vacuum*, *Nucl. Phys.* **B609** (2001) 387–409, [hep-ph/0104016].

[10] J. Ellis, J. R. Espinosa, G. F. Giudice, A. Hoecker and A. Riotto, *The Probable Fate of the Standard Model*, *Phys. Lett.* **B679** (2009) 369–375, [0906.0954].

[11] G. Degrassi, S. Di Vita, J. Elias-Miro, J. R. Espinosa, G. F. Giudice, G. Isidori et al., *Higgs mass and vacuum stability in the Standard Model at NNLO*, *JHEP* **08** (2012) 098, [1205.6497].

[12] S. Alekhin, A. Djouadi and S. Moch, *The top quark and Higgs boson masses and the stability of the electroweak vacuum*, *Phys. Lett.* **B716** (2012) 214–219, [1207.0980].

[13] O. Lebedev, *On Stability of the Electroweak Vacuum and the Higgs Portal*, *Eur. Phys. J.* **C72** (2012) 2058, [1203.0156].

[14] L. A. Anchordoqui, I. Antoniadis, H. Goldberg, X. Huang, D. Lust, T. R. Taylor et al., *Vacuum Stability of Standard Model$^{++}$*, *JHEP* **02** (2013) 074, [1208.2821].

[15] Y. Tang, *Vacuum Stability in the Standard Model*, *Mod. Phys. Lett.* **A28** (2013) 1330002, [1301.5812].

[16] J. R. Espinosa, *Vacuum Stability and the Higgs Boson*, *PoS* **LATTICE2013** (2014) 010, [1311.1970].

[17] J. Casas, J. Espinosa and M. Quiros, *Improved Higgs mass stability bound in the standard model and implications for supersymmetry*, *Phys. Lett. B* **342** (1995) 171–179, [hep-ph/9409458].

[18] J. Casas, J. Espinosa and M. Quiros, *Standard model stability bounds for new physics within LHC reach*, *Phys. Lett. B* **382** (1996) 374–382, [hep-ph/9603227].

[19] G. Bertone and D. Hooper, *History of dark matter*, *Rev. Mod. Phys.* **90** (2018) 045002, [1605.04909].

[20] F. Zwicky, *Die Rotverschiebung von extragalaktischen Nebeln*, *Helv. Phys. Acta* **6** (1933) 110–127.

[21] V. C. Rubin and W. K. Ford, Jr., *Rotation of the Andromeda Nebula from a Spectroscopic Survey of Emission Regions*, *Astrophys. J.* **159** (1970) 379–403.

[22] K. G. Begeman, A. H. Broeils and R. H. Sanders, *Extended rotation curves of spiral galaxies: dark haloes and modified dynamics*, *Monthly Notices of the Royal Astronomical Society* **249** (04, 1991) 523–537, [https://academic.oup.com/mnras/article-pdf/249/3/523/18160929/mnras249-0523.pdf

[23] D. Clowe, M. Bradac, A. H. Gonzalez, M. Markevitch, S. W. Randall, C. Jones et al., *A direct empirical proof of the existence of dark matter*, *Astrophys. J.* **648** (2006) L109–L113, [astro-ph/0608407].

[24] E. Hayashi and S. D. M. White, *How Rare is the Bullet Cluster?*, *Mon. Not. Roy. Astron. Soc.* **370** (2006) L38–L41, [astro-ph/0604443].

[25] W. Hu and S. Dodelson, *Cosmic microwave background anisotropies*, *Ann. Rev. Astron. Astrophys.* **40** (2002) 171–216, [astro-ph/0110414].

[26] S. Dodelson, *Modern Cosmology*. Academic Press, Amsterdam, 2003.

[27] A. A. Penzias and R. W. Wilson, *A Measurement of Excess Antenna Temperature at 4080 Mc/s.*, **142** (July, 1965) 419–421.

[28] WMAP collaboration, D. N. Spergel et al., *Wilkinson Microwave Anisotropy Probe (WMAP) three year results: implications for cosmology*, *Astrophys. J. Suppl.* **170** (2007) 377, [astro-ph/0603449].

[29] N. Jarosik et al., *Seven-Year Wilkinson Microwave Anisotropy Probe (WMAP) Observations: Sky Maps, Systematic Errors, and Basic Results*, *Astrophys. J. Suppl.* **192** (2011) 14, [1001.4744].

[30] Planck collaboration, P. A. R. Ade et al., *Planck 2013 results. XVI. Cosmological parameters*, *Astron. Astrophys.* **571** (2014) A16, [1303.5076].

[31] SDSS collaboration, D. J. Eisenstein et al., *Detection of the Baryon Acoustic Peak in the Large-Scale Correlation Function of SDSS Luminous Red Galaxies*, *Astrophys. J.* **633** (2005) 560–574, [astro-ph/0501171].

[32] SDSS collaboration, K. N. Abazajian et al., *The Seventh Data Release of the Sloan Digital Sky Survey*, *Astrophys. J. Suppl.* **182** (2009) 543–558, [0812.0649].

[33] WMAP, *Wilkinson microwave anisotropy probe 9yr pie chart*.

[34] P. J. E. Peebles, *Large-scale background temperature and mass fluctuations due to scale-invariant primeval perturbations*, **263** (Dec., 1982) L1–L5.

[35] VIRGO Consortium collaboration, A. Jenkins, C. Frenk, F. Pearce, P. Thomas, J. Colberg, S. D. White et al., *Evolution of structure in cold dark matter universes*, *Astrophys. J.* **499** (1998) 20, [astro-ph/9709010].

[36] Planck collaboration, N. Aghanim et al., *Planck 2018 results. VI. Cosmological parameters*, 1807.06209.

[37] T. Lin, *Dark matter models and direct detection*, *PoS* **333** (2019) 009, [1904.07915].

[38] T. D. Brandt, *Constraints on MACHO Dark Matter from Compact Stellar Systems in Ultra-Faint Dwarf Galaxies*, *Astrophys. J. Lett.* **824** (2016) L31, [1605.03665].

[39] G. Jungman, M. Kamionkowski and K. Griest, *Supersymmetric dark matter*, *Phys. Rept.* **267** (1996) 195–373, [hep-ph/9506380].

[40] P. Gondolo, *Non-baryonic dark matter*, *NATO Sci. Ser. II* **187** (2005) 279–333, [astro-ph/0403064].

[41] G. Bertone, D. Hooper and J. Silk, *Particle dark matter: Evidence, candidates and constraints*, *Phys. Rept.* **405** (2005) 279–390, [hep-ph/0404175].

[42] J. L. Feng, *Dark Matter Candidates from Particle Physics and Methods of Detection*, *Ann. Rev. Astron. Astrophys.* **48** (2010) 495–545, [1003.0904].

[43] J. Conrad, *Indirect Detection of WIMP Dark Matter: a compact review*, in *Interplay between Particle and Astroparticle physics (IPA2014) London, United Kingdom, August 18-22, 2014*, 2014. 1411.1925.

[44] E. W. Kolb and M. S. Turner, *The Early Universe*, *Front. Phys.* **69** (1990) 1–547.

[45] F. Couchot, S. Henrot-Versillé, O. Perdereau, S. Plaszczynski, B. Rouillé d'Orfeuil, M. Spinelli et al., *Cosmological constraints on the neutrino mass including systematic uncertainties*, *Astron. Astrophys.* **606** (2017) A104, [1703.10829].

[46] J. R. Bond, G. Efstathiou and J. Silk, *Massive neutrinos and the large-scale structure of the universe*, *Phys. Rev. Lett.* **45** (Dec, 1980) 1980–1984.

[47] D. Hooper and S. Profumo, *Dark Matter and Collider Phenomenology of Universal Extra Dimensions*, *Phys. Rept.* **453** (2007) 29–115, [hep-ph/0701197].

[48] L. D. Duffy and K. van Bibber, *Axions as Dark Matter Particles*, *New J. Phys.* **11** (2009) 105008, [0904.3346].

[49] B. Carr, K. Kohri, Y. Sendouda and J. Yokoyama, *New cosmological constraints on primordial black holes*, *Phys. Rev. D* **81** (2010) 104019, [0912.5297].

[50] S. Bird, I. Cholis, J. B. Muñoz, Y. Ali-Haïmoud, M. Kamionkowski, E. D. Kovetz et al., *Did LIGO detect dark matter?*, *Phys. Rev. Lett.* **116** (2016) 201301, [1603.00464].

[51] R. Allahverdi, J. Dent and J. Osinski, *Nonthermal production of dark matter from primordial black holes*, *Phys. Rev. D* **97** (2018) 055013, [1711.10511].

[52] B. Carr, K. Kohri, Y. Sendouda and J. Yokoyama, *Constraints on Primordial Black Holes*, 2002.12778.

[53] J. L. Feng, A. Rajaraman and F. Takayama, *SuperWIMP dark matter signals from the early universe*, *Phys. Rev. D* **68** (2003) 063504, [hep-ph/0306024].

[54] J. R. Ellis, K. A. Olive, Y. Santoso and V. C. Spanos, *Gravitino dark matter in the CMSSM*, *Phys. Lett. B* **588** (2004) 7–16, [hep-ph/0312262].

[55] J. L. Feng, S. Su and F. Takayama, *Supergravity with a gravitino LSP*, *Phys. Rev. D* **70** (2004) 075019, [hep-ph/0404231].

[56] L. Covi, J. Hasenkamp, S. Pokorski and J. Roberts, *Gravitino Dark Matter and general neutralino NLSP*, *JHEP* **11** (2009) 003, [0908.3399].

[57] P. Gondolo and G. Gelmini, *Cosmic abundances of stable particles: Improved analysis*, *Nucl. Phys.* **B360** (1991) 145–179.

[58] J. Edsjo and P. Gondolo, *Neutralino relic density including coannihilations*, *Phys. Rev. D* **56** (1997) 1879–1894, [hep-ph/9704361].

[59] M. Bauer and T. Plehn, *Yet Another Introduction to Dark Matter: The Particle Physics Approach*, vol. 959 of *Lecture Notes in Physics*. Springer, 2019, 10.1007/978-3-030-16234-4.

[60] S. Bhattacharya, P. Ghosh, N. Sahoo and N. Sahu, *Mini Review on Vector-Like Leptonic Dark Matter, Neutrino Mass, and Collider Signatures*, *Front. in Phys.* **7** (2019) 80, [1812.06505].

[61] G. Arcadi, M. Dutra, P. Ghosh, M. Lindner, Y. Mambrini, M. Pierre et al., *The waning of the WIMP? A review of models, searches, and constraints*, *Eur. Phys. J. C* **78** (2018) 203, [1703.07364].

[62] M. W. Goodman and E. Witten, *Detectability of Certain Dark Matter Candidates*, *Phys. Rev.* **D31** (1985) 3059.

[63] R. H. Helm, *Inelastic and elastic scattering of 187-mev electrons from selected even-even nuclei*, *Phys. Rev.* **104** (Dec, 1956) 1466–1475.

[64] J. Liu, X. Chen and X. Ji, *Current status of direct dark matter detection experiments*, *Nature Phys.* **13** (2017) 212–216, [1709.00688].

[65] R. W. Schnee, *Introduction to dark matter experiments*, in *Physics of the large and the small, TASI 09, proceedings of the Theoretical Advanced Study Institute in Elementary Particle Physics, Boulder, Colorado, USA, 1-26 June 2009*, pp. 775–829, 2011. 1101.5205. DOI.

[66] LUX collaboration, D. S. Akerib et al., *Results from a search for dark matter in the complete LUX exposure*, *Phys. Rev. Lett.* **118** (2017) 021303, [1608.07648].

[67] PandaX-II collaboration, X. Cui et al., *Dark Matter Results From 54-Ton-Day Exposure of PandaX-II Experiment*, *Phys. Rev. Lett.* **119** (2017) 181302, [1708.06917].

[68] PandaX collaboration, H. Zhang et al., *Dark matter direct search sensitivity of the PandaX-4T experiment*, *Sci. China Phys. Mech. Astron.* **62** (2019) 31011, [1806.02229].

[69] XENON collaboration, E. Aprile et al., *Physics reach of the XENON1T dark matter experiment*, *JCAP* **1604** (2016) 027, [1512.07501].

[70] XENON collaboration, E. Aprile et al., *Dark Matter Search Results from a One Tonne$\times$Year Exposure of XENON1T*, 1805.12562.

[71] DARWIN collaboration, J. Aalbers et al., *DARWIN: towards the ultimate dark matter detector*, *JCAP* **1611** (2016) 017, [1606.07001].

[72] LUX collaboration, D. S. Akerib et al., *Results on the Spin-Dependent Scattering of Weakly Interacting Massive Particles on Nucleons from the Run 3 Data of the LUX Experiment*, *Phys. Rev. Lett.* **116** (2016) 161302, [1602.03489].

[73] PandaX-II collaboration, C. Fu et al., *Spin-Dependent Weakly-Interacting-Massive-Particle–Nucleon Cross Section Limits from First Data of PandaX-II Experiment*, *Phys. Rev. Lett.* **118** (2017) 071301, [1611.06553].

[74] S. Knapen, T. Lin and K. M. Zurek, *Light Dark Matter: Models and Constraints*, *Phys. Rev.* **D96** (2017) 115021, [1709.07882].

[75] A. Berlin and N. Blinov, *Thermal Dark Matter Below an MeV*, *Phys. Rev. Lett.* **120** (2018) 021801, [1706.07046].

[76] D. Green and S. Rajendran, *The Cosmology of Sub-MeV Dark Matter*, *JHEP* **10** (2017) 013, [1701.08750].

[77] M. Dutra, M. Lindner, S. Profumo, F. S. Queiroz, W. Rodejohann and C. Siqueira, *MeV Dark Matter Complementarity and the Dark Photon Portal*, *JCAP* **1803** (2018) 037, [1801.05447].

[78] R. Barkana, N. J. Outmezguine, D. Redigolo and T. Volansky, *Strong constraints on light dark matter interpretation of the EDGES signal*, *Phys. Rev.* **D98** (2018) 103005, [1803.03091].

[79] M. Bauer, P. Foldenauer and J. Jaeckel, *Hunting All the Hidden Photons*, *JHEP* **07** (2018) 094, [1803.05466].

[80] A. Berlin and N. Blinov, *Thermal neutrino portal to sub-MeV dark matter*, *Phys. Rev.* **D99** (2019) 095030, [1807.04282].

[81] P. F. Depta, M. Hufnagel, K. Schmidt-Hoberg and S. Wild, *BBN constraints on the annihilation of MeV-scale dark matter*, *JCAP* **1904** (2019) 029, [1901.06944].

[82] L. Buonocore, P. deNiverville and C. Frugiuele, *The hunt for sub-GeV dark matter at neutrino facilities: a survey of past and present experiments*, 1912.09346.

[83] W. Wang, L. Wu, J. M. Yang, H. Zhou and B. Zhu, *Sub-GeV Gravity-mediated Dark Matter in Direct Detections*, 1912.09904.

[84] R. M. Geilhufe, F. Kahlhoefer and M. W. Winkler, *Dirac Materials for Sub-MeV Dark Matter Detection: New Targets and Improved Formalism*, *Phys. Rev.* **D101** (2020) 055005, [1910.02091].

[85] N. Sabti, J. Alvey, M. Escudero, M. Fairbairn and D. Blas, *Refined Bounds on MeV-scale Thermal Dark Sectors from BBN and the CMB*, *JCAP* **2001** (2020) 004, [1910.01649].

[86] F. Acanfora, A. Esposito and A. D. Polosa, *Sub-GeV Dark Matter in Superfluid He-4: an Effective Theory Approach*, *Eur. Phys. J.* **C79** (2019) 549, [1902.02361].

[87] M. Cirelli, G. Corcella, A. Hektor, G. Hutsi, M. Kadastik, P. Panci et al., *PPPC 4 DM ID: A Poor Particle Physicist Cookbook for Dark Matter Indirect Detection*, *JCAP* **1103** (2011) 051, [1012.4515].

[88] A. Ibarra, D. Tran and C. Weniger, *Indirect Searches for Decaying Dark Matter*, *Int. J. Mod. Phys.* **A28** (2013) 1330040, [1307.6434].

[89] J. M. Gaskins, *A review of indirect searches for particle dark matter*, *Contemp. Phys.* **57** (2016) 496–525, [1604.00014].

[90] T. R. Slatyer, *Indirect Detection of Dark Matter*, in *Proceedings, Theoretical Advanced Study Institute in Elementary Particle Physics : Anticipating the Next Discoveries in Particle Physics (TASI 2016): Boulder, CO, USA, June 6-July 1, 2016*, pp. 297–353, 2018. 1710.05137. DOI.

[91] D. Hooper, *TASI Lectures on Indirect Searches For Dark Matter*, *PoS* **TASI2018** (2019) 010, [1812.02029].

[92] A. Geringer-Sameth, S. M. Koushiappas and M. G. Walker, *Comprehensive search for dark matter annihilation in dwarf galaxies*, *Phys. Rev. D* **91** (2015) 083535, [1410.2242].

[93] H.E.S.S. collaboration, A. Abramowski et al., *Search for dark matter annihilation signatures in H.E.S.S. observations of Dwarf Spheroidal Galaxies*, *Phys. Rev. D* **90** (2014) 112012, [1410.2589].

[94] Fermi-LAT collaboration, M. Ackermann et al., *Searching for Dark Matter Annihilation from Milky Way Dwarf Spheroidal Galaxies with Six Years of Fermi Large Area Telescope Data*, *Phys. Rev. Lett.* **115** (2015) 231301, [1503.02641].

[95] Fermi-LAT, DES collaboration, A. Albert et al., *Searching for Dark Matter Annihilation in Recently Discovered Milky Way Satellites with Fermi-LAT*, *Astrophys. J.* **834** (2017) 110, [1611.03184].

[96] J. Silk and M. Srednicki, *Cosmic-ray antiprotons as a probe of a photino-dominated universe*, *Phys. Rev. Lett.* **53** (Aug, 1984) 624–627.

[97] F. W. Stecker, S. Rudaz and T. F. Walsh, *Galactic antiprotons from photinos*, *Phys. Rev. Lett.* **55** (Dec, 1985) 2622–2625.

[98] M. S. Turner and F. Wilczek, *Positron line radiation as a signature of particle dark matter in the halo*, *Phys. Rev. D* **42** (Aug, 1990) 1001–1007.

[99] M. Kamionkowski and M. S. Turner, *Distinctive positron feature from particle dark-matter annihilations in the galatic halo*, *Phys. Rev. D* **43** (Mar, 1991) 1774–1780.

[100] L. Bergstrom, J. Edsjo and P. Ullio, *Cosmic anti-protons as a probe for supersymmetric dark matter?*, *Astrophys. J.* **526** (1999) 215–235, [astro-ph/9902012].

[101] F. Donato, N. Fornengo, D. Maurin and P. Salati, *Antiprotons in cosmic rays from neutralino annihilation*, *Phys. Rev. D* **69** (2004) 063501, [astro-ph/0306207].

[102] D. Hooper, T. Linden and P. Mertsch, *What Does The PAMELA Antiproton Spectrum Tell Us About Dark Matter?*, *JCAP* **03** (2015) 021, [1410.1527].

[103] V. Pettorino, G. Busoni, A. De Simone, E. Morgante, A. Riotto and W. Xue, *Can AMS-02 discriminate the origin of an anti-proton signal?*, *JCAP* **10** (2014) 078, [1406.5377].

[104] T. Bringmann, M. Vollmann and C. Weniger, *Updated cosmic-ray and radio constraints on light dark matter: Implications for the GeV gamma-ray excess at the Galactic center*, *Phys. Rev. D* **90** (2014) 123001, [1406.6027].

[105] G. Giesen, M. Boudaud, Y. Génolini, V. Poulin, M. Cirelli, P. Salati et al., *AMS-02 antiprotons, at last! Secondary astrophysical component and immediate implications for Dark Matter*, *JCAP* **09** (2015) 023, [1504.04276].

[106] C. Evoli, D. Gaggero and D. Grasso, *Secondary antiprotons as a Galactic Dark Matter probe*, *JCAP* **12** (2015) 039, [1504.05175].

[107] I. Cholis, T. Linden and D. Hooper, *A Robust Excess in the Cosmic-Ray Antiproton Spectrum: Implications for Annihilating Dark Matter*, *Phys. Rev. D* **99** (2019) 103026, [1903.02549].

[108] IceCube collaboration, M. Aartsen et al., *Search for annihilating dark matter in the Sun with 3 years of IceCube data*, *Eur. Phys. J. C* **77** (2017) 146, [1612.05949].

[109] Super-Kamiokande collaboration, S. Desai et al., *Search for dark matter WIMPs using upward through-going muons in Super-Kamiokande*, *Phys. Rev. D* **70** (2004) 083523, [hep-ex/0404025].

[110] C. Blanco and D. Hooper, *Constraints on Decaying Dark Matter from the Isotropic Gamma-Ray Background*, *JCAP* **03** (2019) 019, [1811.05988].

[111] T. Cohen, K. Murase, N. L. Rodd, B. R. Safdi and Y. Soreq, $\gamma$ *-ray Constraints on Decaying Dark Matter and Implications for IceCube*, *Phys. Rev. Lett.* **119** (2017) 021102, [1612.05638].

[112] W. Liu, X.-J. Bi, S.-J. Lin and P.-F. Yin, *Constraints on dark matter annihilation and decay from the isotropic gamma-ray background*, *Chin. Phys. C* **41** (2017) 045104, [1602.01012].

[113] A. Boyarsky, D. Malyshev, A. Neronov and O. Ruchayskiy, *Constraining DM properties with SPI*, *Mon. Not. Roy. Astron. Soc.* **387** (2008) 1345, [0710.4922].

[114] K. Perez, K. C. Y. Ng, J. F. Beacom, C. Hersh, S. Horiuchi and R. Krivonos, *Almost closing the $\nu$MSM sterile neutrino dark matter window with NuSTAR*, *Phys. Rev. D* **95** (2017) 123002, [1609.00667].

[115] K. Murase and J. F. Beacom, *Constraining Very Heavy Dark Matter Using Diffuse Backgrounds of Neutrinos and Cascaded Gamma Rays*, *JCAP* **10** (2012) 043, [1206.2595].

[116] A. Ibarra, A. S. Lamperstorfer and J. Silk, *Dark matter annihilations and decays after the AMS-02 positron measurements*, *Phys. Rev. D* **89** (2014) 063539, [1309.2570].

[117] L. M. Carpenter, A. Nelson, C. Shimmin, T. M. P. Tait and D. Whiteson, *Collider searches for dark matter in events with a Z boson and missing energy*, *Phys. Rev.* **D87** (2013) 074005, [1212.3352].

[118] T. Lin, E. W. Kolb and L.-T. Wang, *Probing dark matter couplings to top and bottom quarks at the LHC*, *Phys. Rev.* **D88** (2013) 063510, [1303.6638].

[119] P. Agrawal, B. Batell, D. Hooper and T. Lin, *Flavored Dark Matter and the Galactic Center Gamma-Ray Excess*, *Phys. Rev.* **D90** (2014) 063512, [1404.1373].

[120] D. Abercrombie et al., *Dark Matter Benchmark Models for Early LHC Run-2 Searches: Report of the ATLAS/CMS Dark Matter Forum*, 1507.00966.

[121] F. S. Queiroz, *Dark Matter Overview: Collider, Direct and Indirect Detection Searches*, in *Proceedings, 51st Rencontres de Moriond on Electroweak Interactions and Unified Theories: La Thuile, Italy, March 12-19, 2016*, pp. 427–436, ARISF, ARISF, 2016. 1605.08788.

[122] F. Kahlhoefer, *Review of LHC Dark Matter Searches*, *Int. J. Mod. Phys.* **A32** (2017) 1730006, [1702.02430].

[123] ATLAS collaboration, M. Aaboud et al., *Search for new phenomena in events with a photon and missing transverse momentum in $pp$ collisions at $\sqrt{s} = 13$ TeV with the ATLAS detector*, *JHEP* **06** (2016) 059, [1604.01306].

[124] CMS Collaboration collaboration, *Search for a high-mass resonance decaying into a dilepton final state in 13 $fb^{-1}$ of pp collisions at $\sqrt{s} = 13$ TeV*, Tech. Rep. CMS-PAS-EXO-16-031, CERN, Geneva, 2016.

[125] ATLAS collaboration, G. Aad et al., *Search for dark matter in events with heavy quarks and missing transverse momentum in $pp$ collisions with the ATLAS detector*, *Eur. Phys. J.* **C75** (2015) 92, [1410.4031].

[126] ATLAS collaboration, M. Aaboud et al., *Search for dark matter and other new phenomena in events with an energetic jet and large missing transverse momentum using the ATLAS detector*, *JHEP* **01** (2018) 126, [1711.03301].

[127] ATLAS collaboration, M. Aaboud et al., *Search for dark matter at $\sqrt{s} = 13$ TeV in final states containing an energetic photon and large missing transverse momentum with the ATLAS detector*, *Eur. Phys. J.* **C77** (2017) 393, [1704.03848].

[128] U. Haisch and E. Re, *Simplified dark matter top-quark interactions at the LHC*, *JHEP* **06** (2015) 078, [1503.00691].

[129] U. Haisch, P. Pani and G. Polesello, *Determining the CP nature of spin-0 mediators in associated production of dark matter and $t\bar{t}$ pairs*, *JHEP* **02** (2017) 131, [1611.09841].

[130] CMS collaboration, C. Collaboration, *Search for dark matter in association with a top quark pair at $\sqrt{s} = 13$ TeV in the dilepton channel*, .

[131] CMS Collaboration collaboration, *Search for dark matter in association with a top quark pair at sqrt$(s)$=13 TeV*, Tech. Rep. CMS-PAS-EXO-16-005, CERN, Geneva, 2016.

[132] ATLAS collaboration, G. Aad et al., *Constraints on new phenomena via Higgs boson couplings and invisible decays with the ATLAS detector*, *JHEP* **11** (2015) 206, [1509.00672].

[133] CMS collaboration, V. Khachatryan et al., *Searches for invisible decays of the Higgs boson in pp collisions at $\sqrt{s} = 7$, 8, and 13 TeV*, *JHEP* **02** (2017) 135, [1610.09218].

[134] CMS collaboration, *Search for dark matter, invisible Higgs boson decays, and large extra dimensions in the $\ell\ell + E_{\mathrm{T}}^{\mathrm{miss}}$ final state using 2016 data*, .

[135] ATLAS collaboration, M. Aaboud et al., *Combination of searches for invisible Higgs boson decays with the ATLAS experiment*, *Phys. Rev. Lett.* **122** (2019) 231801, [1904.05105].

[136] J. Goodman, M. Ibe, A. Rajaraman, W. Shepherd, T. M. Tait and H.-B. Yu, *Constraints on Dark Matter from Colliders*, *Phys. Rev. D* **82** (2010) 116010, [1008.1783].

[137] P. J. Fox, R. Harnik, J. Kopp and Y. Tsai, *Missing Energy Signatures of Dark Matter at the LHC*, *Phys. Rev. D* **85** (2012) 056011, [1109.4398].

[138] J. Kumar, D. Marfatia and D. Yaylali, *Vector dark matter at the LHC*, *Phys. Rev. D* **92** (2015) 095027, [1508.04466].

[139] S. Giagu, *Wimp dark matter searches with the atlas detector at the lhc*, *Frontiers in Physics* **7** (2019) 75.

[140] G. Busoni, A. De Simone, E. Morgante and A. Riotto, *On the Validity of the Effective Field Theory for Dark Matter Searches at the LHC*, *Phys. Lett. B* **728** (2014) 412–421, [1307.2253].

[141] G. Busoni, A. De Simone, J. Gramling, E. Morgante and A. Riotto, *On the Validity of the Effective Field Theory for Dark Matter Searches at the LHC, Part II: Complete Analysis for the $s$-channel*, *JCAP* **06** (2014) 060, [1402.1275].

[142] H. Dreiner, D. Schmeier and J. Tattersall, *Contact Interactions Probe Effective Dark Matter Models at the LHC*, *EPL* **102** (2013) 51001, [1303.3348].

[143] A. De Simone and T. Jacques, *Simplified models vs. effective field theory approaches in dark matter searches*, *Eur. Phys. J. C* **76** (2016) 367, [1603.08002].

[144] A. Belyaev, E. Bertuzzo, C. Caniu Barros, O. Eboli, G. Grilli Di Cortona, F. Iocco et al., *Interplay of the LHC and non-LHC Dark Matter searches in the Effective Field Theory approach*, *Phys. Rev. D* **99** (2019) 015006, [1807.03817].

[145] L. J. Hall, K. Jedamzik, J. March-Russell and S. M. West, *Freeze-In Production of FIMP Dark Matter*, *JHEP* **03** (2010) 080, [0911.1120].

[146] X. Chu, T. Hambye and M. H. G. Tytgat, *The Four Basic Ways of Creating Dark Matter Through a Portal*, *JCAP* **1205** (2012) 034, [1112.0493].

[147] R. T. Co, F. D'Eramo, L. J. Hall and D. Pappadopulo, *Freeze-In Dark Matter with Displaced Signatures at Colliders*, *JCAP* **1512** (2015) 024, [1506.07532].

[148] N. Bernal, X. Chu, C. Garcia-Cely, T. Hambye and B. Zaldivar, *Production Regimes for Self-Interacting Dark Matter*, *JCAP* **1603** (2016) 018, [1510.08063].

[149] N. Bernal, M. Heikinheimo, T. Tenkanen, K. Tuominen and V. Vaskonen, *The Dawn of FIMP Dark Matter: A Review of Models and Constraints*, *Int. J. Mod. Phys.* **A32** (2017) 1730023, [1706.07442].

[150] M. Duch, B. Grzadkowski and D. Huang, *Strongly self-interacting vector dark matter via freeze-in*, *JHEP* **01** (2018) 020, [1710.00320].

[151] S. Heeba, F. Kahlhoefer and P. Stöcker, *Freeze-in production of decaying dark matter in five steps*, *JCAP* **1811** (2018) 048, [1809.04849].

[152] M. Becker, *Dark Matter from Freeze-In via the Neutrino Portal*, *Eur. Phys. J.* **C79** (2019) 611, [1806.08579].

[153] A. Biswas, D. Borah and A. Dasgupta, *UV complete framework of freeze-in massive particle dark matter*, *Phys. Rev.* **D99** (2019) 015033, [1805.06903].

[154] S. Peyman Zakeri, S. Mohammad Moosavi Nejad, M. Zakeri and S. Yaser Ayazi, *A Minimal Model For Two-Component FIMP Dark Matter: A Basic Search*, *Chin. Phys.* **C42** (2018) 073101, [1801.09115].

[155] J. H. Chang, R. Essig and A. Reinert, *Light(ly)-coupled Dark Matter in the keV Range: Freeze-In and Constraints*, 1911.03389.

[156] O. Lebedev and T. Toma, *Relativistic Freeze-in*, *Phys. Lett.* **B798** (2019) 134961, [1908.05491].

[157] F. Elahi, C. Kolda and J. Unwin, *UltraViolet Freeze-in*, *JHEP* **03** (2015) 048, [1410.6157].

[158] S.-L. Chen and Z. Kang, *On UltraViolet Freeze-in Dark Matter during Reheating*, *JCAP* **05** (2018) 036, [1711.02556].

[159] N. Bernal, F. Elahi, C. Maldonado and J. Unwin, *Ultraviolet Freeze-in and Non-Standard Cosmologies*, *JCAP* **1911** (2019) 026, [1909.07992].

[160] A. G. Hessler, A. Ibarra, E. Molinaro and S. Vogl, *Probing the scotogenic FIMP at the LHC*, *JHEP* **01** (2017) 100, [1611.09540].

[161] ATLAS collaboration, M. Aaboud et al., *Search for heavy long-lived charged R-hadrons with the ATLAS detector in 3.2 fb$^{-1}$ of proton–proton collision data at $\sqrt{s} = 13$ TeV*, *Phys. Lett.* **B760** (2016) 647–665, [1606.05129].

[162] CMS collaboration, V. Khachatryan et al., *Search for long-lived charged particles in proton-proton collisions at $\sqrt{s} = 13$ TeV*, *Phys. Rev.* **D94** (2016) 112004, [1609.08382].

[163] L. Lee, C. Ohm, A. Soffer and T.-T. Yu, *Collider Searches for Long-Lived Particles Beyond the Standard Model*, *Prog. Part. Nucl. Phys.* **106** (2019) 210–255, [1810.12602].

[164] J. Alimena et al., *Searching for Long-Lived Particles beyond the Standard Model at the Large Hadron Collider*, 1903.04497.

[165] A. Haas, C. S. Hill, E. Izaguirre and I. Yavin, *Looking for milli-charged particles with a new experiment at the LHC*, *Phys. Lett. B* **746** (2015) 117–120, [1410.6816].

[166] V. V. Gligorov, S. Knapen, M. Papucci and D. J. Robinson, *Searching for Long-lived Particles: A Compact Detector for Exotics at LHCb*, *Phys. Rev. D* **97** (2018) 015023, [1708.09395].

[167] J. L. Feng, I. Galon, F. Kling and S. Trojanowski, *ForwArd Search ExpeRiment at the LHC*, *Phys. Rev. D* **97** (2018) 035001, [1708.09389].

[168] MATHUSLA collaboration, H. Lubatti et al., *MATHUSLA: A Detector Proposal to Explore the Lifetime Frontier at the HL-LHC*, 2019. 1901.04040.

[169] Z. Kang, *View FImP miracle (by scale invariance) à la self-interaction*, *Phys. Lett.* **B751** (2015) 201–204, [1505.06554].

[170] R. Campbell, S. Godfrey, H. E. Logan, A. D. Peterson and A. Poulin, *Implications of the observation of dark matter self-interactions for singlet scalar dark matter*, *Phys. Rev.* **D92** (2015) 055031, [1505.01793].

[171] H. Ruegg and M. Ruiz-Altaba, *The Stueckelberg field*, *Int. J. Mod. Phys.* **A19** (2004) 3265–3348, [hep-th/0304245].

[172] N. F. Bell, Y. Cai and R. K. Leane, *Impact of mass generation for spin-1 mediator simplified models*, *JCAP* **1701** (2017) 039, [1610.03063].

[173] Y. Farzan and A. R. Akbarieh, *VDM: A model for Vector Dark Matter*, *JCAP* **1210** (2012) 026, [1207.4272].

[174] S. Baek, P. Ko, W.-I. Park and E. Senaha, *Higgs Portal Vector Dark Matter : Revisited*, *JHEP* **05** (2013) 036, [1212.2131].

[175] L. Bian, R. Ding and B. Zhu, *Two Component Higgs-Portal Dark Matter*, *Phys. Lett.* **B728** (2014) 105–113, [1308.3851].

[176] S. Y. Choi, C. Englert and P. M. Zerwas, *Multiple Higgs-Portal and Gauge-Kinetic Mixings*, *Eur. Phys. J.* **C73** (2013) 2643, [1308.5784].

[177] S. Baek, P. Ko and W.-I. Park, *Hidden sector monopole, vector dark matter and dark radiation with Higgs portal*, *JCAP* **1410** (2014) 067, [1311.1035].

[178] S. Baek, H. Okada and T. Toma, *Two loop neutrino model and dark matter particles with global B-L symmetry*, *JCAP* **1406** (2014) 027, [1312.3761].

[179] S. Baek, P. Ko, W.-I. Park and Y. Tang, *Indirect and direct signatures of Higgs portal decaying vector dark matter for positron excess in cosmic rays*, *JCAP* **06** (2014) 046, [1402.2115].

[180] P. Ko, W.-I. Park and Y. Tang, *Higgs portal vector dark matter for* GeV *scale $\gamma$-ray excess from galactic center*, *JCAP* **1409** (2014) 013, [1404.5257].

[181] S. Baek, P. Ko and W.-I. Park, *The 3.5 keV X-ray line signature from annihilating and decaying dark matter in Weinberg model*, 1405.3730.

[182] P. Ko and Y. Tang, *Galactic center $\gamma$-ray excess in hidden sector DM models with dark gauge symmetries: local $Z_3$ symmetry as an example*, *JCAP* **1501** (2015) 023, [1407.5492].

[183] M. Duch, B. Grzadkowski and M. McGarrie, *A stable Higgs portal with vector dark matter*, *JHEP* **09** (2015) 162, [1506.08805].

[184] A. Beniwal, F. Rajec, C. Savage, P. Scott, C. Weniger, M. White et al., *Combined analysis of effective Higgs portal dark matter models*, *Phys. Rev.* **D93** (2016) 115016, [1512.06458].

[185] T. Kamon, P. Ko and J. Li, *Characterizing Higgs portal dark matter models at the ILC*, *Eur. Phys. J.* **C77** (2017) 652, [1705.02149].

[186] M. Duch and B. Grzadkowski, *Resonance enhancement of dark matter interactions: the case for early kinetic decoupling and velocity dependent resonance width*, *JHEP* **09** (2017) 159, [1705.10777].

[187] G. Arcadi, P. Ghosh, Y. Mambrini, M. Pierre and F. S. Queiroz, *$Z'$ portal to Chern-Simons Dark Matter*, *JCAP* **1711** (2017) 020, [1706.04198].

[188] S. Baek and C. Yu, *Dark matter for $b \to s\mu^+\mu^-$ anomaly in a gauged $U(1)_X$ model*, *JHEP* **11** (2018) 054, [1806.05967].

[189] S. Yaser Ayazi and A. Mohamadnejad, *Conformal vector dark matter and strongly first-order electroweak phase transition*, *JHEP* **03** (2019) 181, [1901.04168].

[190] G. Servant and T. M. Tait, *Is the lightest Kaluza-Klein particle a viable dark matter candidate?*, *Nucl. Phys. B* **650** (2003) 391–419, [hep-ph/0206071].

[191] A. Birkedal, A. Noble, M. Perelstein and A. Spray, *Little Higgs dark matter*, *Phys. Rev. D* **74** (2006) 035002, [hep-ph/0603077].

[192] T. Hambye, *Hidden vector dark matter*, *JHEP* **01** (2009) 028, [0811.0172].

[193] T. Hambye and M. H. Tytgat, *Confined hidden vector dark matter*, *Phys. Lett. B* **683** (2010) 39–41, [0907.1007].

[194] C. Arina, T. Hambye, A. Ibarra and C. Weniger, *Intense Gamma-Ray Lines from Hidden Vector Dark Matter Decay*, *JCAP* **03** (2010) 024, [0912.4496].

[195] S. Di Chiara and K. Tuominen, *A minimal model for $SU(N)$ vector dark matter*, *JHEP* **11** (2015) 188, [1506.03285].

[196] C.-W. Chiang, T. Nomura and J. Tandean, *Nonabelian Dark Matter with Resonant Annihilation*, *JHEP* **01** (2014) 183, [1306.0882].

[197] V. V. Khoze and G. Ro, *Dark matter monopoles, vectors and photons*, *JHEP* **10** (2014) 061, [1406.2291].

[198] C.-H. Chen and T. Nomura, *$SU(2)_X$ vector DM and Galactic Center gamma-ray excess*, *Phys. Lett. B* **746** (2015) 351–358, [1501.07413].

[199] J. L. Diaz-Cruz and E. Ma, *Neutral $su(2)$ gauge extension of the standard model and a vector-boson dark-matter candidate*, *Physics Letters B* **695** (2011) 264 – 267.

[200] J. Diaz-Cruz and E. Ma, *Neutral $SU(2)$ Gauge Extension of the Standard Model and a Vector-Boson Dark-Matter Candidate*, *Phys. Lett. B* **695** (2011) 264–267, [1007.2631].

[201] S. Bhattacharya, J. L. Diaz-Cruz, E. Ma and D. Wegman, *Dark Vector-Gauge-Boson Model*, *Phys. Rev.* **D85** (2012) 055008, [1107.2093].

[202] Y. Hochberg, E. Kuflik, T. Volansky and J. G. Wacker, *Mechanism for Thermal Relic Dark Matter of Strongly Interacting Massive Particles*, *Phys. Rev. Lett.* **113** (2014) 171301, [1402.5143].

[203] S.-M. Choi, Y. Hochberg, E. Kuflik, H. M. Lee, Y. Mambrini, H. Murayama et al., *Vector SIMP dark matter*, *JHEP* **10** (2017) 162, [1707.01434].

[204] S.-M. Choi, H. M. Lee, Y. Mambrini and M. Pierre, *Vector SIMP dark matter with approximate custodial symmetry*, *JHEP* **07** (2019) 049, [1904.04109].

[205] I. Chaffey and P. Tanedo, *Vector self-interacting dark matter*, *Phys. Rev. D* **101** (2020) 075005, [1907.10217].

[206] G. Arcadi, C. Gross, O. Lebedev, Y. Mambrini, S. Pokorski and T. Toma, *Multicomponent Dark Matter from Gauge Symmetry*, *JHEP* **12** (2016) 081, [1611.00365].

[207] A. Poulin and S. Godfrey, *Multicomponent dark matter from a hidden gauged $SU(3)$*, *Phys. Rev.* **D99** (2019) 076008, [1808.04901].

[208] P. Ko and Y. Tang, *Residual Non-Abelian Dark Matter and Dark Radiation*, *Phys. Lett. B* **768** (2017) 12–17, [1609.02307].

[209] K2K collaboration, S. H. Ahn et al., *Detection of accelerator produced neutrinos at a distance of 250-km*, *Phys. Lett.* **B511** (2001) 178–184, [hep-ex/0103001].

[210] LSND collaboration, A. Aguilar-Arevalo et al., *Evidence for neutrino oscillations from the observation of $\bar{\nu}_e$ appearance in a $\bar{\nu}_\mu$ beam*, *Phys. Rev.* **D64** (2001) 112007, [hep-ex/0104049].

[211] KARMEN collaboration, B. Armbruster et al., *Upper limits for neutrino oscillations muon-anti-neutrino —¿ electron-anti-neutrino from muon decay at rest*, *Phys. Rev.* **D65** (2002) 112001, [hep-ex/0203021].

[212] C. Rubbia et al., *Underground operation of the ICARUS T600 LAr-TPC: first results*, *JINST* **6** (2011) P07011, [1106.0975].

[213] T2K collaboration, K. Abe et al., *Observation of Electron Neutrino Appearance in a Muon Neutrino Beam*, *Phys. Rev. Lett.* **112** (2014) 061802, [1311.4750].

[214] MINOS+ collaboration, P. Adamson et al., *Search for sterile neutrinos in MINOS and MINOS+ using a two-detector fit*, *Phys. Rev. Lett.* **122** (2019) 091803, [1710.06488].

[215] Hyper-Kamiokande collaboration, K. Abe et al., *Hyper-Kamiokande Design Report*, 1805.04163.

[216] MiniBooNE collaboration, A. A. Aguilar-Arevalo et al., *Significant Excess of ElectronLike Events in the MiniBooNE Short-Baseline Neutrino Experiment*, *Phys. Rev. Lett.* **121** (2018) 221801, [1805.12028].

[217] P. Minkowski, *e at a rate of one out of 109 muon decays?*, *Physics Letters B* **67** (1977) 421 – 428.

[218] R. N. Mohapatra and G. Senjanović, *Neutrino mass and spontaneous parity nonconservation*, *Phys. Rev. Lett.* **44** (Apr, 1980) 912–915.

[219] M. Gell-Mann, P. Ramond and R. Slansky, *Complex Spinors and Unified Theories*, *Conf. Proc.* **C790927** (1979) 315–321, [1306.4669].

[220] M. Magg and C. Wetterich, *Neutrino mass problem and gauge hierarchy*, *Physics Letters B* **94** (1980) 61 – 64.

[221] J. Schechter and J. W. F. Valle, *Neutrino masses in $su(2) \otimes u(1)$ theories*, *Phys. Rev. D* **22** (Nov, 1980) 2227–2235.

[222] C. Wetterich, *Neutrino masses and the scale of b-l violation*, *Nuclear Physics B* **187** (1981) 343 – 375.

[223] G. Lazarides, Q. Shafi and C. Wetterich, *Proton lifetime and fermion masses in an $so(10)$ model*, *Nuclear Physics B* **181** (1981) 287 – 300.

[224] R. N. Mohapatra and G. Senjanović, *Neutrino masses and mixings in gauge models with spontaneous parity violation*, *Phys. Rev. D* **23** (Jan, 1981) 165–180.

[225] R. Foot, H. Lew, X. G. He and G. C. Joshi, *Seesaw Neutrino Masses Induced by a Triplet of Leptons*, *Z. Phys.* **C44** (1989) 441.

[226] E. Ma, *Pathways to naturally small neutrino masses*, *Phys. Rev. Lett.* **81** (Aug, 1998) 1171–1174.

[227] E. Ma and D. P. Roy, *Heavy triplet leptons and new gauge boson*, *Nucl. Phys.* **B644** (2002) 290–302, [hep-ph/0206150].

[228] T. Hambye, Y. Lin, A. Notari, M. Papucci and A. Strumia, *Constraints on neutrino masses from leptogenesis models*, *Nucl. Phys.* **B695** (2004) 169–191, [hep-ph/0312203].

[229] B. Bajc and G. Senjanovic, *Seesaw at LHC*, *JHEP* **08** (2007) 014, [hep-ph/0612029].

[230] R. N. Mohapatra and G. Senjanovic, *Neutrino Mass and Spontaneous Parity Nonconservation*, *Phys. Rev. Lett.* **44** (1980) 912.

[231] J. Schechter and J. W. F. Valle, *Neutrino Masses in $SU(2)$ x $U(1)$ Theories*, *Phys. Rev.* **D22** (1980) 2227.

[232] E. K. Akhmedov, G. C. Branco and M. N. Rebelo, *Seesaw mechanism and structure of neutrino mass matrix*, *Phys. Lett.* **B478** (2000) 215–223, [hep-ph/9911364].

[233] K. S. Babu and C. N. Leung, *Classification of effective neutrino mass operators*, *Nucl. Phys.* **B619** (2001) 667–689, [hep-ph/0106054].

[234] Z.-z. Xing and S. Zhou, *Neutrinos in particle physics, astronomy and cosmology*. 2011.

[235] E. Ma, *Verifiable radiative seesaw mechanism of neutrino mass and dark matter*, *Phys. Rev.* **D73** (2006) 077301, [hep-ph/0601225].

[236] P.-H. Gu and U. Sarkar, *Radiative Neutrino Mass, Dark Matter and Leptogenesis*, *Phys. Rev.* **D77** (2008) 105031, [0712.2933].

[237] J. C. Pati and A. Salam, *Lepton number as the fourth "color"*, *Phys. Rev. D* **10** (Jul, 1974) 275–289.

[238] H. Georgi and S. L. Glashow, *Unity of all elementary-particle forces*, *Phys. Rev. Lett.* **32** (Feb, 1974) 438–441.

[239] H. Georgi, H. R. Quinn and S. Weinberg, *Hierarchy of interactions in unified gauge theories*, *Phys. Rev. Lett.* **33** (Aug, 1974) 451–454.

[240] R. Slansky, *Group Theory for Unified Model Building*, *Phys. Rept.* **79** (1981) 1–128.

[241] G. Senjanovic, *SO(10): A Theory of fermion masses and mixings*, in *CP Violation and the Flavour Puzzle: Symposium in Honour of Gustavo C. Branco. GustavoFest 2005, Lisbon, Portugal, July 2005*, 2006. hep-ph/0612312.

[242] B. Allanach, *Beyond the Standard Model Lectures for the 2016 European School of High-Energy Physics*, in *2016 European School of High-Energy Physics*, pp. 123–152, 2017. 1609.02015. DOI.

[243] Super-Kamiokande collaboration, K. Abe et al., *Search for proton decay via $p \to e^+\pi^0$ and $p \to \mu^+\pi^0$ in 0.31 megaton·years exposure of the Super-Kamiokande water Cherenkov detector*, *Phys. Rev.* **D95** (2017) 012004, [1610.03597].

[244] Planck collaboration, P. A. R. Ade et al., *Planck 2015 results. XIII. Cosmological parameters*, *Astron. Astrophys.* **594** (2016) A13, [1502.01589].

[245] B. Barman, S. Bhattacharya, S. K. Patra and J. Chakrabortty, *Non-Abelian Vector Boson Dark Matter, its Unified Route and signatures at the LHC*, *JCAP* **1712** (2017) 021, [1704.04945].

[246] V. Andreev, P. Osland and A. Pankov, *Precise determination of Z-Z' mixing at the CERN LHC*, *Phys. Rev. D* **90** (2014) 055025, [1406.6776].

[247] A. Flórez, A. Gurrola, W. Johns, Y. D. Oh, P. Sheldon, D. Teague et al., *Searching for New Heavy Neutral Gauge Bosons using Vector Boson Fusion Processes at the LHC*, *Phys. Lett. B* **767** (2017) 126–132, [1609.09765].

[248] J. Hisano, K. Ishiwata, N. Nagata and M. Yamanaka, *Direct Detection of Vector Dark Matter*, *Prog. Theor. Phys.* **126** (2011) 435–456, [1012.5455].

[249] J. Hisano, R. Nagai and N. Nagata, *Effective Theories for Dark Matter Nucleon Scattering*, *JHEP* **05** (2015) 037, [1502.02244].

[250] J. Chakrabortty and A. Raychaudhuri, *GUTs with dim-5 interactions: Gauge Unification and Intermediate Scales*, *Phys. Rev. D* **81** (2010) 055004, [0909.3905].

[251] F. Del Aguila and L. Ibáñez, *Higgs bosons in so(10) and partial unification*, *Nuclear Physics B* **177** (1981) 60 – 86.

[252] J. Alwall, R. Frederix, S. Frixione, V. Hirschi, F. Maltoni, O. Mattelaer et al., *The automated computation of tree-level and next-to-leading order differential cross sections, and their matching to parton shower simulations*, *JHEP* **07** (2014) 079, [1405.0301].

[253] S. Fraser, E. Ma and M. Zakeri, *$SU(2)_N$ model of vector dark matter with a leptonic connection*, *Int. J. Mod. Phys.* **A30** (2015) 1550018, [1409.1162].

[254] B. Barman, S. Bhattacharya and M. Zakeri, *Multipartite Dark Matter in $SU(2)_N$ extension of Standard Model and signatures at the LHC*, *JCAP* **1809** (2018) 023, [1806.01129].

[255] Y. Mambrini, S. Profumo and F. S. Queiroz, *Dark Matter and Global Symmetries*, *Phys. Lett. B* **760** (2016) 807–815, [1508.06635].

[256] S. Durr et al., *Lattice computation of the nucleon scalar quark contents at the physical point*, *Phys. Rev. Lett.* **116** (2016) 172001, [1510.08013].

[257] XENON collaboration, E. Aprile et al., *First Dark Matter Search Results from the XENON1T Experiment*, *Phys. Rev. Lett.* **119** (2017) 181301, [1705.06655].

[258] S. Bhattacharya, P. Poulose and P. Ghosh, *Multipartite Interacting Scalar Dark Matter in the light of updated LUX data*, *JCAP* **1704** (2017) 043, [1607.08461].

[259] B. Barman, S. Bhattacharya and M. Zakeri, *Non-Abelian Vector Boson as FIMP Dark Matter*, *JCAP* **2002** (2020) 029, [1905.07236].

[260] K. Jedamzik, *Big bang nucleosynthesis constraints on hadronically and electromagnetically decaying relic neutral particles*, *Phys. Rev.* **D74** (2006) 103509, [hep-ph/0604251].

[261] K. Jedamzik and M. Pospelov, *Big Bang Nucleosynthesis and Particle Dark Matter*, *New J. Phys.* **11** (2009) 105028, [0906.2087].

[262] AMS collaboration, M. Aguilar et al., *Antiproton Flux, Antiproton-to-Proton Flux Ratio, and Properties of Elementary Particle Fluxes in Primary Cosmic Rays Measured with the Alpha Magnetic Spectrometer on the International Space Station*, *Phys. Rev. Lett.* **117** (2016) 091103.

[263] A. Belyaev, N. D. Christensen and A. Pukhov, *CalcHEP 3.4 for collider physics within and beyond the Standard Model*, *Comput. Phys. Commun.* **184** (2013) 1729–1769, [1207.6082].

[264] R. Placakyte, *Parton Distribution Functions*, in *Proceedings, 31st International Conference on Physics in collisions (PIC 2011): Vancouver, Canada, August 28-September 1, 2011*, 2011. 1111.5452.

[265] MoEDAL collaboration, N. E. Mavromatos and V. A. Mitsou, *Physics reach of MoEDAL at LHC: magnetic monopoles, supersymmetry and beyond*, *EPJ Web Conf.* **164** (2017) 04001, [1612.07012].

[266] G. Bélanger et al., *LHC-friendly minimal freeze-in models*, *JHEP* **02** (2019) 186, [1811.05478].

[267] CMS collaboration, C. Collaboration, *Search for heavy stable charged particles with* 12.9 $\text{fb}^{-1}$ *of 2016 data*, .

[268] M. Duch, B. Grzadkowski and J. Wudka, *Classification of effective operators for interactions between the Standard Model and dark matter*, *JHEP* **05** (2015) 116, [1412.0520].

[269] V. Gonzalez Macias and J. Wudka, *Effective theories for Dark Matter interactions and the neutrino portal paradigm*, *JHEP* **07** (2015) 161, [1506.03825].

[270] B. Barman, S. Bhattacharya and B. Grzadkowski, *Feebly coupled vector boson dark matter in effective theory*, 2009.07438.

[271] K. Kannike, *Vacuum Stability Conditions From Copositivity Criteria*, *Eur. Phys. J.* **C72** (2012) 2093, [1205.3781].

[272] K. Kannike, *Vacuum Stability of a General Scalar Potential of a Few Fields*, *Eur. Phys. J.* **C76** (2016) 324, [1603.02680].

[273] M. Duch, B. Grzadkowski and M. McGarrie, *Vacuum stability from vector dark matter*, *Acta Phys. Polon.* **B46** (2015) 2199, [1510.03413].

[274] B. Barman, D. Borah and R. Roshan, *Effective Theory of Freeze-in Dark Matter*, 2007.08768.

[275] D. Tucker-Smith and N. Weiner, *Inelastic dark matter*, *Phys. Rev.* **D64** (2001) 043502, [hep-ph/0101138].

[276] M. Chala, F. Kahlhoefer, M. McCullough, G. Nardini and K. Schmidt-Hoberg, *Constraining Dark Sectors with Monojets and Dijets*, *JHEP* **07** (2015) 089, [1503.05916].

[277] ATLAS collaboration, M. Aaboud et al., *Search for new phenomena in final states with an energetic jet and large missing transverse momentum in* $pp$ *collisions at* $\sqrt{s} = 13$ *TeV using the ATLAS detector*, *Phys. Rev. D* **94** (2016) 032005, [1604.07773].

[278] Particle Data Group collaboration, M. Tanabashi, K. Hagiwara, K. Hikasa, K. Nakamura, Y. Sumino, F. Takahashi et al., *Review of particle physics*, *Phys. Rev. D* **98** (Aug, 2018) 030001.

[279] T. Sjostrand, S. Mrenna and P. Z. Skands, *PYTHIA 6.4 Physics and Manual*, *JHEP* **05** (2006) 026, [hep-ph/0603175].